

https://dspace.org/

In situ x-ray diffraction analysis of Fischer Tropsch synthesis.

Chiwaye, Natsayi

2013-07-15
http://hdl.handle.net/10539/12835

Downloaded from a DSpace repository. https://dspace.org/

IN SITU X-RAY DIFFRACTION ANALYSIS OF FISCHER TROPSCH SYNTHESIS

Natsayi Chiwaye

A dissertation submitted to the Faculty of Engineering and the Built Environment, University of the Witwatersrand, Johannesburg, in fulfilment of the requirements for the degree of Master of Science in Engineering

Johannesburg 2012

DECLARATION

I declare that the work presented in this dissertation is my own unaided work. It is being submitted for the Degree of Master of Science in Engineering to the University of the Witwatersrand, Johannesburg. It has not been submitted before for any degree or examination in any other University.

.....

Natsayi Chiwaye

On this…….**day of** ……..**2012 at** ……

ABSTRACT

Fe-Co/$CaCO_3$ catalysts for the synthesis of multi walled carbon nanotubes were synthesised by an incipient wetness impregnation method. This catalyst was then characterised by in situ variable temperature X-ray diffraction (XRD) and in situ XRD reduction. Other characterisation techniques such as temperature programmed reduction (TPR), thermal gravimetric analysis (TGA) and transmission electron microscopy (TEM) were used to analyse the catalyst. As the temperature was raised $CaCO_3$ decomposed to CaO and also a Ca_2FeCoO_5 phase could be identified. Upon reduction an FeCo alloy was also identified.

MWCNTs were synthesised by pyrolysis of acetylene at 700 ˚C over this 10% Fe-Co/$CaCO_3$ catalyst. The synthesis was carried out for 1 hour with nitrogen as the carrier gas in a ratio N_2: C_2H_2 (1: 2.7). The product was then purified by nitric acid to remove the Fe-Co/$CaCO_3$ catalyst particles as well as amorphous carbon. Purification was done by refluxing the product in 55% nitric acid at 120 ˚C for 6 hours. The as-grown and purified MWCNTs were analysed by various techniques such as, Raman spectroscopy, TEM, surface area analysis and TGA. TEM confirmed that MWCNTs had indeed been synthesised. The as grown MWCNTs had an average outer diameter of 29 nm whilst the diameter of the purified sample was 24 nm. TGA showed that most of the catalyst particles had been removed after acid purification. Fourier Transform infra-red spectroscopy confirmed that functional groups such as carboxylic groups had been introduced by acid treatment.

These MWCNTs were used as support for a ruthenium catalyst. 10% Ru/MWCNTs were synthesised by the incipient wetness impregnation (IMP) method and deposition precipitation (DPM) method using urea as deposition agent. TEM analysis revealed that the dispersion of the ruthenium metal on the MWCNTs was better on the DPM catalyst than on IMP. The DPM catalyst had smaller Ru particles (2.4 nm) with a narrower size range than Ru particles produced by the IMP method (5.2 nm). Addition of Ru metal onto the MWCNT surface aided in the thermal decomposition of the MWCNTs in air. TPR revealed that the DPM catalyst was easier to reduce than the IMP catalyst. The catalyst was heat treated under N_2 at 400 ˚C to decompose the precursor salt. It was observed that RuO_2 was reduced

to Ru metal under these conditions with the extent of reduction for the DPM catalyst reaching 100% whereas for the IMP catalyst was 80%.

The catalysts were tested for FT using syngas at reaction temperatures of 220 ˚C and 250 ˚C and 8 bar pressure, in the ratio 2:1 of H_2: CO. As expected the activity at 250 ˚C was greater than at 220 ˚C and selectivity to heavier hydrocarbons was realised at the lower reaction temperature. The preparation method influenced the dispersion and the Ru particle size but it only had a slight impact on the activity and selectivity of the FT synthesis reaction.

DEDICATION

To Linda Jewell: For giving me a chance.

ACKNOWLEDGEMENTS

I would like to express my heartfelt gratitude to the following people who assisted me in this research.

- My supervisor Professor Linda. L. Jewell and co-supervisors Professor Dave G. Billing and Professor Neil. J. Coville for their unending support and guidance throughout this research.
- Professor Zigler, head of the Microscopy unit at the University of the Witwatersrand for teaching me how to use the Fei Tecnai Spirit microscope for TEM analysis.
- Dr Rudolph Erasmus for Raman spectroscopy analysis.
- Professor D. Naidoo and Mr Mehluli Ncube for assisting with Fe Mossbauer.
- Basil Chassoulas for helping with setting up and operating the FT rig.
- My colleagues in the CATOMMAT reseach group; Manoko, Isaac, Themba, George, Myriam, Zikhona, Angelica, Sibongile, Thobeka, Michele and Wilson.
- The University of the Witwatersrand Postgraduate Merit Award and NRF Thuthuka Fund for financial assistance.

PRESENTATIONS RESULTING FROM THIS WORK

Poster presentations

1. Material Research Society **(MRS)** Africa conference 2011 , Victoria Falls, Zimbabwe

   In-situ PXRD Study of Fe-Co/$CaCO_3$ Bimetallic Catalysts for the Synthesis of Multi Walled Carbon Nanotubes

2. South Africa Institute of Chemical Engineering **(SAIChe),** conference 2012 Drakensburg, South Africa

   Ruthenium Supported on Carbon nanotubes catalyst for Fischer - Tropsch Synthesis

TABLE OF CONTENTS

DECLARATION..... i

ABSTRACT..... ii

DEDICATION..... iv

ACKNOWLEDGEMENTS..... v

PRESENTATIONS RESULTING FROM THIS WORK..... vi

TABLE OF CONTENTS..... vii

LIST OF FIGURES..... xii

LIST OF TABLES..... xvii

LIST OF SYMBOLS..... xix

CHAPTER 1..... 1

1 INTRODUCTION..... 1

1.1 Introduction..... 1

1.2 Motivation..... 3

1.3 Objective 3

1.4 Aims..... 3

1.5 Methodology..... 4

1.6 Outline of this dissertation..... 4

CHAPTER 2..... 6

2 LITERATURE REVIEW..... 6

2.1 Carbon nanotubes..... 6

2.1.1 Introduction..... 6

2.1.2 Properties of carbon nanotubes 6

2.1.3 CNTs synthesis..... 8

2.1.4 Catalytic Chemical Vapour Deposition..... 9

2.1.5 Mechanism of CNT growth..... 14

2.1.6 Purification of carbon nanotubes..... 18

2.1.7 Use of carbon nanotubes in catalysis..... 19
2.2 Fischer-Tropsch Synthesis..... 20
2.2.1 Introduction..... 20
2.2.2 FT reaction..... 20
2.2.3 FT catalysts..... 21
2.2.4 Fischer-Tropsch catalyst supports..... 22
2.2.5 Carbon nanotubes as supports for FT catalysts 23
2.2.6 Auto-reduction of metal oxides supported on carbon supports..... 25
2.2.7 Promoters..... 25
2.2.8 Ru/CNTs for FT..... 27
2.2.9 Preparations methods..... 27
2.3 Powder X-ray diffraction analysis..... 28
2.3.1 Introduction..... 28
2.3.2 History of X-ray diffraction..... 28
2.3.3 Basic concepts of PXRD analysis..... 29
2.3.4 Intensity of reflection peak in powder diffraction..... 31
2.3.5 Rietveld refinement method..... 33
2.3.6 Uses of PXRD technique in analysing catalytic materials..... 36
2.3.7 In situ diffraction analysis – some case studies..... 38
CHAPTER 3..... 44
3 EXPERIMENTAL METHODS..... 44
3.1 Synthesis Procedures..... 44
3.1.1 Preparation of Fe-Co/CaCO3 catalysts for the synthesis of CNTs..... 44
3.1.2 Synthesis of multi walled carbon nanotubes..... 44
3.1.3 Purification of carbon nanotubes..... 45
3.1.4 Synthesis of catalysts for Fischer-Tropsch..... 46
3.2 Characterisation Techniques..... 46
3.2.1 Thermal gravimetric analysis 46
3.2.2 Transmission electron microscopy 47
3.2.3 Raman spectroscopy..... 48

3.2.4 BET Surface area analysis…… 48
3.2.5 Temperature programmed reduction …….. 48
3.2.6 Fourier transform infra-red spectroscopy…… 49
3.2.7 Powder X-Ray Diffraction ……49
3.2.8 Calibration of Instruments ……54
3.2.9 Powder X-ray Diffraction Data Analysis……55
3.3 Fischer Tropsch synthesis…… 57
3.3.1 Fischer Tropsch synthesis Rig……57
3.3.2 Fischer Tropsch Synthesis……59
3.3.3 Analysis of Fischer-Tropsch data…… 61
CHAPTER 4…… 66
4 IN SITU PXRD STUDY OF A Fe-Co/$CaCO_3$ CATALYST FOR THE SYNTHESIS OF CARBON NANOTUBES……66
4.1 Introduction……66
4.1.2 Experimental…….. 67
4.2 Thermal response of Fe-Co/$CaCO_3$ catalysts…… 69
4.2.1 Surface area analysis…… 69
4.2.2 Transmission electron microscopy……70
4.2.3 In situ VT-XRD study of $CaCO_3$…… 73
4.2.4 In situ VT-PXRD study of10% Fe/$CaCO_3$ …… 77
4.2.5 In situ VT-PXRD study of 10% Co/$CaCO_3$…… 80
4.2.6 In situ VT-PXRD study of 10% Fe-Co/$CaCO_3$ …… 82
4.2.7 Thermal gravimetric analysis …… 91
4.2.8 Iron Mossbauer spectroscopy studies of 10% Fe-Co/$CaCO_3$…… 93
4.3 Reduction Studies……95
4.3.1 TPR study of Fe, Co/$CaCO_3$ catalysts……96
4.3.2 In situ PXRD reduction of 10% Fe-Co/$CaCO_3$ …… 97
4.3.3 In situ PXRD reduction of 10% Co/$CaCO_3$ and 10% Fe/$CaCO_3$……100
4.4 Conclusion……102
CHAPTER 5……103

5 RUTHENIUM CATALYST SUPPORTED ON MULTI WALLED CARBON NANOTUBES FOR USE IN THE FISCHER TROPSCH SYNTHESIS……103

5.1 Introduction…… 103

5.1.1 Experimental……104

5.1.2 PXRD Analysis……104

5.2 Characterisation of multi walled carbon nanotubes…… 105

5.2.1 Transmission electron microscopy ……103

5.2.2 Raman spectroscopy analysis……105

5.2.3 Thermal gravimetric analysis ……109

5.2.4 Powder X-ray diffraction ……111

5.2.5 FTIR spectroscopy……112

5.3 Characterisation of Catalysts for FTS…… 113

5.3.1 PXRD of catalysts……113

5.3.2 In situ variable temperature PXRD study of 10Ru/CNTR6-IMP……115

5.3.3 Surface area analysis……116

5.3.4 Transmission electron microscopy……117

5.3.5 TGA of synthesised FTS catalysts……119

5.3.6 In situ variable temperature PXRD reduction……121

5.3.7 Temperature programmed reduction (TPR) ……123

5.4 Catalytic performance…… 125

5.4.1 Effect of reaction temperature on FTS……125

5.4.2 Effect of preparation method on FTS…… 128

5.4.3 Analysis of spent catalysts……129

5.5 Conclusion……133

CHAPTER 6 …… 134

6 CONCLUSIONS AND RECOMMENDATIONS…… 134

6.1 Conclusion ……134

6.2 Recommendations …… 135

REFERENCES …… 136

APPENDICES……. **158**

Appendix A……. **158**

Appendix B……. **179**

LIST OF FIGURES

Figure 2.1: Some of the allotropes of carbon……..6

Figure 2.2: Proposed reaction scheme for MWNTs production explaining the observed byproducts…… 12

Figure 2.3: Tip-growth mechanism (b) base-growth mechanism …… 15

Figure 2.4: Magrez et al` s triple point joint cartoon…….. 17

Figure 2.5: Reaction pathways for the growth of CNTs…… 17

Figure 2.6: Unit cell structures……30

Figure 2.7: Arrangement of atoms in hkl planes in a NaCl unit cell…… 30

Figure 2.8: X-rays interacting with a solid material…….. 31

Figure 2.9: PXRD patterns showing the reduction of Co_3O_4/ ϒ-Al_2O_3 at different temperature …… 41

Figure 2.10: Patterns (i) and (iii) were taken at room temperature but before and after reaction respectively……..43

Figure 3.1: Reactor set up for the synthesis of MWCNTs…… 45

Figure 3.2: FEI-Tecnai G^2 Spirit microscope for transmission electron microscopy Analysis……48

Figure 3.3: A picture of the Bruker D8 Advance diffractometer……51

Figure 3.4: Schematic pictures of the Anton Paar XRK 900 showing its components……. 52

Figure 3.5: Gas supply system to the XRK……53

Figure 3.6: A plot of Okada et al experimental Si lattice parameter against temperature and that of Si NIST SRM 460 over a temperature range of 0-1200 K…….. 55

Figure 3.7: Fischer-Tropsch Synthesis rig……..58

Figure 3.8: Picture showing a thermocouple and the micro reactor…… 58

Figure 3.9: catalyst packing inside the fixed bed reactor..... 59

Figure 3.10: Typical trace of synthesis gas on the TCG GC……..61

Figure 3.11: Typical trace of the calibration gas on the FID GC…… 62

Figure 4.1: TEM Images of $CaCO_3$, 10% Fe/$CaCO_3$, 10% Co/ $CaCO_3$,

10% Fe-Co/ $CaCO_3$……71

Figure 4.2: TEM images of 10%Fe/$CaCO_3$; $CaCO_3$, 10% Fe/$CaCO_3$,10% Co/$CaCO_3$,

10% Fe-Co/ $CaCO_3$ and 10% Co/$CaCO_3$ amorphous material after heat treatment……72

Figure 4.3: 3D figure showing patterns collected during in situ VT-PXRD of $CaCO_3$……73

Figure 4.4: Phase abundance variation during VT-PXRD of $CaCO_3$……74

Figure 4.5: Refinement results for pattern collected at 50 ˚C during VT-PXRD of

$CaCO_3$……75

Figure 4.6: Refinement results for pattern collected at 730 ˚C during VT-PXRD of

$CaCO_3$……75

Figure 4.7: Phase abundance variation during VT-PXRD of $CaCO_3$…….. 76

Figure 4.8: Variation of particle size during VT-PXRD heat treatment of $CaCO_3$……..77

Figure 4.9: VT-PXRD patterns over temperature for 10% Fe/$CaCO_3$…….. 78

Figure 4.10: Structure of dicalcium diiron (III) oxide ($Ca_2Fe_2O_5$) 78

Figure 4.11: Phase abundance variation during VT-PXRD analysis of 10% Fe/$CaCO_3$…….. 79

Figure 4.12: Particle size variation during VT-PXRD of 10% Fe/$CaCO_3$…….. 80

Figure 4.13: Phase abundance variation during VT-PXRD of 10% Co/$CaCO_3$……81

Figure 4.14: Phase abundance variation during VT-PXRD of 10% Co/$CaCO_3$.....81

Figure 4.15: Particle size variation during VT-PXRD of 10% Co/$CaCO_3$……..82

Figure 4.16: VT-PXRD profile of 10% Fe-Co/$CaCO_3$.....84

Figure 4.17: XRD pattern of 10%Fe-Co/$CaCO_3$ collected at room temperature……85

Figure 4.18: XRD pattern of 10%Fe-Co/$CaCO_3$ collected at room temperature using a Co X-ray source…… 85

Figure 4.19: PXRD pattern of 10% Fe-Co/$CaCO_3$ at 700 ˚C showing Ca_2FeCoO_5……..86

Figure 4.20: XRD pattern showing of pure Fe_2CoO_4 as reported by Magrez et al. (2005) Cu source…… 86

Figure 4.21: XRD pattern showing Fe_2CoO_4 diffraction peaks as reported by Li et al. (2008) Cu source…… 87

Figure 4.22: Structure of dicalcium iron cobalt pentaoxide (Ca_2FeCoO_5)……..87

Figure 4.23: Phase abundance variation during VT-PXRD of 10% Fe-Co/$CaCO_3$…….. 88

Figure 4.24: Particle size variation of phases during VT-PRXD of 10% Fe-Co/$CaCO_3$……89

Figure 4.25: XRD patterns of the catalysts heated at 700 ˚C for 30 min under N_2……90

Figure 4.26: TGA profiles of the Fe-Co catalysts…… 92

Figure 4.27: TGA weight derivatives of the various Fe-Co/$CaCO_3$ catalysts……92

Figure 4.28: ^{57} Fe Mossbauer spectrum collected at room temperature (as synthesised sample)……93

Figure 4.29: ^{57} Fe Mossbauer spectrum collected at room temperature (thermally treated at 700 °C)…….. 94

Figure 4.30: TPR profiles of the catalysts…… 97

Figure 4.31: TPR profiles of the 10% Fe/$CaCO_3$ further heated for 10 hours …… 97

Figure 4.32: In-situ Reduction of 10% Fe-Co/$CaCO_3$……98

Figure 4.33: Variation of phase abundance with time……..100

Figure 4.34: Variation of phase particle size with time during reduction…… 100

Figure 4.35: In situ reduction of 10% $Co/CaCO_3$ at 700 ˚C…… 101

Figure 4.36: In situ reduction of 10% $Fe/CaCO_3$ at 700 ˚C…… 102

Figure 5.1: As grown MWCNTs; arrow shows encapsulated particle…… 106

Figure 5.2: Histograms showing the distribution of diameter sizes for the outer and inner diameters of as-grown MWCNTs……107

Figure 5.3: TEM image of purified MWCNTs…… 108

Figure 5.4: Histograms showing the distribution of the diameter sizes for the outer and inner diameters of acid washed MWCNTs…… 108

Figure 5.5: Spectra of as grown and purified MWCNTs…… 109

Figure 5.6: TGA profiles of as grown (AGCNTs) and acid washed carbon nanotubes (CNTR6)…… 110

Figure 5.7: Derivative plots of TGA profiles for as grown (AGCNT) and acid washed carbon nanotubes (CNTR6)……111

Figure 5.8: TGA profile of CNTR6 annealed at 600 ˚C under N_2 for 1 hour…… 111

Figure 5.9: PXRD pattern of as grown and purified CNTs…… 112

Figure 5.10: FTIR profiles of AGCNT and CNTR6…… 113

Figure 5.11: XRD patterns of 10Ru/CNTR6-IMP before and after heat treatment at 400 ˚C…… 114

Figure 5.12: XRD patterns of 10Ru/CNTR6-DMP before and after heat treatment at 400 ˚C for 3.5 hours…… 115

Figure 5.13: VT-PXRD calcination study of 10Ru/CNT-IMP……116

Figure 5.14: TEM image of 10%Ru/CNT-IMP……118

Figure 5.15: TEM image of 10%Ru/CNT-DPM…… 118

Figure 5.16: TGA plot 10Ru/CNTR6 prepared by impregnation before heat treatment and its derivative curve……..119

Figure 5.17: TGA plot of 10Ru/CNT-IMP and 10Ru/CNT-DPM after heat treatment at 400 ˚C under N_2 for 4 hours…….. 120

Figure 5.18: Derivative TGA plot of 10Ru/CNT-IMP and 10Ru/CNT-DPM after heat treatment at 400 ˚C under N_2 for 4 hours……121

Figure 5.19: VT-PXRD reduction of 10Ru/CNT-IMP…… 122

Figure 5.20: Particle size variation of Ru metal during VT-PXRD reduction……..123

Figure 5.21: TPR profiles of synthesised catalyst and CNTs…… 124

Figure 5.22: CO conversion over a period of 120 hours in FTS…… 126

Figure 5.23: Olefin to paraffin ratio…… 129

Figure 5.24: Spent catalysts after FTS……131

Figure 5.25: TGA profile of spent 10Ru/CNTs-DPM for FTS carried out at 250 ˚C and its derivative …… 132

Figure 5.26: TGA profile of spent 10Ru/CNTs-DPM for FTS carried out at 220 ˚C and its derivative …… 132

LIST OF TABLES

Table 2.1: Unit cell structures……..29

Table 3.1: Specifications and settings of Bruker D2 Phaser…….. 50

Table 3.2: Specifications and settings of the Bruker D8 Advance…….. 50

Table 3.3: Specifications and properties of the macor sample holder……..53

Table 3.4: In-situ experiments done to analyse the Fe-Co/$CaCO_3$ catalyst used in this Study……..57

Table 4.1: Experimental details of in situ VT-PXRD of $CaCO_3$ and 10% Fe/$CaCO_3$……..68

Table 4.2: Experimental details of the in situ VT-PXRD of $CaCO_3$ and 10% Fe-Co/$CaCO_3$…….. 68

Table 4.3: Experimental details of the in situ reduction of the catalysts carried at 700 ˚C……69

Table 4.4: BET Surface area…….. 70

Table 4.5: 2θ positions of Fe_2CoO_4 as reported by Magrez et al. and Li et al……..86

Table 4.6: Phase abundance of $Ca_2M_2O_5$ in the catalysts at various temperatures during VT-PXRD…….. 89

Table 4.7: % weight loss at various temperature points…….. 93

Table 4.8: Mossbauer parameters for synthesised sample……..94

Table 4.9: Mossbauer parameters for thermally treated sample…….. 94

Table 5.1: Quantitative Rietveld refinement analysis of CNTR6/CaF_2…….. 105

Table 5.2: Raman spectroscopy; I_D/I_G ratio of as grown and purified carbon nanotubes…. 109

Table 5.3: BET surface areas for MWNTs and catalysts synthesised…….. 117

Table 5.4: VT-PXRD reduction results of 10Ru/CNT-IMP at 30 ˚C and 270 ˚C ……..123

Table 5.5: Activity and selectivity of catalysts during FTS……..... 127

Table 5.6: Olefin to paraffin ratio of the catalyst…….. 127

Table 5.7: Ru particle size of spent catalysts …… 130

LIST OF SYMBOLS

ASF	Anderson-Schulz-Flory
BET	Brunauer-Emmett-Teller
BCC	Body-centered cubic
CVD	Chemical vapour deposition
CNTs	Carbon nanotubes
EM	Electron microscopy
FCC	Face-centered cubic
FDS	Fixed divergence slit
FT	Fischer-Tropsch
FTS	Fischer-Tropsch synthesis
GC	Gas chromatography
G.o.F	Goodness of fit
mL/min	Millilitre per minute
NIST	National Institute for Standards and Technology
SWNTs	Single walled carbon nanotubes
SRM	Standard reference material
Syngas	Synthesis gas
TCD	Thermal conductivity detector
TEM	Transmission electron microscopy
TGA	Thermogravimetric analysis
TPR	Temperature programmed reduction
XRD	X-ray diffraction

PXRD	Powder X-ray diffraction
VT-PXRD	Variable temperature X-ray diffraction
α	Alpha value

CHAPTER 1

1 INTRODUCTION

1.1 Introduction

Crude oil reserves continue to be depleted with known reserves poised to last for only 50 years (McMahon, 2010). With crude oil prices continuing to increase, the need for alternatives to petroleum cannot be over emphasised. Fischer-Tropsch Synthesis (FTS), a technology developed by Fischer and Tropsch in 1926 continues to be of much interest in today's world as it offers an alternative route in the production of fuel (Dancuart, 2007).

FTS involves the catalytic conversion of syngas (CO+ H_2) into various types of hydrocarbons (Schulz, 1999). Syngas sources include partial combustion of hydrocarbons, gasification of coal (Coal to Liquid Plants), natural gas (Gas to Liquid Plants) and biomass (Biomass to Liquid plants) (Sie & Krishna, 1999). Useful products of the Fischer-Tropsch synthesis include diesel fuel, waxes and other chemicals such as olefins and alcohols (Henrici-Olive & Olive, 1976). Countries which have large coal or natural gas reserves can utilise these resources to produce their own fuel rather than importing crude oil for their fuel needs. In South Africa for example FTS plays a pivotal role in reducing quantities of imported petroleum products. Going the FTS route is viable when the cost of crude oil is above $ 20 per barrel as reported by (Morales & Weckhuysen, 2007). Since the year 2000 crude oil has been consistently above $20 per barrel and hit the $100 mark in 2011 and continues to rise (Statita, 2012). This has led to new FT plants going online recently such as the one in Malaysia and the one in Qatar since the crude oil has consistently been above this $ 20 mark in recent years (Van Wecham & Sendon, 1994; Eilers et al., 1990)

Fuels produced from FTS are more environmentally friendly than crude oil based fuels. It has been shown that diesel produced from FTS is biodegradable (Dry, 2008). FT synthesis results in high quality hydrocarbons that are sulphur and nitrogen free which makes the combustion much cleaner than combustion of crude oil products. FT fuels also contain relatively less benzene which is a toxic chemical. FT synthesis also results in many other useful products being produced such as linear alkenes which cannot be produced from crude oil (Morales, 2007).

Due to many advantages of FTS, it is therefore necessary to have more information concerning the possible catalyst systems used in FTS. Four possible catalysts i.e. iron; cobalt ruthenium and nickel have been studied for FT and Fe and Co are the ones currently used on an industrial scale (Schulz, 1999; Simonetti et al., 2007). Various supports have also been tested for FTS and these include alumina, titania and silica (Reuel & Bartholomew, 1984). In this study Ru supported on carbon nanotubes was tested for FTS. It is known that Ru is the most active of all the FT catalysts, operating at low reaction temperatures it results in a higher selectivity to heavier hydrocarbons (Schulz, 1999). Although application at industrial level is uneconomic because Ru is expensive, Ru catalyst may find use in small bio-mass to liquid plants since a highly active catalyst is required (Simonetti et al., 2007; Claeys & Van Steen, 2002). MWCNTs have also recently been studied for FT and have been shown to be stable under reaction conditions (Bahome et al., 2005; Bahome et al., 2007). Ru/MWCNTs catalyst has not been intensely studied for FTS (Kang et al., 2010).

The nature of the catalyst system has a great influence on the rate at which CO is converted as well as the range of products obtained. New materials are continuously being tested as catalyst supports such as zeolites and various carbon materials (tubes, spheres and fibres) (Reuel & Bartholomew, 1984; Bartholomew, 1991; Hayek et al., 1997, Motchelaho et al., 2011; Moyo et al., 2011).

Carbon nanotubes have received much attention not only for their application in catalysis (Xiong et al., 2010) but also because of their suitable application in the synthesis of various electronic devices and medicinal applications (Avouris, 2002; Lei, 2011). The popular way of synthesising carbon nanotubes involves the use of catalysts (Couteau et al., 2003; Lupu et al., 2003; Okamoto & Shinohara, 2005). Hence a study of one of the most promising catalysts Fe-Co/$CaCO_3$ was carried out to produce CNTS for use as a catalyst support.

Various characterisation techniques were employed to analyse these catalysts and among them are XRD, TEM, and TGA etc. Powder X-ray diffraction is a powerful technique which allows identification of single and multiple phases present in crystalline substances. Amorphous content can also be recognised from the XRD patterns if present in partially crystalline substances (Young, 1993; Will, 2006). Rietveld refinement analysis of XRD data

also allows quantification of the identified phases. (Rietveld, 1969; Young, 1993; Will, 2006). X-ray reaction chambers have recently been developed to allow in situ XRD analysis to be carried out (Richter & Dopler, 1997). Catalytic reactions can therefore also be analysed in real time and active phases identified using this XRD technique. Knowledge of the active phase allows modifications that make the active phase more available for reaction therefore increasing the production of the desired products.

1.2 Motivation

The FT catalyst goes through various phase transformations during pre-treatment and during the FT synthesis which can only be identified by in situ characterisation techniques. Knowledge of these phases may help in determining modifications that can improve the performance of the catalyst.

1.3 Objective

The main objectives of this study were

- To investigate the phase transitions that occur in the Fe-Co/$CaCO_3$ catalysts used to produce MWCNTs during heat treatment and reduction by use of an in situ XRD technique.
- To investigate the effect of synthesis method and reaction temperature and on FT synthesis using a Ru/MWCNTs catalyst.

1.4 Aims

I. To synthesise 10% Fe/$CaCO_3$, 10% Co/$CaCO_3$ and 10% Fe-Co/$CaCO_3$ catalysts and investigate how they respond to thermal treatment and reduction.

II. To study the Fe-Co/$CaCO_3$ catalysts by an in situ variable temperature XRD technique and by in situ XRD reduction and to identify phases that form and quantify these phases by Reitveld refinement analysis.

III. To synthesise multi walled carbon nanotubes by a catalytic chemical vapour deposition (CCVD) method using a 10% Fe-Co/$CaCO_3$ catalysts using acetylene as the carbon precursor.

IV. To purify the synthesised multi walled carbon nanotubes and characterise them by techniques such as transmission electron microscopy (TEM), Raman spectroscopy and XRD, amongst others.

V. To make ruthenium supported on carbon nanotubes catalyst by two synthesis methods; (incipient wetness impregnation and deposition precipitation) and to characterise the catalysts.

VI. To investigate the phase formation and transitions that occur in the ruthenium supported catalyst during thermal treatment and hydrogen reduction by use of an in situ XRD technique.

VII. Quantify the phases identified by the Rietveld refinement method and study the effects of these phases on the catalyst performance.

VIII. Investigate the effect of the catalyst preparation method and reaction temperature on the FT synthesis

1.5 Methodology

The objectives of this study were addressed by employing various characterisation techniques on the synthesised materials. Some of the main characterisation techniques used in this study are listed below:

- Thermal gravimetric analysis method : to investigate the thermal stability of the synthesised nanotubes and catalyst
- Temperature programmed reduction : to investigate the reduction process of the catalyst by hydrogen
- Raman spectroscopy: to measure the structural quality of the synthesised CNTs
- Transmission electron microscopy: to show the shape, wall structure and inner cavity of the CNTs and how the metal loaded is dispersed.
- Brunauer-Emmet-Teller (BET) analysis : to determine surface area of the catalyst
- X-ray diffraction: to identify and quantify crystalline phases and amorphous content in the partially crystalline phases.

1.6 Outline of this dissertation

This chapter (Chapter 1) is an introduction to the study to be performed.

The next chapter (Chapter 2) contains a review of the literature and work done by other authors related to this study. Chapter 3 describes the equipment and experimental procedures followed in carrying out this investigation.

Chapter 4 presents the results obtained from the study of the Fe-Co/$CaCo_3$ catalyst for the synthesis of carbon nanotubes by an in situ PXRD technique. Results of VT-PXRD studies carried out on three catalysts are reported and comparisons made. TGA, TEM and Fe Mossbauer results are also reported and discussions on these results are presented.

Chapter 5 presents the results and discussion on the study of ruthenium catalyst supported on carbon nanotubes for use in the Fischer Tropsch synthesis.

Chapter 6 describes the conclusion reached from this study as well recommendations for future work

CHAPTER 2

2 LITERATURE REVIEW

2.1 Carbon nanotubes

2.1.1 Introduction

Carbon occurs in various forms, such as graphite, diamond, fullerenes, onions, carbon spheres and carbon nanotubes. This is so because of the different hybridisation that carbon can assume in the form of electronic configurations sp, sp^2 and sp^3 (De La Puente & Nierengarten, 2012). Of all the carbon nano materials, carbon nanotubes have received the greatest attention because of their wide ranging applications (Ajayan, 1999). Figure 2.1 shows some of the allotropes of carbon.

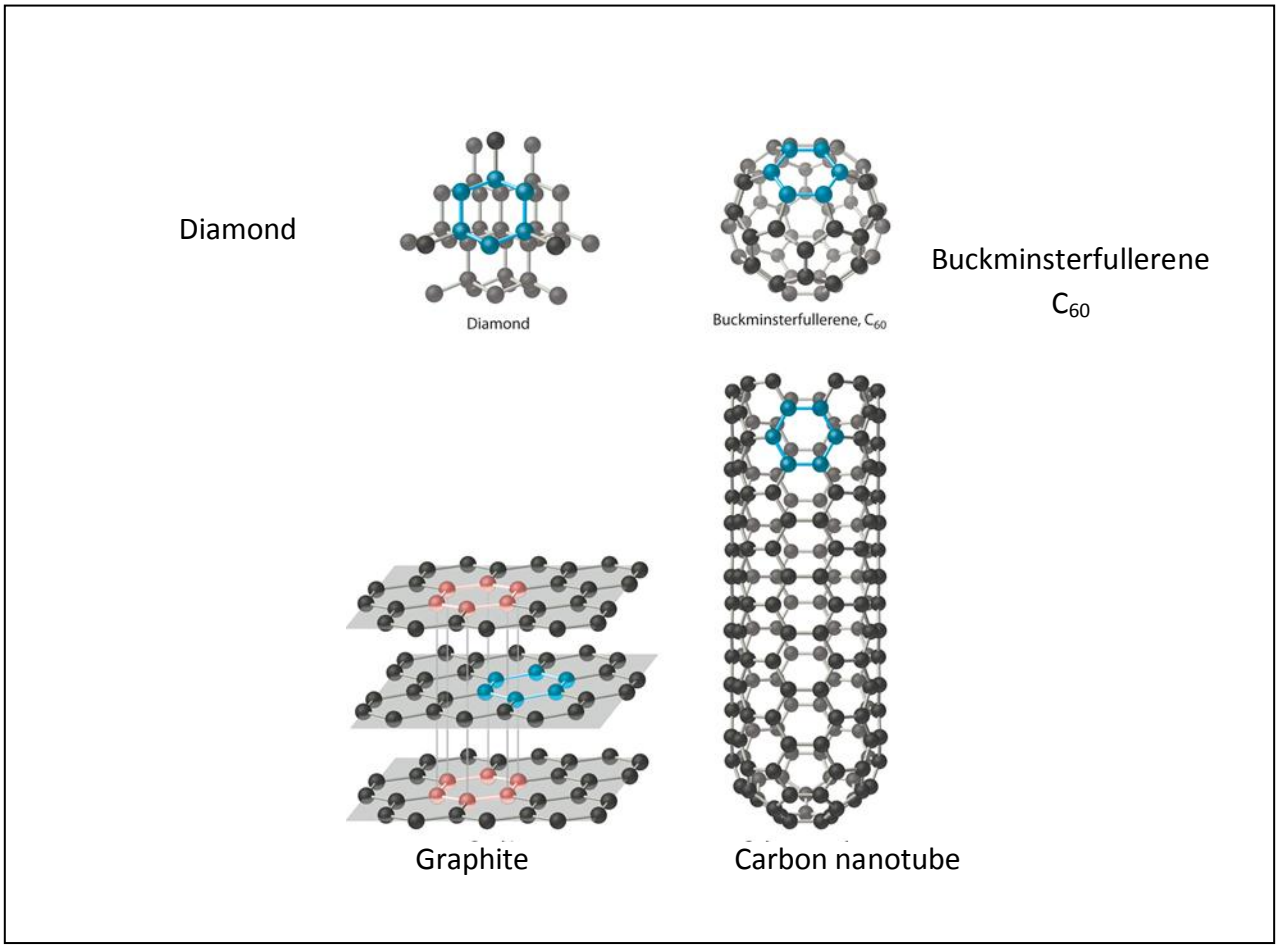


Figure 2.1: Some of the allotropes of carbon

Carbon nanotubes consist of graphite sheets, rolled into seamless cylinders, and have a fullerene structure to cap the open ends (Bernholc et al., 1997).

There are basically two types of carbon nanotubes i.e. single walled carbon nanotubes (SWNTs) and multi walled carbon nanotubes (MWCNTs). MWCNTs are made of several layers of concentric graphitic cylinders placed around a central hollow whereas SWNTs have one layer (Iijima, 1991; Yamada et al., 2006). Double walled carbon nanotubes have also been reported with two walls. The interlayer spacing between graphitic layers in MWCNTs is 0.34 nm (Ajayan, 1999; Yamada et al., 2006).

2.1.2 Properties of carbon nanotubes

Physical properties

Carbon nanotubes (CNTs) possess superior and novel properties that make them suitable for various applications. Some SWNTs can be semi conducting or metallic conducting which makes them suitable for field emission and for use as transistors devices. (Avouris, 2002; Lei, 2011). The study of the electrical properties of MWCNTs lags behind because of the complexity involved when using the multi graphitic layers (Nessim, 2010). CNTs possess superior mechanical properties; this is due to the formation of strong covalent σ sp^2 bonds between carbon atoms (Ruoff et al., 2003). Various studies have shown that a CNT is the hardest material, surpassing diamond. Its Young modulus of ca. 1000 GPa shows that its strength is 5 times that of steel (Walters et al., 1999). CNTs also exhibit high thermal conductivity and low heat capacity (Kim et al., 2001). Hone et al. (1999) found that the thermal conductivity of CNTs deviated from that of graphite. They reported that the thermal conductivity was dependent on temperature, ranging from 1800 to 6000 W/mK which is in agreement with the value of Kim et al. (2001) of 3000 W/MK which was found experimentally. However synthesised CNTs normally have defects in their structure and this adversely affects their properties (Nessim, 2010)

Chemical properties of carbon nanotubes

CNTs are found to be more reactive than graphite but less reactive when compared to fullerenes. This is so because graphite sheets are planar and hence more stable whereas the

curvature of CNTs causes misalignment of the π-orbitals and pyramidalisation (De La Puente & Nierengarten, 2012), hence the hemispherical fullerene capped ends are known to be more reactive than their graphitic walls (Ajayan et al., 1993; Ajayan, 1999). Otherwise the CNTs are insoluble in most solvents such as acetone, nitric acid and hydrochloric acid (Lin et al., 2003).The structure of carbon nanotubes however can be modified by various methods. Attachment of hydrocarbon chains to CNTs was found to increase their solubility. Carboxylic groups and other oxygen groups can be attached to the walls. CNTs can also be doped by various other elements such as N_2, B, Au etc. This modifies the electronic properties of the surface of the walls of CNTs (Duclaux, 2002; Tetana et al., 2012).

Though there are numerous possible applications of CNTs, manufacturing of these products has been hampered by several challenges. These include the difficulty in the mass production of pure CNTs of uniform size (Kumar et al., 2010; Trojanowicz, 2006). These challenges have been difficult to address because the growth mechanism is not fully understood (Yasuda et al., 2002).

2.1.3 CNTs synthesis

CNTs may be synthesised by various techniques which include laser ablation, arc discharge, plasma heating and various chemical vapour deposition (CVD) methods (Ando et al., 2004).

Arc discharge

Current is made to pass through two graphite electrodes which are placed end to end in an inert gas filled environment. A high potential difference of 20 KV and current ranging from 20 to 100 A is applied causing a high temperature discharge ca. 4000 ˚C. The heat causes sublimation of carbon on the positive electrode which then deposits on the negative end of the electrode forming CNTs. Although highly crystalline CNTs are produced, the efficiency is poor as the product contains above 60% impurities. This process is also energy intensive which inhibits large scale CNT production using this method (Iijima, 1991; Zhao et al., 1997; Journet et al., 1997).

Laser ablation

A high power laser beam is focused onto a target block of carbon placed in a reactor which is placed in a heated furnace with an inert gas flowing through. The gas carries the carbon vapour product off the block which then condenses and deposits in a cooler region called a collector. Graphite, fullerene, composites of graphite and various catalysts are some of the materials that have been used as precursors in this process. Although the produced CNTs are more pure than those synthesised by the arc discharge method, the yield is low. Making CNTs by this method is also more expensive than by using the arc discharge method (Guo et al., 1995; Guo et al., 1995; Zhang & Iijima, 1999; Thess et al., 1996).

Chemical vapour deposition

Chemical vapour deposition (CVD) involves passing a carbon source over a transition metal catalyst in a reactor placed in a heated furnace operating at high temperature (550 ˚C -1100 ˚C) (Ando et al., 2004). The heat is a source of energy which causes decomposition of the carbon source and the CNTs deposit and grows on the metal catalyst. The product is collected after the synthesis period (30-60 min) when the reactor has cooled down (Ando et al., 2004, Tetana et al., 2012).

Compared to the other synthesis methods CVD is relatively less energy intensive, making it a favourable way to make CNTs. The CVD method has received great attention because it offers a promising route to the production of cheap, bulk, pure and well aligned CNTs. The morphology of the produced CNTs can be controlled by controlling the synthesis parameters such as catalyst particle, reaction temperature and carbon source (Couteau et al., 2003; Lupu et al., 2003; Okamoto & Shinohara, 2005). The CVD method was the method employed in this study.

2.1.4 Catalytic Chemical Vapour Deposition

Catalyst systems used in CVD

Various studies have shown that the catalyst support used in the synthesis has an effect on the morphology and yield of the CNTs produced. Several catalyst supports such as silica,

alumina, zeolites, magnesium oxide and calcium carbonate have been used for the synthesis of CNTs. The nature of the catalyst and support influence the growth mechanism, quality and the yield of the CNTs produced (Coutea et al., 2003; Magrez et al., 2005; Mhlanga et al., 2009).

The use of $CaCO_3$ has been recommended as it results in high yields and almost 100% selectivity. The product obtained can also be purified by use of a mild acid (Coutea et al., 2003). Various transition metal elements have also been used in the synthesis of CNTs however iron; cobalt and nickel have received the greatest attention (Coville et al., 2011; Su et al., 2000; Hsieh et al., 2009).

Magrez and co-workers in 2005 investigated the use of various carbonates as supports for Fe, Co and Fe/Co catalysts using C_2H_2 as precursor. When the Co concentration was not 33 mol% in the bimetallic catalyst, more particles were seen to be encapsulated in the MWNT. The encapsulated particles were found to be Co and mainly Fe_3C because of its low activity in CNT synthesis. When catalyst particles are encapsulated they become shielded from the carbon source; this is a form of catalyst poisoning. The amount of encapsulated particles was 80% when $Co/CaCO_3$ was employed (Magrez et al., 2005).

Compared to other metal carbonate (MCO_3) supports ($MgCO_3$ $BaCO_3$ $SrCO_3$), $CaCO_3$ was found to be the best, producing high yields. (Magrez et al., 2005; Hata et al., 2004).

Quite a number of groups have studied the use of Fe and Co as well as Fe-Co bimetallic catalysts for MWCNTs synthesis. Cobalt was found to be more active than iron. The Fe-Co bimetallic catalyst performs better in terms of yield, quality and selectivity. This was confirmed by studying the activity of metals on various catalyst supports. Studies have attributed the excellent performance of the bimetallic catalyst to the active FeCo alloy that forms upon introduction of precursor gas at reaction temperature (Kathyayini et al 2004; Zhu et al., 2003; Magrez et al., 2005; Mhlanga et al., 2010; Cheng et al., 2005; Li et al., 2008).

Kathyayini et al. (2004) studied Fe and Co catalysts supported on Ca and Mg salts using acetylene and ethylene as precursor gases for CNT production by CVD. Their findings were

similar to the findings of Magrez et al. (2005) `s. $CaCO_3$ was found to be a better support than $MgCO_3$, giving a higher carbon deposit. They also observed that the use of acetylene was to be preferred to ethylene. An Fe-Co bimetallic catalyst also gave the best results (Kathyayini et al., 2004; Magrez et al., 2005).

CVD using $CaCO_3$ as support

At high temperature $CaCO_3$ converts to CO_2 and CaO. $CaCO_3$ may not completely decompose at a reaction temperature of 700 ˚C. This means that CNTs could grow over two supports ($CaCO_3$ and CaO), which have different crystallite size. CNTs with different outer diameter widths would then be obtained (Schmitt et al., 2006). Schmitt et al. (2006) analysed effluent gases from CVD by acetylene by use of various types of gas chromatographs. In the early stages of the synthesis, less acetylene was observed in the effluent. However, later during the synthesis period they noticed a higher concentration of C_2H_2. This meant that the amount of acetylene used in the reaction decreased with time. At the beginning of the synthesis, more C_2H_2 was consumed because the catalyst was exposed to the gas. After a longer reaction time graphitic layers and amorphous carbon formed, shielding the carbon source from the catalyst metal and hindering pyrolysis of the gas on the catalyst. Hydrocarbons also increased in concentration with time in the effluent stream because decomposition of C_2H_2 would then happen elsewhere and not on the catalyst. But-1-en-3-yne, dimers, trimers of acetylene benzene, and cycloocta-1,3,5,7-tetraene were some of the hydrocarbons identified in the effluent from the synthesis of CNTs (Schmitt et al., 2006). Figure 2.2 shows how these by-products could form (Schmitt et al., 2006).

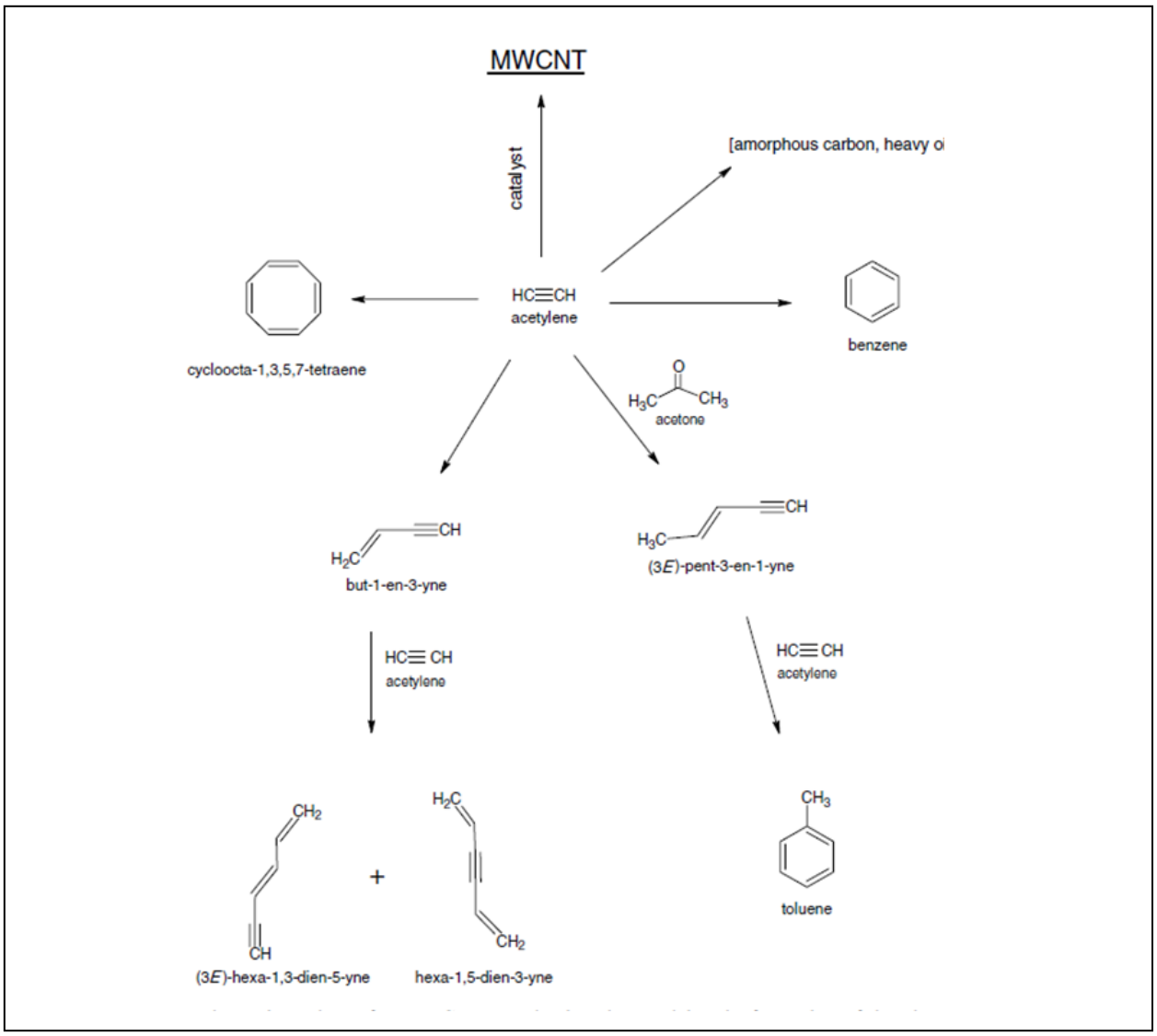


Figure 2.2: Proposed reaction scheme for MWNTs production explaining the observed byproducts (Schmitt et al., 2006).

Carbon sources used in CVD

Numerous hydrocarbon sources have been studied for growing CNTs; amongst them are methane, acetylene, benzene, xylene, and carbon monoxide (Coville et al., 2011; Su et al., 2000; Hsieh et al., 2009).

The reduction of the catalyst by acetylene

It has been shown that reducing the catalyst by H_2 is not necessary when C_2H_2 is used as the carbon source for CVD (Hernadi et al., 1997). Acetylene is able to reduce the catalyst under reaction conditions irrespective of the support employed. It has been found that reducing

the catalyst with H_2 lowered the selectivity to CNTs and resulted in low quality CNTs (Hernadi et al., 2007; Mhlanga et al., 2007).

Emmenegger et al. (2003) investigated the growth mechanism of CNTs over an aluminium substrate coated with iron nitrate solution. They carried out a high temperature in-situ X-ray study of the synthesis. As the temperature was ramped up they found that an Fe_2O_3 film formed on the substrate. Upon introduction of C_2H_2 the film fragmented and the Fe_2O_3 was then reduced to Fe_3O_4 and then wustite (FeO). They suggested that decomposition of C_2H_2 provided a source of H_2 during the reaction which reduced the iron oxides. With time the FeO formed an iron carbide (Fe_3C) phase which eventually decomposed to iron and graphite. This resulted in huge amounts CNTs being formed at that moment in time. They then concluded that CNTs grew on an iron carbide phase (Emmenegger et al., 2003).

Effect of the ratio of carbon precursor gas to carrier gas

Synthesis parameters were also found to significantly influence the products obtained using the CVD method. Mhlanga et al. (2009). investigated the effect of synthesis parameters on the iron-cobalt catalysts supported on $CaCO_3$. They found that the ratio of the carbon source to the carrier gas had an effect on the yield and selectivity of the product. When a carrier gas was not used in the synthesis mainly microspheres were obtained with just minimum amounts of nano-fibres. At a high carbon source to carrier gas a mixture of products was produced which included microspheres, nano-fibres and CNTs. Mhlanga et al. (2009) found a ratio (1:2.6) for C_2H_2:N_2 to be optimum giving almost 100% MWCNTs selectivity.

Effect of reaction time

CNT morphology also depends on the reaction time. A shorter reaction time yields CNTs with thinner outer diameters and a long reaction time gives short, thick and fibrous MWCNTs because of continued carbon deposit on the formed CNTs. Therefore the synthesis time has to be limited to less than an hour to get a high quality product (Mhlanga et al., 2009; Emmenegger et al., 2003).

Effect of reaction temperature

Reaction temperature has a significant effect on the growth rate, purity and yield of CNTs (Kumar & Ando, 2010; Bai et al., 2005; Atthipalli et al., 2011). Temperature employed for CNTs synthesis by CVD typically varies from 550 ˚C to 900 ˚C (Kumar & Ando, 2010). The growth rate and crystallinity of the CNTs increase with synthesis temperature (Lee et al., 2001).

Effect of catalyst particle size

The particle size of the catalyst also has an effect on the CNTs produced. Nano particles of size 1-2 nm are said to favour the growth of SWNT whilst bigger particles favour MWCNT. The size of the catalyst particle also influences the diameter size of the CNTs produced (Kumar & Ando, 2010; Ajayan, 2007)

2.1.5 Mechanism of CNT growth

Two growth mechanisms have been proposed for the growth of CNTs. The mechanism that occurs depends on the wettability of the metal catalyst on the substrate. When the hydrocarbon vapour comes in contact with the metal catalyst it decomposes to form H_2 and carbon. The carbon dissolves and diffuses through the catalyst and then eventually precipitates crystallising as CNTs. How the catalyst interacts with the support determines the growth mechanism. If the interaction is weak the carbon flows down and nucleates at the bottom of the metal nanoparticle pushing it up and off the substrate (Figure 2.3a). This is called the tip growth mechanism. The top part of the metal particle remains exposed to the hydrocarbon vapour so the CNT grows in length until the top part is covered by a carbon product that does not permit further tube growth. In the case where the metal interacts strongly with the substrate, the carbon fails to affect the metal-support interaction. Precipitation of the carbon then occurs at the top of the metal catalyst particles. This leaves the bottom sides exposed to fresh hydrocarbon vapour and the CNT grows from the bottom as shown in fig 2.3b. This mechanism has been termed the base growth mechanism (Kumar & Ando, 2010; Song et al., 2004; Song et al., 2004; Merkulov et al., 2001).

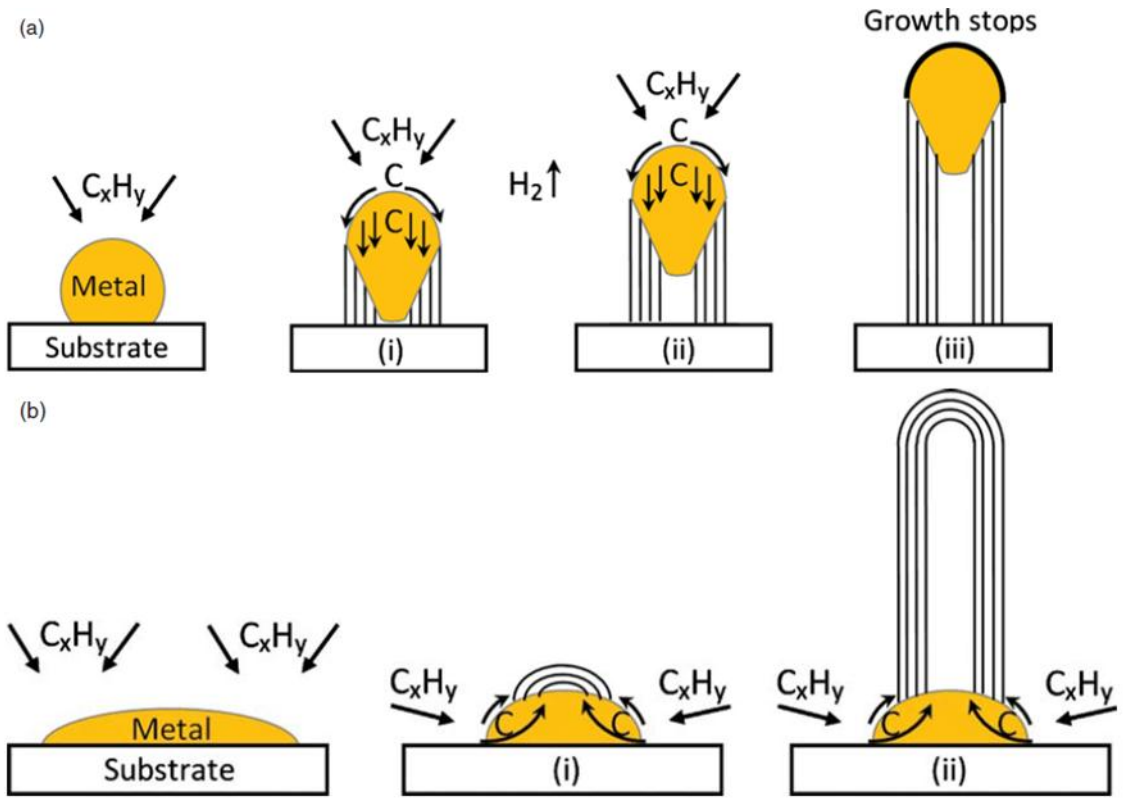


Figure 2.3: (a) tip-growth mechanism (b) base-growth mechanism (Kumar & Ando, 2010)

The solubility of the carbon in a metal particle depends on the synthesis temperature and the metal particle size. More aligned CNTs are grown when tip growth occurs whilst a base growth mode results in a random oriented product being produced (Magrez et al., 2010; Moisala et al., 2003).

It has been shown that CNTs with few walls grow by the base growth mechanism from a small catalyst particle whereas multi walled CNTs grow by a tip growth mechanism from large catalyst particles. This is because there are stronger support metal interactions with the smaller metal particle (> 5 nm) than with a large (< 5 nm) supported metal catalyst particle (Gohier et al., 2008; Ducati et al., 2004; Torredo et al., 2009). However other parameters such as reaction time, type of CVD process (floating catalyst or plasma CVD) could affect the morphology of the CNTs produced as well (Terrado et al., 2009; Li et al., 2005; Xiang et al. 2007).

Magrez et al.'s Triple joint theory for Fe-Co/$CaCO_3$ catalyst

Magrez et al. in 2005 and 2007 studied MWCNT growth on Fe-Co/$CaCO_3$ catalyst using C_2H_2 at various temperatures. They showed that CO_2 formation from the decomposing carbonate support at reaction temperature was what made $CaCO_3$ a better support for CNT synthesis than other supports. Since decomposition of the other MCO_3 supports occurs either below or above 700 ˚C, they suggested that the presence of CO_2 from the decomposing $CaCO_3$ at reaction temperature (700 ˚C) played a role in the growth of CNTs. This was in agreement with Hata et al. (2004)'s results which showed that oxygen species enhanced CNT growth and reduced impurities in the product. Hata et al. (2004) had previously reported that O_2 species reacted with the hydrogen in the C_2H_2 precursor forming H_2O thereby aiding pyrolysis of the hydrocarbon vapour. O_2 also aided by etching the amorphous carbonaceous materials which slowed down catalyst poisoning (Magrez et al., 2005; Hata et al., 2004).

Magrez et al. (2007) found that the CO_2: C_2H_2 ratio also had an effect on the CNT yield as well as CNT selectivity, the optimum being 1:1. At 820 °C, a zero MWCNT yield was recorded and this was attributed to the absence of CO_2 since all the $CaCO_3$ had decomposed to CaO. Deviation from a (CO_2/C_2H_2) ratio of 1 was also marked with an increase in amorphous carbonaceous material. It was hence deduced that the presence of CO_2 inhibited the formation of by-products during the synthesis. When CO_2, C_2H_2 and a Fe_2Co metal catalyst are close together as shown in figure 2.4, CNT production is favoured. The point of contact between the reactants was termed a triple-point joint (Magrez et al., 2007; Magrez et al., 2005).

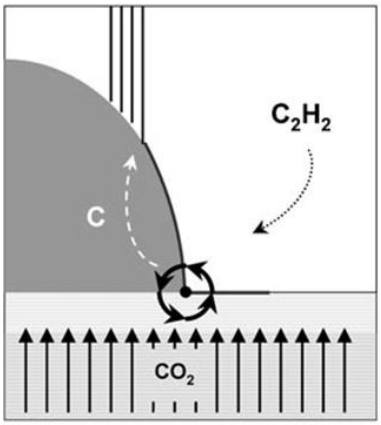


Figure 2.4: Magrez et al` s triple point joint cartoon (Magrez et al., 2007)

Magrez et al. (2007) suggested two chemical reactions to explain the role of CO_2, which also gave two reaction pathways (figure 2.5).

$$C_2H_2 + CO_2 \leftrightarrow 2C + H_2O + CO$$

$$C_2H_2 + CO_2 \leftrightarrow C + 2CO + H_2$$

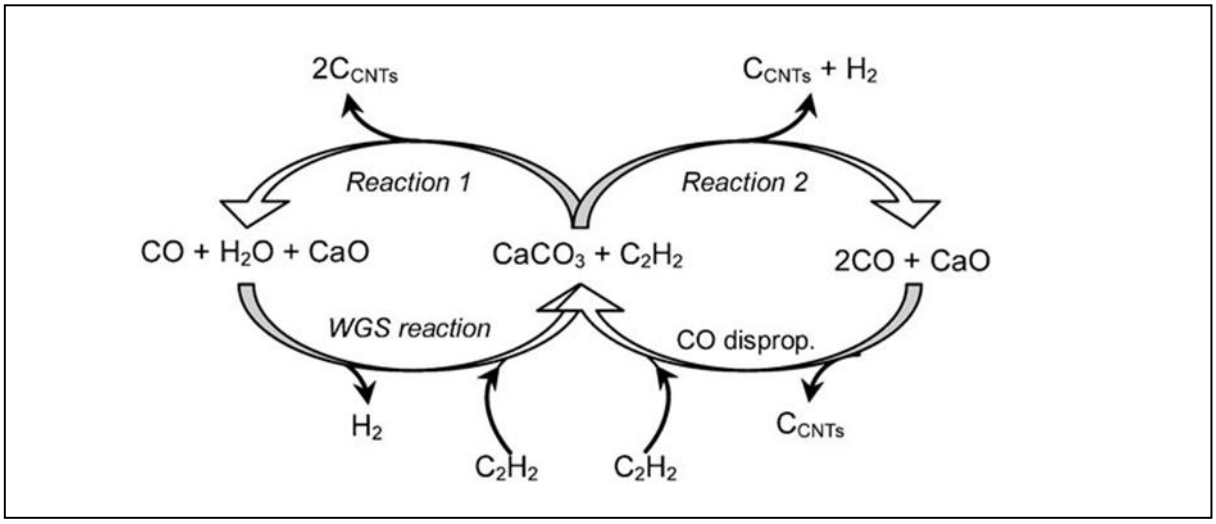


Figure 2.5: reaction pathways for the growth of CNTs (Magrez et al., 2007)

A water gas shift reaction was also suggested

$$H_2O + CO \rightleftharpoons CO_2 + H_2$$

i.e. $CO \leftrightarrow CO_2$

Through this reaction CO_2 is produced and aids in the synthesis of MWCNTs (Magrez et al., 2007).

2.1.6 Purification of carbon nanotubes

When CNTs are synthesised via a catalysed reaction, purification is necessary because the catalyst that aids the synthesis process becomes a contaminant. Most applications require CNTs of high purity. The as-synthesised CNTs are often produced together with amorphous carbon substances. Therefore the CNTs often have to be purified before they are used for a specific application (Endo et al., 2006).

Most popular methods of CNT purification rely on oxidation methods. Oxidation purification methods can be classified into two groups which are gas oxidation and liquid oxidation (Hou & Chen, 2008) Amorphous carbon gets oxidised easier than CNTs because of structural defects and dangling bonds which cause it to be more reactive (Hou & Chen et al., 2008). Therefore the impurities are usually oxidised leaving pure CNTs behind. Gas oxidising agents include air, HCl, O_2 and H_2S. The main disadvantage of this method is that it does not remove catalyst particles which necessitate a second purification step for CNTs produced in a catalytic synthesis. Some CNTs can also be oxidised together with the amorphous carbonaceous materials (Li et al., 2004).

Liquid oxidation is more popular in CNT purification, being able to simultaneously remove carbonaceous particles as well as catalyst particles. Various agents have been used for liquid oxidation and these include H_2O_2, H_2SO_4, HNO_3 (Aviles et al., 2009), $KMnO_4$ and NaOH. The choice of oxidising agent depends on the catalyst used to synthesise the CNTs. Nitric acid is the most widely used reagent because it is mild resulting in minimal damage to the CNTs and is capable of removing catalyst particles as well as amorphous carbon (Hou et al., 2008). Some oxidants such as H_2SO_4 introduce secondary impurities which need to be removed by another purification step (Li et al., 2004).

Usually the CNTs are sonicated before being refluxed or stirred. This is followed by the filtration and washing of the CNTs until the pH becomes neutral. If harsh conditions such as strong acid or reflux or stirring for long periods are employed, the CNTs become damaged and fragmented and their fullerene capped ends open up. Damage is more severe in SWNTs than in MWNTs. The oxidation of the CNTs changes their chemical and mechanical properties (Bonard et al., 1997).

Purification also introduces functional groups on the surface of the CNTs which is good in certain applications but a drawback in others. This has led to research into physical methods of CNTs purification (Li et al., 2004). For example salts have been used to remove catalysts used in the synthesis of CNTs; a Ni catalyst was successfully removed from synthesised carbon nanotubes (Li et al., 2006).

Functionalisation of carbon nanotubes

CNTs in most cases have to be functionalised before application. The introduced hydroxyl and carboxylic acid groups make the CNTs reactive enabling other groups to attach to the CNTs. Purification and functionalization of CNTS can be done in a one step process when such agents as HNO_3 are used to purify them. HNO_3 has the ability to functionalise the CNTs (Avile´s et al., 2009).

2.1.7 Use of carbon nanotubes in catalysis

MWCNTs have been extensively studied as a catalyst support mainly because they have large surface areas, many examples can be found in the literature. Pt and Pd / MWCNT catalysts have been used for hydrogenation reaction (Oosthuizen & Nyamori et al., 2011). MWCNTs have been used as a catalyst support in heterogeneous catalysis of hydrogenation of cinnamaldehyde, (Planeix et al., 1994) and in Fischer Tropsch synthesis (Xiong et al., 2010; Motchelaho et al., 2010). This work will focus on Fischer –Tropsch synthesis.

2.2 Fischer-Tropsch Synthesis

2.2.1 Introduction

Fischer-Tropsch synthesis (FTS) is a technology that was invented by two German scientists Franz Fischer (1877-1947) and Hans Tropsch (1889-1935) in 1923 when they were working at a research institute in Germany - the Kaiser Wilhelm Coal Research Institute in Mulheim. The first FT plants went on line just before the Second World War in 1936 and were a source of the much needed fuel during the war for Germany. The process continues to be of much interest in today's world as it offers an alternative route in the production of fuel (Dancuart, 2007).

Syngas sources include coal, natural gas and biomass which are used in coal-to-liquid plants, gas-to-liquid plants and biomass-to-liquid plants respectively (Sie, & Krishna 1999). Useful products of the Fischer-Tropsch synthesis include diesel fuel, waxes and other chemicals such as olefins and alcohols (Henrici-Olive & Olive, 1976).

2.2.2 FT reaction

Fischer Tropsch synthesis is a reaction that occurs when CO and H_2 react to give various hydrocarbons and other by-products such as alkanes, alkenes and alcohols.

$$CO + 2H_2 \rightarrow -(CH_2)- + H_2O$$

$$nCO + (2n+1)H_2 \rightarrow C_nH_{2n+2} + nH_2O$$

Although the mechanism of the FT reaction is a matter of controversy, there is general agreement that a step-wise chain growth process is involved similar to monomer polymerisation with CH_2 units as the building blocks. The CH_2 units are formed by hydrogenation of adsorbed CO on the metal catalyst surface (Schulz, 1999).

The probability of chain growth determines the distribution of the hydrocarbon products (Dry, 1996; Dry, 2001). The Anderson, Schulz and Flory (ASF) model gives an expression of the probability of chain growth. The ASF model is given by;

$$W_n/_n = (1-n)^2\alpha^{n-1} \qquad \textit{(1-1)}$$

where

W= weight fraction of product containing **n** number of atoms

α= probability of chain growth

The value of α can be determined from a plot of log Wn/n against the carbon number n. The slope of the straight line is the chain growth probability. ASF model can be written as a linear expression by taking the logarithms of the appropriate terms.

$$\log\left(W_n/_n\right) = nlog(\alpha) + log\left((1-\alpha)^2/_\alpha\right) \qquad \textit{(1-2)}$$

Syngas composition, temperature, pressure and the catalyst used influence the probability of chain growth. Operating at high temperature results in increased activity but it also causes increased production of undesired methane which is the most thermodynamically stable product. The rate of deposition of carbon also increases with temperature. Carbon deposition results in catalyst particle disintegration, therefore synthesis must be carried out under a compromised temperature. Carbon deposition occurs via the Boudouard reaction;

$2CO \rightarrow C + CO_2$ (Schulz, 1999)

2.2.3 FT catalysts

Most of the transition metals are active in FT synthesis but nickel, iron, cobalt and ruthenium are the only ones that are active enough to make commercial application possible. Nickel has a high methane selectivity and nickel carbonyls are formed which make

it unfavourable for application in large scale FT synthesis. Iron and cobalt are the most popular FT catalysts because they are abundant and relatively cheap which makes them suitable for use at an industrial scale (Schulz, 1999).

The water gas shift reaction is observed in FT synthesis when iron is used as a catalyst.

$CO + H_2O \rightarrow CO_2 + H_2$

Cobalt exhibits higher activity, giving less water gas shift activity and longer life than iron. This is because it is relatively resistant to oxidation and carburisation (Dry, 1996, Schulz, 1999).

Ruthenium is the most active of all the FT catalysts. It needs no promoter and is active at lower temperatures than the other FT catalysts. Ruthenium produces high molecular weight hydrocarbons although higher FT temperature results in a higher selectivity to methane (Schulz, 1999). As a promoter of iron, it makes the bimetallic (Fe-Ru) catalyst stable but methane is a major product (Bahome et al., 2007). Ruthenium has also been intensively used as a promoter for cobalt and iron based FT catalysts. However large-scale industrial application is uneconomic because ruthenium is less abundant and therefore expensive. Ruthenium may however find use in the conversion of syngas from biomass in small biomass-to-liquid (BTL) plants as this process requires a catalyst that is highly active under higher water partial pressures (Schulz, 1999; Simonetti et al., 2007; Claeys & Van Steen, 2002).

2.2.4 FT catalyst supports

Different studies have shown that the structure of the support has a significant effect on the activity, selectivity and chemical nature of a supported catalyst. The main role of a catalyst support is to offer a large surface area which assists in metal dispersion which is a factor in the performance of a catalyst. Further, the spreading of the metal on a support increases the lifetime of the catalyst by slowing down the rate of sintering. The support must present good mechanical properties such as resistance to attrition as well as thermal stability under reaction conditions. Alumina, titania, silica, carbon nano-materials and many other oxides

have been investigated as catalyst supports for Fischer – Tropsch synthesis. (Reuel & Bartholomew, 1984; Bartholomew, 1991; Hayek et al., 1997)

The reduction profiles of the same metal supported on different supports are usually different. For instance, when cobalt is supported on alumina it reduces at a lower temperature than when it is supported on silica. This is because metal support interactions are stronger in Co/silica than in the Co/alumina system (Trepanier et al., 2008). The smaller the particle size the stronger the metal support interactions leading to the increased difficulty in reduction (Trepanier et al., 2008).

Carbon materials have received attention in the past decade as FT catalyst supports because they possess excellent properties that make them suitable supports (Bahome et al., 2007; Bahome et al., 2005)

2.2.5 Carbon nanotubes as supports for FT catalysts

The many unique characteristics of CNTs such as their high surface area, inert surface and their resistivity to acids and alkali media make them suitable catalyst supports in a wide variety of reactions (Serp et al., 2003). CNTs are relatively thermally stable decomposing at ca. 600 ˚C in air. They are also more resistant to oxidation than activated carbon. The precious metals used in catalysis can also be recovered by simply burning off the CNTs (Serp et al., 2003).

Several factors however were found to affect the performance of CNT supported catalysts in FTS.

CNTs can be chemically and thermally activated so as to modify and introduce functional groups on the surface which aids in dispersing the active metal on the surface of MWCNTs (Serp et al. 2003). The degree of functionalisation of the CNTs also contributes to the performance of the CNT supported catalysts. Motchelaho et al. (2011) found that Fe catalyst supported on MWCNTs which had more functional groups was more active in the Fischer-Tropsch synthesis than the Fe that was supported on MWCNTs which had less functional

groups. The better the dispersion the more active the catalyst is likely to be (Motchelaho et al., 2011). CNTs can also be doped with nitrogen and boron. Doping with nitrogen makes the surface of the MWCNTs more electronegative thereby increasing the number of nucleation sites which are anchoring sites for the metal. This increases the degree of metal dispersion on the support. (Mabena et al., 2011, Mothchelaho et al., 2011)

In a Fischer-Tropsch synthesis study carried out by Abbaslou et al. (2010) it was shown that an iron filled MWCNTs catalyst was more active and more useful hydrocarbons were realised as compared to the activity when the catalyst particles were supported outside the CNTs. They suggested that the iron particles trapped inside the pores increased contact time between reactants and the iron particles which resulted in more active carbide intermediates forming. Iron filled CNT catalysts were also found to be more stable than the iron decorated CNTs. Chen et al. (2008) had observed the same results. They observed that the iron particle size was similar before FTS, however after the reaction the size of the iron particles outside (Fe-out) the CNTs was bigger than those of the catalyst that had iron inside (Fe-in) the tube which had not increased significantly. This meant that the catalyst with active sites on the surface of CNTs had sintered thus making the catalyst with active sites inside the CNTs more stable during FTS. The Fe-in catalyst was easier to reduce at low temperature than Fe-out and this was attributed to the electron deficiency of the inner surface of CNTs (Abbaslou et al., 2009, Chen et al., 2008).

Chen et al (2008) also found that iron particles confined inside CNTs (Fe-in) were easier to reduce and their FT activity was higher than that of Fe-out catalyst. Using in-situ XRD they identified more iron carbides which they suppose were responsible for the good performance of the catalyst.

Zaman et al. (2008) observed that the CO conversion for Co/CNT catalysts was high but selectivity to useful products was low. Addition of CNTs to traditional FT supports such as alumina and magnesia was found to enhance the selectivity of C_{5+} and decrease the methane selectivity for the cobalt catalyst. When a composite CNT-MgO support was used as a cobalt catalyst the olefin/paraffin ratio increased significantly in comparison to the use of MgO alone (Zaman et al., 2008).

2.2.6 Auto-reduction of metal oxides supported on carbon supports

Carbon supports have also been found to reduce the metal catalyst in an inert atmosphere (Xiong et al., 2010). This has been termed auto-reduction. This occurs when the carbon (carbon spheres or CNTs) are oxidised by the loaded metal oxide to form CO_2. Xiong et al. found that cobalt supported on a nitrogen doped carbon sphere catalyst reduced in this way was a better FT catalyst than the same catalyst reduced in situ by hydrogen. They attributed this to better dispersed cobalt particles in the cavities formed when the carbon was removed by oxidation (Xiong et al., 2010).

However CNTs decompose at 230 ˚C in oxygen atmosphere and c.a. 600 ˚C in air which is lower in comparison with other supports such as alumina and titania. It has been observed that active metals supported on MWCNTs catalyse the decomposition process and bring down the decomposition temperature (Bom et al., 2002).

2.2.7 Promoters

A promoter is a substance that changes the catalytic properties of a substance but itself does not take part in the reaction. It is normally added to a catalyst in small amounts (Cornils et al., 2000). Several elements have been studied as FT promoters and these include potassium, ruthenium, copper, rhenium, indium, platinum and even boron (Li et al., 2001; Trepanier et al., 2008; Das et al., 2003; Hexana et al., 2010). Good promoters suppress methane formation; enhance selectivity of higher molecular hydrocarbons, increase paraffin olefin ratios and increase activity (Pour et al., 2008). Promoters can also aid resistance to oxidation of the active site (Gaube, 2008). However, other promoters increase the rate of carbon deposition on the active sites hence leading to deactivation (Pour et al., 2008; Jacobs et al., 2001; Gaube, 2008). Promoters also enhance dispersion of the metal on the support.

Promoters can be classified into two categories i.e. structural and chemical promoters. Chemical promoters work by influencing the electronic nature of the active metal. This normally makes the reactant gas more unstable when it gets in contact with the catalyst (Cornilis et al., 2000). In FTS, such promoters work by increasing the strength of CO chemisorption onto the catalyst surface so that breaking down the C-O bond occurs (Dry

1996). Structural promoters have an influence on support-metal interactions (Cornils et al., 2000). Therefore promoters also play a major role in FTS in many different ways.

The promoters are often used to improve the reducibility of the catalyst therefore increasing the quantity of the active metallic sites available for the reaction (Das et al., 2003). Strong metal support interactions cause difficulties in reducibility hence in this case the promoter works by reducing this interaction. When there is weak interaction between the metal and the support little promoter effect is observed. Jacobs et al. (2002) investigated the effect of adding noble metal promoters (Pt, Ru,) to cobalt supported on various metal oxides (silica, titania, alumina) they found that reducibility and therefore activity was enhanced on addition of the promoters to Co/TiO_2 and Co/Al_2O_3 but that was not the case for Co/SiO_2 which showed weak metal support interactions.

Ru as FT promoter

Trepanier et al. (2008) investigated the effect of various promoters on cobalt supported on CNTs for FTS. Ruthenium was found to decrease the reduction temperature of the Co catalyst. This was in agreement with what happens when ruthenium is used as a promoter on other catalysts (Bahome et al., 2007). They also found that addition of small amounts (up to 1%) of Ru enhanced the cobalt dispersion on the CNTs support as well as causing the cobalt particle to decrease in size which was not the case when potassium was added (Trepanier et al., 2008). Li et al. (2001) also studied the effects of promoting cobalt catalyst by Ru, Re and B, and found that promotion with Ru resulted in an increase in the conversion of CO and also the selectivity of methane decreased by 6%. However the cobalt particle size remained almost unchanged. The same was also observed by Trepanier et al. (2008) who observed that methane selectivity decreased by 4% when Co/CNTs catalyst was promoted by Ru.

For Co/Al_2O_3, addition of Ru as a promoter enabled reduction of small clusters which normally form because of a cobalt-alumina interaction. This means that more active sites become available and therefore the initial rate of reaction was high. However in this case the Ru promotion was found to quicken deactivation (Jacobs et al., 2001). Tavalosi and

Karimi (2005) also found the same result for Ru promoted Co/Al_2O_3. Coke deposition as well as formation of cobalt aluminates were cited as some of the reasons for this observation.

2.2.8 Ru/CNTs for FT

Kang et al found that ruthenium supported on MWCNTs showed the highest selectivity to C_{10}-C_{20} compared to other supports such as SiO_2, TiO_2, ZrO, MgO, graphene etc. This was proposed to be due to acidic functional groups on the CNTs which caused hydrocracking to a certain extent. The high selectivity towards hydrocarbons of C_{10}-C_{20} was attributed to the size of the ruthenium particles. Methane selectivity was below 10% over a total time of 120 hours (Kang et al., 2010).

2.2.9 Preparations methods

Several methods have been used in the synthesis of catalysts. Incipient wetness impregnation and deposition precipitation are the two most common methods employed. As they have been used in this study a brief outline of their use is given.

Incipient wetness impregnation

This method is relatively simple to use in making a catalyst. A calculated amount of precursor salt is dissolved in a solvent and added drop wise to the catalyst support until the pores are filled with solution under stirring conditions. The amount of solvent should correspond to the pore volume. The catalyst is then dried and heated to get rid of the precursor salt (Kang et al., 2010; Van Steen, 2002). Catalysts made using this method are usually characterised by poor dispersion and a non-uniform particle size distribution.

Deposition precipitation method

A hydrolysing agent such as urea is used to precipitate metal hydroxides from solution onto the surface of the support. A calculated amount of the precursor salt is dissolved in water and then added to the support and the urea under stirring and low temperature heating, normally 90 ˚C. Precipitation is allowed to occur at a certain temperature over a period of time. Thereafter the mixture is filtered and washed several times to remove undesired ions (Moyo et al., 2012; Van Steen et al., 2002).

This method is useful as it produces a catalyst with good metal particle dispersion as well as narrow size distribution (Xiong et al., 2010).

Effect of particle size

The metal particle size has an influence on the performance of a catalyst (Cano et al. 2010). The size distribution should be in a narrow range. The particle size is known to affect the selectivity.

Catalyst deactivation

The lifetime of the catalyst should be reasonable therefore care should be taken to prevent catalyst deactivation whenever possible (Delmon, 1980). Thermal, chemical and mechanical conditions can result in blocking of the active sites or loss of active sites. In FTS, catalysts can be poisoned due to carbon deposition on the surface of the metallic active sites (Dry, 1996).

2.3 Powder X-ray diffraction analysis

2.3.1 Introduction

Catalysts and MWCNTs are characterised by many techniques. These include temperature programmed reduction, transmission electron microscopy, scanning electron microscopy, powder X-ray diffraction, etc.

Powder X-ray diffraction technique will now be discussed in detail since it was the main characterisation technique used in this study. This technique finds application in various industries which include mineralogy, pharmaceuticals, hard materials, catalysis, engineering, forensics conservation, archaeology and geology (Clearfield et al., 2008).

2.3.2 History of X-ray diffraction

X-rays were discovered by Wilhelm Conrad Röntgen in 1895. They are a form of short-wave electromagnetic radiation having a wavelength varying from 0.1-10 nm (0.02 Å-100 Å) which is similar to the diameter of an atom and much shorter than that of visible light. Therefore

X-rays possess more energy which makes it possible for them to penetrate solid materials. Laue in 1912 observed diffraction of X-rays from a single crystal. Bragg was however the first to determine a crystal structure by use of X-ray diffraction when he solved the structure of NaCl in 1913 (Pecharsky & Zavalij, 2009).

2.3.3 Basic concepts of PXRD analysis

Crystals

Crystalline solid materials are characterised by a long range ordered arrangement of molecules or atoms in space. Solids are termed amorphous if the arrangement of the atoms or molecules is not ordered. A phase may consist of either crystalline or amorphous content or both. Phases could also refer to liquid or gases. In this case, the study only looks at solid phases. The crystal structure is described by a unit cell that describes the lattice. A unit cell is the smallest repeating structure in the crystal. The unit cells are usually described in terms of their Bravais lattice shown in Table 2.1.

Table 2.1: Unit cell structures

	lattice	**angles**	**types**
Cubic	a=b=c	α=β=γ=90	P, BC, FC,
tetragonal	a=b≠c	α=β= γ =90	P, BC,
orthorhombic	a≠b≠c	α=β= γ =90	P, BC, FC, SC,
hexagonal	a=b≠c	α= β=90 γ =120	P,
trigonal	a=b=c	α= β= γ ≠90	P,
monoclinic	a ≠b ≠c	α= γ =90 β ≠120	P, SC,
triclinic	a ≠b ≠c	α ≠ β ≠ γ ≠90	P,

P primitive or simple, BC body centred, FC face centred, SC side centred. (Hammond, 2001)

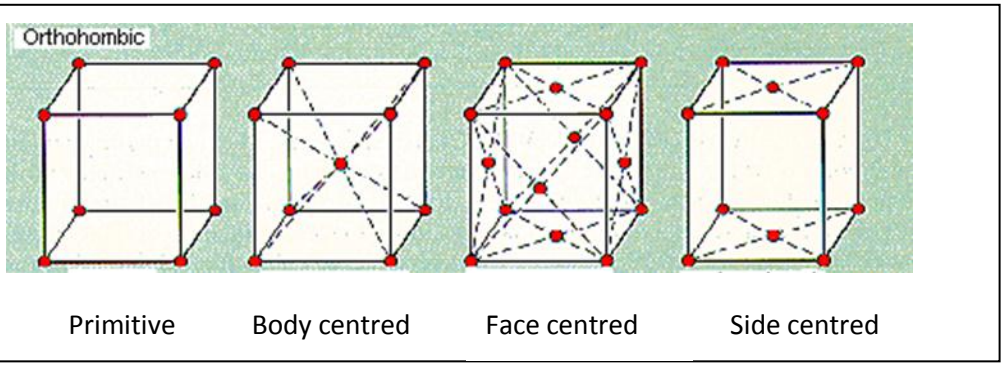
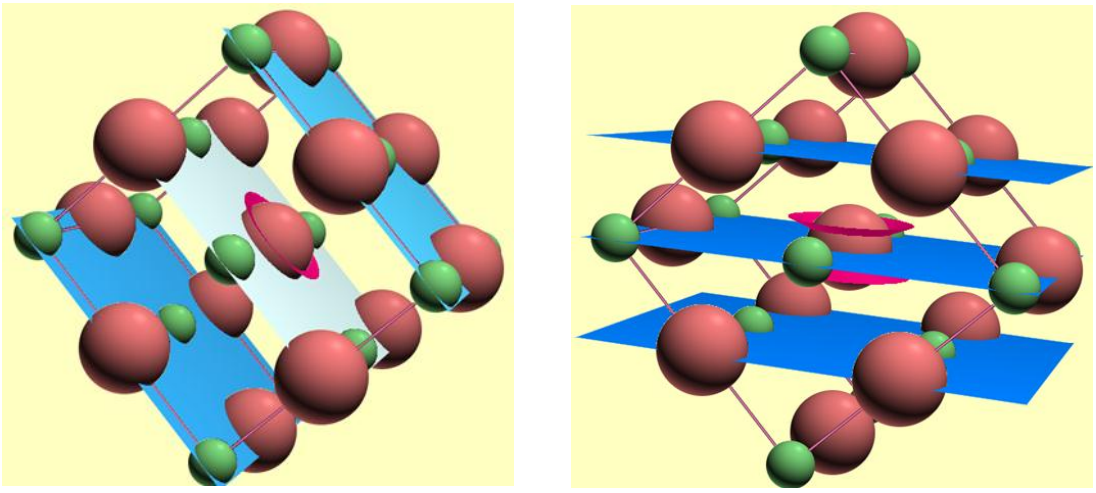


Figure 2.6: Unit cell structures (Bodnar, 2012)

Figure 2.6 shows the layout of atoms arranged to primitive, body centred, face centred and side centred/ end-centred on an orthorhombic unit cell.

Miller indices (hkl planes)

The arrangement of atoms in a unit cell may be described by hkl planes called Miller indices. $\left(\frac{h}{a},\frac{k}{b},\frac{l}{c}\right)$ (Figure 2.7) The distance between parallel hkl planes is constant throughout the lattice and is called the d spacing.



2 0 0 planes of atoms in NaCl unit 220 planes in NaCl

Figure 2.7: Arrangement of atoms in hkl planes in a NaCl unit cell (Speakman, 2012)

Braggs' law

When the X-ray waves penetrate a crystalline solid, they are diffracted by atoms arranged in various hkl planes. A reflection signal is detected when constructive interference of the X-

rays occurs (Figure 2.8). In an amorphous sample only destructive interference occurs because of the disorder in the arrangement of the atoms (Hammond, 2001).

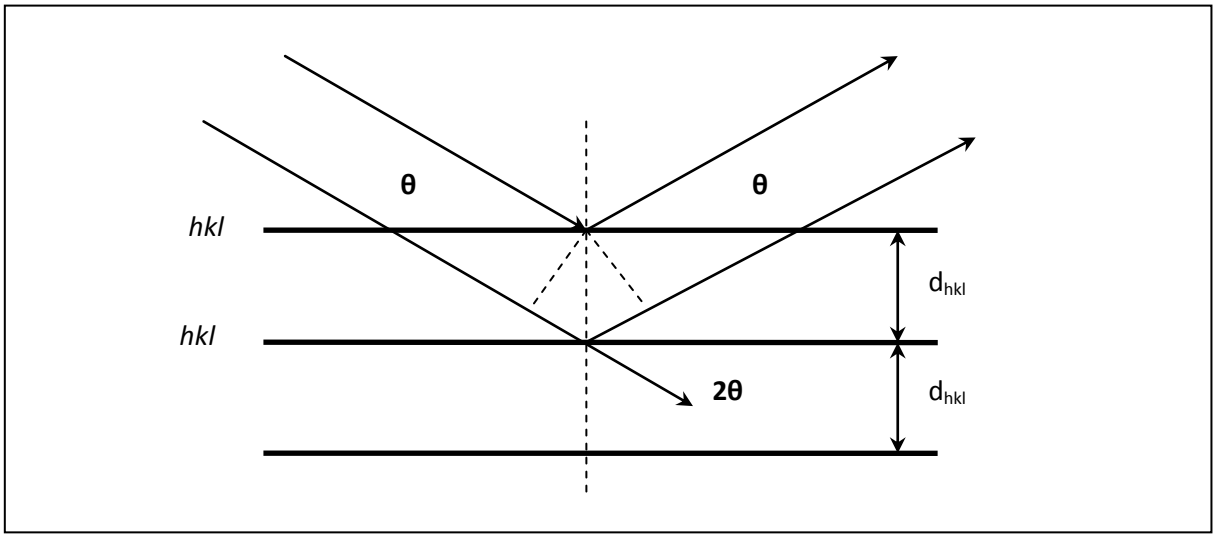


Figure 2.8: X-rays interacting with a solid material

$$2dsin\theta = n\lambda \qquad \textit{(2-3)}$$

where;

d – inter-planar distance

θ –angle of incidence

λ – wavelength of the X-rays

n – integer 1, 2, 3…..

2.3.4 Intensity of reflection peak in powder diffraction

The intensity of a peak is defined as the integral area under that peak. There are several factors that affect the intensity of the peak (Perchasky & Zavalij, 2009). Intensity is mainly dependent on the way the atoms are arranged in the unit cell and their ionic states but it also depends on the geometric setup of the instrument. The following expression gives the many parameters that affect the intensity of a peak (Perchasky & Zavalij, 2009).

$$I_{hkl} = S \times P_{hkl} \times L_\theta \times P_\theta \times A_\theta \times T_{hkl} \times E_{hkl} \times |F_{hkl}|^2$$

(2-4)

where;

I=integral intensity

S=scale factor

P=multiplicity factor describing the number of symmetrical equivalent reflections

L=Lorenz polarisation factor

P_θ=polarisation factor

A=absorption multiplier

T=preferred orientation factor

E=extinction factor

F=structure factor

The observed intensity is therefore a convolution of all these factors. These terms are described below.

Structure factor (F): The structure factor accounts for the contribution of a phase to the overall intensity profile. It depends on the nature of atoms/ions, their arrangement in the unit cell and the size of the unit cell. The structure factor is determined by a number of elements such as the number of atoms in unit cell and their coordination, the motion of atoms due to temperature, the atomic scattering factor, as well as the multiplicity of the reflections of the hkl indices. In summary the structure factor describes the contribution of the crystal structure to the diffraction pattern (Perchasky & Zavalij, 2009).

The structure factor is defined by the following expression;

$$F_{hkl} = \sum_{j=1}^{n} g^j t^j(s) f^j(s) \, exp\left[2\pi i\left(hx^j + ky^j + lz^j\right)\right]$$

(2-5)

where:

F = structure factor

g^j = occupation factor of atom j; it is only 1 when a site is totally occupied

t^j= temperature factor for atom number j

s =is sin θ_{hkl}/λ

(Perchasky & Zavalij 2009)

Lorenz polarisation factor (L): The Lorenz polarisation factor (L) which depends on the detector, geometry, beam size and sample. The monochromator angle has the most influence.

Absorption (A): Some X-rays are transmitted whilst some are absorbed when an X-ray beam interacts with a substance. The amount that is absorbed depends on the nature of the sample as well as the instrument set up (Perchasky & Zavalij, 2009).

Preferred orientation (T): Crystallites are assumed to be randomly oriented in PXRD analysis, however at times this is not the case. The shape of the crystal may affect the plane in which crystals lie during analysis. This has an effect on the intensity of various peaks. Care must therefore be taken during sample preparation of materials that are to be analysed (Perchasky & Zavalij, 2009).

Extinction (E): At times the diffracted wavelets are reflected back within a crystal which causes them to be out of phase with the incident beam. This results in a decreased detected intensity. In a sample which consists of multi phases the reflected beam may be re-reflected by a crystallite of a different phase, and this decreases the detected intensities (Perchasky & Zavalij, 2009).

2.3.5 Rietveld refinement method

Before the introduction of the Rietveld technique, analysis of diffraction data was done by analysing a single peak at a time. Peaks would be integrated manually, and there was no way of dealing with overlapping peaks and this made analysing diffraction data almost impossible. The development of computer software and the development of a whole pattern analysis technique to analyse diffraction data by Hugo Rietveld changed this (Will, 2006).

The method was originally called the 'full pattern refinement' method. This was then changed to Rietveld refinement in 1978 in honour of Hugo Rietveld who developed the method. He solved a number of crystal structures analysed from neutron diffraction (Rietveld, 1967; Rietveld, 1969). The application of the method was later extended to X-ray diffraction from 1977 when scientists determined other peak functions to describe the peak shape of the X-ray diffraction data in addition to the common Gaussian peak given by neutron diffraction. The Rietveld method is employed in solving crystal structure of substances, calculating crystallite size and carrying out quantitative analysis of several compounds in a sample. Today data obtained from a synchrotron can also be analysed by use of this method (Young, 1993; Will, 2006).

Rietveld showed that the total intensity observed was a sum of background and the intensity function described by equation 2-4 (Young, 1993).

This method involves the use of a least squares method to fit a calculated diffraction pattern to an observed one. The best fit occurs when the square of the residual is minimised. The residual is the difference between the observed value and the calculated value from the created model (Young, 1993), given by:

$$WSS = \sum_i w_i \, (Y_{oi} - Y_{ci})^2 \qquad \textbf{(2-6)}$$

where:

WSS=minimum weighted sum of squares –weigted residual value.

w_i=weight function

Y_{io}=intensity observed at point i

Y_{ic}=calculated value of the intensity for point i on the curve

WSS is defined as the sum of standard deviations of the background and that of normal counting statistics.

The starting model is built from a sensible estimation of starting parameters of the ideal values. Rietveld method only modifies a model which has been built from background knowledge of the crystal. Collecting high quality data minimises the difference between the calculated profile and the observed profile. Various software programs are available; some is free ware (GSAS, Maud) and others commercial (Topas, HighScore).

Figures of merit

There are several indicators that can be calculated to show how good a fit has been determined. These are known as Residual-indices (R-values). R_{wp} (equation 2-7) is a meaningful indicator of all the R factors because it takes into account the residuals calculated from the least squares method (Young, 1993).

$$R_{wp} = \left[\frac{w_i(Y_{oi} - Y_{ci})^2}{\sum w_i\,(Y_{oi})^2}\right]^{1/2} \qquad \textbf{(2-7)}$$

R_{exp}

$$R_{exp} = \left[\frac{N - P}{\sum_i^N w_i(y_{oi})^2}\right]^{1/2} \qquad \textbf{(2-8)}$$

Where R_{exp} is the R expected

N = observed

P= variance

The goodness of fit (x^2) is a relatively good indicator of the quality of the refinement and x^2 is the ratio of the R weighted pattern to the R expected

$$x^2 = \frac{R_{wp}}{R_{exp}} \qquad \textbf{(2-9)}$$

This can be reduced to

$$x^2 = \left[\frac{Wss}{N - P}\right] \qquad \textbf{(2-10)}$$

R_{wp} should be close to R_{exp}. Ideally, when the refinement has been done properly and the built model is ideal, the value of x^2 should be 1. In reality this rarely occurs, therefore a goodness of fit of just above 1 e.g 1.3 is a good fit. However a high value e.g. higher than 2 indicates an inadequacy of the starting model. If x^2 is significantly less than 1 then the model built is wrong and should be discarded. The result obtained should not be used since it is unreliable (Young, 1993; McCusker et al., 1999; Will, 2006).

2.3.6 Uses of PXRD technique in analysing catalytic materials

Qualitative analysis

PXRD is most commonly used to identify the compounds that are in a sample. This is done by comparing the diffraction pattern obtained with the diffraction patterns of known compounds which are stored in a database. This is made possible because chemical compounds have unique diffraction pattern similar to finger print. Qualitative analysis is now mainly done by an algorithm in XRD analysis softwares such as Diffracplus, Eva, Match!, HighScore etc. (Match, 2012; HighScore, 2012). Some of the electronic crystal structure databases that are available are the Powder Diffraction File which is owned by the International Centre for Diffraction Data (ICDD) (ICDD 2012) and the online International Crystal Structure Database (ICSD 2012) by Karlsruhe (Karlsruhe, 2012).

Quantification of phases

A diffraction method is the only method which may be used to identify and quantify solid crystalline compounds whereas there are many other techniques that can identify elemental composition (Pecharsky & Zavalij, 2009).

Various methods have been proposed over time by different authors. All the methods are based on comparing peak intensities of a phase with the intensity of a standard (Klug & Alexander, 1974). Rietveld refinement analysis of samples containing various phases can also provide relative concentrations accurately. Doing quantitative analyses of diffraction data by Rietveld refinement/whole pattern analysis has the advantage of having no need to calibrate using a standard. This is so because the peak intensity is calculated directly from crystal structure parameters.

Quantitative phase analysis is based on the fact that each crystalline phase has a unique pattern described by its peak intensity and peak position. The intensity of the peaks is proportional to the amount of the phase present. The quantitative analysis is based on the weighting relationship suggested by Hill and Howard (Hill & Howard, 1987);

$$W_\alpha = \frac{S_\alpha (ZMV)_\alpha}{\sum_i^n S_i (ZMV)_i} \qquad \textbf{(2-11)}$$

where

W =weight fraction of phase α in the mixture

S =Rietveld scale factor

Z=number of formula units per unit cell

M=mass of formula unit

V=unit cell volume

Crystallite size analysis

PXRD also allows estimation of the crystallite size of the phases in the sample. This information is useful in applications such as catalysis (Cano et al., 2010).

The crystallite size is calculated mainly based on peak broadening observed by Scherrer as first reported in 1918 (Scherrer 1918). As described in section (2.3.4) there are several factors that influence the peak shape such as instrument broadening and specimen broadening. A standard whose peak profile and hence full width at half maximum (FWHM) is properly documented is normally used to account for instrument broadening before the Scherrer equation is applied. However this is not necessary in Rietveld refinement analysis because the instrument contribution is taken into account in describing the peak profile if the fundamentals approach is employed (Langford &Wilson, 1978). The Scherrer equation is given by;

$$B(2\theta) = \frac{K\boldsymbol{\lambda}}{L\cos\theta} \qquad \textbf{(2-12)}$$

where;

B=FWHM

K=Scherrer constant

L=Crystallite size

λ=wavelength of radiation

θ=from observed 2θ values

The constant of proportionality named the Scherrer constant depends on the shape of the crystallites that are being analysed. The constant K varies from 0.62 to 2 with 0.94 being its value for spherical crystals. From the equation above it can be seen that B increases when L is small. This result in the broadening of the peak; normally large crystal sizes give narrow peaks and small crystals give broad peaks (Scherrer, 1918; Thompson et al., 1987).

2.3.7 In situ diffraction analysis – some case studies

In situ studies offer an opportunity to follow reactions in real time. Most characterisation techniques are carried out in ex situ environment and the actual form of the reactants during the reaction is lost. Information gained during in situ analysis is useful in controlling, modifying and manipulating the reaction so that a desired outcome may be realised.

The use of in situ PXRD in the field of catalysis has been steadily increasing in recent years (Perrillat et al., 2005; McPherson, 2010; Chen et al., 2008). The advances that have been made in laboratory based XRD instruments has made this possible e.g. the development of the high temperature, high pressure X-ray reaction chamber and other such non-ambient reactor chambers. In 1997 Richter and Dopler (1997) described an X-ray chamber which could be used to monitor the structural changes that take place in a catalyst during the reaction. Most of these attachments are manufactured by Anton Paar (2005).

The study of the synthesis of CNTs has intrigued many researchers. Several of them have used the XRD technique under in situ conditions to obtain more information on the phase transitions that take place during synthesis. Li et al. (2008) studied an Fe, Co as an Fe-Co/ $CaCO_3$ bimetallic catalyst for the synthesis of CNTs. In their studies they followed the reduction of these catalysts by real time in situ PXRD analysis. The authors used radio

frequency heating to heat the reaction furnace. At high temperature (500 ˚C) the formation of a spinel (Fe_2CoO_4) on the bimetallic catalyst was observed. They also carried out reduction studies on the catalysts and studied them by PXRD in real time at different temperatures. Emmenegger et al (2003) investigated the growth mechanism of CNTs over an aluminium substrate coated with iron nitrate solution. Details have been given in section 2.1.4.. Nishimura et al. (2004) described an in situ XRD study of the synthesis of MWCNTs from a thin iron film based catalyst in detail (Section 2.3.7).

Several researchers have employed the in situ XRD technique for FTS studies. Chen et al. (2008) carried out a study to analyse whether there was a difference in activity and selectivity when iron particles were loaded onto the outside walls of CNTs as compared to those particles confined inside the CNTs. The authors also monitored the catalyst phase changes that occur by use of an in situ PXRD technique. In Enache at al. (2002) used in situ PXRD analysis to study the effect of thermal treatment on several Co based catalysts for FTS. Ducreux et al. (2009) studied the reduction of Co/silica catalyst by in situ XRD. Bulavchenko et al. (2009) studied the reduction of nano crystalline Co_3O_4 (see section 2.3.7 below).

Some examples of studies that have been done based on in situ PXRD analysis of catalytic materials is reviewed here.

In situ XRD study of nano crystalline cobalt oxide reduction

Bulavchenko et al. (2009) carried out a study which was aimed at understanding the reduction mechanism of nano crystalline Co_3O_4. This Co catalyst is used in the Fischer Tropsch reaction. They investigated the effect of catalyst reduction conditions such as temperature and reduction time on the structure of the catalyst and the particle size. The resulting phases were found to play a role in the performance of the catalyst i.e. activity, selectivity and catalyst stability. Bulk Co_3O_4 and supported $Co_3O_4/\gamma\text{-}Al_2O_3$ catalysts were analysed in situ using the X-ray diffraction technique (Bulavchenko et al., 2009).

Two Co_3O_4 catalysts were obtained from the decomposition of $Co(OH)_2CO_3$ at 300 ˚C and 500 ˚C and they were named 1 and 2 respectively. An 18% Co $Co_3O_4/\gamma\text{-}Al_2O_3$ catalyst was

synthesised by the incipient wetness impregnation method on γ-Al_2O_3 using $Co(NO_3)_2$ as the precursor salt and consequently calcined at 250 ˚C. A high temperature X-ray reaction chamber attached to a Siemens D5000 X-ray diffractometer was used for the study. 100% H_2 gas as well as a mixture of 6% H_2 and 94% He gas at atmospheric pressure was used to reduce the oxides of Co. The temperature was ramped up at 25 ˚C/min. The catalysts were also analysed by BET, TPR, and electron microscopy (Bulavchenko et al., 2009).

PXRD patterns of the catalyst were obtained before the reduction and the structures of the compounds were interpreted. The Co_3O_4 occurred as a spinel structure $Co^{2+}Co_2^{3+}O_4$ with space group Fd3m (Bulavchenko et al., 2009).

When reduction was carried out in a 100% H_2 atmosphere the supported and unsupported oxides went through different reduction steps. The unsupported Co_3O_4 went through a one-step reduction process whilst the supported catalyst went through 2 steps (see below).

$Co_3O_4 \rightarrow Co$	stage 1 reduction
$Co_3O_4 \rightarrow CoO \rightarrow Co$	stage 2 reduction

Reduction of unsupported oxides to metallic Co began at 190 ˚C. The Co_3O_4/γ-Al_2O_3 began to reduce to CoO at 180 ˚C and then Co (fcc) peaks appeared at 260 ˚C; even at 350 ˚C the presence of CoO was still observed. This showed that the Co_3O_4/γ -Al_2O_3 catalyst was more difficult to reduce as compared to the unsupported Co_3O_4. This was attributed to metal support interactions (Bulavchenko et al., 2009).

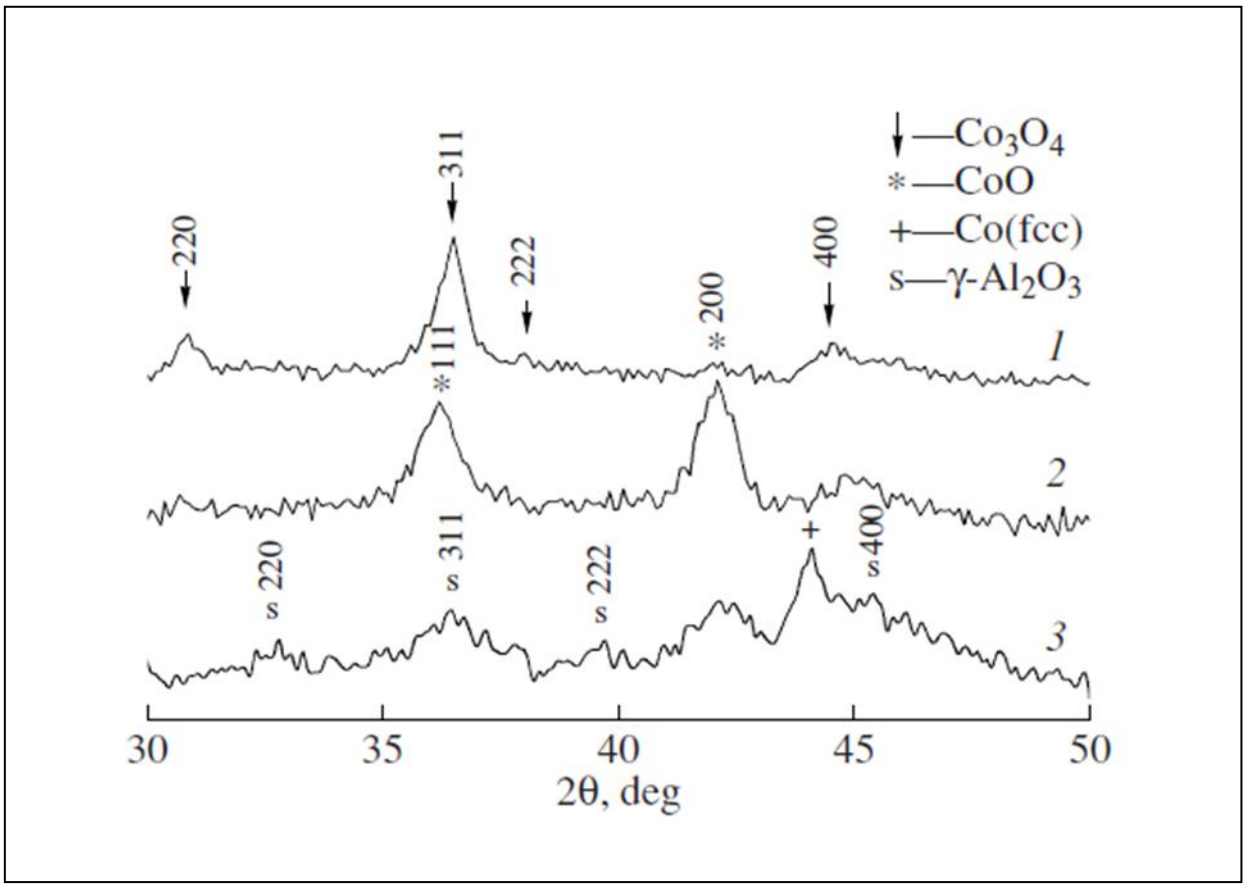


Figure 2.9: PXRD patterns showing the reduction of Co_3O_4/ ϒ-Al_2O_3 at different temperature 1 (25 ˚C), 2 (190 ˚C), 3(350 ˚C) (Bulavchenko et al., 2009).

When the reduction was carried out in 6% H_2 balance He as both the unsupported and supported catalyst showed two reduction steps illustrated above in Figure 2.9 (Bulavchenko et al., 2009).

In situ study of iron catalysts for carbon nanotube growth using X-ray diffraction analysis

Nishimura et al. (2004) investigated the growth of vertically aligned MWCNTs by a CVD method by use of an in-situ XRD technique. Their aim was to determine the nature of the metal during the synthesis since up to that point only ex situ forms of the metal catalyst had been reported. Different researchers had identified Fe_3C by PXRD analysis of the product in the Fe catalysed synthesis of CNTs (Nishimura et al., 2004).

A thin film of iron was deposited on a silicon support that was used for synthesising MWCNTs. Their CVD set up system was equipped with an XRD analyser system. The CVD reactor chamber was depressurised first and then helium was allowed to flow through the catalyst to bring the pressure back to atmospheric. This process was repeated several times to completely purge out oxygen from the system. The temperature was then ramped up to 700 ˚C under a He flow of 50 mL/min. XRD patterns were recorded as the temperature was ramped. C_2H_2 was then introduced at 700 ˚C and XRD patterns were recorded (Nishimura et al., 2004).

On heating the catalyst to 700 ˚C iron was identified in different states at different temperatures. At room temperature, the iron was in metallic form; then at 200 ˚C magnetite peaks were identified and at 700 ˚C all the magnetite had converted to Fe_2O_3. The authors attributed this oxidation of the catalyst to moisture that was trapped within the catalyst and the substrate. Silicon peaks were also present throughout (Nishimura et al., 2004).

On feeding the C_2H_2 to the reaction chamber, Fe_2O_3 was reduced back to magnetite. XRD patterns were collected as a function of time. The 3rd XRD pattern that was recorded (after the 19th min of C_2H_2 flow) revealed the formation of iron carbide (Fe-C) (figure 2.9). After 26 minutes graphite peaks were identified which were evidence that MWCNTs had been formed. However the Fe-C peaks diminished as the carbide (Fe_3C) peaks emerged. Both these phases were proposed to be possible active phases for the CNT CVD process. The authors suggested that Fe_3C was the more active phase; it had not been identified before because it is unstable in carbon rich and high temperature environments (Nishimura et al., 2004).

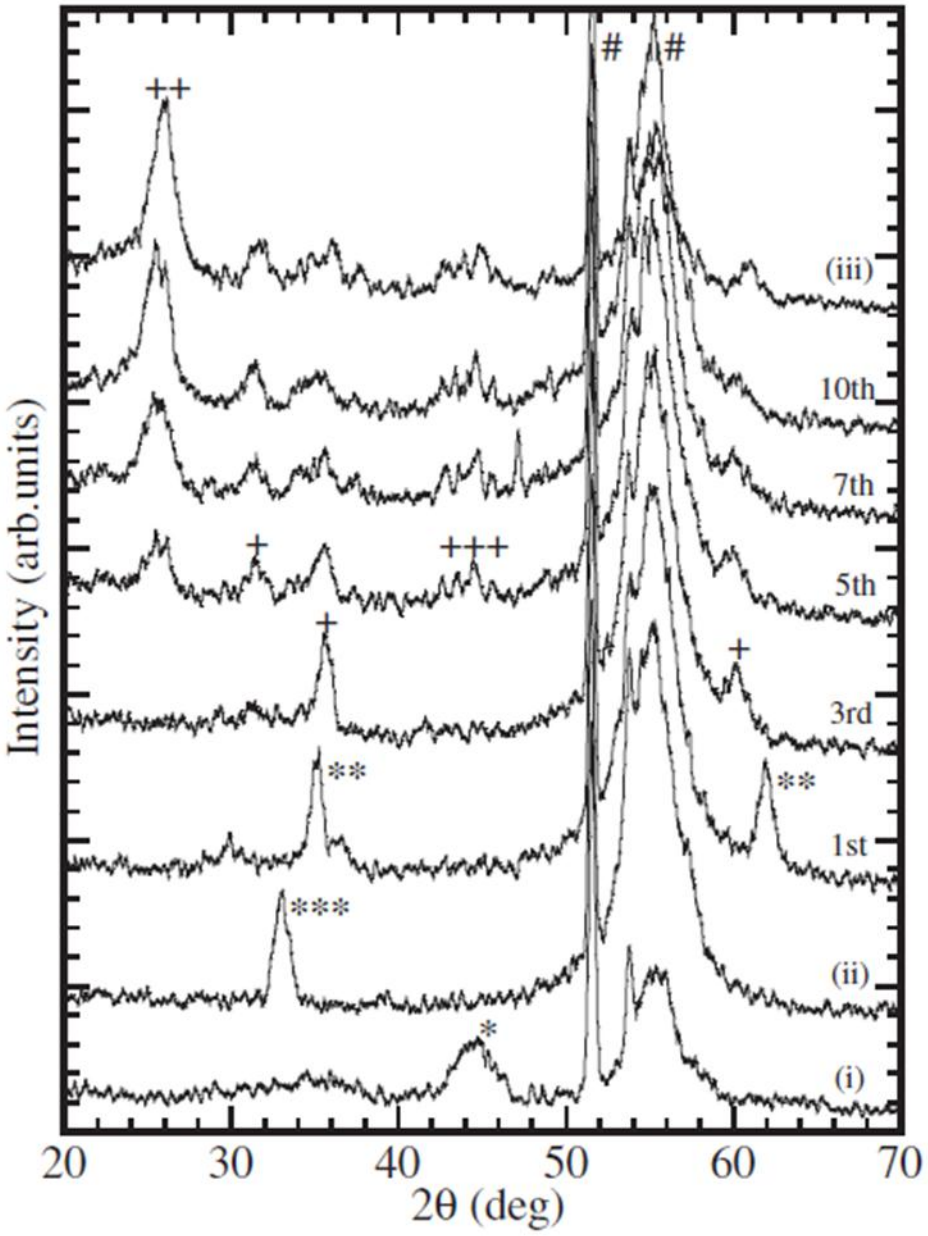


Figure 2.10: Patterns (i) and (iii) were taken at room temperature but before and after reaction respectively. (ii) was taken at 700˚C before C_2H_2 was introduced. 1^{st}, 3^{rd}, 5^{th}, 7^{th} and 10^{th} were taken every 6 min interval as 1^{st} 2^{nd} 3^{rd} for each interval (Nishimura et al., 2004).

These two examples show useful information that can be obtained by an in situ analysis method.

CHAPTER 3

3 EXPERIMENTAL METHODS

3.1 Synthesis Procedures

3.1.1 Preparation of Fe-Co/$CaCO_3$ catalysts for the synthesis of CNTs

A 10% by weight Fe-Co (1:1) catalyst was synthesised by the incipient wetness impregnation method. $CaCO_3$ (9 g) purchased from Merck was used as support for the active metals. $Fe(NO_3)_3.9H_2O$ (3.6 g) and $Co(NO_3)_2.6H_2O$ (2.4 g) reagents from Sigma Aldrich were mixed together and gently milled before being dissolved in 25 mL of distilled water. This solution was then added drop wise to the weighed $CaCO_3$. The mixture was then stirred for 5 hours under heating at 90 °C until semi dry. The catalyst was then dried for 18 hours in an oven at 120 °C and thereafter ground and sieved with a 150 µm sieve. The catalyst was then calcined at 400 °C for 16 hours in a static air furnace to remove the nitrates by decomposition.

Both 10% Co/$CaCO_3$ and 10% Fe/$CaCO_3$ catalysts were also prepared the same way using calculated amounts of precursor salts.

3.1.2 Synthesis of multi walled carbon nanotubes

Multi walled carbon nanotubes (MWCNTs) were synthesised by the chemical vapour deposition method according to the procedure detailed elsewhere (Mhlanga et al., 2009).

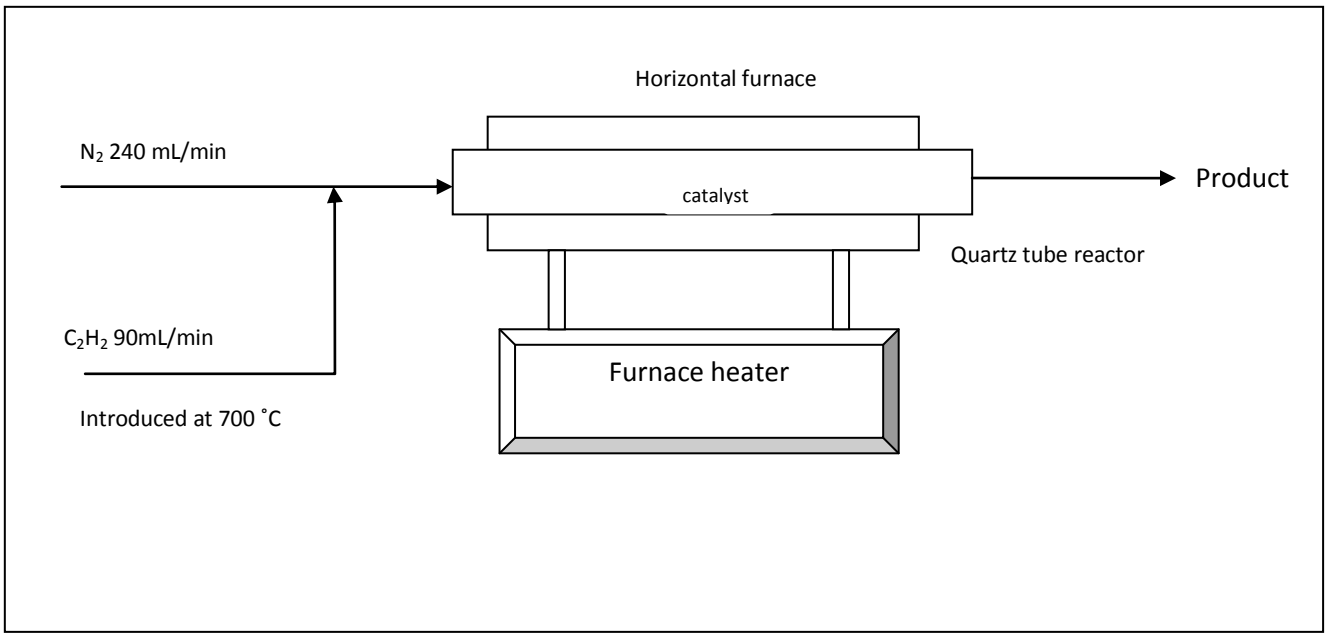


Figure 3.1: Reactor set up for the synthesis of MWCNTs

Figure 3.1 shows the reactor setup that was employed to synthesise MWCNTs. Acetylene (C_2H_2) gas was used as the carbon source and N_2 as the carrier gas. About 1 g of the catalyst was spread in a quartz boat (120 mm X 15 mm) and placed in a quartz tube reactor which was then placed in a horizontal furnace. N_2 gas at 40 mL/min flow rate was allowed to flow whilst the furnace was being heated to 700 °C at a rate of 10 °C/min. When the temperature reached 700 °C the N_2 gas flow rate was increased to 240 mL/min and then C_2H_2 gas was introduced at 90mL/min. After 1 hour of reaction, the C_2H_2 flow was stopped and the furnace was allowed to cool to room temperature with N_2 flowing at 40 mL/min. The product (about 2 g) was thereafter collected and weighed and then later characterised by various techniques such as transmission electron microscopy and Raman spectroscopy.

3.1.3 Purification of carbon nanotubes

The as-synthesised MWCNTs were purified to remove the catalyst particles that were used to make them. The purification step also introduced functional groups on the MWCNTs that are useful in anchoring the metal catalyst for FT synthesis thereby improving their dispersion. The as-synthesised MWCNTs were purified by 55% HNO_3 acid. MWCNTs (2 g) were added to 200 mL of HNO_3 and this mixture was sonicated for 30 minutes and thereafter refluxed for 6 hours in an oil bath which was kept at a temperature of 110 °C. The mixture was then left to cool down to room temperature and then it was diluted with

distilled water. The diluted mixture was then filtered by use of a Büchner funnel and filter paper and the MWCNTs were subsequently washed with distilled water until the filtrate pH was about 7 as indicated by universal indicator paper. The residue (MWCNTs) was then dried at 120 °C in an oven for 10 hours.

3.1.4 Synthesis of catalysts for Fischer-Tropsch

Ruthenium was supported on MWCNTs and prepared by two different synthesis methods; the incipient wetness impregnation and the deposition precipitation methods.

Incipient wetness impregnation

The catalyst was prepared by the incipient wetness impregnation method (Van Steen et al. 2002; Xiong et al. 2010). $RuCl_3.xH_2O$ salt (0.373 g) was dissolved in 3 mL deionised water and the solution was added drop wise using a pipette to 1.3 g of purified CNTS to make a 10% Ru/MWCNT sample. This mixture was left for 4 hours to allow for aging of the catalyst before the slurry was dried at 120 °C for 12 hours in an oven. The catalyst was then heated under N_2 gas at 400 °C for 3.5 hours to decompose the chlorides. This calcination temperature was determined from TGA analysis.

Deposition precipitation method

The catalyst was also made by the deposition precipitation method using urea (Van Steen et al., 2002; Motchelaho et al., 2011). Calculated amounts of $RuCl_3.xH_2O$ salt and urea were dissolved in 9 mL deionised water. The ratio of urea to Ru was 1.5:1. This solution was added drop wise to the 1.9 g MWCNTs and the mixture was sonicated for 15 min. The slurry was then heated in an oil bath at 90 °C for 2 hours. The temperature was thereafter reduced to 70 °C and left over a period of 2 hours to allow for evaporation of water. When the catalyst was semi-dry it was then dried further at 100 °C for 12 hours in an oven.

3.2 Characterisation Techniques

3.2.1 Thermal gravimetric analysis

Thermal gravimetric analysis (TGA) is a technique used to determine the thermal stability of a substance by taking note of the weight loss that occurs during heating at different

temperatures (Allcock, 2008). Metal weight loading on the CNTs was also confirmed by use of TGA.

TGA was performed on a Perkin Elmer Thermo-gravimetric Analyzer (TGA 4000). The specimen was loaded on a ceramic pan and the analysis of ca. 9-11 mg was done under air and under a N_2 atmosphere. A heating rate of 10 °C/min was employed from room temperature to 950 °C.

3.2.2 Transmission electron microscopy

The morphology of the Fe-Co/$CaCO_3$ catalysts, MWCNTs and the FT catalysts was analysed by transmission electron microscopy (TEM). The TEM revealed the dispersion of metals on the support and the sizes of catalyst particles. J Image software was used to measure 120 particle diameters of the samples that were analysed.

About 1 mL of the specimen was placed in methanol and ultra-sonicated for 10 mins at room temperature so that the particles become dispersed in the suspension. A drop of the suspended specimen was placed on SPI-carbon copper grids and was allowed to dry before analysis was carried out on the microscope. A FEI Tecnai Spirit G^2 electron microscope (Figure 3.2) operating at 120 KV was used for TEM analysis. The microscope works in conjunction with a Gatan microscopy suite which includes DigitalMicrograph software which was used to capture the pictures (Software Products Gatan).

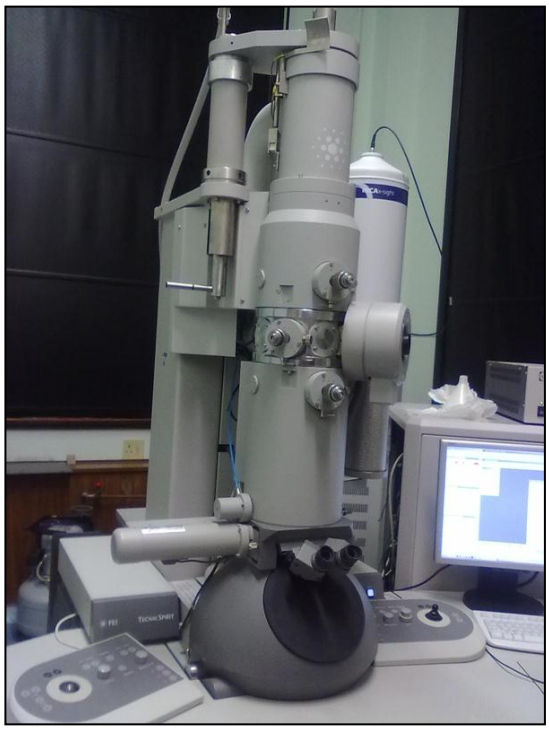


Figure 3.2: FEI-Tecnai G^2 Spirit microscope for transmission electron microscopy analysis

3.2.3 Raman spectroscopy

Raman spectroscopy gives information with regards to the quality of the graphitic structure of carbon that makes up the MWCNTs. A Jobin-Yvon T64000 Raman spectrometer was used to analyse the as-synthesised and purified MWCNTs.

3.2.4 BET Surface area analysis

Surface area and pore volume analysis of the synthesised materials were determined by the nitrogen physisorption technique. Brunauer-Emmet-Teller (BET) data was collected on a Micrometrics TRISTAR 3000 analyzer. About 0.2 g – 0.3 g of the sample was analysed after degassing under N_2 at a temperature of 250 °C for 4 hours. BET surface area and pore volume were read from the instrument directly without doing a full isotherm study.

3.2.5 Temperature programmed reduction

The reduction profile of the catalyst was determined by the temperature programmed reduction technique. About 0.1 g of the specimen was analysed in a U tube reactor. The specimen was firstly degassed at 150 °C under an argon flow of 20 mL/min at a pressure of 1

bar for 30 minutes. This was done to remove moisture in the sample. The sample was thereafter cooled down to 45 °C. Hydrogen gas (5%: balance Ar) was then allowed to flow through the sample at a flow rate of 50 mL/min at atmospheric pressure and reduce the catalyst as it was heated to 800 °C at a heating rate of 10 °C/min. H_2 uptake was monitored by a TCD chromatograph.

3.2.6 Fourier transform infra-red spectroscopy

Fourier transform infra-red (FTIR) spectroscopy provides information with regards to which type of bonds are present in molecules. This is because bonds of different lengths, strengths and torsional features absorb different wavelengths of infrared radiation (Allcock, 2008)

The un-purified and purified MWCNTs were also characterised by FTIR spectroscopy to check whether the purification stage had resulted in functional groups being introduced on the surface of the walls of the MWCNTs. FTIR spectroscopy was carried out on a Bruker TENSOR 27 FTIR spectrometer.

3.2.7 Powder X-Ray Diffraction

PXRD diffractometers

The Powder X-ray diffraction (PXRD) technique was the main technique used in this study. PXRD analysis of various catalysts was done on two X-ray diffractometers. These are the Bruker D2 Phaser and the Bruker D8 Advance which was equipped with an Anton Paar X-ray reaction chamber (XRK) (Anton Paar, 2005).

Bruker D2 Phaser

A Bruker D2 Phaser X-ray diffractometer is a bench top type diffractometer operated at 30 KV and 10 mA current. Diffraction patterns were collected on the diffractometer with the settings and specifications given in Table 3.1.

Table 3.1: Specifications and settings of Bruker D2 Phaser

Component	Value
Goniometer circle radius	141.1 mm
X-ray source tube type	Copper; λ =1.5405929
Detector type	LynxEye PSD
Primary and secondary soller slits	2.5 mm
Receiving Slit	2.5 mm
Fixed Divergence Slit	0.6 mm
Detector angle range	5°
Nickel Filter	yes

Bruker D8 Advance

In situ studies were carried out on the Bruker D8 Advance diffractometer (Figure 3.3). It is equipped with a copper tube which operates at 40 kV and 40 mA. A Gobel mirror was installed later in the course of the study; most of the experiments were done in the absence of the Gobel mirror. Table 3.2 gives the settings and specifications under which the experiments were done.

Table 3.2: Specifications and settings of the Bruker D8 Advance

Component	Value
Goniometer circle radius	250 mm
X-ray source tube type	Copper; λ =1.5405929
Detector type	Vantec-1 linear PSD
Primary and secondary soller slits	2.5 mm
Receiving slit	10.6 mm
Fixed Divergence Slit	0.6 mm
Monochromator	yes
Detector angle range	3°
Nickel filter	yes

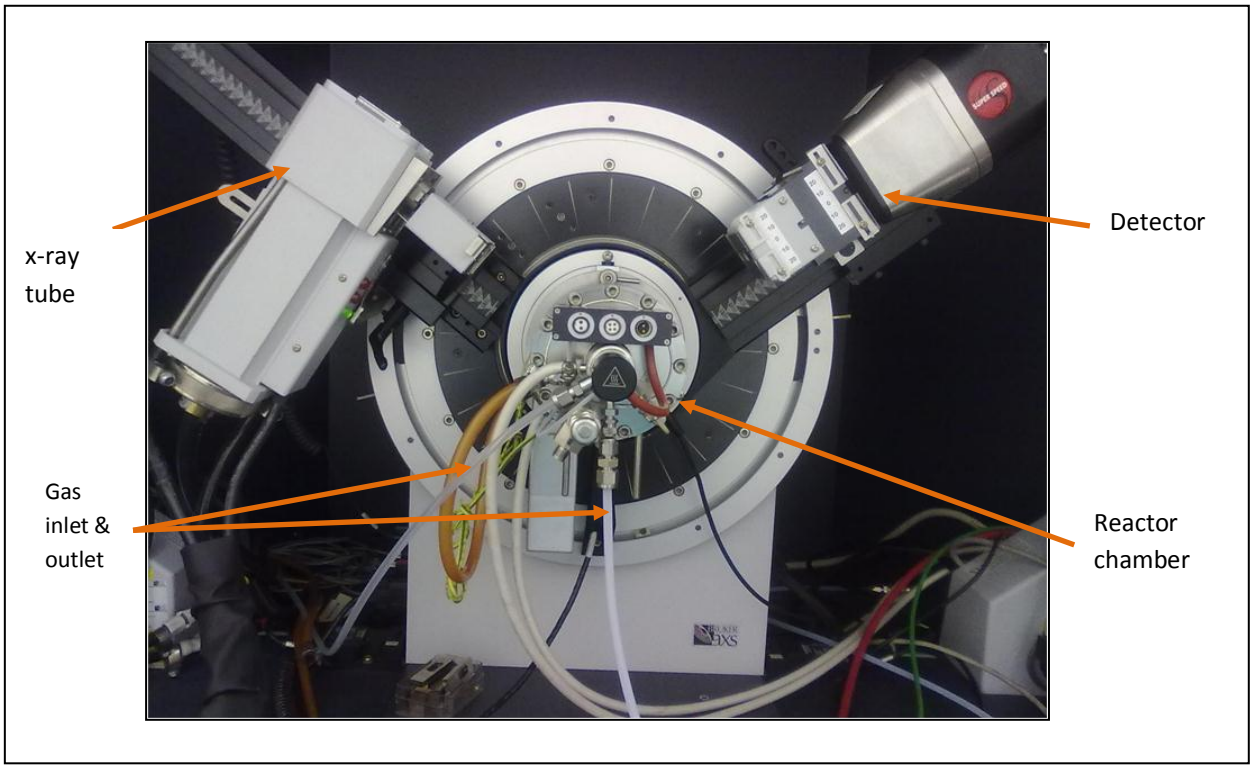


Figure 3.3: A picture of the Bruker D8 Advance diffractometer

Anton Paar X-ray reactor chamber

The XRK operates at temperatures up to 900 °C. The heating rate can be set to a maximum of 18 °C /min. A beryllium window surrounds the XRK cell and allows X-rays to pass through. Figure 3.4 shows the components of the XRK in detail.

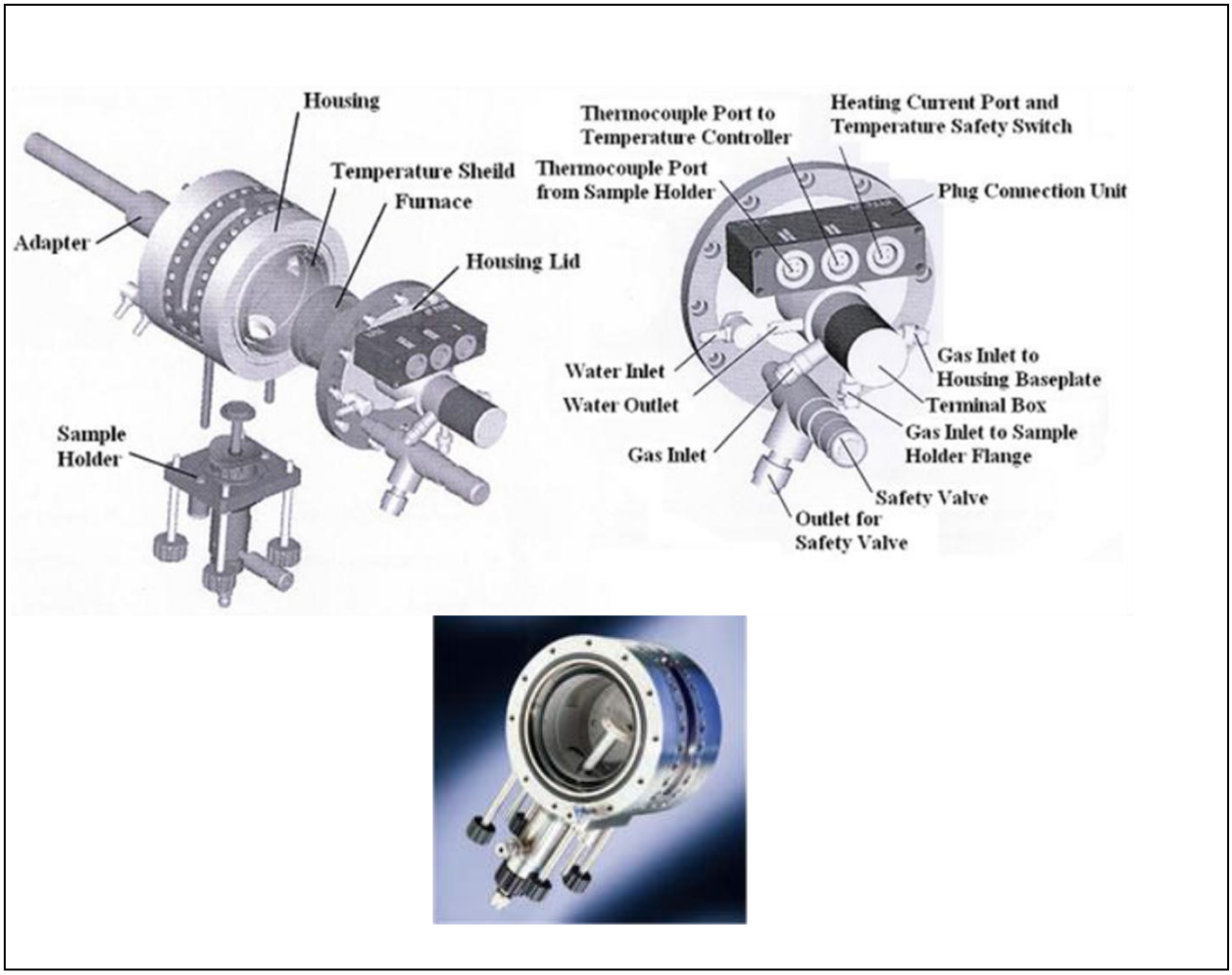


Figure 3.4: Schematic pictures of the Anton Paar XRK 900 showing its components (Anton Paar 2005)

Macor® Sample holder

Macor® is a non-porous material composed of 55% mica crystal and 45% matrix glass. It has a relatively good chemical resistance and can withstand temperatures of up to 1000 °C (Macor, 2012). Table 3.3 shows the properties of the sample holder in detail.

Table 3.3: Specifications and properties of the macor sample holder.

Property	Specification
Operating temperature	Ambient to 900 °C
Temperature measurement	NiCr/NiAl thermocouple
Maximum housing temperature	150 °C
Operating pressure	1 mbar to 10 bar
Sample diameter	14 mm
Sample holder material	Glass ceramic – Macor®

Gas connection to the XRK

The gases used for in situ analysis in the XRK were all purchased from Afrox. The gas flowed to the XRK cell and was controlled by valves. From the XRK cell the gas would flow through a bubble flow meter before being released to the atmosphere, as shown in Figure 3.5 below.

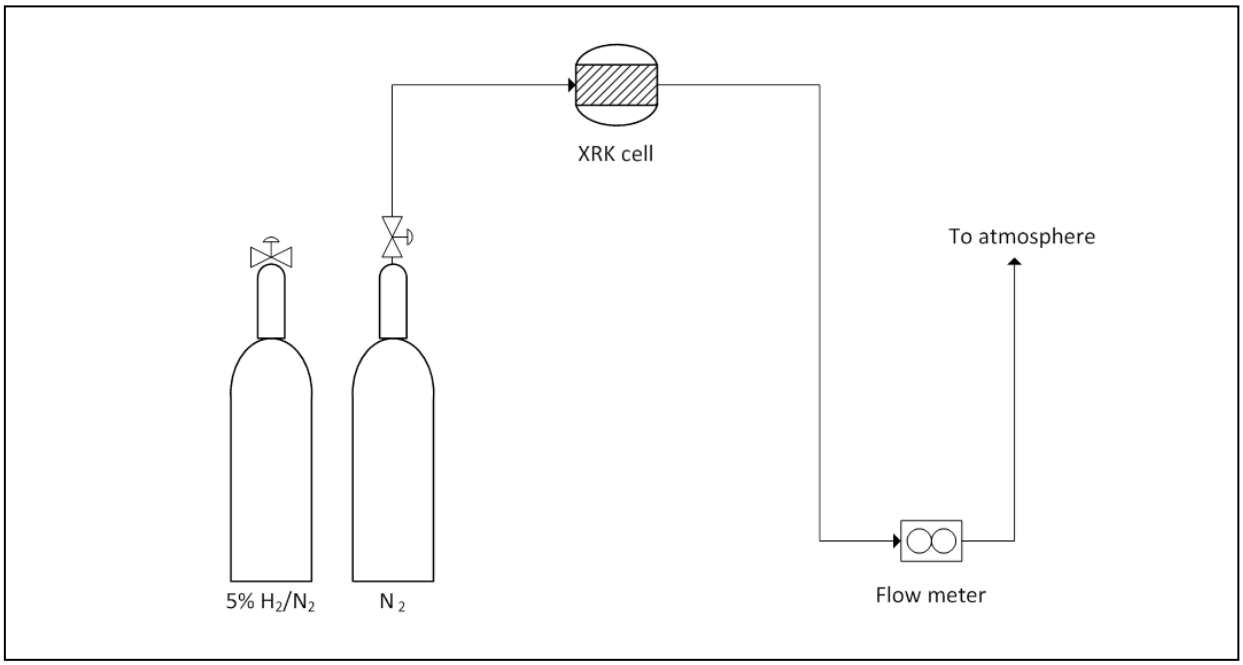


Figure 3.5: Gas supply system to the XRK

3.2.8 Calibration of Instruments

Calibration of the Bruker D8 Advance

Experiments were carried out using the same diffractometer settings described by Rayner (2011) and Forbes (2011). They carried out numerous experiments to determine that these settings gave accurate readings of peak positions and intensities. They used a LaB_6 standard made by the National Institute for Standards and Technology (NIST) to benchmark the diffractometer. They collected a diffraction pattern and refined it by Rietveld refinement. They found a lattice parameter which was different from that of the standard by only 0.02%. The peak position was only found to differ by 0.03% (Rayner, 2011). These differences were regarded as negligible. In this study it was assumed that these settings had not changed.

Calibration of the XRK

The XRK was calibrated to check temperature accuracy. This is important because the thermocouple is situated about 3 mm from the actual sample in the reaction chamber. This meant that there could be differences between the recorded temperature and the actual sample temperature. The Si NIST Standard Reference Material (SRM) 460 which has a simple cubic structure was used for this calibration. The lattice parameters of this material at various temperatures are well documented (Okada & Tokumaru., 1984).

A variable temperature PXRD analysis was carried out on the material. The sample was heated from 30 ˚C to 900 ˚C whilst patterns were collected at every 50 ˚C interval. Rietveld refinement was done by use of Topas software (Coelho, 2007). A fundamentals approach was used to describe the peak shape in this refinement. Background, absorption, zero error, scale factor of 1, crystallite size parameter and lattice parameters were refined in this instance. An average R_{wp} of 12.680 and an average goodness of fit of 1.68 were found after the refinement process. The lattice parameters of Si after refinement were compared with Okada et al.' s calculated lattice parameters of Si (Okada et al., 1984) documented for various temperatures. A plot of the two is given in figure 3.6 below, the graphs show negligible differences in the lattice size. Therefore the temperature recorded by the instrument was reliable and could be taken as correct.

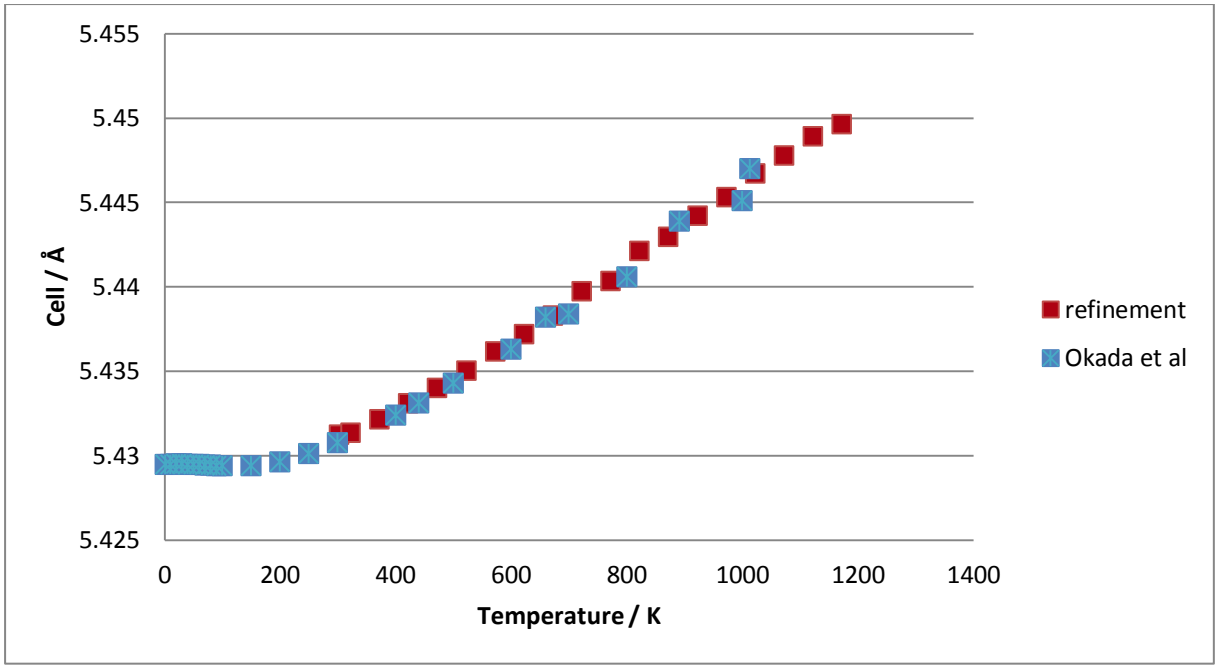


Figure 3.6: A plot of Okada et al (Okada et al., 1984) experimental Si lattice parameter against temperature and that of Si NIST SRM 460 over a temperature range of 0-1200 K

3.2.9 Powder X-ray Diffraction Data Analysis

PXRD patterns of each sample were obtained from the Bruker D2 Phaser diffractometer before an in situ experiment was carried out on that sample on the D8 Advance. When gases were involved in the in-situ experiment, a scan was collected with no gas flowing at room temperature and another with the gas flowing. This was done to confirm that the sample had not been blown away upon introduction of the gas thereby changing the sample height. Height errors result in slight peak shifts being witnessed.

Qualitative analysis of PXRD data

The diffraction patterns obtained were analysed and identification of compounds in the sample was done by use of Diffrac$_{plus}$ Eva software together with a powder diffraction file (PDF) database (PDF-2004) (Karlsruhe, 2010; ICDD website). This software uses a search match algorithm.

Quantification analysis of PXRD data

The International Crystal Structure Database (ICSD) numbers for identified compounds were noted from the PDF database. These ICSD numbers were then used to download the

crystallography information file (CIF). The CIF files were used in Rietveld refinement as a source of the crystal structure of the various phases identified for a particular sample. Rietveld refinement was done by use of Topas.4.2 software (Coelho 2007) mainly in the graphical user inter-face (GUI)mode. Percentage weights of the phases and crystallite sizes were an output result of the refinement.

According to Hill and Howard (1987) the weight of a phase in a mixture is proportional to the scale factor as shown by the following expression.

$$W_c = \frac{S_c(ZMV)_c}{\sum_i S_i\, i} \qquad \textbf{(3-1)}$$

where:

W_c = percentage weight of compound c

S_c = Rietveld scale factor

Z = number of formula units per unit cell

M = mass of the formula unit

V = volume of the unit cell

For more information refer to chapter 2

Analysing in situ PXRD Data

PXRD data obtained from in-situ runs was available as a single large raw file. From the raw file obtained after an in-situ run, scans taken at each temperature reading were pulled out and analysed individually. Each pattern was exported in EVA and saved as a raw file; then a qualitative analysis was done for each pattern.

Sequential Refinement

A sequential refinement method for analysing large in situ PXRD data was employed. In this method the output refinement result of the first scan was used as the input model for refinement of the next pattern (Styles et al., 2010). The input model was modified whenever there was a phase change to introduce the crystallography information of the new phase as well as to remove the crystallography information of a phase that had been depleted.

Calcination and reduction in-situ experiments were carried out on the samples. The H_2 content of the reducing gas was limited to 5% H_2-N_2 gas to prevent corrosion of XRK cell components. Table 3.4 lists some of the experiments that were done. The output files (Fe, $Co/CaCO_3$) and pro files (Ru/CNT) which show the models used for the refinement process can be found on the CD attached to this dissertation (Appendix A).

Table 3.4: In-situ experiments done to analyse the Fe-$Co/CaCO_3$ catalyst used in this study

Sample	**VT-PXRD N_2**	**VT-PXRD reduction**
5%Fe5%$Co/CaCO_3$	√	√
10%$Fe/CaCO_3$	√	√
10%$Co/CaCO_3$	√	√
$CaCO_3$	√	

Crystal structure pictures presented

The crystal structure pictures presented were created using Diamond software (Pennington 1999). This was achieved by use of the CIF files downloaded and used for quantitative Rietveld refinement.

3.3 Fischer Tropsch synthesis

3.3.1 Fischer Tropsch synthesis Rig

Fischer Tropsch synthesis (FTS) was carried out in the catalysis laboratory in the School of Chemistry. Syngas was made to flow through the catalyst in a reactor bed. The effluent gas was analysed by online chromatograph while the oil and wax was analysed offline. Figure 3.7 below shows the reactor system set up and Figure 3.8 shows the reactor and the thermocouple.

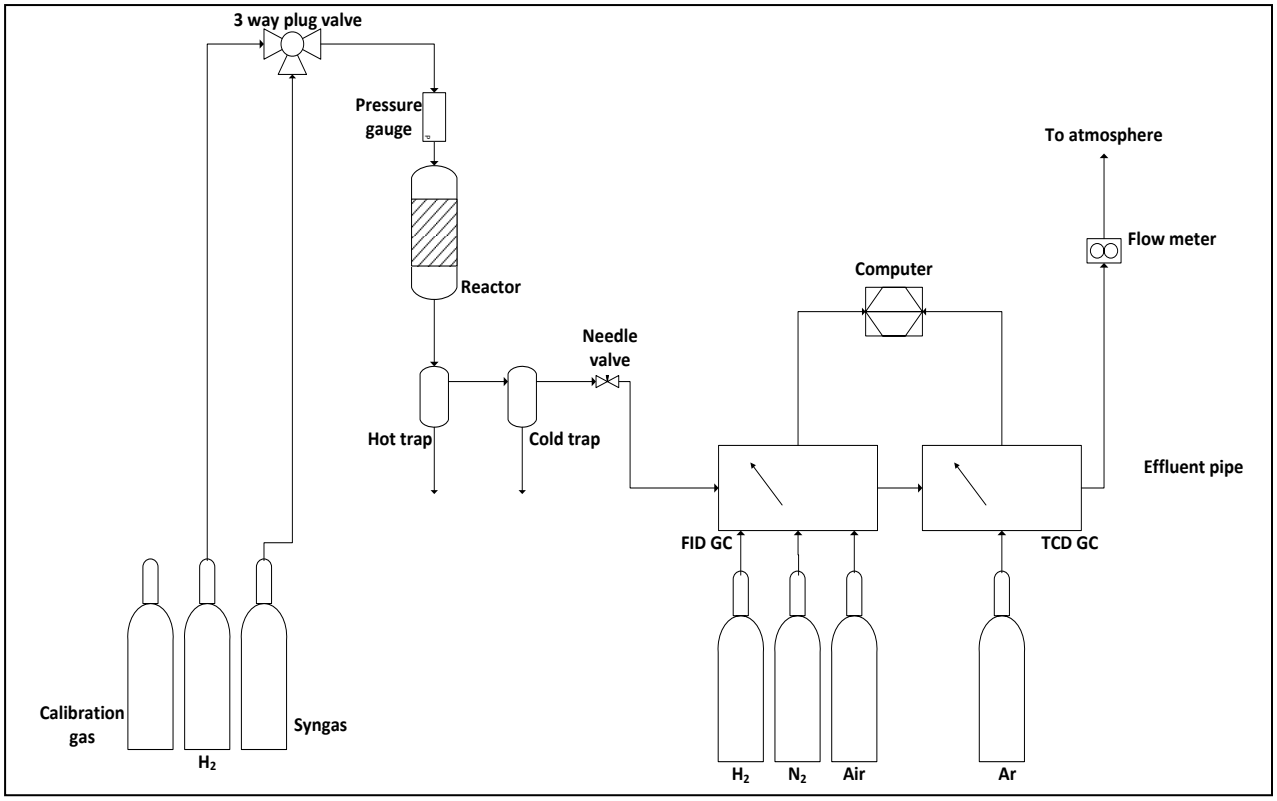


Figure 3.7: Fischer-Tropsch Synthesis rig

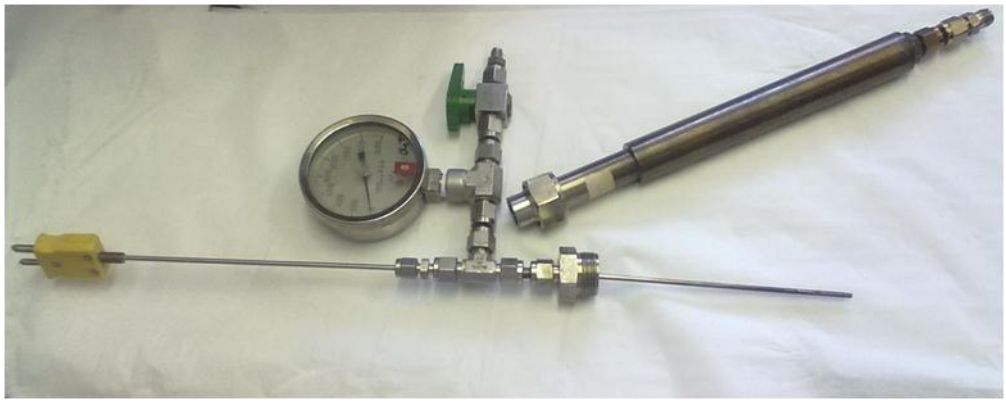


Figure 3.8: Picture showing a thermocouple and the micro reactor

The catalyst was held in place by quartz wool as shown in figure 3.9. On top of the catalyst bed was placed steel balls to facilitate uniform heating in the reactor.

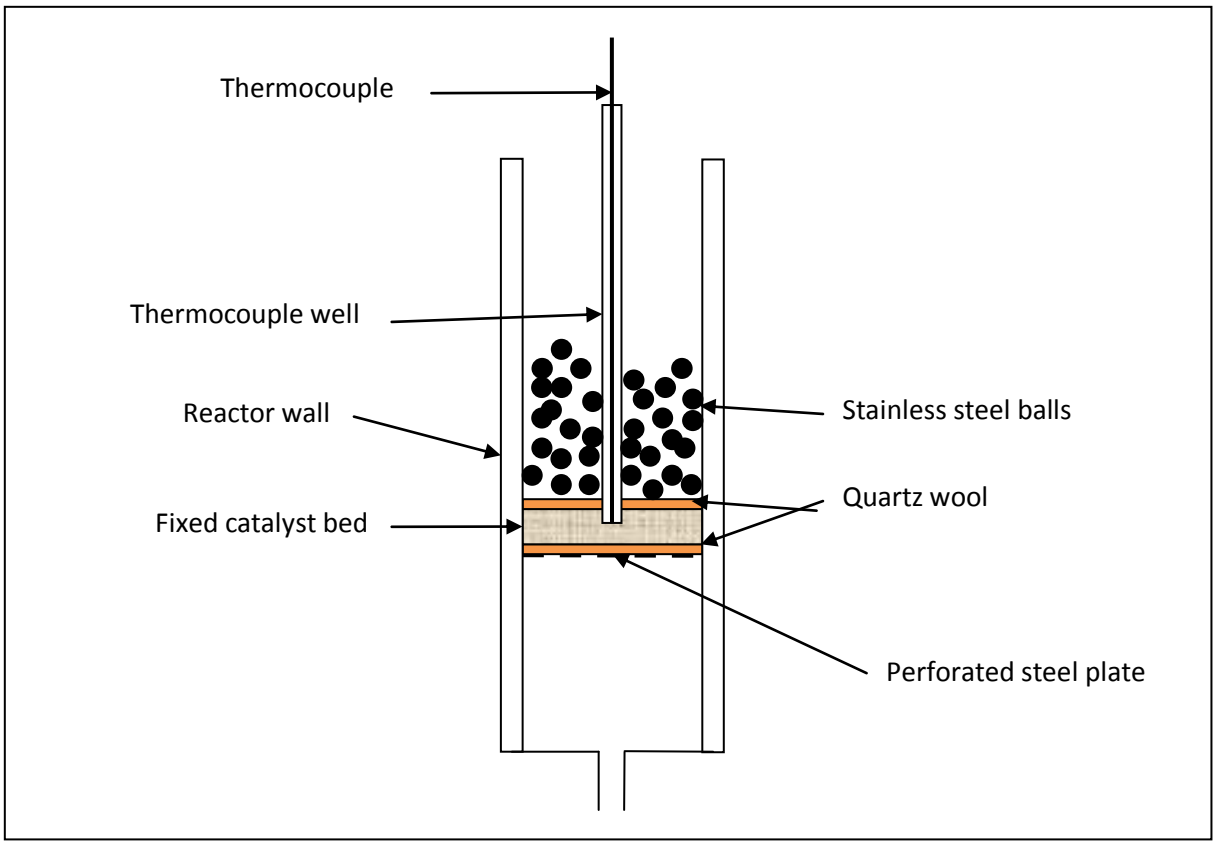


Figure 3.9: catalyst packing inside the fixed bed reactor

3.3.2 Fischer-Tropsch Synthesis

Catalyst and Gases

The catalyst used was synthesised as described elsewhere (section 3.1.4).The gases that were used were all Ultra High Purity Gases (UHP) and they were all purchased from AFROX.

Reaction Conditions

For each FT reaction 0.5 g of catalyst was used. The catalyst was reduced by H_2 gas in situ at 280 °C and a flow rate of 30 mL/min for 16 hours and thereafter the reactor was allowed to cool to room temperature under a H_2 flow. Synthesis gas with a H_2: CO ratio of 2:1 was then made to flow through the reactor operating at a pressure of 8 bar at 20 mL/min flow rate. The pressure was reduced to 1 bar by a regulator which is placed after the reactor but just before the GCs. The temperature was increased to the reaction temperature in 2 hours. FTS was carried out at a constant reaction temperature for 120 hours for each catalyst.

The flow rate was measured using a stopwatch and bubble flow meter placed at the outlet of the FT rig. The tail gas flow rate was checked every day to make sure that it did not vary during the period of the synthesis.

Test for leaks

Before each FT reaction a pressure test was conducted. This was done by pressurising the reactor and then isolating it by shutting off the valves. After 10 hours the pressure was checked again and a zero pressure drop signified no leaks in the system. In the event that the pressure gauge reading had dropped, nuts were tightened and the pressure test repeated again.

At the end of the reaction the knockout pots were emptied and the products weighed. Wax was collected from the hot trap and water and oil were collected from the cold trap. The water was separated from the wax and weighed.

***Gas Chromatograms (GCs*)**

Two online GCs (a flame ionisation detector (FID) and thermal conductivity detector (TCD)) and 1 offline GC were employed for analysing the different FT products. The FID was used to analyse the hydrocarbons of carbon number less than nine and the TCD GC was used to analyse non-hydrocarbon gases such as H_2, N_2 CO_2 and CO.

The FID was equipped with a 2 m poropak-Q (PPQ) column. It makes use of H_2 and air to separate the hydrocarbons from C_1 to C_8 with N_2 as the carrier gas. The TCD makes use of Ar as a carrier gas. Clarity software was used to record the results from the GCs.

The offline GC which has TCD and FID capabilities was used to analyse waxes and liquids collected at the end of the reaction time.

3.3.3 Analysis of Fischer Tropsch data

Calibration of the GC

The GCs were calibrated before each FTS run. Calibration was done by use of syngas (H2: CO; 2:1) and a special calibration gas from Afrox ((2.5%), C_2H_4 (0.2%), C_2H_6 (0.5%), CO (10.0%), CO_2 (5.0%) and balance of Ar).

Below are shown examples of some of the GC traces recorded using Clarity software (Figure 3.10, Figure 3.11)

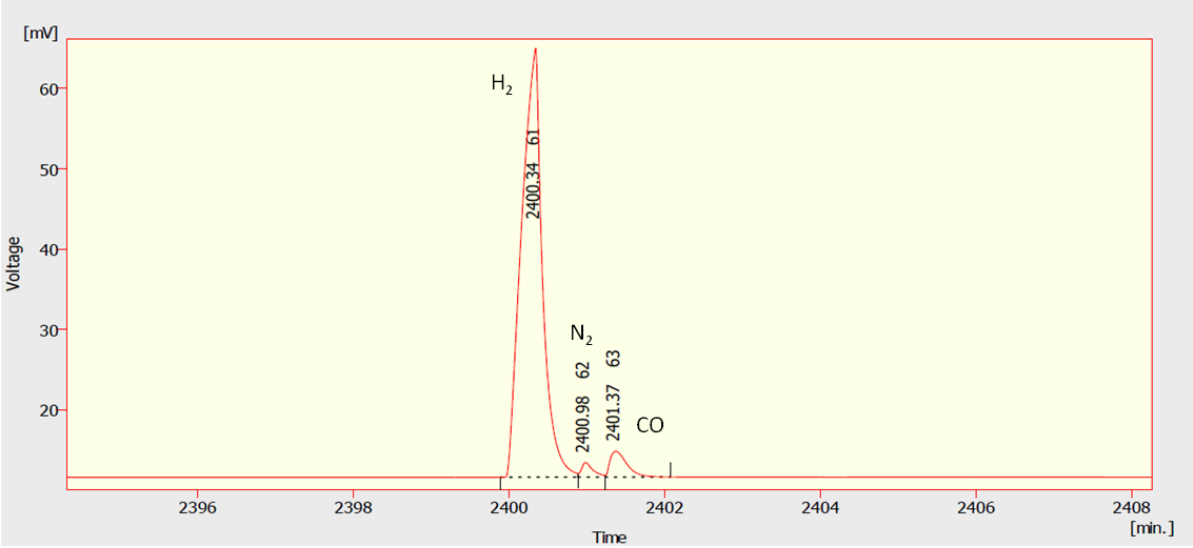


Figure 3.10: Typical trace of synthesis gas on the TCG GC

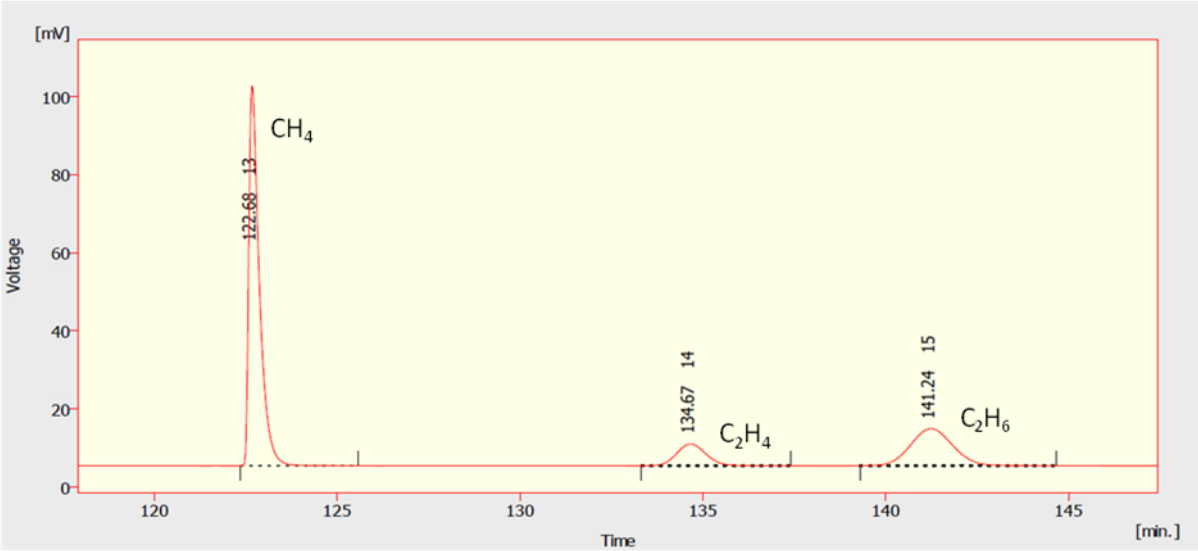


Figure 3.11: Typical trace of the calibration gas on the FID GC

FT calculations

From the calibration the number of moles of a gas component was calculated as follows;

$$n_c = \frac{A_c}{A_{c,cal}} \times X_{c,cal} \times F_{out} \times t \qquad \textit{(3-2)}$$

where:

n_c = number of moles of component c

A_c = integrated area of component c

$A_{c,cal}$ = integrated area of component c in the calibration gas

$X_{c,cal}$ = mole fraction of component c in the calibration gas

Molar response factors and reference compounds were used for hydrocarbons whose calibration data could not be found in the calibration mixture. A response factor of 1.0 was adopted for hydrocarbons with carbon number greater than 15. Therefore the mass composition was directly read from the GC reading. Listed is the equation used to determine mole fraction of hyrocarbons.

$$X_{\theta,i} = \frac{RF_i \times A_{\theta,i}}{A_{c2,cal}} \times X_{c2,cal}$$

(3-3)

where:

$X_{\theta,i}$ = mole fraction of hydrocarbon with carbon number i

RF = response factor for carbon number i

$A_{\theta,i}$ = integrated GC area for hydrocarbon with carbon number i

$A_{c2,cal}$ = peak area of the C_2 hydrocarbon in the calibration gas

$X_{c2,cal}$ = mole fraction of the C_2 hydrocarbon in the calibration gas

For hydrocarbons of carbon number greater than 15 (RF=1) the expression becomes

$$m_i = \frac{A_{\theta,i}}{\sum A_{\theta,i}}$$

(3-4)

The mass balance calculations used are similar to those used by Motchelaho, Moyo, Duvenhage (Motchelaho 2011, Moyo 2012, Duvenhage 1994). Clarity software gave integrated areas for the peaks; however a check was done to make sure that all the relevant peaks had been selected properly.

Since the tail gas flow rate was measured during the reaction, the inlet flow rate was determined from the trace gas which in this case was N_2, and it was calculated as follows.

$$F_{in} = \left(\frac{X_{N_{2,in}}}{X_{N_{2,Out}}}\right) \times F_{out}$$

(3-5)

where:

F_{in}= the total feed molar flow rate (mol/s)

F_{out} = the total tail gas molar flow rate (mol/s)

$X_{N2,\ in}$ = the mole fraction of nitrogen in the feed (syngas)

$X_{N2,\ out}$ = the mole fraction of nitrogen in the tail gas

The moles of carbon in the syngas feed was calculated by:

$$n_c = F_{in} \times t \times X_{Co,in}$$

(3-6)

where:

n_c = the number of moles of carbon in the feed to the reactor

F_{in} =the total flow rate in mol/s

t = the total mass balance time

$X_{co,in}$ = the CO mole fraction in the feed syngas

The % conversion of CO was calculated as

$$\%CO = \left\{ \frac{X_{CO,in} - X_{CO,out}\left(\frac{X_{N_{2,in}}}{X_{N_{2,out}}}\right)}{X_{CO,in}} \right\} \times 100$$

(3-7)

where:

%CO is the CO percentage conversion

$\frac{X_{N_{2,in}}}{X_{N_{2,out}}}$

is the gas contraction factor

The rate of CO conversion was calculated as follows

$$r_{co} = \frac{F_{co,in} - F_{co,out}}{m_{cat}}$$

(3-8)

where:

r_{Co} = rate of conversion of CO

$F_{co,in}$ = molar flow rate of CO in the feed to the reactor (mol/s)

$F_{co,out}$= molar flow rate of CO in the tail gas (mol/s)

m_{cat} = mass of catalyst

Selectivity for a hydrocarbon θ_i as a percentage was calculated as;

$$S_{\theta,i} = \frac{n_{\theta,i}}{r_{co} \times t} \times 100$$

(3-9)

where:

$S_{\theta,i}$ = selectivity of hydrocarbon with carbon number i

$n_{\theta,i}$ = number of moles of hydrocarbon of carbon number i

t = mass balance time

r_{co} = rate of CO conversion

The olefin to paraffin ratio was calculated as;

$$Olefin\ to\ paraffin\ ratio = \frac{mass\ of\ olefin}{total\ mass\ of\ hydrocarbon\ number\ ci}$$

(3-10)

where

c_i = hydrocarbon with number of carbon atoms i

CHAPTER 4

4 IN SITU PXRD STUDY OF A Fe-Co/$CaCO_3$ CATALYST FOR THE SYNTHESIS OF CARBON NANOTUBES

4.1 Introduction

Carbon nanotubes (CNTs) have various applications and have been used in catalysis, drug delivery and electronic devices (Terrones et al., 2004). Hence there is a need to understand the CNT synthesis processes in depth; this would ultimately lead to the realisation of optimum conditions for their production.

CNTs are typically made by passing a carbon source over a metal catalyst with the catalyst spread over a support material to enhance the catalyst support area. Many studies have been reported on the synthesis of CNTS and the mechanism of the reaction is known in reasonable detail. Studies in the School of Chemistry at the University of the Witwatersrand have in the last decade focussed on the synthesis of CNTs and other shaped carbon materials. A catalyst system that has been found to be effective for the synthesis of both CNTs and nitrogen doped CNTs (N-CNTs) is the Fe-Co/$CaCO_3$ catalyst. Studies in our laboratory have been reported in which the reaction system to make CNTs and N-CNTs using the Fe-Co/$CaCO_3$ has been optimised. (Mhlanga et al., 2009; Tetana et al., 2012)

This system has numerous advantages which include the following:

- It has been studied by many others (Coteau et al., 2002; Magrez et al., 2005)
- Very few carbon by-products are formed i.e. it has a high selectivity to CNTs.
- $CaCO_3$ can easily be removed by a mild acid treatment.
- $CaCO_3$ is a cheap material.

This study was therefore carried out to get more information about this catalyst system. This was done by employing an in situ PXRD technique to get information with regards to phase transition and crystallite changes which are useful in explaining the performance of

the catalyst under conditions such as temperature and/or pressure. Li et al. (2008) carried out a study on the Fe-Co/$CaCO_3$ catalyst also by in situ XRD. They used radio frequency inductive heating to heat their specimen.

In this study the catalysts were characterised by TEM to verify how the iron and cobalt oxides were dispersed on the support ($CaCO_3$). Thermal response studies were done by use of mainly the in situ PXRD technique. This was done so as to identify the actual form of the catalyst that is available for reaction before the introduction of the carbon source (C_2H_2). Thermal gravimetric analysis was also used to investigate the effect of heat treatment. Reduction studies were also carried out to study the reducibility of the catalysts. This was done because it is known that the hydrocarbon source (C_2H_2) sufficiently reduces these catalysts during synthesis (Hernadi et al., 1997). A variation in reducibility could explain the difference in performances observed in CNT synthesis when these catalysts are used. The characterisation techniques employed in this investigation were TPR and in situ reduction in the in situ XRD chamber (XRK-900). In both these techniques 5% H_2 gas in N_2 was used as the carrier.

4.1.2 Experimental

Various catalysts (10% Co/$CaCO_3$, 10% Fe/$CaCO_3$ and 10% Fe-Co/$CaCO_3$) were synthesised by incipient wetness impregnation as described previously (section 3.1.1). The 10% Fe-Co/$CaCO_3$ catalyst comprised of 5% Fe and 5% Co. In situ experiments were carried out on the D8 Advance diffractometer which is equipped with a Cu tube as X-ray source (section 3.2.7. The details of the experiments including the number of patterns analysed by Rietveld refinement are listed in the Tables shown (Table 4.1, Table 4.2 and Table 4.3). The samples were not spiked hence the amorphous content of the samples could not be quantified. This is because silicon which is usually used as a spike phase showed that it reacted with $CaCO_3$ at elevated temperatures. In situ variable temperature powder X-ray diffraction (VT-PXRD) runs were carried out with XRD patterns collected every 50 ˚C. VT-PXRD runs were repeated for $CaCO_3$ and 10% Fe-Co/$CaCO_3$ with patterns collected at 20 ˚C intervals to obtain more detailed data. The results observed were similar for these 2 sets of data.

Table 4.1: Experimental details of in situ VT-PXRD of $CaCO_3$ and 10% Fe/$CaCO_3$

	$CaCO_3$	**10% Fe/$CaCO_3$**
Temperature range (°C)	30 ˚C- 850 ˚C	30˚C – 850 ˚C
Temperature increment	20 ˚C	50 ˚C
Number of patterns	25	18
Angular 2θ range (°)	15-50	10-90
Step size (°/sec)	0.021	0.021
Time per step (sec)	1.5	0.8
Average Rwp	6.08	4.09
Average G.O.F	1.5	1.07

Table 4.2: Experimental details of the in situ VT-PXRD of $CaCO_3$ and 10% Fe-Co/$CaCO_3$

	10% Co/$CaCO_3$	**10% Fe-Co/ $CaCO_3$**
Temperature range (°C)	30 ˚C - 900 ˚C	350 ˚C - 850˚C
Temperature increment	50 ˚C	20 ˚C
Number of patterns	19	24
Angular 2θ range (°)	10-90	10-90
Step size (°/sec)	0.021	0.021
Time per step (sec)	0.8	0.8
Average Rwp	5.71	4.33
Average G.O.F	1.21	1.13

Table 4.3: Experimental details of the in situ reduction of the catalysts carried at 700 ˚C

	10% Fe/$CaCO_3$	**10% Co/$CaCO_3$**	**10% Fe-Co/$CaCO_3$**
Temperature range (˚C)	700 ˚C	700 ˚C	700 ˚C
Number of patterns	25	25	25
Angular 2θ range (°)	10-75	10-75	10-75
Step size (°/sec)	0.021	0.021	0.021
Time per step (sec)	1.00	1.00	1.00
Average Rwp	4.21	6.27	3.92
Average G.O.F	1.33	1.48	1.15

4.2 Thermal response of Fe-Co/$CaCO_3$ catalysts

4.2.1 Surface area analysis

Nitrogen adsorption data was fitted to the BET equation and used to analyse the surface area (Brunauer et al., 1938). The results show that the catalysts are low surface area catalysts (Table 4.4). $CaCO_3$ has the highest surface area of 13.20 m^2/g followed by 10% Fe/$CaCO_3$ with 11.60 m^2/g. It can be seen that when iron and cobalt are loaded onto $CaCO_3$, the catalyst surface area decreases. This is because the pores are filled with the metal salts. The pore volume of $CaCO_3$ decreased by 50% when iron and cobalt were added onto it, this is because the metal salts and finally the oxides filled the pores of the $CaCO_3$. The surface area of all the catalysts decreased by ca. 50% when the catalysts were heated at 700 °C for 1 hour. This is because some of the $CaCO_3$ support decomposes to CaO at this temperature. $CaCO_3$ has a higher surface area than CaO. The pore volume also decreased after heat treatment at 700 °C.

Table 4.4: BET Surface area

Sample	Surface area (m^2/g)	Pore Volume cm^3/g
$CaCO_3$	13.20	0.066
10% $Fe/CaCO_3$	11.60	0.037
10% $Co/CaCO_3$	6.20	0.037
10% Fe-Co/ $CaCO_3$	7.00	0.032
$CaCO_3$ (700 ˚C)	3.12	0.009
10% $Fe/CaCO_3$ (700 ˚C)	4.09	0.020
10% $Co/CaCO_3$ (700 ˚C)	4.25	0.016
10% FeCo/ $CaCO_3$ (700 ˚C)	3.73	0.015

(700 ˚C)=heated at 700 ˚C for 1 hour under N_2

4.2.2 Transmission electron microscopy

TEM images revealed that iron and cobalt oxides had successfully been loaded onto the $CaCO_3$. The dispersion was however better for the 10% $Fe/CaCO_3$ than for the 10% $Co/CaCO_3$ and 10% Fe-$Co/CaCO_3$ materials (Figure 4.1). From the images, it can be seen that some of the iron and cobalt particles had agglomerated around the $CaCO_3$ in 10% Fe-$Co/CaCO_3$ and 10% $Co/CaCO_3$ and Fe-$Co/CaCO_3$ (see arrows). The particle size of iron and cobalt particles was small and agglomerated and therefore could not be measured with any accuracy with the TEM facility available.

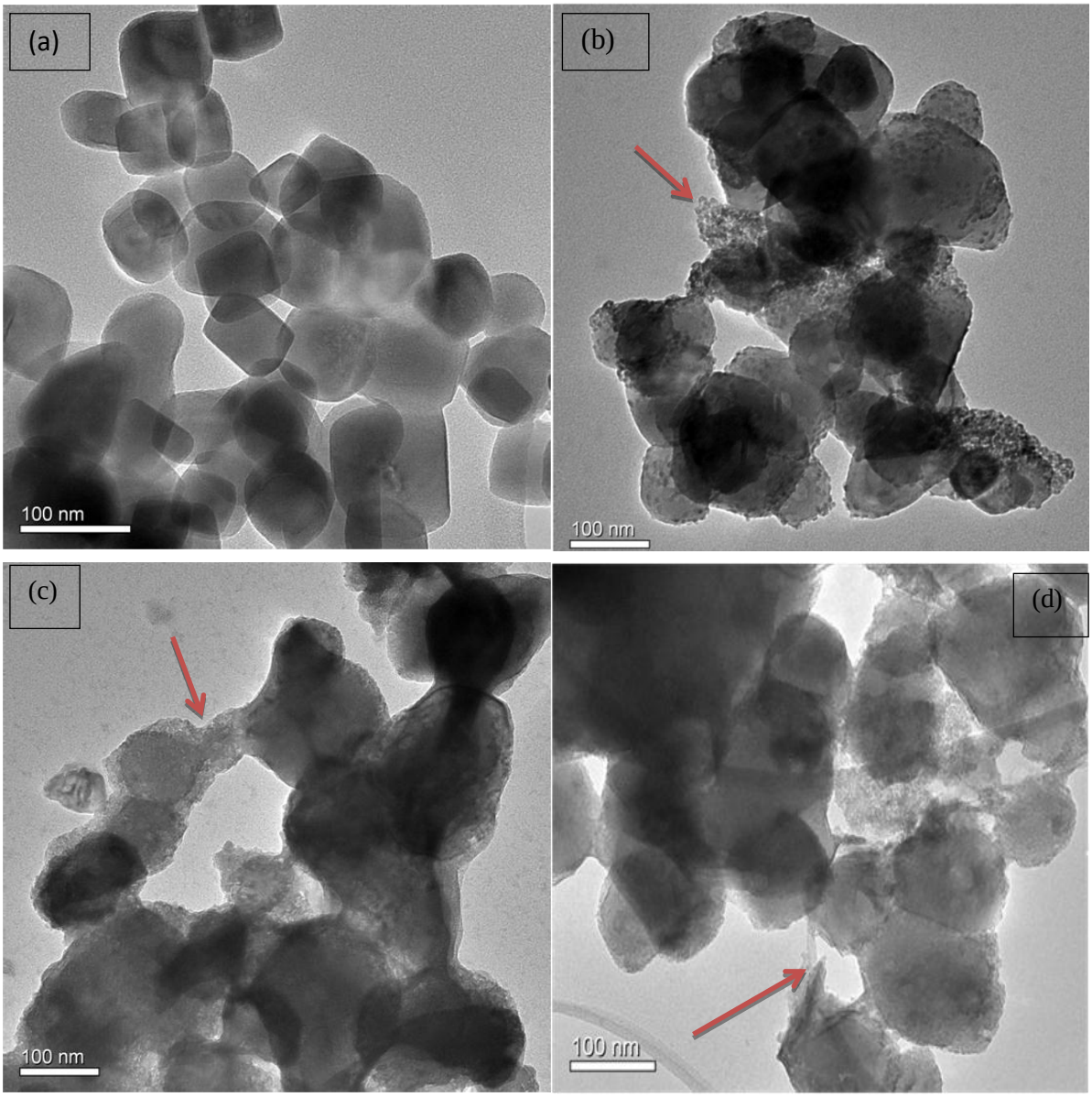


Figure 4.1: TEM Images of; a- $CaCO_3$, b- 10% Fe/$CaCO_3$, c- 10% Co/ $CaCO_3$, d- 10% Fe-Co/ $CaCO_3$.

When the samples were annealed at 700 ˚C the metal particles generally increased in size. Measurement of $CaCO_3$ particle size using Image J software revealed that the crystallite size of $CaCO_3$ increased from an average of 72.8 nm to 216.7 nm after heat treatment at 700 ˚C (Figure 4.2). It should however be noted that the images may also be that of CaO since $CaCO_3$ decomposes under these conditions. After heat treatment some CaO/$CaCO_3$ particles

lost shape during the transition from $CaCO_3$ to CaO (Figure 4.2 (e)). Metal particles had also increased in size in the catalysts (Figure 4.2 (b) and (c)).

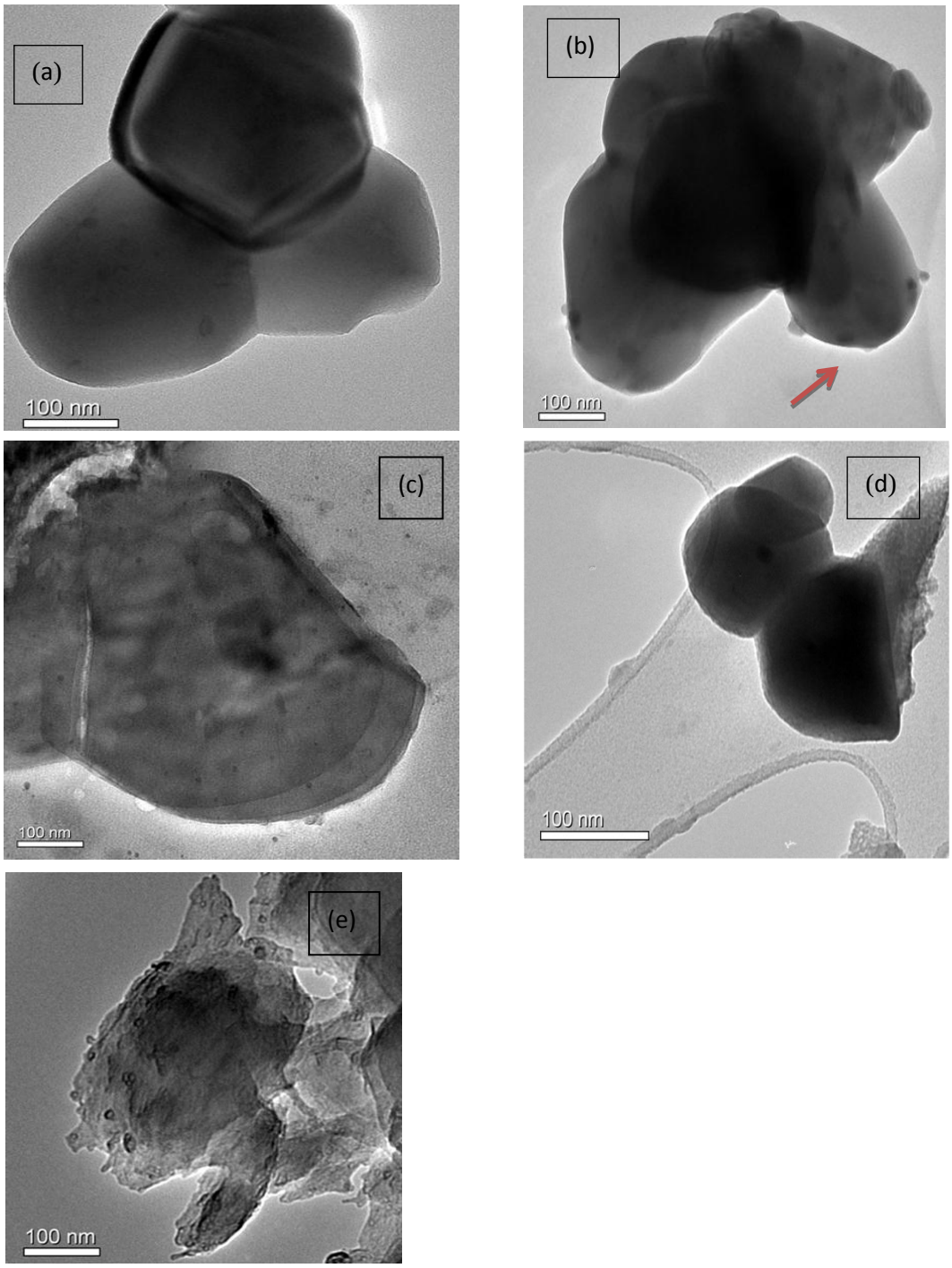


Figure 4.2: TEM images of 10%Fe/$CaCO_3$; a- $CaCO_3$, b- 10% Fe/$CaCO_3$ c- 10% Co/$CaCO_3$, d- 10% Fe-Co/ $CaCO_3$ e – 10% Co/$CaCO_3$ (amorphous material) after heat treatment at 700 ˚C for 30 minutes.

4.2.3 In situ VT-XRD study of $CaCO_3$

In situ variable temperature PXRD studies were carried out on the ($CaCO_3$) support. The sample was heated from room temperature to 850 ˚C under an inert atmosphere with XRD patterns being collected every 20 ˚C. The results are shown in Figures 4.3 and 4.4. Figure 4.3 shows individual patterns whereas Figure 4.4 shows the same picture in a different representation. Figure 4.4 show the intensity of the peaks at three intensity levels, yellow being the least and blue showing the highest level of intensity. Usually a topographical view is presented as some small peaks may be hidden by others in the 3D view.

The results indicate that $CaCO_3$ started decomposing to CaO at 610 °C and all the $CaCO_3$ has decomposed to CaO by 810 °C (Figure 4.3). This is in agreement with literature reports (Rodriguez-Navarro et al., 2009, Magrez et al., 2005). This is also consistent with reports by Schmitt et al. (2006) who reported that at 720 °C the presence of both CaO and $CaCO_3$ was noted and this resulted in MWCNTs with different sizes. However, given sufficient time all the $CaCO_3$ should decompose to CO_2 and $CaCO_3$ at 700 °C.

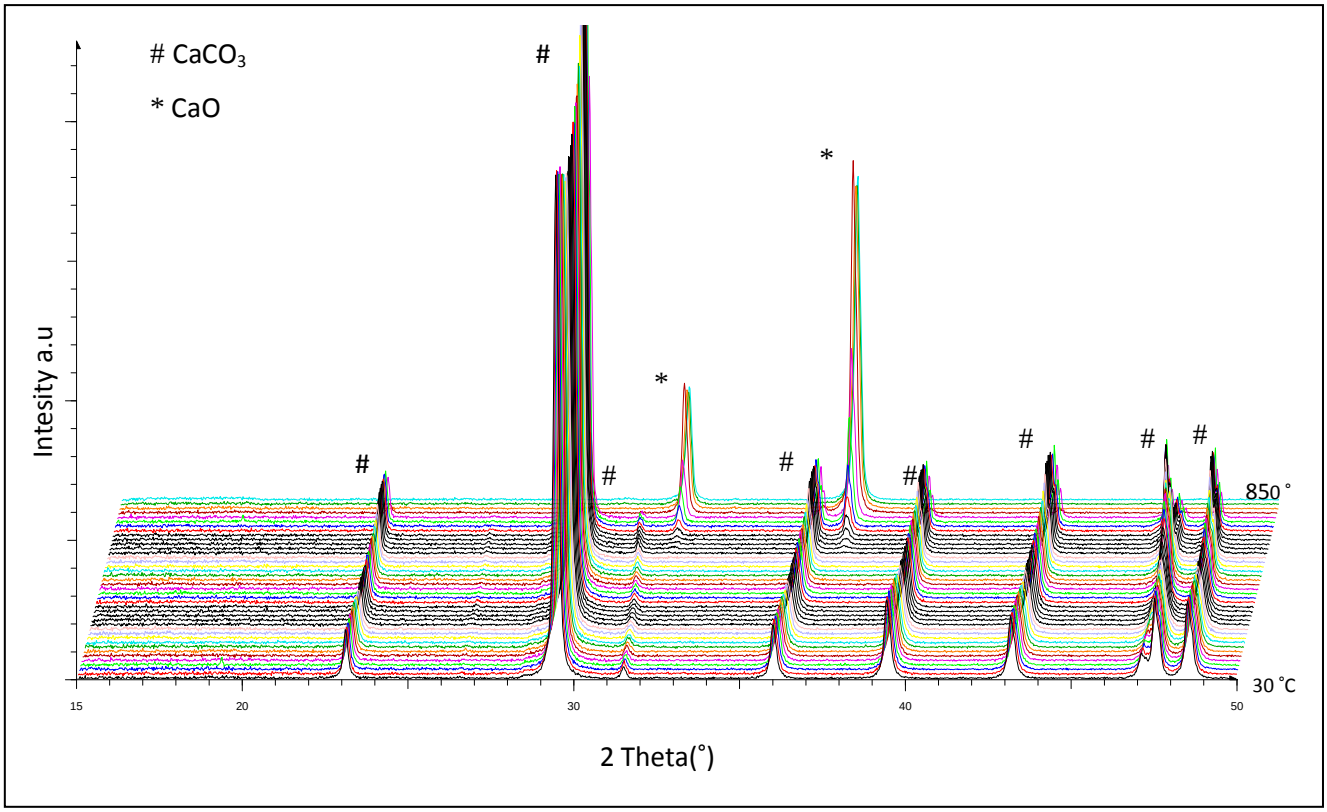


Figure 4.3: 3D figure showing patterns collected during in situ VT-PXRD of $CaCO_3$

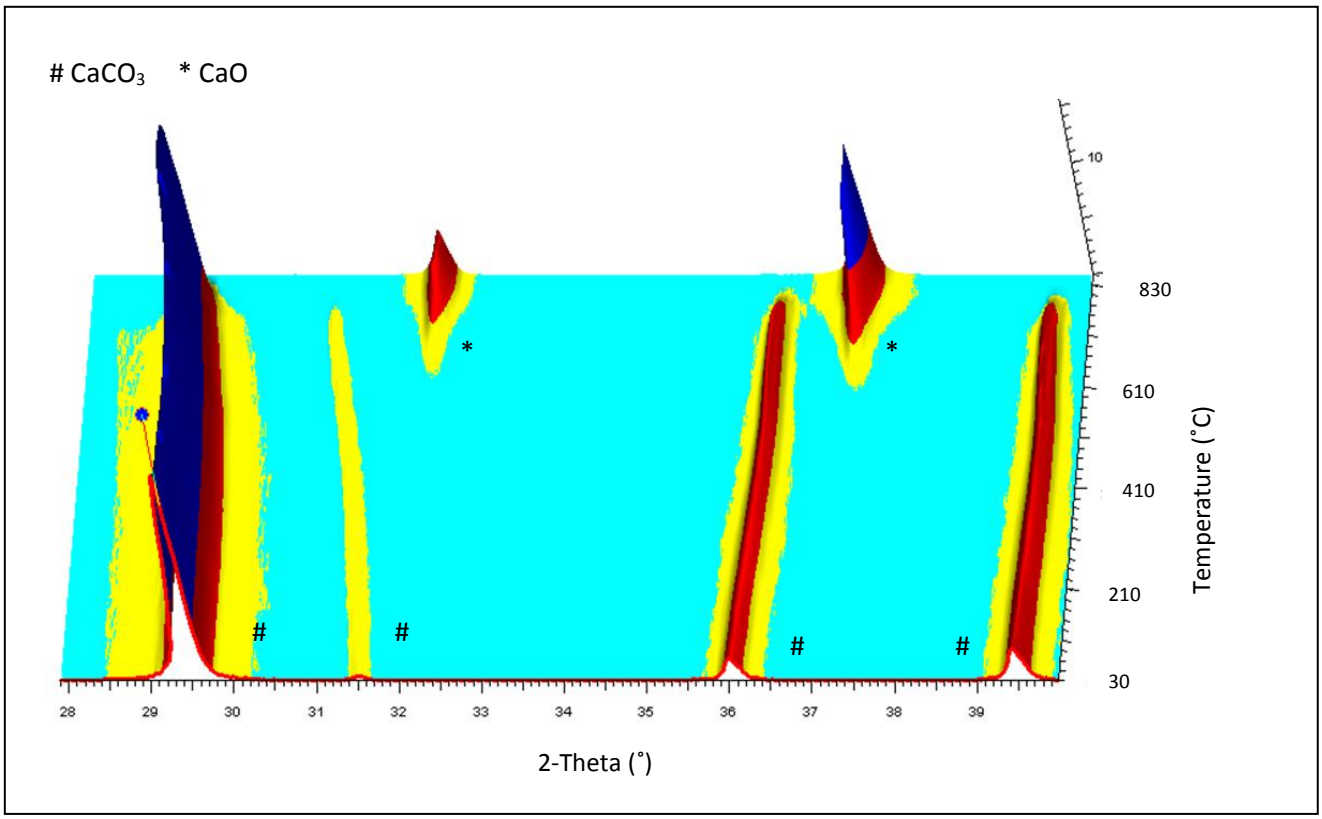


Figure 4.4: Phase abundance variation during VT-PXRD: # CaCO3; * CaO

The phase match is shown in the Appendix.

Quantitative analysis; Rietveld refinement

The Rietveld refinement process has been described in detail elsewhere (section 3.2.7). Topas (Coelho, 2007) software was used for the analysis. Each pattern was analysed individually; but sequential refinement was employed where the results of a previous refinement became the input for the next pattern refinement. Figure 4.5 and Figure 4.6 show the results of the refinement carried out on the patterns collected at 50 ˚C and 730 ˚C. The red profile shows the pattern collected from the instrument, the blue represents the curve calculated from the built model and grey is the difference curve between the two. Rietveld refinement results do not have much meaning when figures of merit are not reported; hence Rwp and goodness of fit are reported to show the reliability of the results. Crystallite size was determined from the Scherrer equation (section 2.3.6.) which is incorporated in Topas. Trends in the changes of the crystallite size with temperature are also presented in this study. When the calculated crystallite size calculated from these XRD results was compared to TEM particle size results, a difference (13%) was noted. The results

presented thus indicate trends rather than absolute sizes. When the temperature reached 730 ˚C a delay time of ca. 2 minutes (Table 4.1) was employed before collection of the XRD data began.

Refinement at 50 ℃

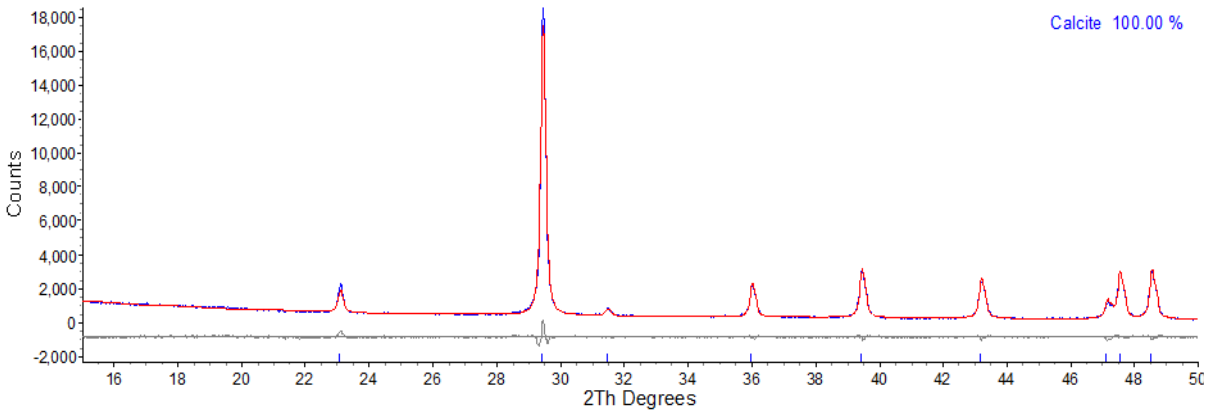


Figure 4.5: Refinement results for pattern collected at 50 ˚C during VT-PXRD of $CaCO_3$

Rwp 5.4; G.O.F 1.5

Refinement at 730 ℃

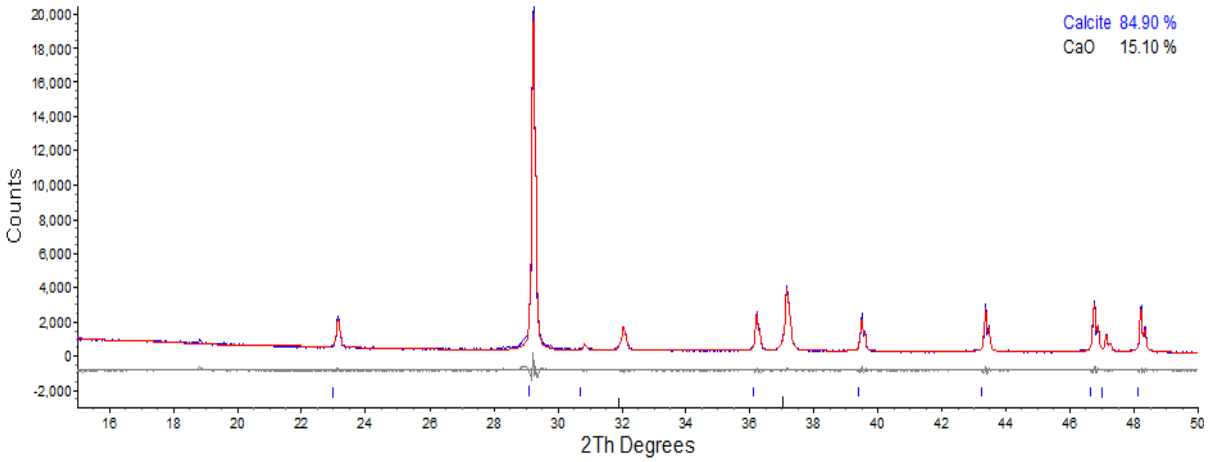


Figure 4.6: Refinement results for pattern collected at 730 ˚C during VT-PXRD of $CaCO_3$

Rwp 6.78; G.O.F 1.76

The change of phase abundances over temperatures from 300 °C to 850 °C is shown in Figure 4.7. The particle size of the $CaCO_3$ increased with increase in temperature (Figure 4.8) from 84 nm reaching a maximum of 234 nm at 730 °C. From 630 °C to 730 °C the particle size increased by 50%. This compares well with TEM results which showed an average particle size of 72.8 nm at room temperature and 216 nm after heat treatment (700 °C). The particle size decreased thereafter; this is because the concentration of $CaCO_3$ is decreased and approached extinction. The particle size of CaO grew slightly (42%) from the emergence of that phase at 630 °C to a maximum of 139 nm at 850 °C. At 700 °C the particle size is 109 nm (Figure 4.8).

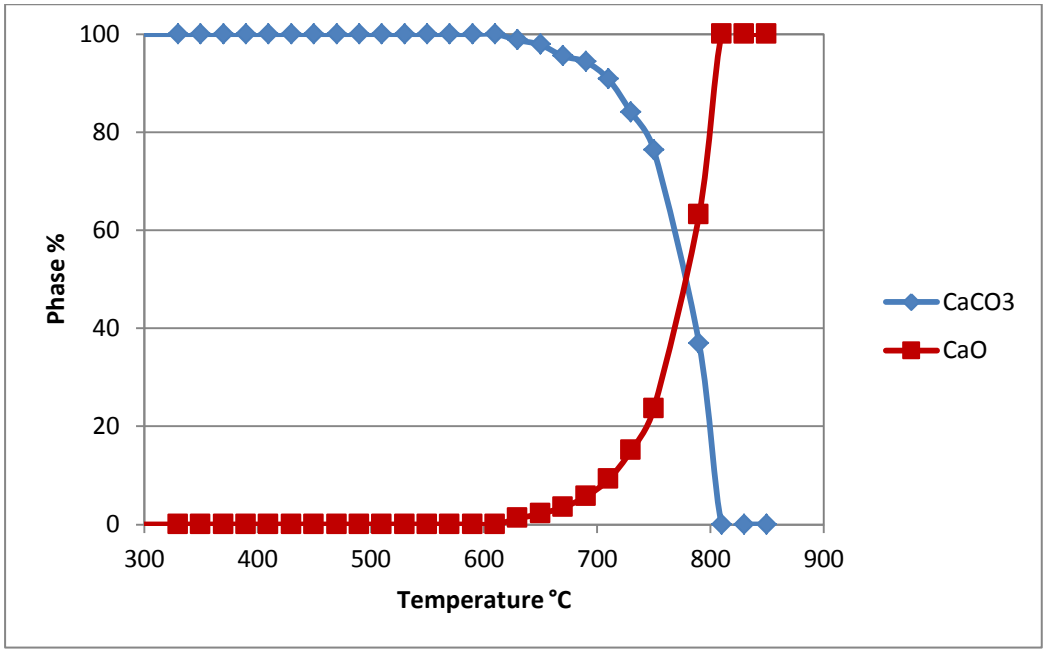


Figure 4.7: Phase abundance variation during VT-PXRD of $CaCO_3$

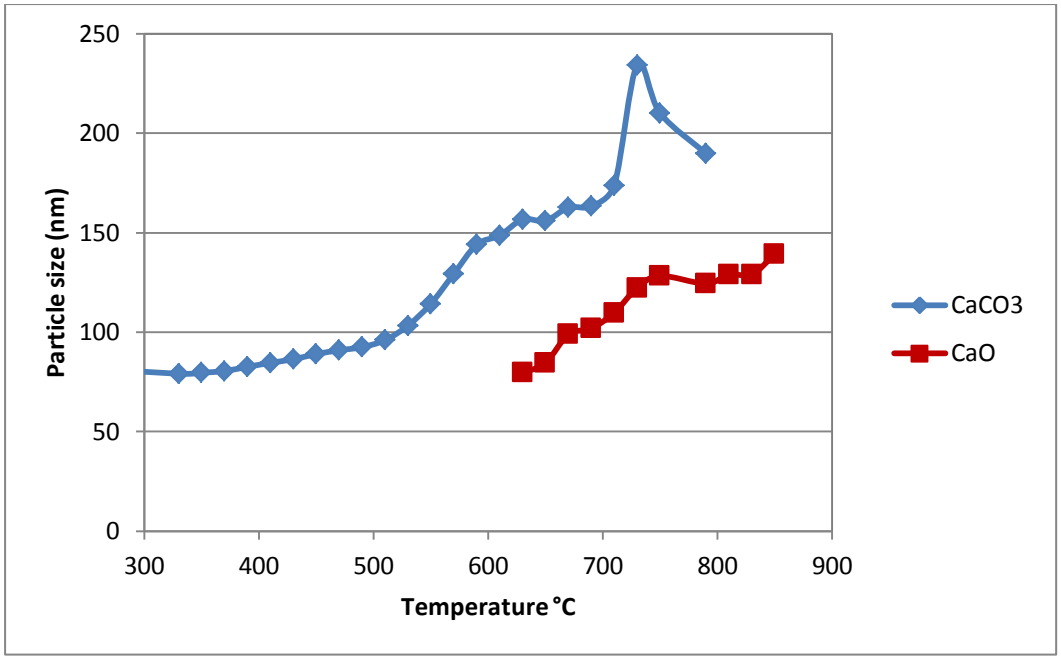


Figure 4.8: Variation of particle size during VT-PXRD heat treatment of $CaCO_3$

4.2.4 In situ VT-PXRD study of10% Fe/$CaCO_3$

10% Fe/$CaCO_3$ was heated from 50 °C to 850 °C whilst XRD patterns were being collected every 50 °C under inert conditions. The pattern taken at room temperature (30 °C) revealed the presence of iron in the form of Fe_3O_4 (magnetite peak at 37 °) (Figure 4.9) and the support $CaCO_3$, $CaCO_3$ decomposed to CaO at a temperature above 650 °C. This decomposition temperature is slightly higher than that previously reported for $CaCO_3$ (section (4.2.3)). This variation could be due to the difference in heating intervals that were employed or it could be that the addition of iron to $CaCO_3$ delays its decomposition. $CaCO_3$ had completely converted to CaO at 800 °C. At 650 °C dicalcium diiron (III) oxide ($Ca_2Fe_2O_5$) peaks emerged (33.2 °). $Ca_2Fe_2O_5$ has an orthorhombic structure with space group Pcmn (66) (Figure 4.10). It is clear that the support has reacted with the metal catalyst. This was also confirmed by an ex situ PXRD study.

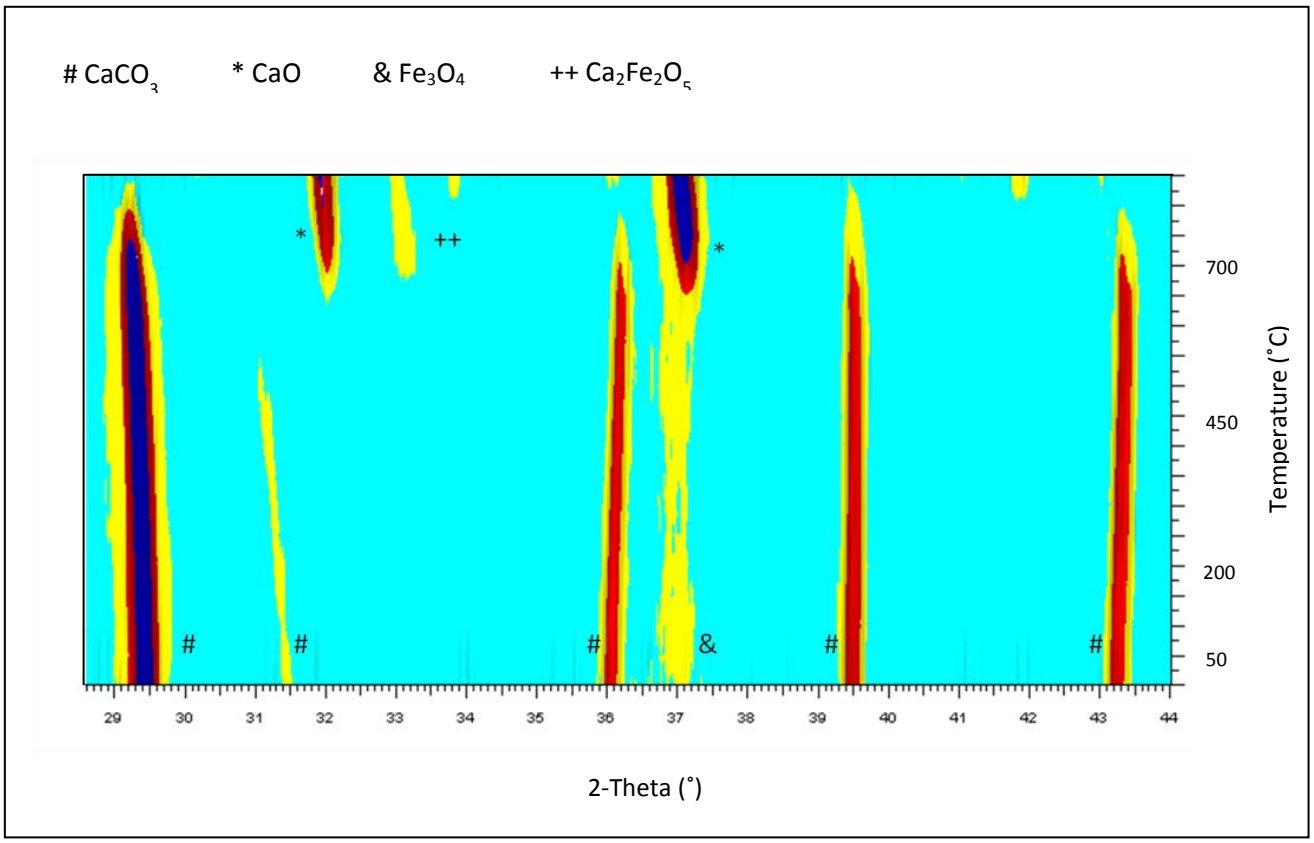


Figure 4.9: VT-PXRD patterns over temperature for 10% Fe/$CaCO_3$: # $CaCO_3$; * CaO; & Fe_3O_4 ; ++ $Ca_2Fe_2O_5$

The iron atoms are bonded to 4 oxygen atoms in this compound as illustrated in Figure 4.10

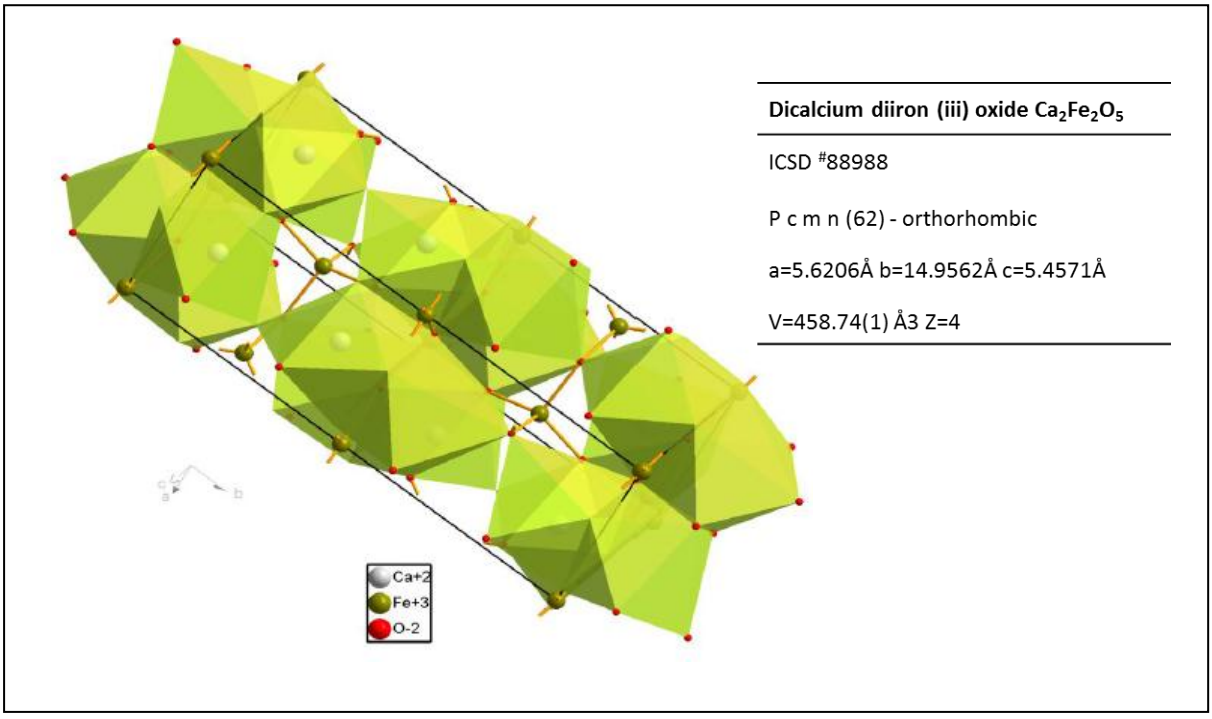


Figure 4.10: Structure of dicalcium diiron (III) oxide ($Ca_2Fe_2O_5$) (Berastegui et al., 1999)

The phase composition remained constant from room temperature to 600 °C with $CaCO_3$ being ~ 88% and magnetite at 12% (Figure 4.11). These concentrations are reasonable as the calculated percentage loading of Fe is 10%. When $Ca_2Fe_2O_5$ appeared at 650 °C the magnetite concentration decreased. The particle size of $CaCO_3$ only reached a maximum of 159 nm at 700 ˚C against a maximum of 234 nm on $CaCO_3$ alone (section 4.2.4). It could be that the metal loaded onto $CaCO_3$ suppressed the growth of the $CaCO_3$ crystals (Figure 4.12). The magnetite particle size remained constant at an average of 9.5 nm at temperatures below 600 °C; however at higher temperature (above 600 ˚C), the crystallite size grew by more than 100% to 26.5 nm at 700 °C. The crystallite size of CaO was found to be 151 nm at 850 °C which was not very different from that previously reported for CaO (section 4.2.4).

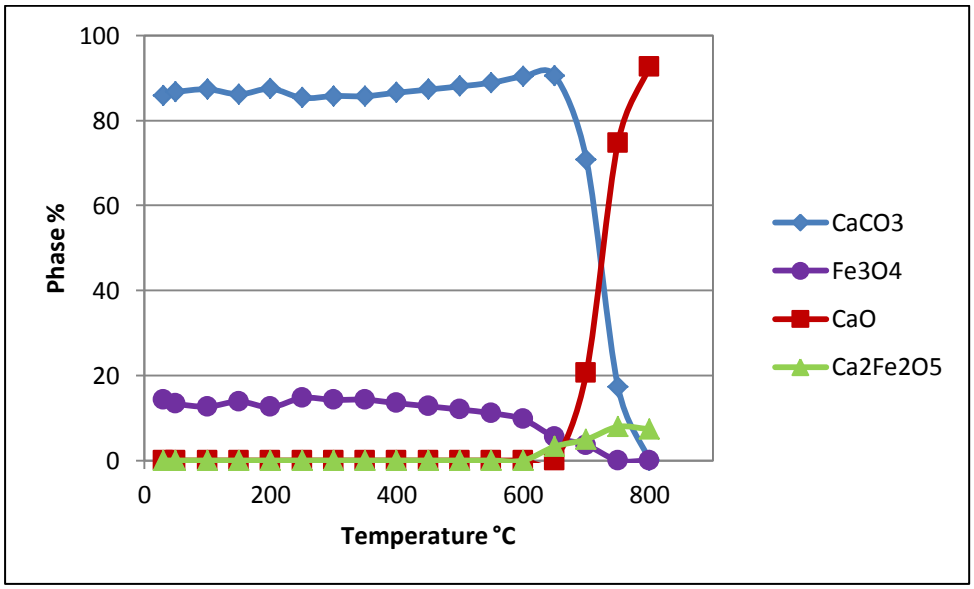


Figure 4.11: Phase abundance variation during VT-PXRD analysis of 10% Fe/$CaCO_3$

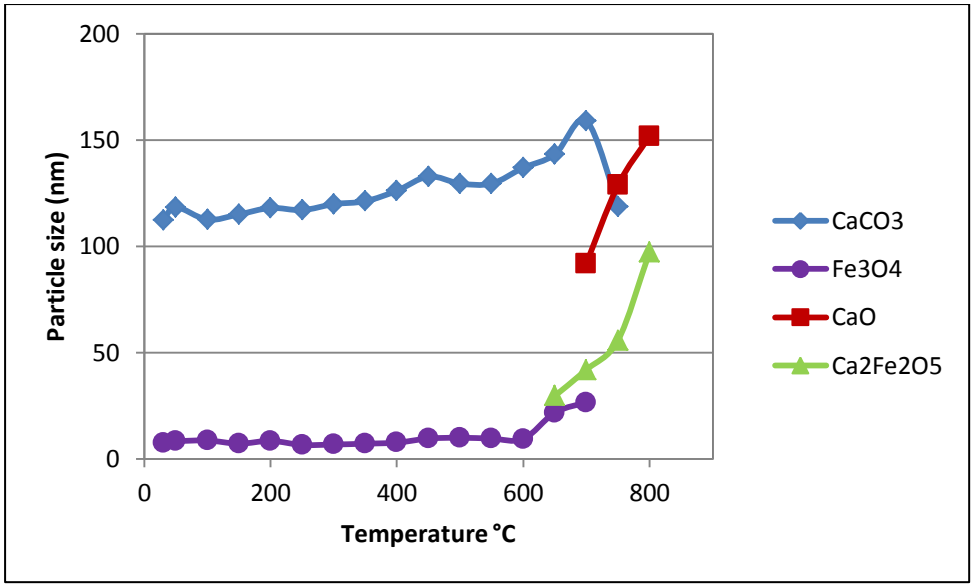


Figure 4.12: Particle size variation during VT-PXRD of 10% Fe/$CaCO_3$

The maximum concentration of $Ca_2Fe_2O_5$ formed was 7.93% at 750 ˚C but this does not account for all the iron present in the sample. This means that not all magnetite in the sample reacted with $CaCO_3$.

4.2.5 In situ VT-PXRD study of 10% Co/$CaCO_3$

When 10% Co/$CaCO_3$ was analysed by in situ VT-PXRD only $CaCO_3$ peaks could be identified in the XRD pattern initially (Figure 4.13). A thorough search match exercise was carried out to rule out possibility of CoO peak overlap with $CaCO_3$. The possibility of fluorescence problems was checked for by carrying out a room temperature XRD scan on 10%Co/$CaCO_3$ using a Co X-ray tube and no Co based phases could be identified. Thermal decomposition of $CaCO_3$ began at temperatures above 600 ˚C as shown by the presence of CaO peaks at 32 ˚ and 37 ˚.At a temperature between 450 ˚C and 500 ˚C peaks at 33.2°, 33.7°, 47.5°, 48.5° emerged. From the database that we used (PDF 2004) there was no compound that would match these peaks. However these peaks matched with that of $Ca_2Fe_2O_5$ previously reported (section 4.2.4). It is therefore speculated that the cobalt oxide present reacts with $CaCO_3$ to form a dicalcium dicobalt oxide ($Ca_2Co_2O_5$). This is reasonable as iron and cobalt are similar at the atomic level and react in a similar manner. $Ca_2Co_2O_5$ was the name given to the sample in this study. This phase ($Ca_2Co_2O_5$) increased in concentration to a maximum

of 37% at 800 ˚C; at the reaction temperature (700 ˚C) the concentration was already 32% (Figure 4.14). At 700 ˚C the particle size of $Ca_2Co_2O_5$ was 36.7 nm (Figure 4.15).

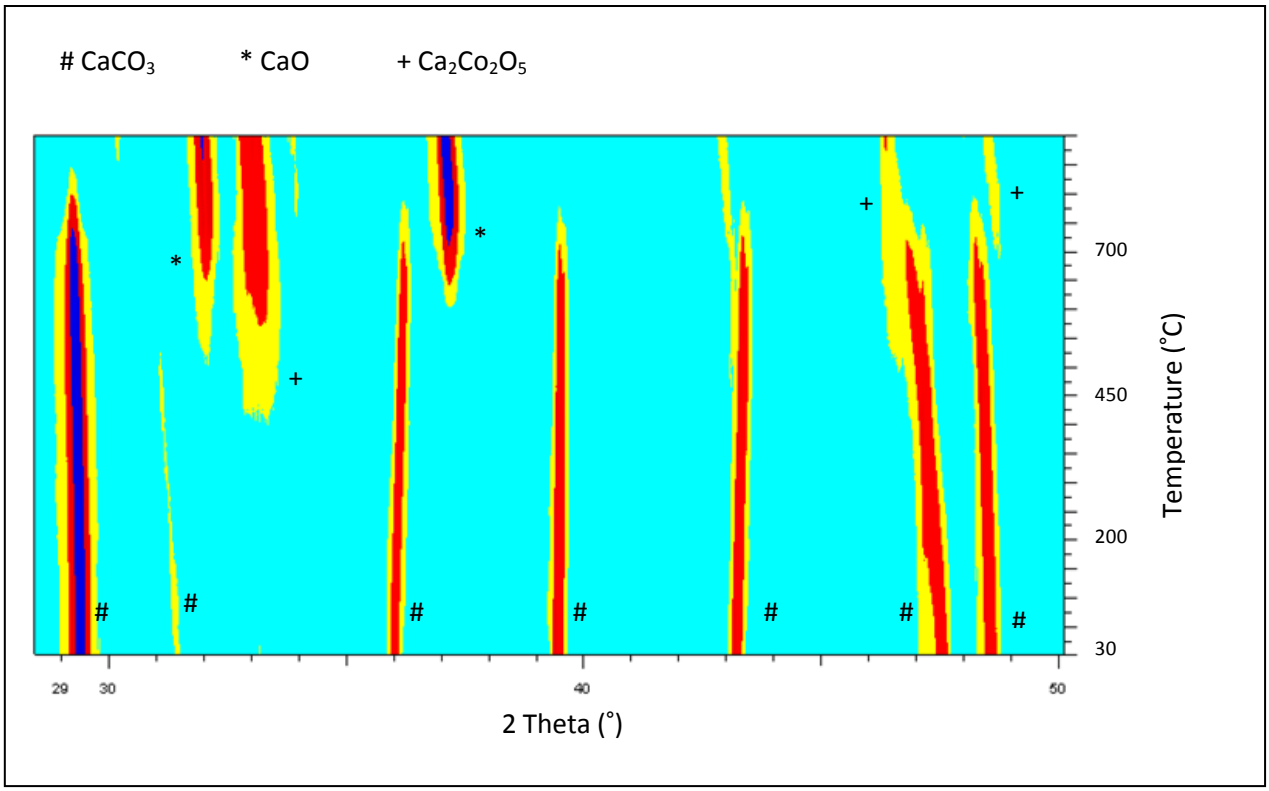


Figure 4.13: Phase abundance variation during VT-PXRD of 10% Co/ $CaCO_3$: # CaCO3; * CaO

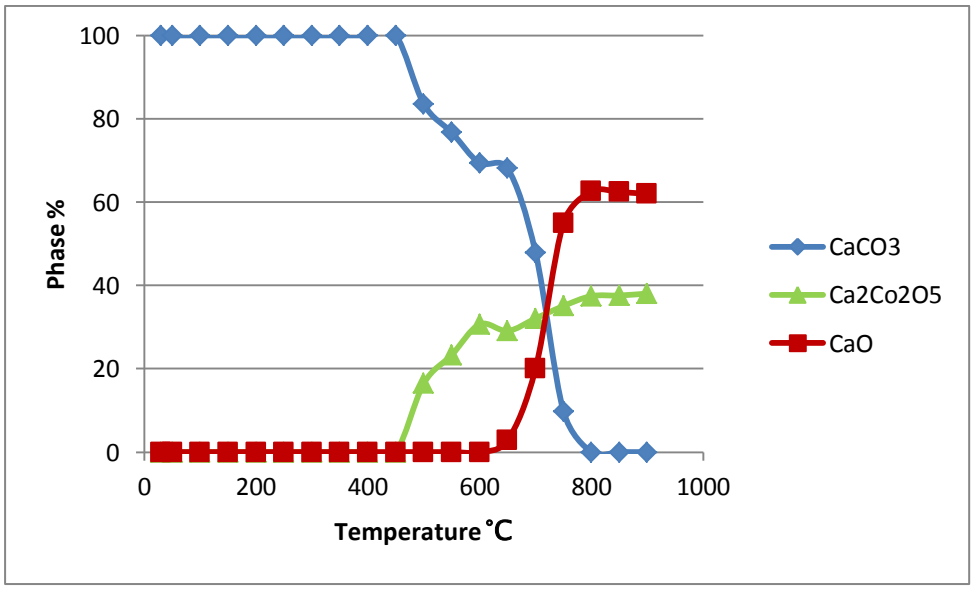


Figure 4.14: Phase abundance variation during VT-PXRD of 10% Co/ $CaCO_3$

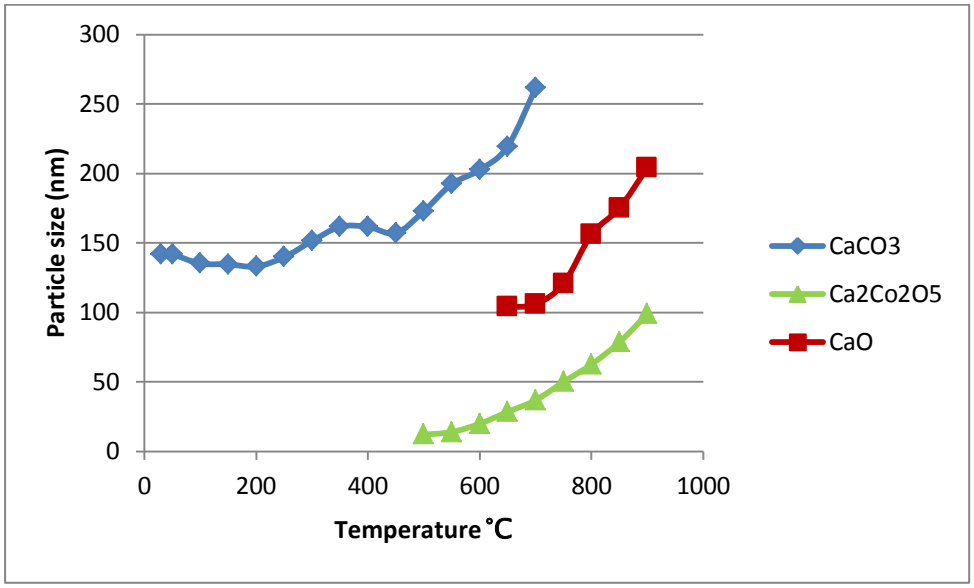


Figure 4.15: Particle size variation during VT-PXRD of 10% Co/$CaCO_3$

4.2.6 In situ VT-PXRD study of 10% Fe-Co/$CaCO_3$

The result of a VT-PXRD study on 10% Fe-Co/$CaCO_3$ under nitrogen flow is shown in Figure 4.16. The XRD pattern at room temperature (30 °C) shows only the presence of $CaCO_3$ peaks though iron and cobalt are also present (Figure 4.16& Figure 4.17). This is probably because the iron and cobalt particles are well dispersed on the surface of the $CaCO_3$; they have very small particle sizes and as such they do not cause a Bragg reflection (Scherrer, 1918). TEM images revealed the presence of iron and cobalt (section 4.2.2) particles dispersed on the surface of the $CaCO_3$ particle. An analysis was done to avoid fluorescence problems. An XRD pattern was collected for the catalyst at room temperature with a cobalt X-ray tube source and no cobalt or iron peaks were observed (Figure 4.18). Therefore the only rational reason could be that iron and cobalt had formed small well disperse particles which were in a probably armophous state. At 550 °C dicalcium iron cobalt pentaoxide (Ca_2FeCoO_5) peaks emerged at (33.2°, 33.7°, 47.5°, 48.5° 2 theta) showing that $CaCO_3$ had reacted with the active metals (Fe, Co) (Fig 4.16 & 4.19). These reflections also correspond to that of $Ca_2Co_{0.4}Fe_{1.6}O_5$ which has a similar crystal structure; for the purpose of this study the formula Ca_2FeCoO_5 was adopted. This is contrary to what other authors have reported (Magrez et al., 2005; Li et al., 2008). Magrez et al. (2005) and Li et al. (2008) reported that the spinel Fe_2CoO_4 formed upon heating the same catalyst (Fe-Co/$CaCO_3$) at 700 °C. In their

study Magrez et al. showed PXRD patterns of the unsupported catalysts, however, there are no PXRD patterns shown for Fe-Co/$CaCO_3$ even though they reported that Fe_2CoO_4 formed in both supported and unsupported catalyst. This makes it difficult for us to comment on the difference between the observations made in our study to those observed by Magrez et al. Li et al. (2008) also observed the spinel Fe_2CoO_4 upon heating Fe-Co/$CaCO_3$ catalyst; however the indicated peaks also correspond to those of the support $CaCO_3$ (Table 4.5) and thus no definitive conclusion can actually be drawn from their study. Magrez et al. (2005) and Li et al. (2008) both reported a Fe_2CoO_4 phase. However the peaks they indicate as matching this phase are at different positions despite the fact that they both use CuKα radiation for their XRD study (Table 4.5 Figure 4.20 & Figure 4.21). CuKα radiation was also used in our study. In our study it was clearly observed from XRD analysis that upon heating only Ca_2FeCoO_5 formed before the decomposition of $CaCO_3$. It is speculated that $CaCO_3$ reacts with iron and cobalt liberating CO_2 in the process (Ramezanipour et al. 2010). Both Magrez et al. (2005) and Li et al. (2008) use varying Fe to Co ratios, with a total loading of only 5% so it is possible an Fe rich spinel (Fe_2CoO_4) rather than Ca_2FeCoO_5 was formed. Li showed an XRD pattern for the Fe rich sample Fe:Co 3.35:1.65. It is to be noted that both Magrez et al. (2005) and Li et al. (2008) added ammonia to their $CaCO_3$ support before dispersing it into the Fe and Co precursor solution during synthesis of these catalysts. This was done to avoid release of CO_2 when the carbonate reacts with acid. In our study no ammonia was added and bubbles of gas were observed during synthesis. This means that some CaO was formed during synthesis which could have influenced the formation of Ca_2FeCoO_5. This difference in synthesis could be the reason for the different phases observed.

The growth of Ca_2FeCoO_5 delayed the formation of CaO. CaO peaks only appeared at 690 °C but when the $CaCO_3$ support alone was heated in the absence of metals the CaO peaks only appeared at 630 °C using the same heating rate.

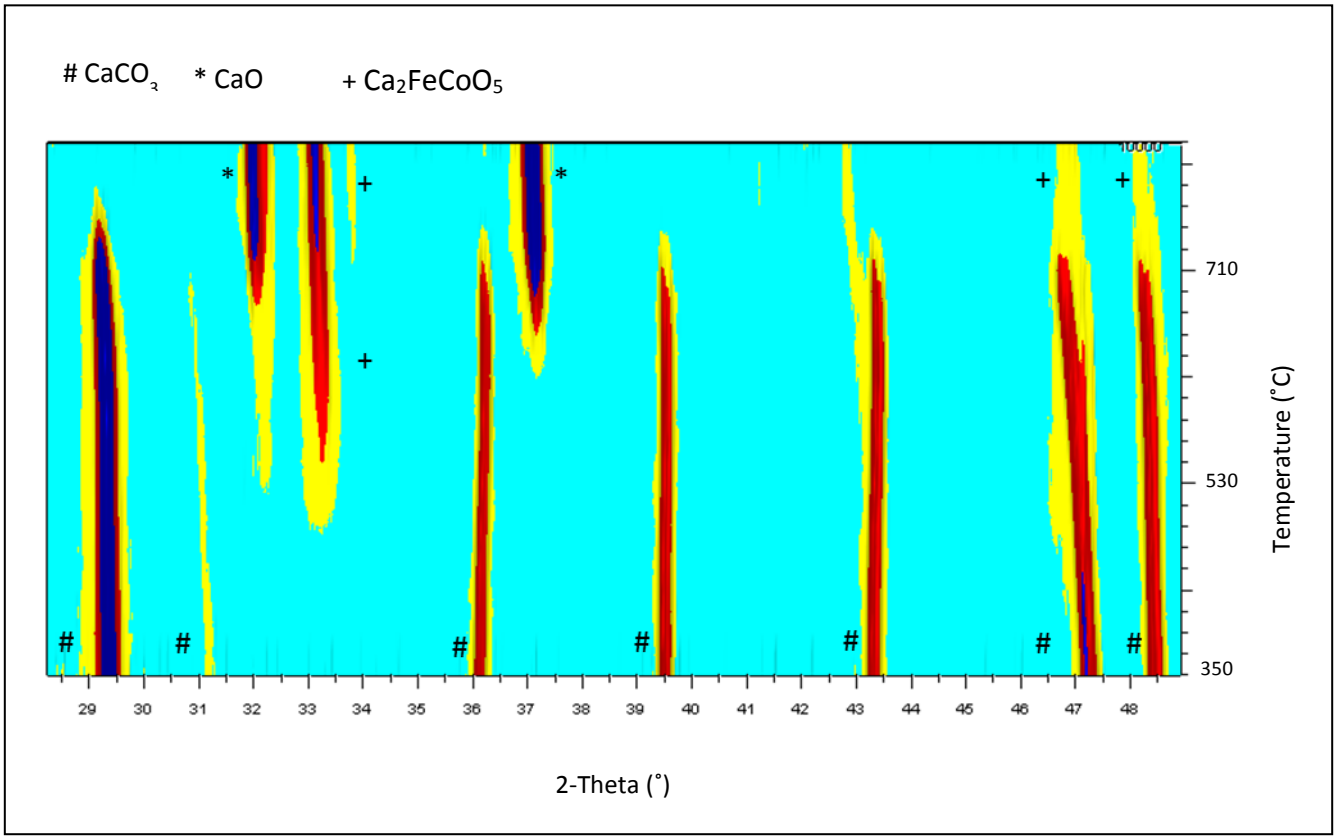


Figure 4.16: VT-PXRD profile of 10% Fe-Co/$CaCO_3$: # $CaCO_3$; * CaO; +

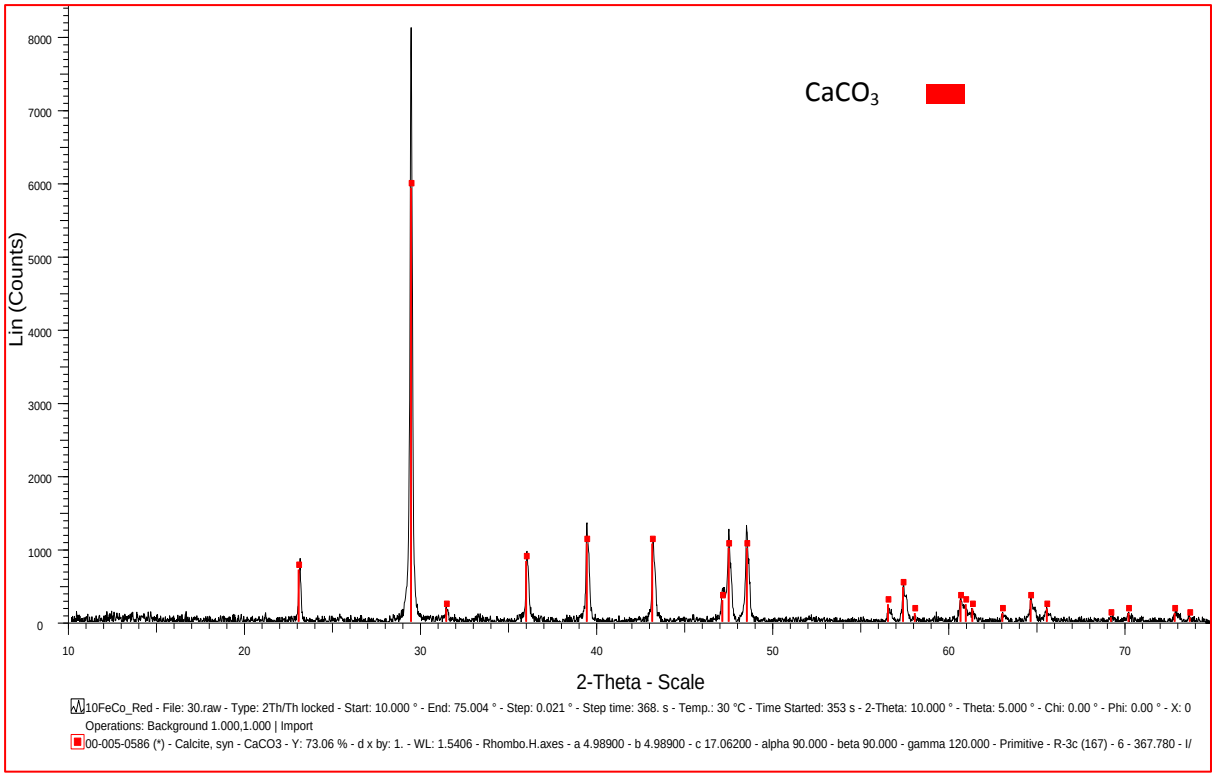


Figure 4.17: XRD pattern of 10%Fe-Co/$CaCO_3$ collected at room temperature

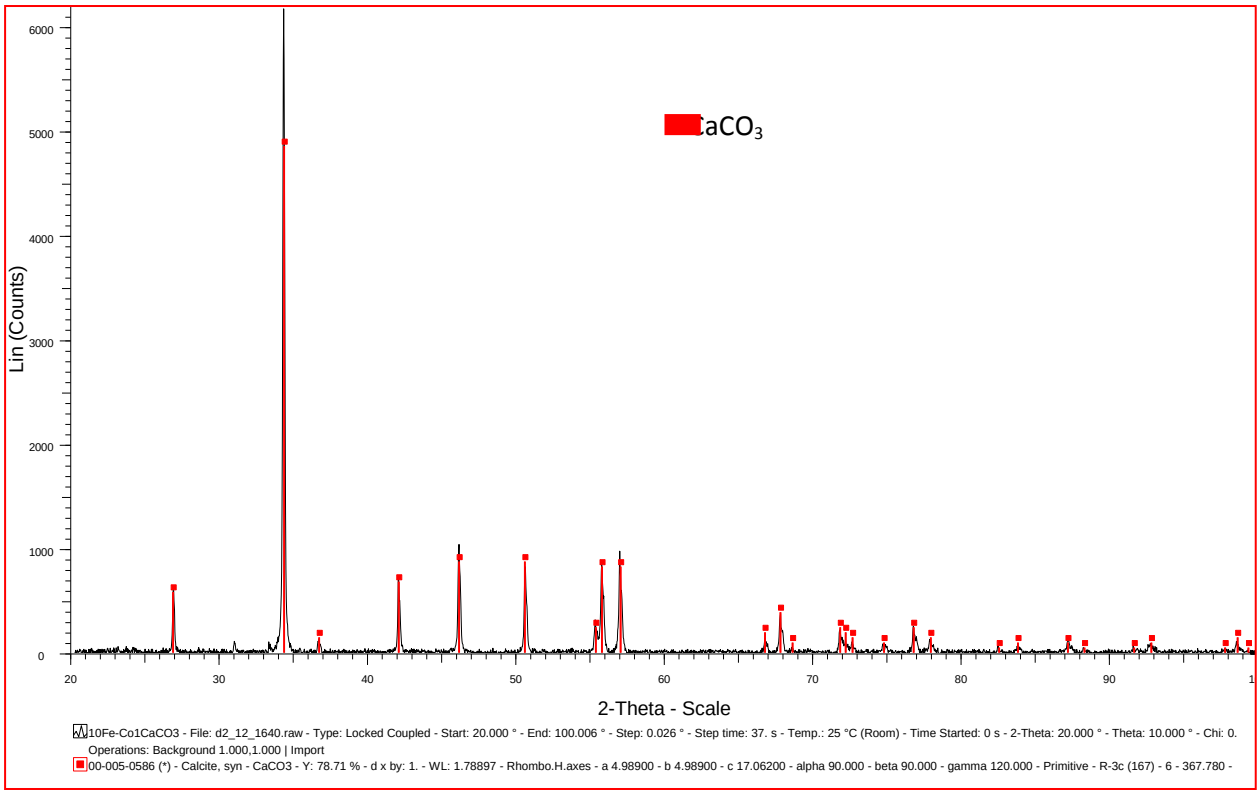


Figure 4.18: XRD pattern of 10%Fe-Co/$CaCO_3$ collected at room temperature using a Co X-ray source

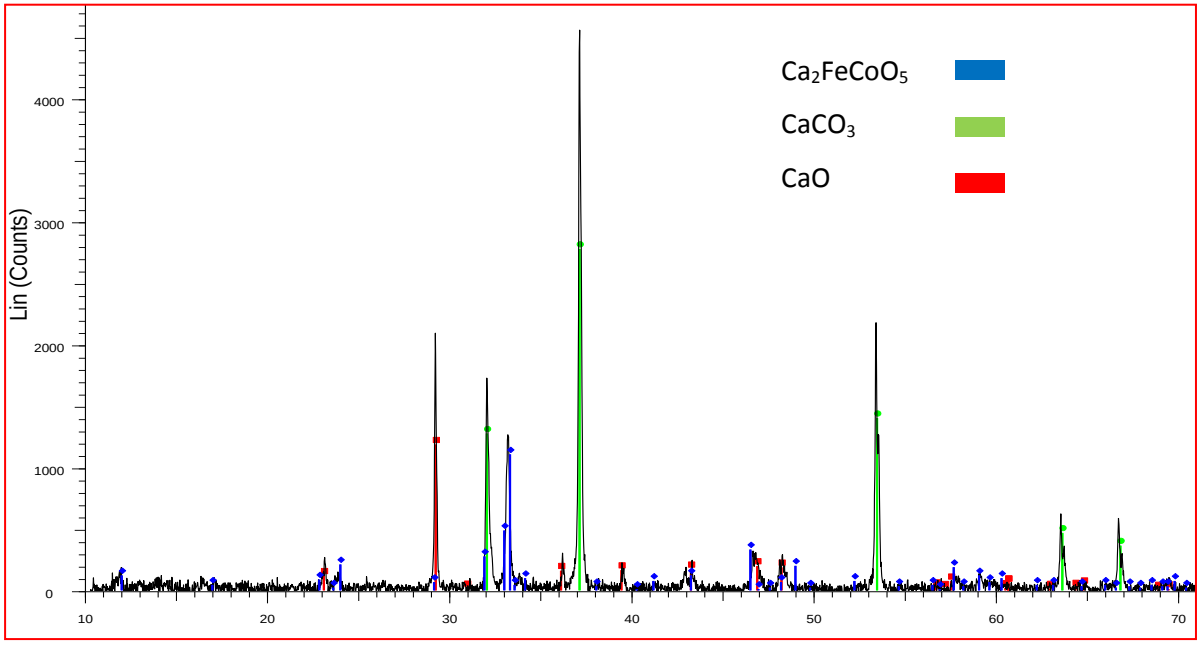


Figure 4.19: PXRD pattern of 10% Fe-Co/$CaCO_3$ at 700 ˚C showing Ca_2FeCoO_5

Table 4.5: 2θ positions of Fe_2CoO_4 as reported by Magrez et al. (2005) and Li et al. (2008)

2 Theta							
Magrez		30		36	37	63	
Li				36	39	43	47	48
$CaCO_3$	23	29		36	37	43	47	48
Ca_2FeCoO_5			33	34			47.5	48.5

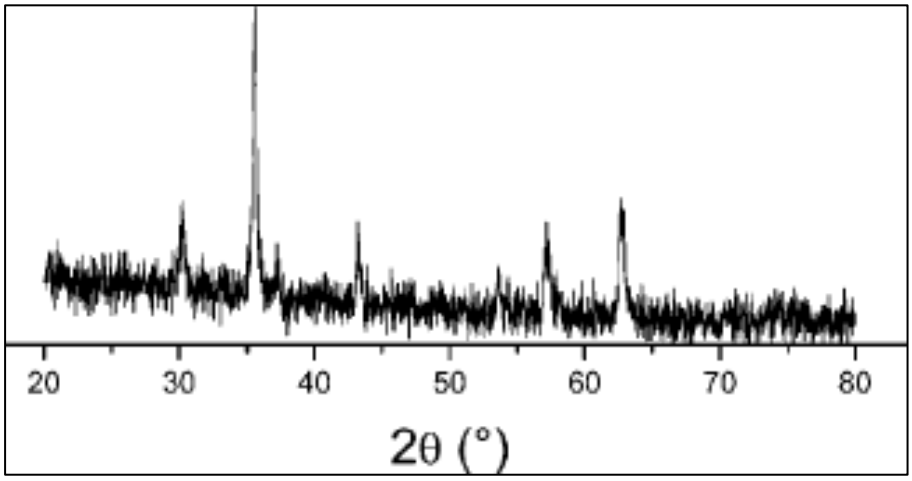


Figure 4.20: XRD pattern showing of pure Fe_2CoO_4 as reported by Magrez et al. (2005) Cu source

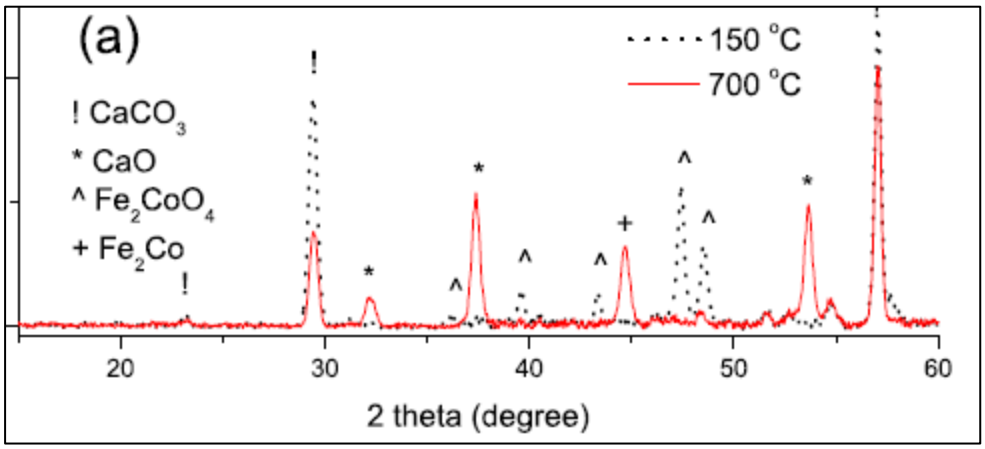


Figure 4.21: XRD pattern showing Fe_2CoO_4 diffraction peaks as reported by Li et al. (2008) Cu source

Ca_2FeCoO_5 has an orthorhombic structure similar to the $Ca_2Fe_2O_5$ (Figure 4.22) perovskite compound. Its spacegroup is Pcmn (57). The iron ion in this compound is Fe^{3+} and the cobalt ion is Co^{3+}.

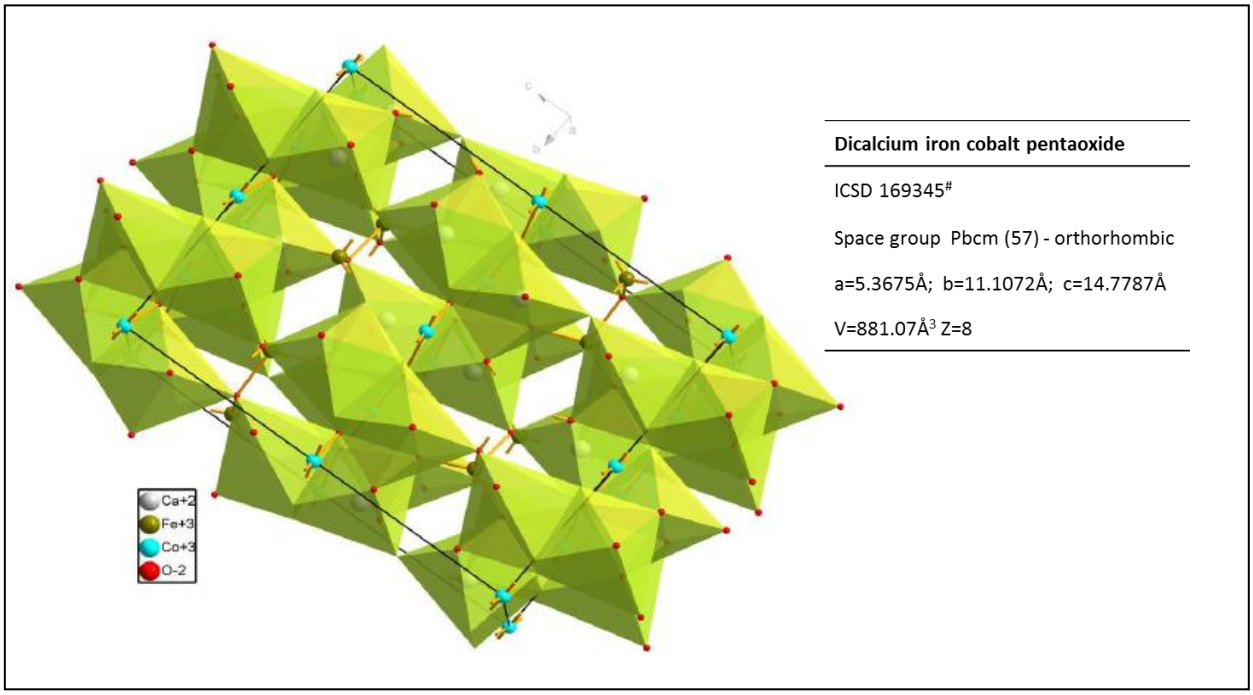


Figure 4.22: Structure of dicalcium iron cobalt pentaoxide (Ca_2FeCoO_5)(Ramezanipour et al., 2010)

The variation in phase concentration with time is shown in Figure 4.23. From 550 °C the concentration of Ca_2FeCoO_5 increased with increasing temperature and reached a maximum of 31% at 800 °C. This translates to 12% of Fe and Co (Appendix) which is in reasonable agreement with the calculated metal loading of 10%. At the reaction temperature (700 °C) the Ca_2FeCoO_5 concentration is only 20%. The Fe and Co not recorded as Ca_2FeCoO_5 are in the form of small and well dispersed particles on $CaCO_3$ and therefore do not cause a Bragg peak. The particle size of $CaCO_3$ is almost constant at ~ 150 nm from room temperature to 610 ˚C (Figure 4.24). The crystallite size thereafter increases by 66% to a maximum of 250 nm before it drops significantly as its concentration drops. It is clear that the crystal growth is related to the decomposition of $CaCO_3$ to CaO. The Ca_2FeCoO_5 particle size increases steadily from 18 nm to 77 nm as the temperature was raised from 550 ˚C to 850 ˚C. At 700 ˚C (reaction temperature) the particle size of Ca_2FeCoO_5 is 48 nm.

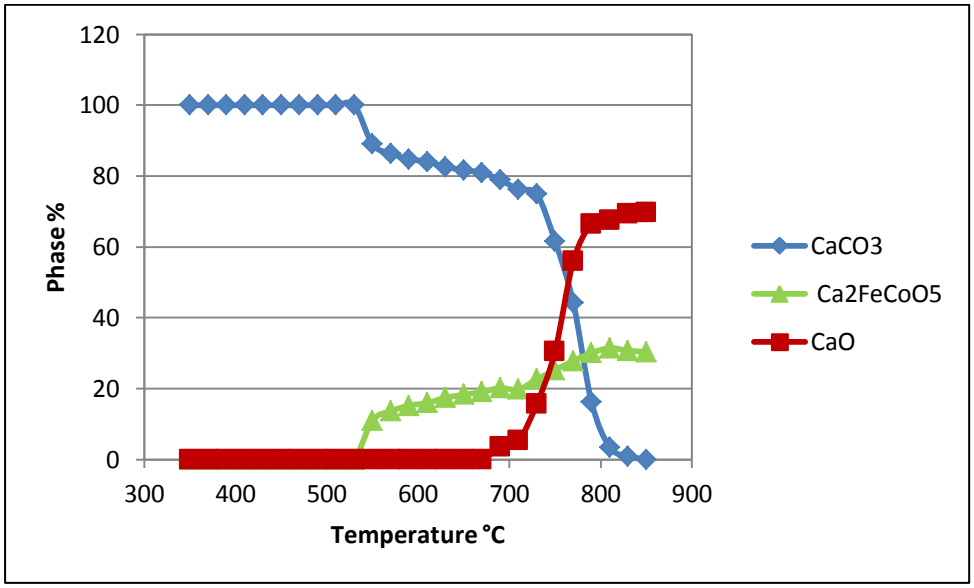


Figure 4.23: Phase abundance variation during VT-PXRD of 10% Fe-Co/$CaCO_3$

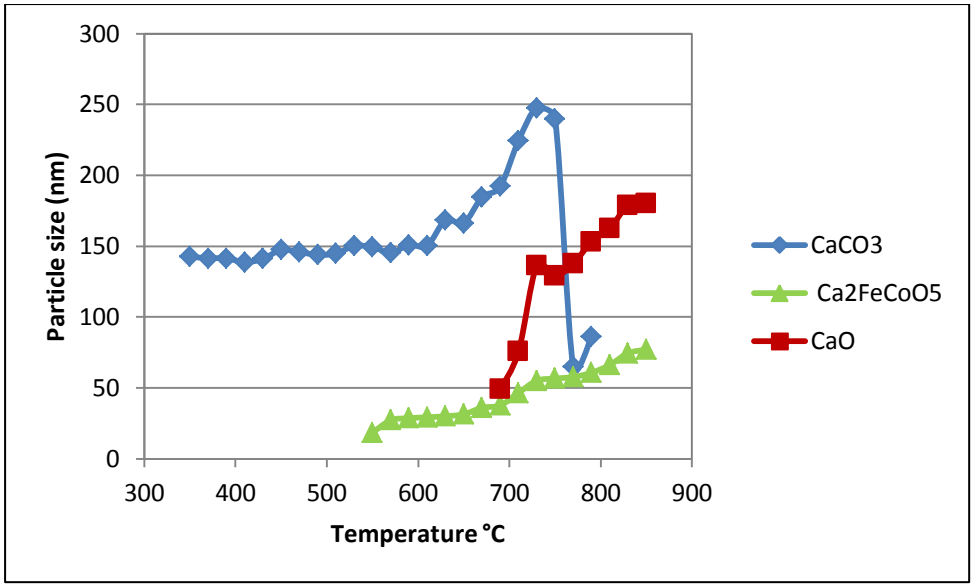


Figure 4.24: Particle size variation of phases during VT-PRXD of 10% Fe-Co/$CaCO_3$

Summary

It can therefore be concluded that in all the three catalysts, the active metals (Fe & Co) react with the support ($CaCO_3$) to form a calcium metal pentaoxide ($Ca_2M_2O_5$) (M= Fe or Co or Fe+Co). The formation of these phases was more pronounced in 10% Co/$CaCO_3$ and least in 10% Fe/$CaCO_3$ (Table 4.6). This is in agreement with TGA results (Section 4.3.7, Table 4.7).

Table 4.6: Phase abundance of $Ca_2M_2O_5$ in the catalysts at various temperatures during VT-PXRD

	600 ˚C	**700 ˚C**	**750 ˚C**	**800 ˚C**	**850 ˚C**
$Ca_2Fe_2O_5$ %	0	5.0	7.9	7.4	7.9
$Ca_2Co_2O_5$ %	30.6	32.1	35.1	37.4	37.6
Ca_2FeCoO_5 %	15	18.2	30.5	31.5	30.4

The formation of $Ca_2M_2O_5$ was confirmed by ex situ studies when the various catalysts were heated to 700 ˚C and held for 30 minutes and then analysed by XRD. The XRD patterns of the 3 catalysts (10% Co/$CaCO_3$, 10% Fe/$CaCO_3$ and 10% Fe-Co/$CaCO_3$ as well as another 20% Fe-Co/$CaCO_3$ which was prepared for this purpose) showed the characteristic XRD peaks expected for these structures (Figure 4.25). The analysis showed that 10% Fe in $CaCO_3$ also

formed Ca_2FeO_5 but quantification results showed that its concentration was the least as compared to Ca_2FeCoO_5 and $Ca_2Co_2O_5$ in 10% Fe-Co/$CaCO_3$ and 10% Co/$CaCO_3$ respectively. Hence $Ca_2Fe_2O_5$ peaks are less intense than those of the other two corresponding phases (Ca_2FeCoO_5 and $Ca_2Co_2O_5$). This resulted in small peaks not being visible in the patterns i.e. 2 θ 24 and 34.

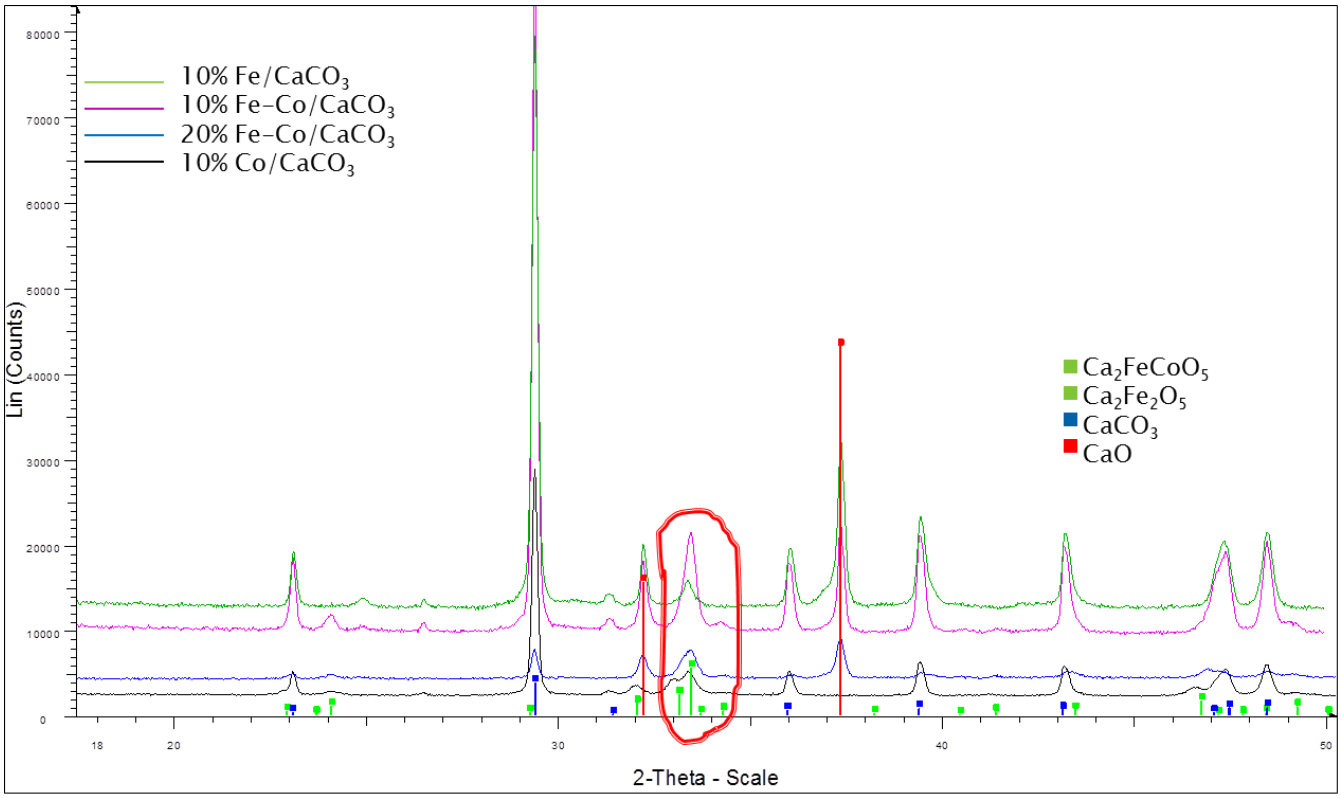


Figure 4.25: XRD patterns of the catalysts heated at 700 ˚C for 30 min under N_2

Ramezanipour et al. (2010) have reported the independent synthesis of the Ca_2FeCoO_5 (brownmillerite structure). $CaCO_3$, Fe_2O_3 and CoO were mixed and ground to a powder before pellets were made and the mixtures heated to a temperature of 1100 ˚C. The product was then ground and pellets remade and heated again (1200 ˚C). This was repeated again at 1250 ˚C for 48 hours. Berastegui et al. (1998) also reported the synthesis of $Ca_2Fe_2O_5$ by a physical method from a mixture of CaO and Fe_2O_3. The XRD pattern was similar to that reported in this study. Hirabayashi et al. (2006) also synthesised $Ca_2Fe_2O_5$

(brownmillerite structure) from CaO and Fe_2O_3 by a physical method which involved calcination. It is concluded that $Ca_2Fe_2O_5$ and $Ca_2Co_2O_5$ (also with a brownmillerite structure) were formed on heating.

4.2.7 Thermal gravimetric analysis (TGA)

The catalysts were also analysed for their thermal response by TGA. $CaCO_3$ showed stability from 35 ˚C to 500 ˚C with no major weight loss; thereafter the $CaCO_3$ started to decompose forming CO_2. After decomposition of pure $CaCO_3$ at 900 ˚C, the residual mass was ~ 60% of the original mass corresponding to the formation of CaO.

$CaCO_{3\,(s)} \rightarrow CaO_{(s)} + CO_{2\,(g)}$

The three catalysts had higher weight % at 900 °C than $CaCO_3$ because of the metals loaded onto them (Figure 4.26). The three catalysts (10% $Co/CaCO_3$, 10% $Fe/CaCO_3$ and 10% Fe-$Co/CaCO_3$) however showed three regimes where weight was lost during the TGA analysis. The weight loss occurred at temperatures of ~ 45 ˚C, 450 ˚C and 772 ˚C (Figure 4.27, Table 4.7). The loss in mass that occurred mostly at ~ 45 ˚C was attributed to loss of absorbed moisture.

The weight loss at ~ 450 °C was attributed to the formation of the Ca_2FeCoO_5, $Ca_2Fe_2O_5$ or $Ca_2Co_2O_5$. CO_2 was evolved when $CaCO_3$ reacted with the iron oxide and cobalt oxide to give the loss in mass. The weight loss is more apparent in 10% $Co/CaCO_3$ where a loss of 14.6% from 35 ˚C to 600 ˚C was recorded. Weight loss below 500 °C was lowest in 10% $Fe/CaCO_3$. Noting that from Figure 4.11 quantitative Rietveld analysis of in situ VT-PXRD of the 10% $Fe/CaCO_3$ showed the lowest formation of the calcium metal oxide ($Ca_2Fe_2O_5$) compared to the other catalysts which could not account for all the iron loaded onto the support. This is confirmed by the lowest weight loss observed (3.3%) as less CO_2 was formed below 600 °C. Table 4.7 shows the concentrations of various compounds at different temperature.

From the derivative curve (Figure 4.27) it can be observed that the third decomposition begins at ~ 650 ˚C for all four samples which is in agreement with VT-PXRD data which showed formation of CaO at about this temperature (section 4.3.3 – section 4.3.6). The peak at ~ 750 ˚C (Figure 4.27) signifies the temperature at which the highest rate of decomposition of $CaCO_3$ to CaO occurs, as explained earlier.

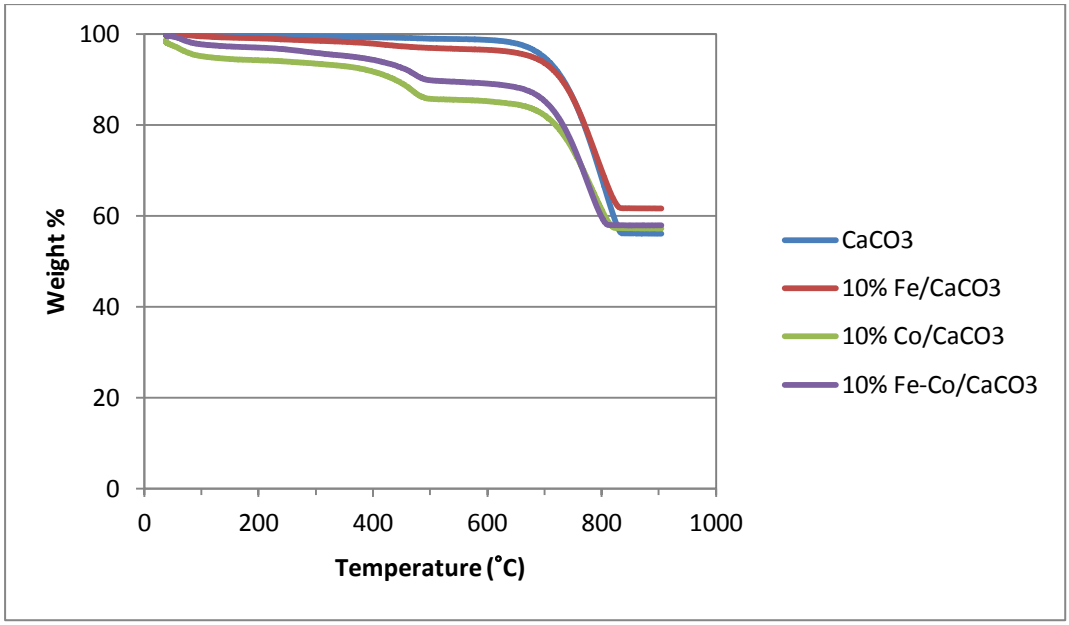


Figure 4.26: TGA profiles of the Fe-Co catalysts

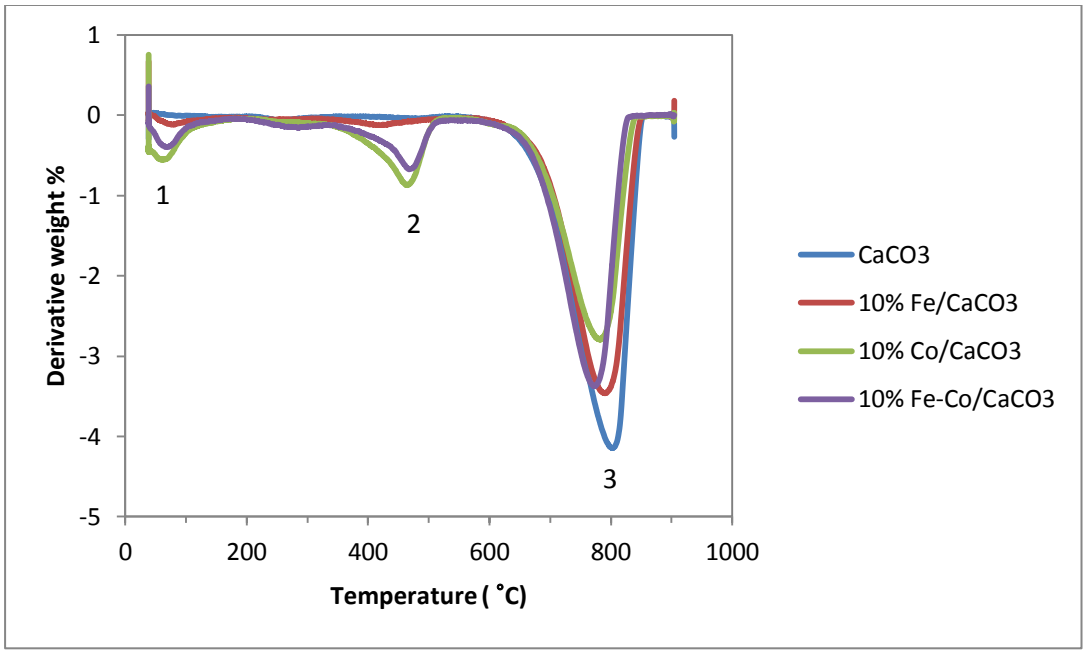


Figure 4.27: TGA weight derivatives of the various Fe-Co/$CaCO_3$ catalysts

Table 4.7: % weight loss at various temperature points

	% weight loss		
	Peak 1	Peak 2	Peak 3
$CaCO_3$	0	1	44
10% $Fe/CaCO_3$	1	3	38
10% $Co/CaCO_3$	6	14	43
10% $Fe\text{-}Co/CaCO_3$	3	11	42

4.2.8 Iron Mossbauer spectroscopy studies of 10% $Fe\text{-}Co/CaCO_3$

Room temperature Mossbauer data was collected on the as-synthesised 10% $Fe\text{-}Co/CaCO_3$ sample and the thermally treated 10% $Fe\text{-}Co/CaCO_3$ sample (700 ˚C for 1 hour). Best fits were obtained by fitting the spectra with two quadrupole split doublets D1 and D2 using Voight lineshapes. Figures 4.28 and Figure 4.29 show the resultant spectra. The spectra are characterised by a single paramagnetic pattern showing broadened features.

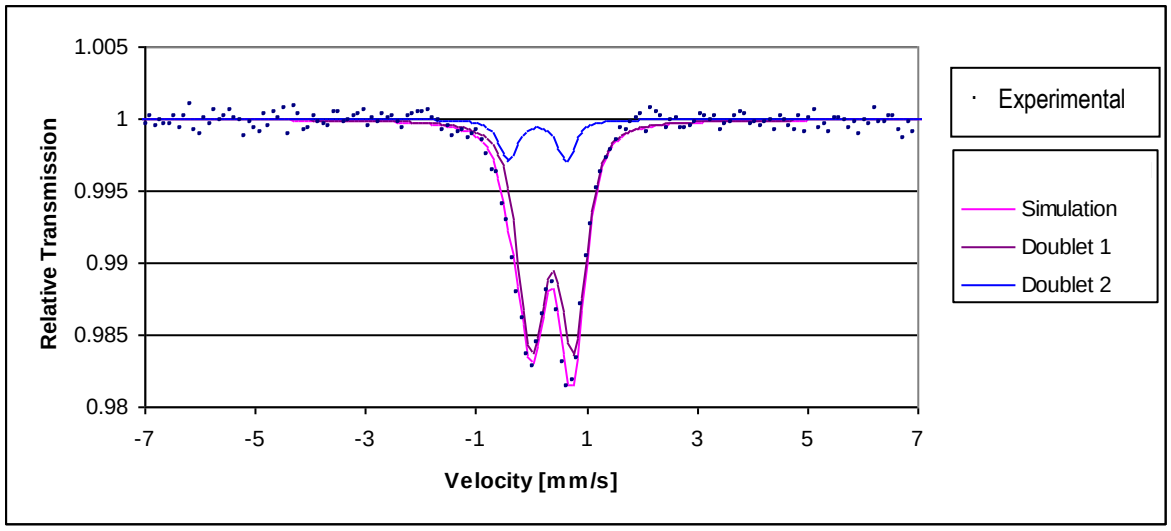


Figure 4.28: ^{57} Fe Mossbauer spectrum collected at room temperature (as synthesised sample)

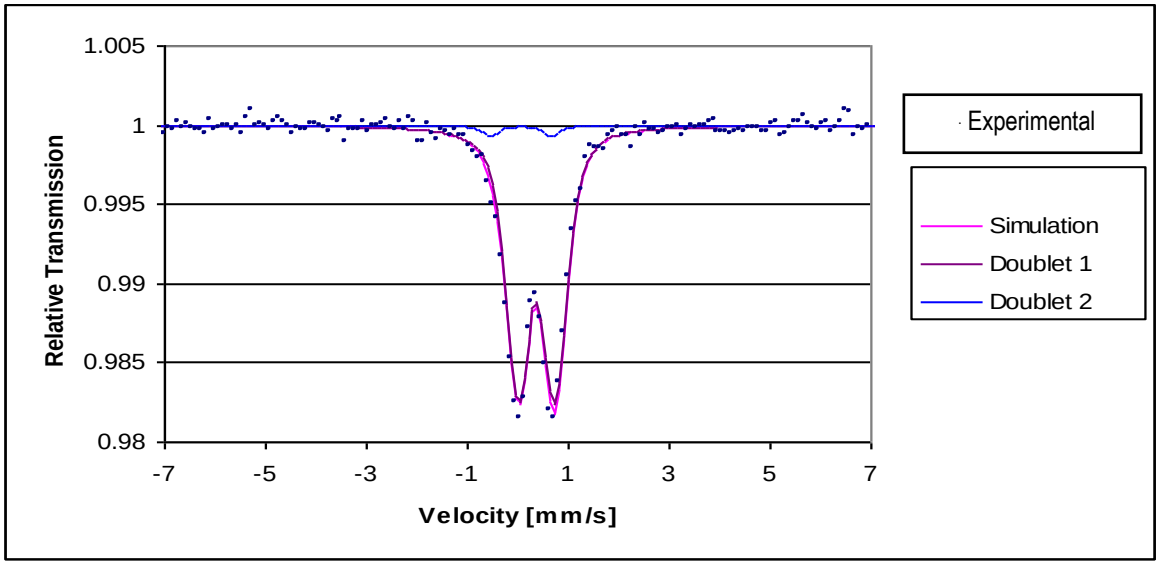


Figure 4.29: ^{57} Fe Mossbauer spectrum collected at room temperature (thermally treated at 700 °C)

Table 4.8 gives a summary of the extracted hyperfine parameters for the as synthesised Fe-Co/$CaCO_3$ catalyst and Table 4.9 gives parameters for the thermally treated sample.

Table 4.8: Mossbauer parameters for as synthesised sample

Parameter	Doublet 1	Doublet 2
δ(mm/s)	0.371639	0.0929541
ΔE_Q(mm/s)	0.756013	1.0446294
Γ(mm/s)	0.34	0.34
σ(δ)(mm/s)	0.159171	0.0562264
Area Fraction (%)	87.65708	12.342916

Table 4.9: Mossbauer parameters for thermally treated sample

Parameter	Doublet 1	Doublet 2
δ(mm/s)	0.362614	0.0768118
ΔE_Q(mm/s)	0.76314	1.2251723
Γ(mm/s)	0.34	0.34
σ(δ)(mm/s)	0.159171	0.0562264
Area Fraction (%)	96.9475	3.0524998

Thermal treatment of the sample results in an increased occupation of lattice sites of doublet 1 (88% to 97 %) and a corresponding decrease in the area fraction of doublet 2 (12 to 3%). Both the isomer shift and quadrupole splitting values for both samples correspond to iron in the 3+ oxidation state.

The isomer of Doublet 1 (δ = 0.36 to 0.37) is acceptable for Fe^{3+} whilst a lower isomer value (δ = 0.05 to 0.08) also indicates Fe^{3+}. These specifications also correspond to those of a similar structure $Sr_2Fe_{2-x}Cr_xO_{5+y}$ (Gibb & Matsuo, 1990). $Sr_2Fe_{2-x}Cr_xO_{5+y}$ has a similar structure to Ca_2FeCoO_5. This confirms that this Ca_2FeCoO_5 is present in the sample at room temperature. Mossbauer results also showed that the phase had iron in the 3+ oxidation with iron ion having a tetrahedral coordination. This is in agreement with Ramezanipour et al. (2010) who characterised Ca_2FeCoO_5 and found that the same coordination. XRD data in the previous section reported the formation of Ca_2FeCoO_5 at elevated temperatures (above 500 ˚C) where iron is in the form of Fe^{3+} ions. Mossbauer data here show that Ca_2FeCoO_5 is present in the sample before the sample is analysed for thermal response. It is speculated that Ca_2FeCoO_5 is formed during synthesis of the catalyst and present before VT-PXRD analysis but in the amorphous state and therefore crystallises as the sample is heated. Therefore XRD shows its presence when Ca_2FeCoO_5 has crystallised.

4.3 Reduction Studies

Reducibility normally has an effect on the activity of a catalyst. In general, the easier it is to reduce a catalyst, the better its activity because more metal active species will be available for the catalytic reaction (Das et al., 2003). Reducibility studies were carried out on the Fe-Co/$CaCO_3$ material since it has been shown that to make CNTs; this catalyst (Fe, Co, or Fe-Co) must be in the metallic state. The carbon source (C_2H_2) used to make CNTs can also be used to reduce this catalyst at the reaction temperature (700 °C) used to make CNTs (Hernadi et al., 1997).

4.3.1 TPR study of Fe, Co/$CaCO_3$ catalysts

Temperature programmed reduction (TPR) studies were carried out as described previously (section 3.2.5). The $CaCO_3$ support profile showed a single peak at 747 ˚C which is attributed to CO_2 gas generated as CaO is formed. A 10% Fe/$CaCO_3$ catalyst had a reduction profile that showed four peaks (Figure 4.30). The first three (236 ˚C, 281 ˚C, 507 ˚C) are due to the reduction of iron oxides. Magnetite was identified by PXRD analysis; this meant that iron initially occurred as Fe^{3+} and Fe^{2+}. The fourth peak at 703 ˚C was due to formation of CO_2 from the decomposing $CaCO_3$. The profile showed that production of CO_2 begins at 550 ˚C.

10% Co/$CaCO_3$ showed four reduction peaks. The first three peaks (434 ˚C, 464 ˚C and 482 ˚C) are due to the reduction of cobalt oxide to metallic cobalt. The fourth peak at 705 ˚C is again due to CO_2 formation. The reduction profile of 10% Fe-Co/$CaCO_3$ showed only two major peaks. The first one at 418 ˚C is attributed to the reduction of Fe-Co oxides and the second one at 705 ˚C is due to CO_2 from the decomposing support. It is clear that addition of the metals to the support reduces the temperature at which thermal decomposition of CO_2 occurs as illustrated previously by TGA (section 4.3.7). 10% Fe/$CaCO_3$ was further heated at 400 ˚C for 10 hours and analysed by TPR. The reduction profile showed that the first major peak (230 ˚C) has significantly reduced in size (Fig 4.31). It was speculated that iron forms a nitrate compound which is not easily broken down during the normal calcination temperature found in other catalysts. Therefore the catalyst may need to be heated under more severe conditions. This could have been the reason for the very poor performance of this catalyst when used in our research group (Mhlanga et al., 2009)

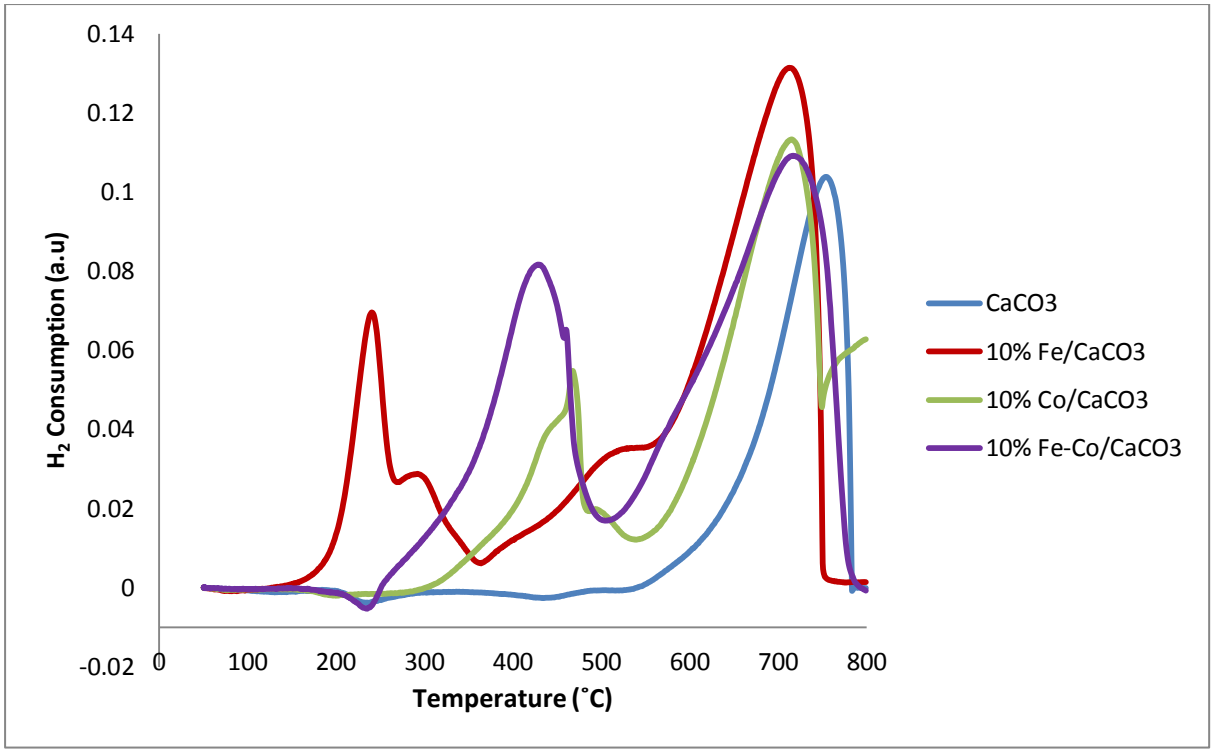


Figure 4.30: TPR profiles of the catalysts

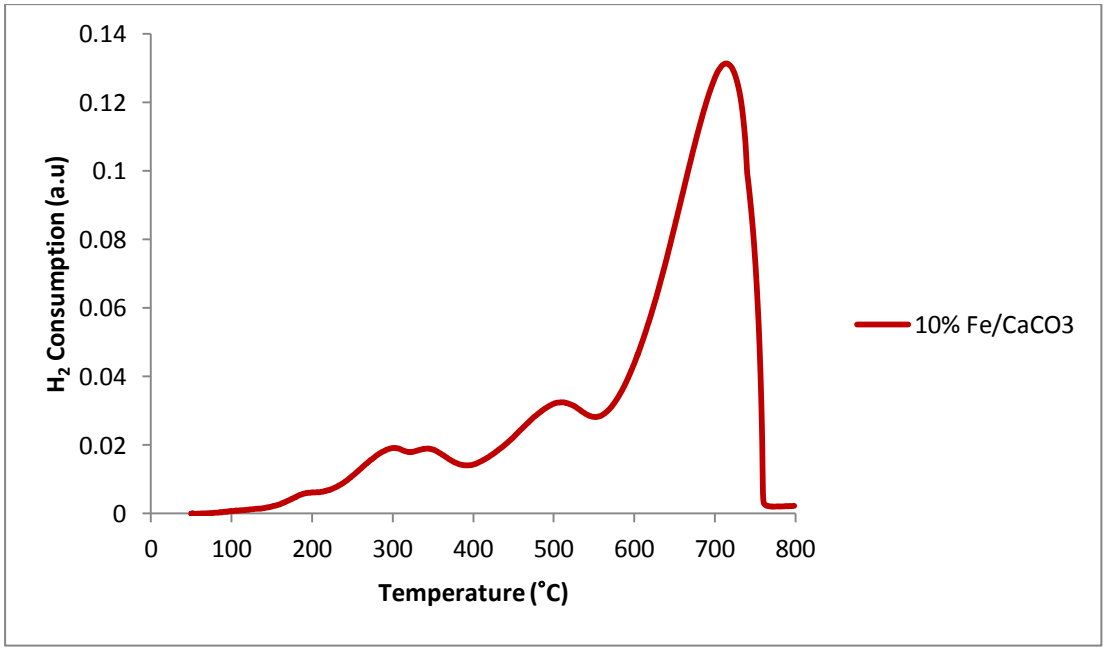


Figure 4.31: TPR profiles of the 10% $Fe/CaCO_3$ further heated for 10 hours

4.3.2 In situ PXRD reduction of 10% $Fe\text{-}Co/CaCO_3$

A 5% H_2 in N_2 mixture gas was passed through the XRK cell at a flow rate of 40 mL/min. An XRD pattern was collected at room temperature and then the temperature was ramped to

700 °C and kept there for 24 hours with H_2 flowing over the sample. XRD patterns were collected every hour to track phase transitions that were occurring in the catalyst. Figure 4.32 shows the results. Pattern number 1 is the pattern collected at 30 °C and it shows only $CaCO_3$ peaks because the iron and cobalt particles are small and well dispersed. The first pattern at 700 ˚C (pattern-2) shows the Ca_2FeCoO_5 peak at 33 °. A wuestite (FeO) peak was also observed at 42 °. After 3 hours the Ca_2FeCoO_5 has been reduced to an iron-cobalt phase and also CaO has formed. It can be speculated that the peak at 45 ˚ was due to Fe_2Co as has been reported by others (Li et al., 2008). However other phases such as Fe_9Co_7, Fe_3Co, Co_3Fe_7 $CoFe_{15.7}$ and CoFe also have a reflection peak at the same 2 theta value. In this study Fe_2Co was adopted as the formula of the catalyst for quantitative Rietveld analysis. Crystallography information was available on the ICSD online database for Fe_2Co. A peak was also observed at 43 ° which was attributed to Co reflection. Other authors also studied a similar catalyst (Li et al., 2008; Magrez et al., 2005)

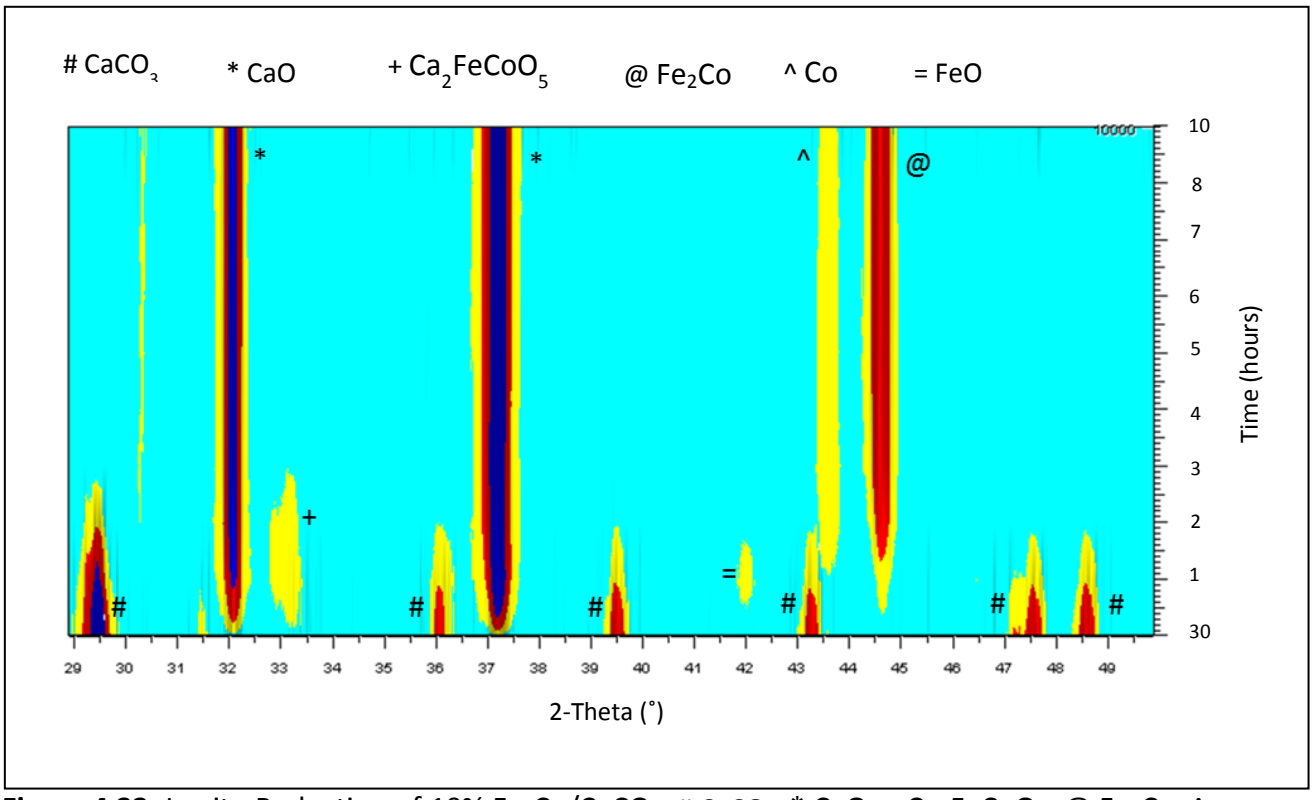


Figure 4.32: In-situ Reduction of 10% Fe-Co/$CaCO_3$: # $CaCO_3$; * CaO; + Ca_2FeCoO_5; @ Fe_2Co; ^ Co; = FeO

After 3 hours of reduction the XRD patterns show the presence of three phases, Fe_2Co, CaO and Co (Figure 4.33). The CaO concentration stabilises at 86% for the rest of the reduction period. Fe_2Co and Co were also constant at 10% and 4% respectively. The total content of the metal was slightly higher than 10% because the support had lost some weight when it decomposed to CaO.

Magrez et al. (2005) studied a series of $Fe_{1-x}Co_x$ supported catalyst for the synthesis of MWCNTs. The authors found that an x value of 0.33 gave the highest yield and high quality CNTs. When x is 0.33 they observed the formation of a Fe_2Co during synthesis with C_2H_2 as carbon source. A deviation from x= 0.33 resulted in the formation of Fe_2CO_3 and CoO. This could explain the Co phase which was observed from XRD in addition to the Fe_2Co since the Fe-Co/$CaCO_3$ catalyst that was used in our study deviated from the x= 0.33 regime.

The particle size of $CaCO_3$ is an average 100 nm, Fe_2Co is 70 nm and Co is 40 nm (Figure 4.34). Though these sizes fall within the diameter range of MWCNTs produced from this catalyst they exceed the MWCNTs average diameter size of 29 nm. This difference could be attributed to differences in experimental time. Synthesis of CNTs is carried out for a period of 1 hour however the experimental time for this in situ reduction exceeded 3 hours which allowed the particles to continue growing.

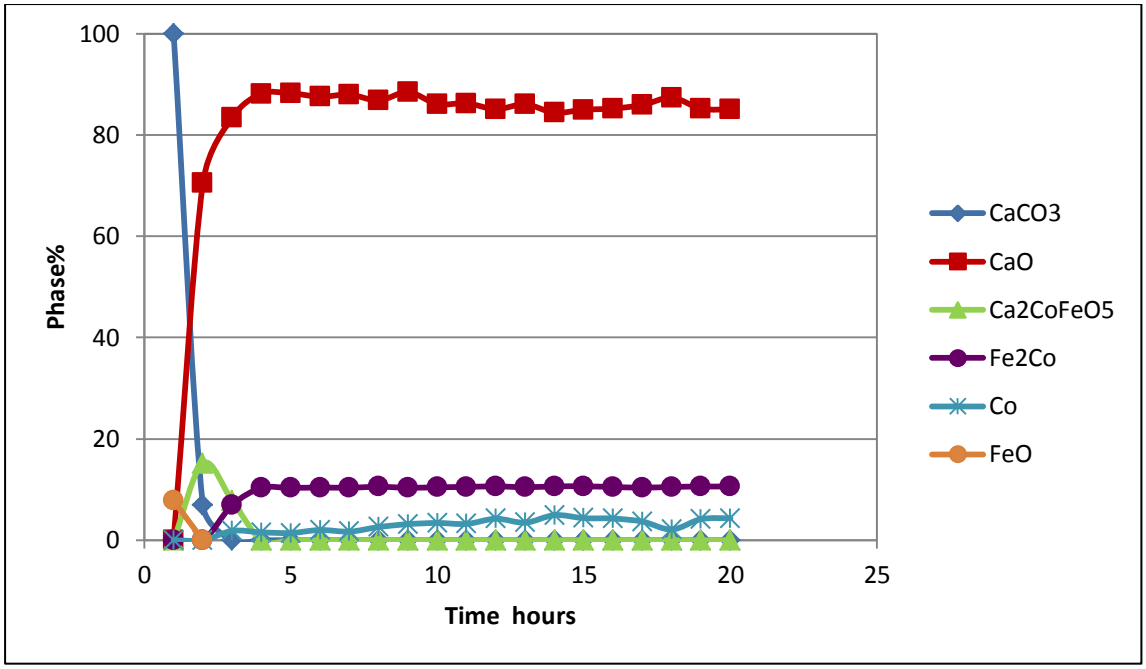


Figure 4.33: Variation of phase abundance with time

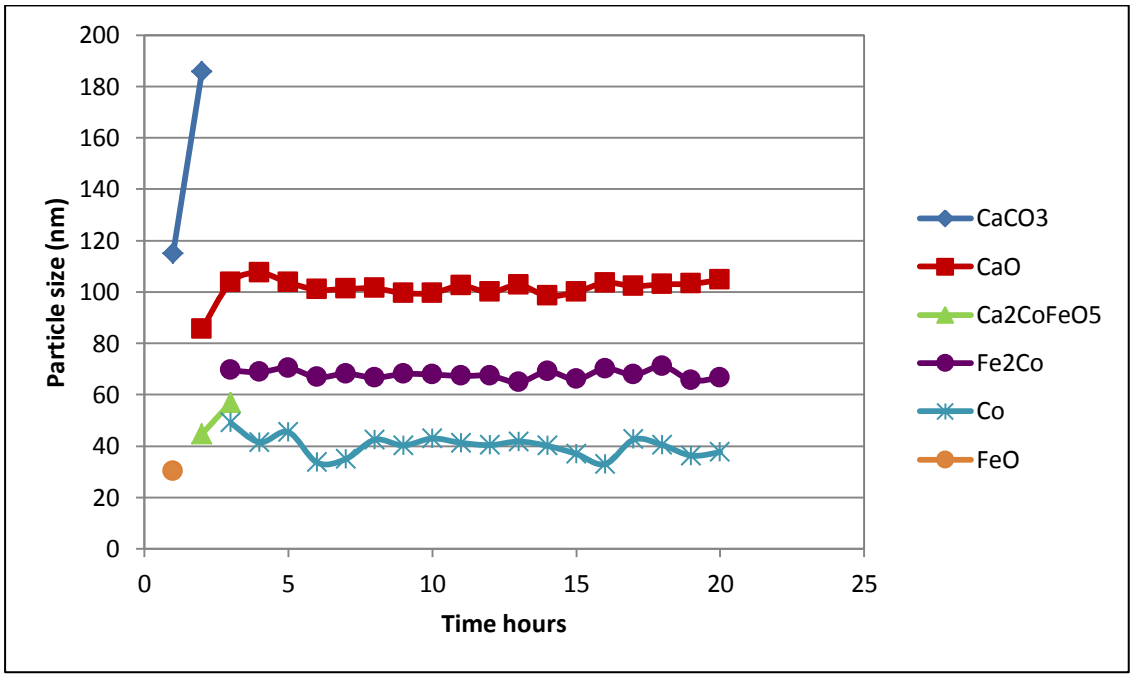


Figure 4.34: Variation of phase particle size with time during reduction

4.3.3 In situ PXRD reduction of 10% $Co/CaCO_3$ and 10% $Fe/CaCO_3$

The in situ reduction experiments on 10% $Co/CaCO_3$ and 10% $Fe/CaCO_3$ were also carried out under similar conditions to those carried out for 10% $Fe\text{-}Co/CaCO_3$. The results are shown in Figures 4.35 and 4.36. The metal oxides could not be reduced to their metallic

states under these reduction conditions. 10% Fe/$CaCO_3$ only reduced from Fe_3O_4 to FeO (Figure 4.35 and Figure 4.36).

Under these conditions it can be speculated that 10% Fe-Co/$CaCO_3$ is easier to reduce than the other two catalysts (10% Co/$CaCO_3$ and 10% Fe/$CaCO_3$). This difference in reducibility could be the reason why the bimetallic catalyst is better than the monometallic ones as has been reported before (Mhlanga et al., 2009). More metal active sites could be available in the synthesis of CNTs using the Fe-Co/$CaCO_3$ catalysts because it is easier to reduce than the monometallic catalysts.

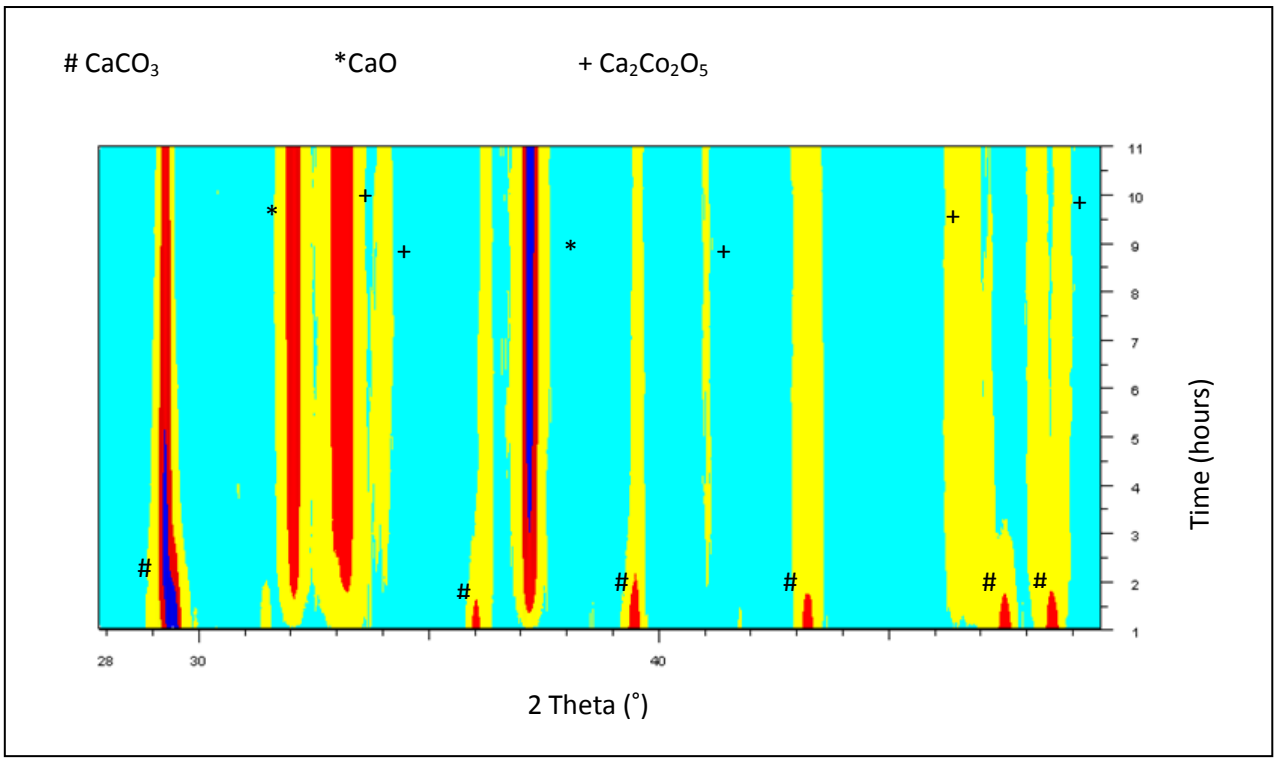


Figure 4.35: In situ reduction of 10% Co/$CaCO_3$ at 700 ˚C

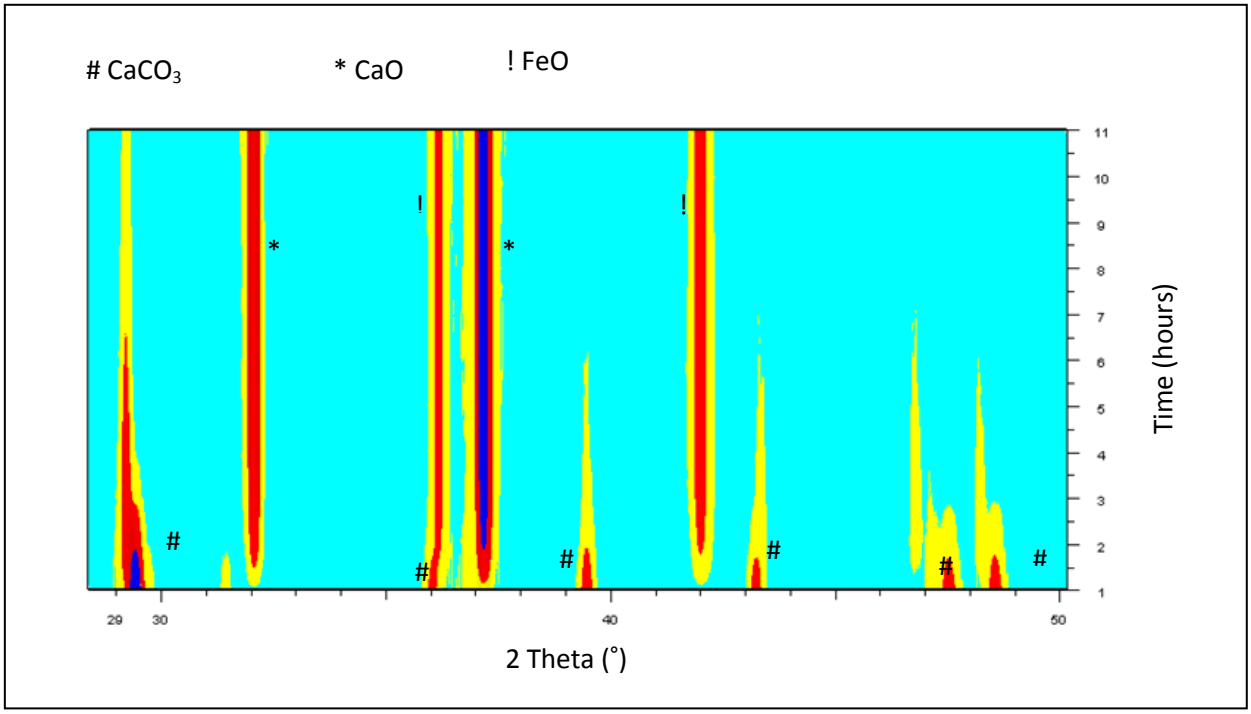


Figure 4.36: In situ reduction of 10% $Fe/CaCO_3$ at 700 ˚C

4.4 Conclusion

The $Fe\text{-}Co/CaCO_3$ catalysts were synthesised and characterised using various techniques. TEM results showed that iron and cobalt were dispersed on the $CaCO_3$ support though the particles were small and agglomerated. In situ variable temperature XRD was also carried out on the samples. It was concluded that the $CaCO_3$ support reacted with the iron and cobalt present in all three catalysts (10% $Fe/CaCO_3$, 10% $Co/CaCO_3$ and 10%$Fe\text{-}Co/CaCO_3$) to give a browmillerite structure with a general formula $Ca_2M_2O_5$ (M= Fe, Co. Fe+Co). However as mentioned earlier other authors (Magrez et al., 2005; Li et al., 2008) observed spinel formation Fe_2CoO_4 when a similar $Fe\text{-}Co/CaCO_3$ was heated to 700 ˚C.

CHAPTER 5

5 RUTHENIUM CATALYST SUPPORTED ON MULTI WALLED CARBON NANOTUBES FOR USE IN THE FISCHER TROPSCH SYNTHESIS

5.1 Introduction

Fischer Tropsch Synthesis (FTS) is the reaction in which CO and H_2 react in the presence of a catalyst to form various alkanes, alkenes, alcohols etc. The synthesis involves a number of steps. It is proposed that CO firstly adsorbs onto the catalyst active surface site and dissociates to form carbon and oxygen atoms. Hydrogen also adsorbs on the catalyst and dissociates on contact with the catalyst to form hydrogen atoms. Some of the hydrogen atoms react with oxygen atoms forming water and others react with carbon atoms forming CH_2 units. The next step is C-C bond formation to generate hydrocarbons of various lengths (equation 5.1); hence new carbon-carbon bonds form from the CH_2 building blocks. The reaction is considered to be a polymerisation reaction with CH_2 units as the building blocks.

$$nCO + 2nH_2 \rightarrow -(CH_2)_n- + nH_2O$$

The use of multi walled carbon nanotubes as a catalyst support continues to attract interest amongst researchers (Planeix et al., 1994; Bahome et al., 2005; Oosthuizen & Nyamori et al., 2011; Motchelaho et al., 2011). Multi walled carbon nanotubes (MWCNTs) are an appropriate support as they have a large surface area and they are relatively inert, making catalyst support interactions minimal. When functional groups are introduced of the surface on the MWCNTs, active metal particles are anchored on the catalyst and dispersion is increased (Serp et al., 2003).

Though ruthenium is the most active of all FT catalysts it has not been as intensely studied as iron and cobalt since application at a large scale is not feasible because of its high cost. It

is possible that FTS based on ruthenium catalysts could be used in biomass to liquid (BTL) FT as BTL plants require a very active catalyst which works well at high water partial pressures (Schulz, 1999; Simonetti et al., 2007; Claeys & Van Steen, 2002; Tungkamani et al., 2007). Ruthenium is the most active of all the FT catalysts (Co, Fe, Ni) and gives hydrocarbons of higher carbon number than the other catalysts. Unlike iron, It works well without a promoter. Ru FT has not been actively studied as a catalyst for FT in comparison to Fe and Co (Schulz, 1999).

In this chapter we report on the use of a ruthenium catalyst supported MWCNTs for use in FTS.

5.1.1 Experimental

The MWCNTs were synthesised and purified by methods described elsewhere (section 3.1). The Ru was loaded onto MWCNTs to make 10% Ru loaded catalysts which were tested for FTS. The catalysts were prepared by two different preparation methods i.e. an incipient wetness impregnation (IMP) and a deposition precipitation method (DPM) using urea as the deposition agent.

5.1.2 PXRD Analysis

Reduction and calcination of these catalysts was studied in situ in an X-ray reaction chamber. In situ variable temperature powder X-ray diffraction (VT-PXRD) analysis was carried out on the synthesised catalysts. In the VT-PXRD experiments, XRD patterns of the sample were collected at regular temperature intervals as the temperature was ramped.

In situ calcination and reduction studies were carried out only on the 10% Ru/CNT-IMP catalyst. To perform routine quantitative Rietveld refinement on the XRD data, the crystal structures of all the identified compounds should be known. MWCNTs however are amorphous, and as such do not have a captured structure.

To address this problem, 4 standard mixtures of purified multi walled carbon nanotubes (CNTR6) and CaF_2 with different ratios were prepared (CNTR6:CaF_2; 1:4; 2:3; 3:2; 1:1). CaF_2 was chosen because it is less susceptible than many materials to preferred orientation

effects. XRD patterns were collected on a Bruker D2 Phaser. The patterns were all collected for a 2 theta range of 10-90 degrees with step size of 0.024 ° per step at a rate of 185 sec/step. Quantitative Rietveld refinement was then carried out on the 4 samples using a graphite structure to model the contribution of CNTR6 to the sample. A fundamental parameter approach was employed to describe the peak shapes.

Table 5.1 gives the results of the refinement. The maximum deviation was 6.5 % whilst the rest of the deviations were less than 5 %. The accuracy is acceptable and therefore the crystallographic structure of graphite was good enough to use to model CNTR6 in a Rietveld refinement.

Table 5.1: Quantitative Rietveld refinement analysis of CNTR6/CaF_2

CNTR6%:CaF %	**20:80**	**40:60**	**50:50**	**60:40**
Rwp	7.06	6.10	5.92	5.57
X^2	1.96	1.97	2.06	2.23
CNTR6 %	13.5	36.6	46.8	62.0
CaF %	86.5	63.4	53.2	38.0
Δ	6.50	3.40	3.16	1.95

5.2 Characterisation of multi walled carbon nanotubes

The multi walled carbon nanotubes (MWCNTs) were synthesised by a catalytic chemical vapour deposition method over a Fe-Co/$CaCO_3$ catalyst (Tetana et al., 2012; Motchelaho et al., 2012). The as-grown MWCNTs were purified and functionalised in a one step process by refluxing the MWCNTs in 55 % nitric acid for 6 hours at 110 °C. The purified MWCNTs were characterised by TEM, TGA, XRD, FTIR and Raman spectroscopy. The as-grown MWCNTs were named AGCNT and the purified MWCNTs were named CNTR6. CNTR6 sample was then used as support to make the 10% ruthenium catalysts.

5.2.1 Transmission electron microscopy (TEM)

As-grown MWCNTs

The morphology of the synthesised MWCNTs was confirmed by TEM. Some metal particles were seen to be encapsulated inside the tubes (Figure 5.1). Most (47%) of the outer diameters of the MWCNTs were in the size range of 20-40 nm (Figure 5.2). The average outer diameter was found to be 29 nm. The average inner diameter of the AGCNTs was found to be 8 nm with most of the tube diameters falling in the size range of 5 - 9 nm (Figure 5.2 b).

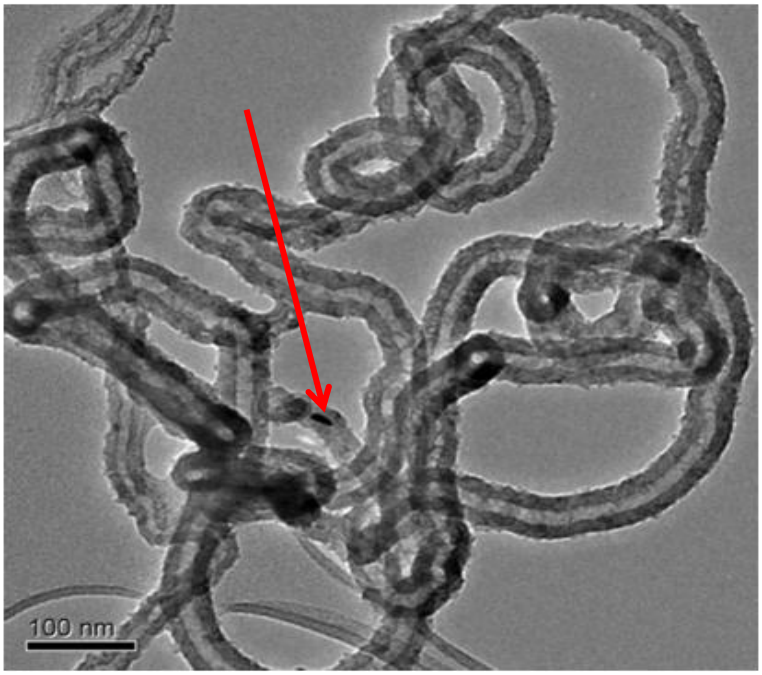


Figure 5.1: As grown MWCNTs; arrow shows encapsulated particle

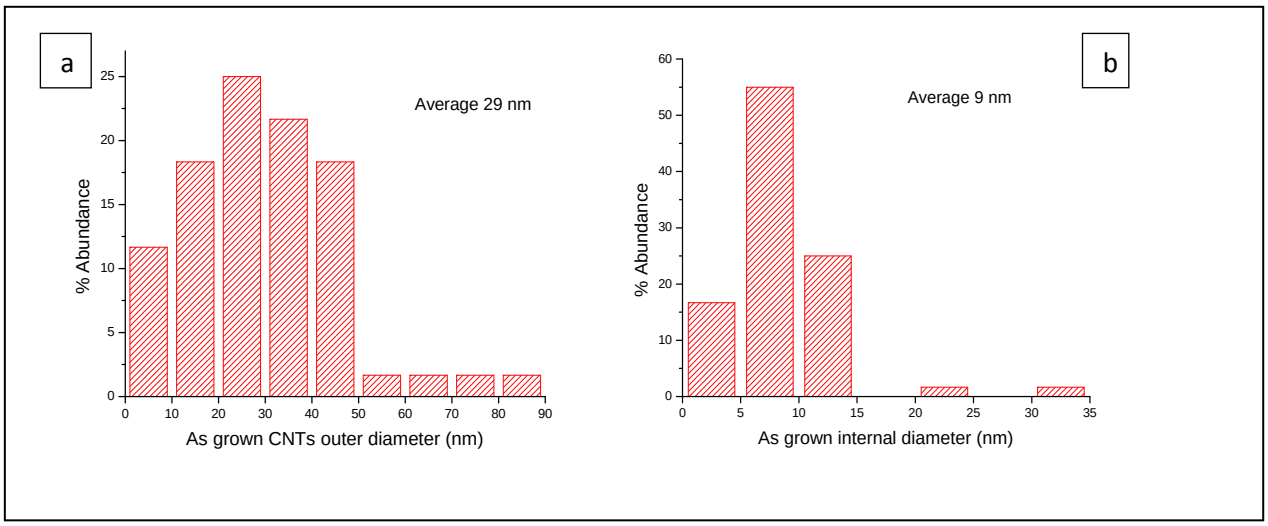


Figure 5.2: Histograms showing the distribution of diameter sizes for the outer and inner diameters of as-grown MWCNTs

Purified MWCNTs

The TEM images of the purified MWCNTs showed that most of the catalyst particles used for the MWCNTs synthesis had been removed during purification (Figure 5.3). A wide range of tube sizes was observed (10-100 nm). Because of the relatively harsh conditions employed for purification, some of the tube ends were opened by the acid. The average size of the outer diameter of the CNTR6 was found to be ca. 24 nm (Figure 5.4 a). This was slightly less than that of the as-grown MWCNTs because when the walls were washed with nitric acid removing any amorphous carbon that could have been on the surface was removed. The outer graphitic walls were also slightly corroded by the acid. The average inner diameter size was 8 nm (figure 5.4 b) with 70% of the MWCNTs size range falling between 5 and 10 nm.

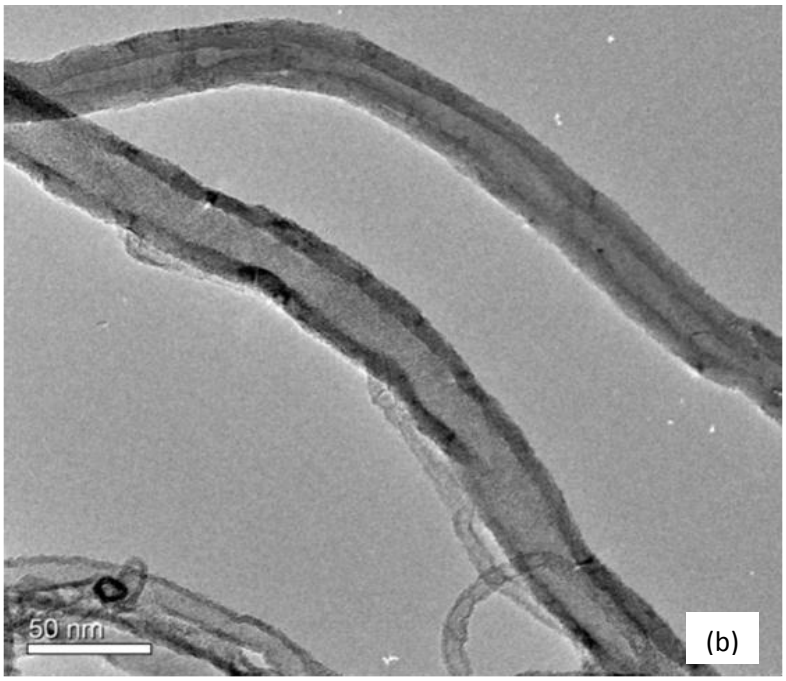


Figure 5.3: TEM image of purified MWCNTs

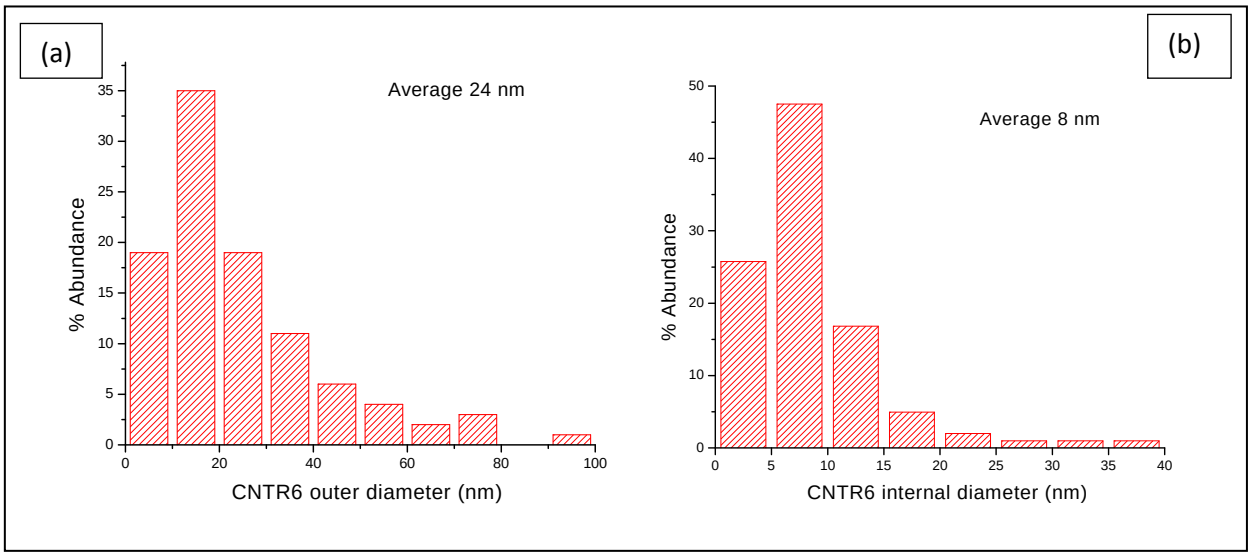


Figure 5.4: Histograms showing the distribution of the diameter sizes for the outer and inner diameters of acid washed MWCNTs.

5.2.2 Raman spectroscopy analysis

Raman spectroscopy was also used to analyse the quality of the graphitic structure of the as-grown and acid washed MWCNTs. The two characteristic Raman peaks which represent the D-band and the G-band were observed (Figure 5.5). The degree of disorder in the

graphitic structure was determined by calculating the I_D/I_G ratio using peak areas. The D band gives an indication of non-crystalline graphite in the case of carbon nanotubes and the G band represents a highly crystalline graphitic structure (Keszler et al., 2004). Therefore highly crystalline carbon nanotubes have a low I_D/I_G ratio. Indeed the I_D/I_G ratio of as-grown MWCNTs was higher (3.0) than that of purified MWCNTs which was 2.1 (Table 5.2). This was because of the presence of some amorphous carbon in the as prepared sample which was not present in the purified sample. Purification could also have introduced defects into the structure of the CNTR6 (Zdrojek et al., 2004)

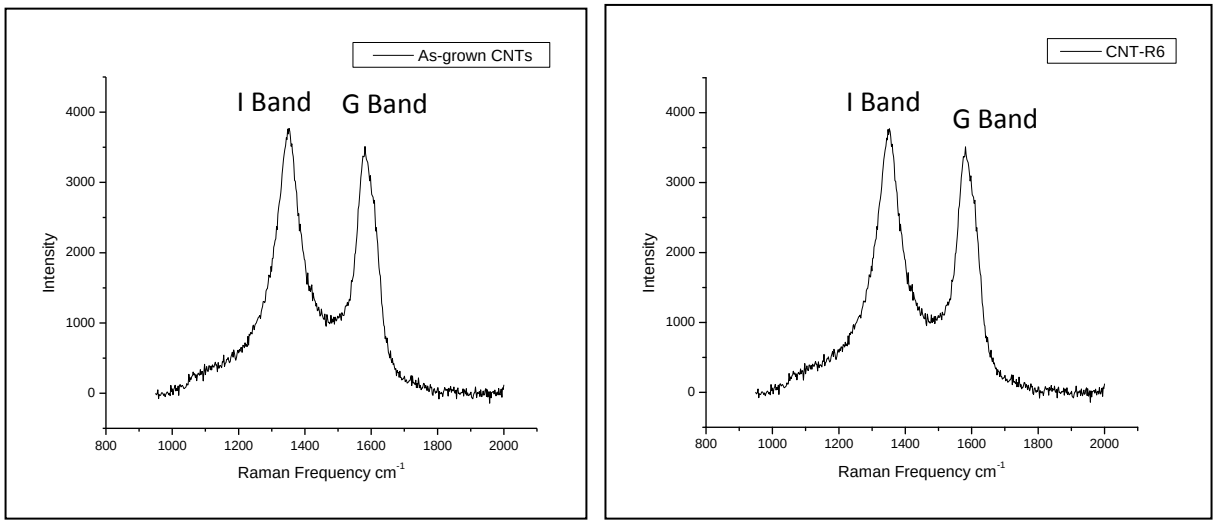


Figure 5.5: Spectra of as grown and purified MWCNTs

Table 5.2: Raman spectroscopy; I_D/I_G ratio of as grown and purified carbon nanotubes

Sample	Position (I)# (cm^{-1})	Position (G)# (cm^{-1})	Area (I)	Area (G)	I_D/I_G ratio
AGCNT	1350	1577	199479.88	64329	3
CNTR6	1344	1582	190005.45	82016	2.1

$\pm$ 2 cm^{-1}

5.2.3 Thermal gravimetric analysis

Thermal gravimetric analysis (TGA) is a useful technique used to determine the thermal stability of a material. For carbon materials the amount of metal impurities can be determined by simply oxidising the carbon which leaves behind a residue of metal oxides.

During heating of the as-synthesised MWCNTs in air, it was observed that the AGCNTs were stable up to ca. 442 ˚C after which a slight weight gain was noted (Figure 5.6). This is due to oxidation of iron to form iron oxide (Huijbregts & Snel, 1972). Above 520 ˚C the mass of the as grown nanotubes decreases rapidly until it becomes constant at 810 ˚C. The TGA profile in Figure 5.6 shows that there was a 25% catalyst impurity in the MWCNTs. It can also be deduced that the amount of amorphous carbon was insignificant because there was no rapid weight loss before 500 °C (Hou et al., 2001). The optimum temperature for AGCNTs decomposition was found to be 643 °C (figure 5.7). A peak observed at 757 ˚C was due to the decomposition of the more stable high quality graphitic structure found in some tubes. The purified and functionalised (CNTR6) sample was less stable than the as grown sample, with most CNTs completely decomposed at T>620 ˚C. This is related to the defects and slight damage that occurs during the purification process. The slight decrease in mass of 6 % at temperatures below 400 ˚C was due to the removal of functional groups on the MWCNTs during heating. This slight decrease in mass was not observed when acid washed MWCNTs were first annealed at 600 ˚C under a nitrogen atmosphere and then analysed by TGA (Figure 5.8). The residual metal in this sample was less than 1.5% and was attributed to catalyst metal particles that were encapsulated inside the tubes and which could not be washed away during acid treatment.

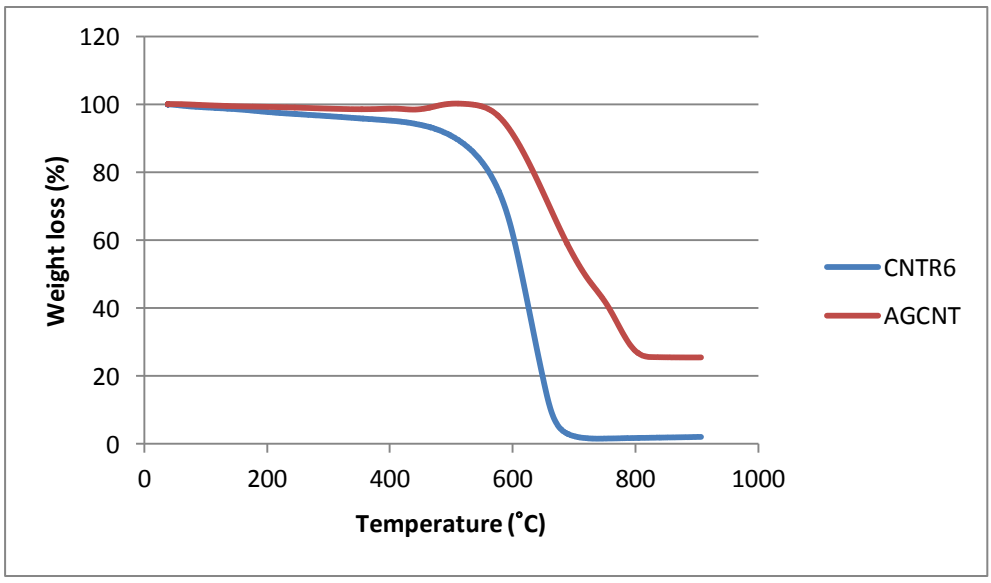


Figure 5.6: TGA profiles of as grown (AGCNTs) and acid washed carbon nanotubes (CNTR6)

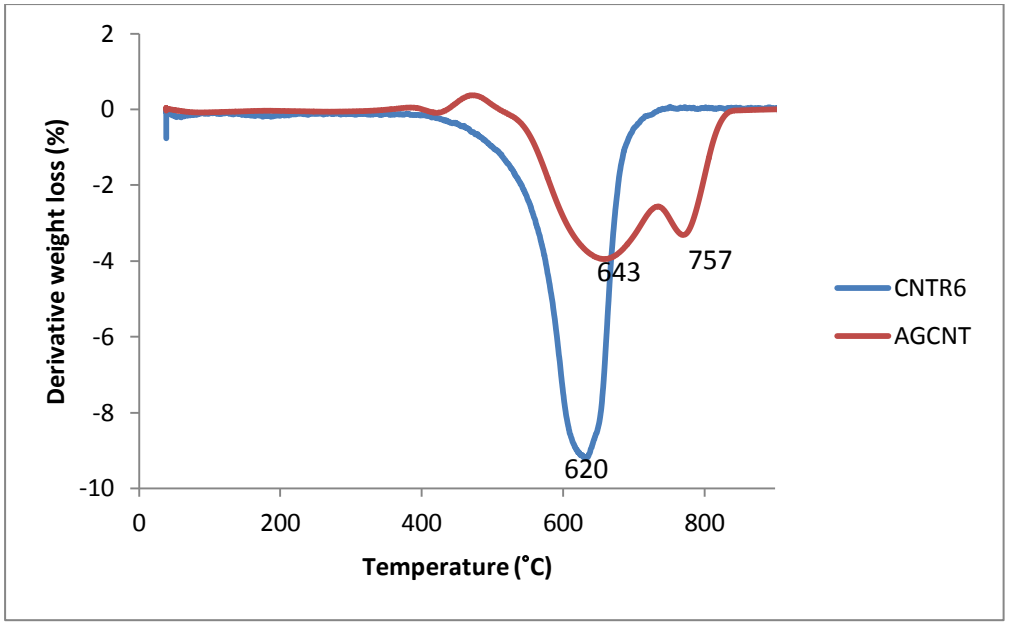


Figure 5.7: Derivative plots of TGA profiles for as grown (AGCNT) and acid washed carbon nanotubes (CNTR6)

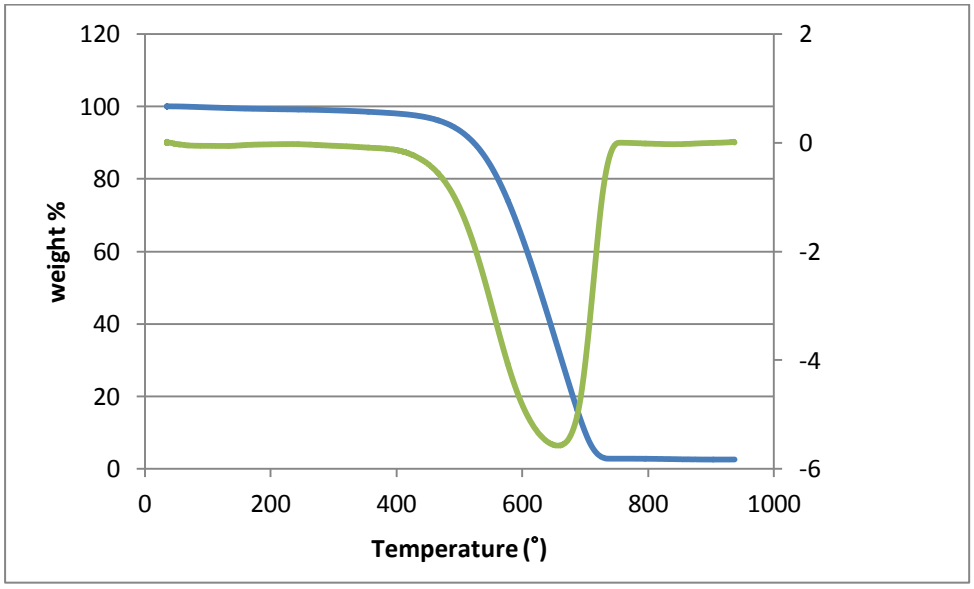


Figure 5.8: TGA profile of CNTR6 annealed at 600 ˚C under N_2 for 1 hour.

5.2.4 Powder X-ray diffraction (PXRD)

The PXRD technique was used to confirm the presence of a graphitic structure in the AGCNT and CNTR6 samples. Two characteristic graphite peaks (Cu K radiation) were identified; i.e. a peak at 26 ˚ (0 0 2) and at 44 ˚ 2θ (1 0 1) with the corresponding d spacing and hkl planes listed in Table 5.4. It was also confirmed that CaO was removed during the purification

process. However iron carbide (Fe_3C) (Figure 5.9) could not be removed by acid washing since it is encapsulated inside the tube and is shielded from the acid during purification. This is in agreement with TGA results which showed a residual of less than 1.5% (Fe_3C). The Appendix shows the results of peak matching that was done using Eva software (Appendix).

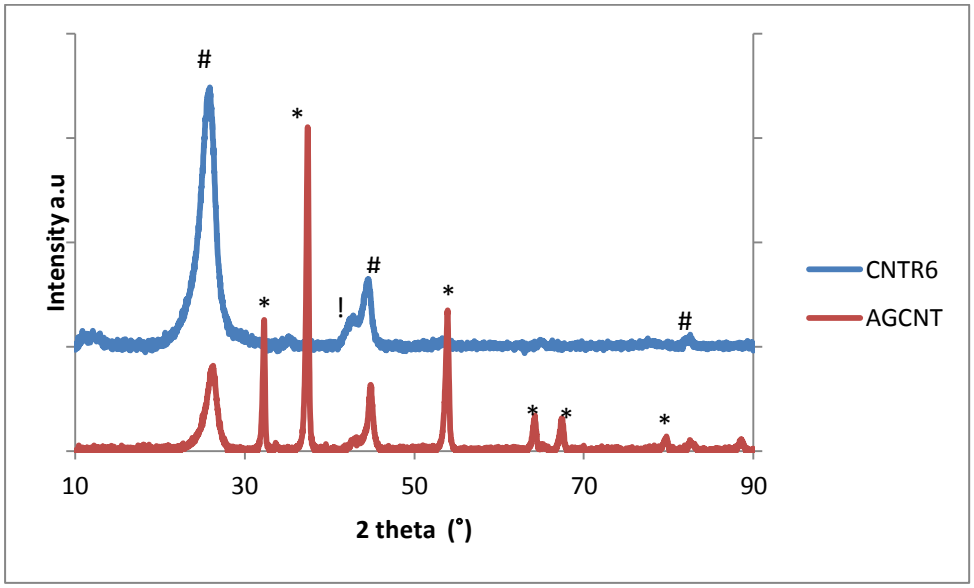


Figure 5.9: PXRD pattern of as grown and purified CNTs.

peaks for graphite wall of CNTs; * CaO peaks;! Fe_3C

5.2.5 FTIR spectroscopy

FTIR spectroscopy was used to check whether surface groups had been introduced onto the CNTs during the purification process using HNO_3. Weak peaks could be identified on CNTR6 which were not present in the AGCNT profile which gave an indication that functional groups had been introduced (Figure 5.10). A weak peak at ~ 1328 cm^{-1} indicated the presence of C-O and O-H bonds (Naseh et al., 2009; Shaffer et al., 1998). Another weak peak was observed at ~ 1662 cm^{-1} which was attributed the stretching band of C=O signifying the presence of carboxylic groups (Kim & Sigmund, 2004).

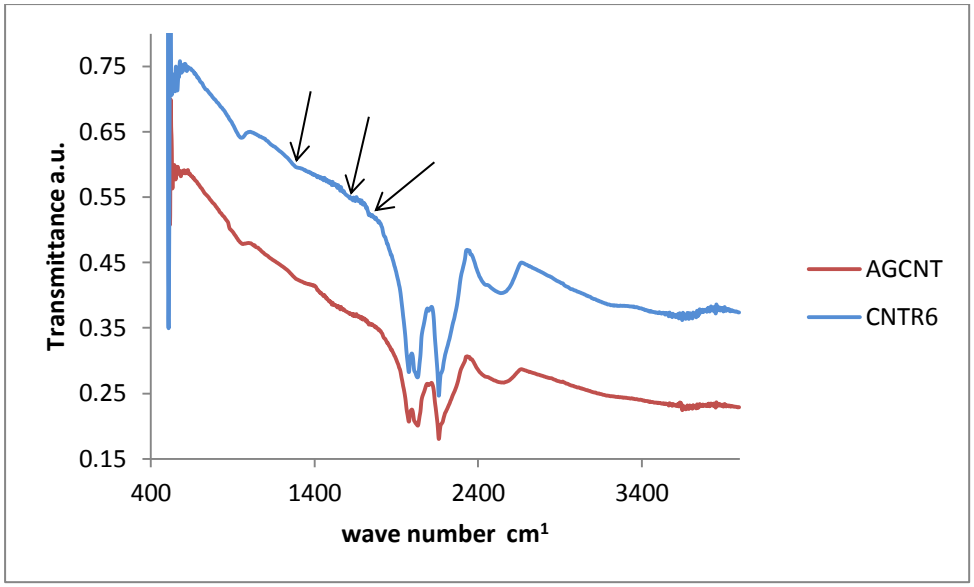


Figure 5.10: FTIR profiles of AGCNT and CNTR6

5.3 Characterisation of catalysts for FTS

The catalysts loaded with 10% Ru were prepared by an incipient wetness impregnation and a deposition precipitation method using urea; the catalysts were named 10Ru/CNTR6-IMP and 10Ru/CNTR6-DPM respectively. The catalysts were pre-heated at 400 ˚C for 3.5 hours under nitrogen to decompose precursor salts (chlorides). These catalysts were characterised by XRD, TGA, TPR and TEM before being tested for FTS in a fixed bed reactor. (Section 3.1.4)

5.3.1 PXRD of catalysts

10Ru/CNTR6-IMP and 10Ru/CNTR6-DPM were analysed by XRD (Cu λ = 1.5406 Å) before and after heat treatment. XRD patterns of 10Ru/CNTR6-IMP did not show the presence of Ru (Figure 5.11) before heat treatment under N_2. However after heat treatment RuO_2 and metallic Ru peaks could be identified. RuO_2 was reduced to the metallic state by the carbon support under the inert atmosphere. This was confirmed by a PXRD in situ study (section 5.3.2).

The 10Ru/CNT-DMP catalyst was also analysed by XRD (Co λ=1.793Å). 10Ru/CNTR6-DPM showed the presence of RuO_2 before heat treatment (Figure 5.12). The RuO_2 particles must have sintered during reflux in the deposition process to result in the Bragg reflection

(section 3.1.4). After heat treatment, RuO_2 peaks were not observed, only Ru metal peaks. Appendix shows the result of the search match undertaken in this study.

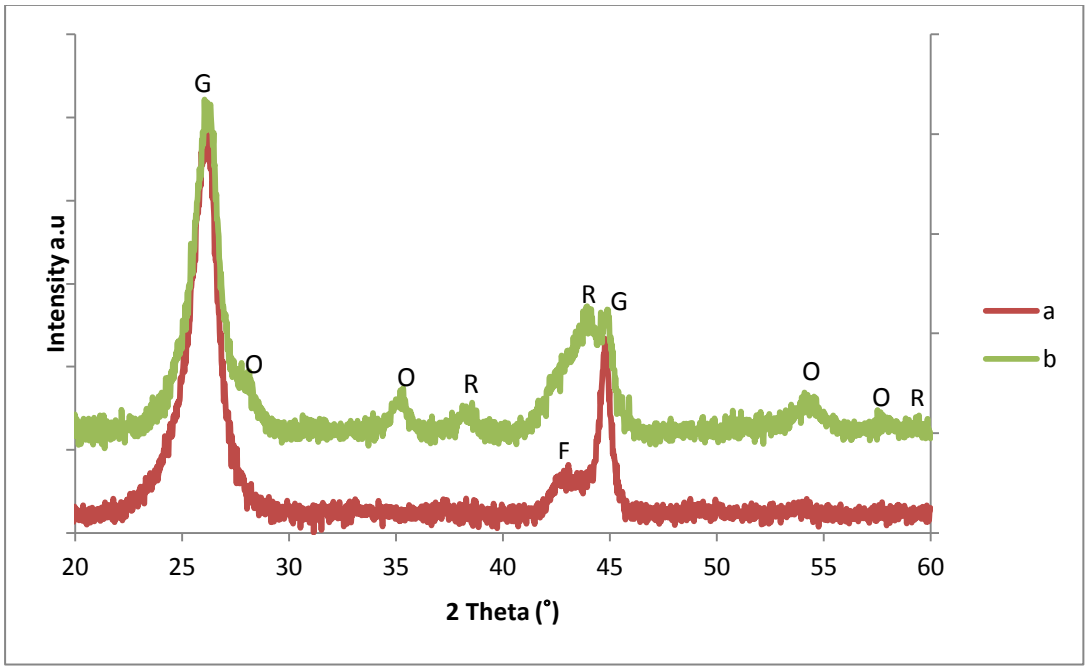


Figure 5.11: XRD patterns of 10Ru/CNTR6-IMP before (a) and after (b) heat treatment at 400 ˚C for 3.5 hours; **G** - graphite (CNTR6), **O** - RuO_2, **R**- Ru, **F**-Fe_3C.

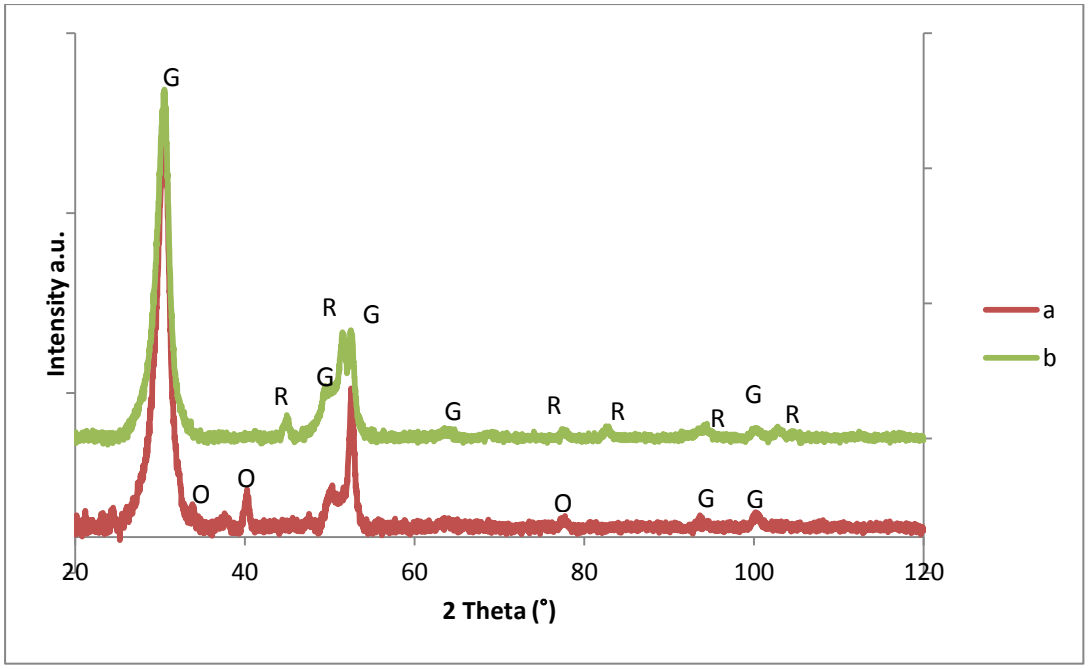


Figure 5.12: XRD patterns of 10Ru/CNTR6-DMP before (a) and after (b) heat treatment at 400 ˚C for 3.5 hours; where **G** - graphite (CNTR6), **O** - RuO_2, **R**- Ru. (Appendix)

5.3.2 In situ variable temperature PXRD study of 10Ru/CNTR6-IMP

An in situ VT-PXRD study was carried out on the 10Ru/CNT-DMP before heat treatment in the X-ray reaction chamber (XRK). The temperature was increased from 30 ˚C to 550 ˚C with XRD patterns being collected at every 20 ˚C interval. N_2 was allowed to flow through the XRK at 60 mL/min during the experiment.

From the first pattern recorded at 30 ˚C, only graphite peaks are present which confirms the presence of the CNTs (Figure 5.13). Though RuO_2 is present in the sample it is not detected at this stage. Ru could not be detected in its precursor state ($RuCl_3$) either. This was attributed to the small crystallite size which could not give Bragg reflections (Scherrer, 1918). As the temperature was increased the RuO_2 particles sintered and became big enough particles to be able to be detected. The RuO_2 peaks emerged at 310 ˚C and grew in intensity up to a maximum at 370 ˚C (Figure 5.14). At 390 ˚C metallic Ru (Figure 5.15) peaks emerged as RuO_2 peaks started to decrease in intensity. At 450 ˚C all the RuO_2 had been converted to metallic Ru. It is clear that RuO_2 is reduced under inert conditions. This auto

reduction of a metal oxide by a carbon support is similar to that observed for Co on carbon as observed by Xiong et al. (2010). The CNTR6 support reacted with the oxygen from the RuO_2 to form CO_2 under the inert conditions.

$$C_{(s)} + RuO_{2\,(s)} \rightarrow CO_{2\,(g)} + Ru_{(s)}$$

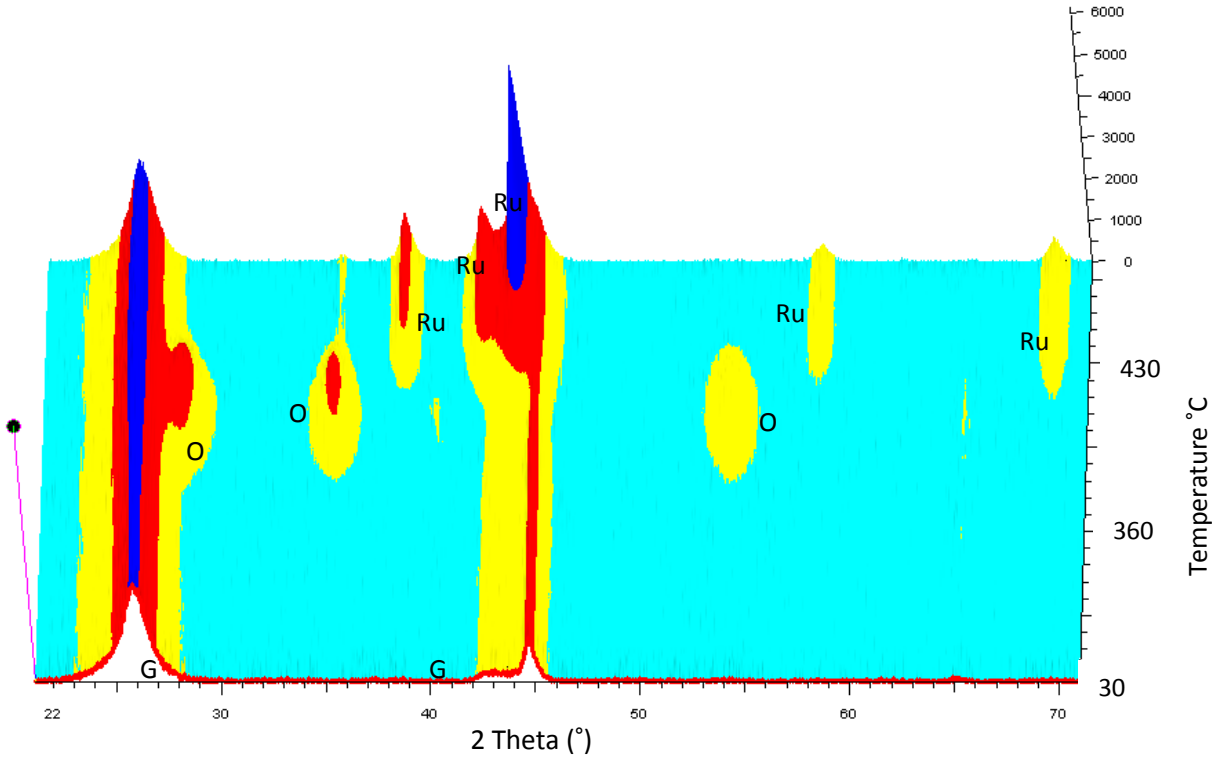


Figure 5.13: VT-PXRD calcination study of 10Ru/CNT-IMP; O-RuO2 peaks, R- Ru metal, G – CNTs

5.3.3 Surface area analysis

BET surface areas were determined as explained in section 3.2.4. The BET surface area of the as-grown MWCNTs was found to be 60.2 m^2/g and the pore volume was 0.22 cm^3/g (Table 5.5). The surface area increased to 87.8 m^2/g and the pore volume also increased to 0.30 cm^3/g (Table 5.3) when the MWCNTs were purified by nitric acid. This is because washing the AGCNT opens up the CNTs pores. The surface area also increased because the low surface area CaO had been removed and also the surface became more rough through acid treatment. When ruthenium metal was loaded onto the CNTR6 the surface as well as the pore volume recorded decreased; this is no doubt due to the pores becoming filled with

metal particles. The high BET area value for 10Ru/CNTR6-DPM is similar to that for the purified unloaded MWCNTs. This is because the particle size is small and hence the pores are not blocked as observed with 10Ru/CNTR6-IMP.

Table 5.3: BET surface areas for MWNTs and catalysts synthesised

Sample	**Surface area (m^2/g)**[a]	**Pore volume (cm^3/g)**[a]
As-grown CNTs	60.2	0.22
CNTR6	87.8	0.30
10Ru/CNTR6-IMP	64.0	0.25
10Ru/CNTR6-DPM	92.3	-

- Not collected

5.3.4 Transmission electron microscopy

10Ru/CNTR6-DPM and 10Ru/CNTR6-IMP were analysed by TEM after heat treatment at 400 ˚C under N_2.TEM results showed that generally the particle size of the catalyst prepared by both methods were in the nano range with average diameter of less than 10 nm (Figure 5.14). Ru dispersion was better in 10Ru/CNT-DPM than 10Ru/CNT-IMP with average particles size of 2.5 nm and 5.3 nm respectively. The deposition precipitation method yielded a narrow Ru particle size range (Figure 5.15) whilst the size distribution range was broader using the incipient wetness impregnation method. The data recorded that 90% of the Ru particles sizes in 10Ru/CNT-DPM were in the 1-4 nm range.

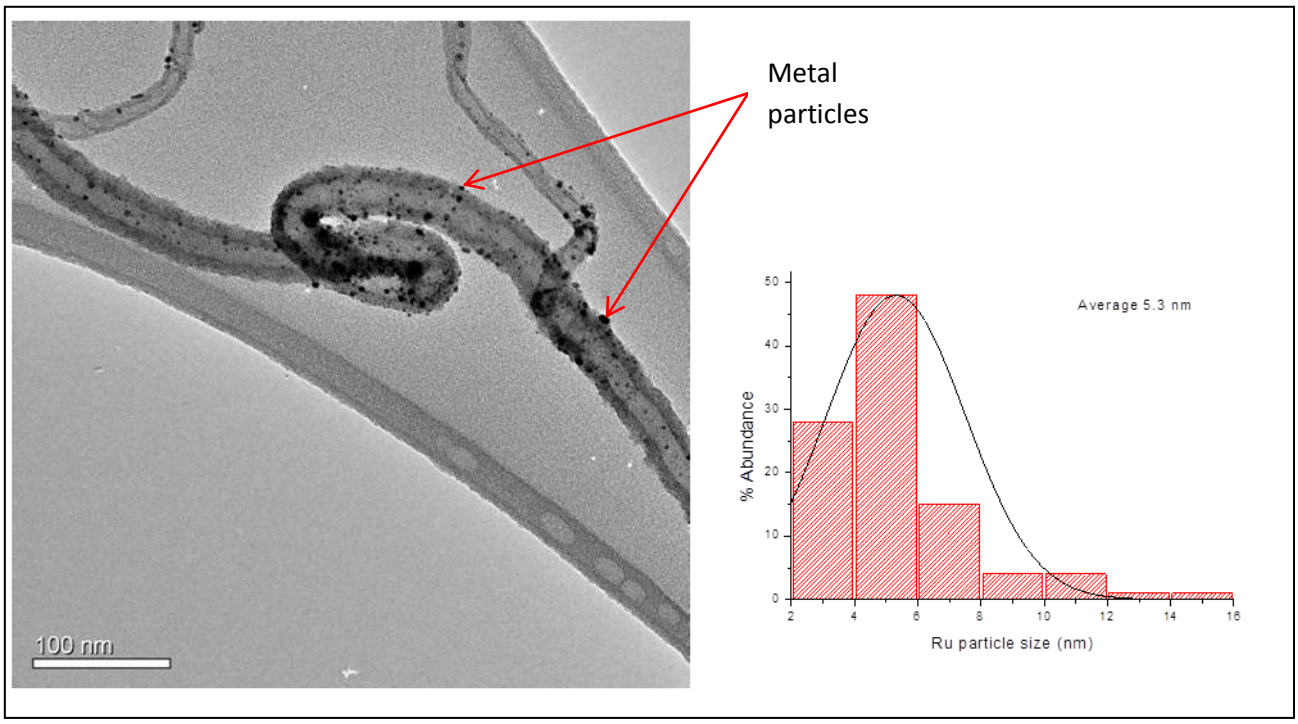


Figure 5.14: TEM image of 10%Ru/CNT-IMP

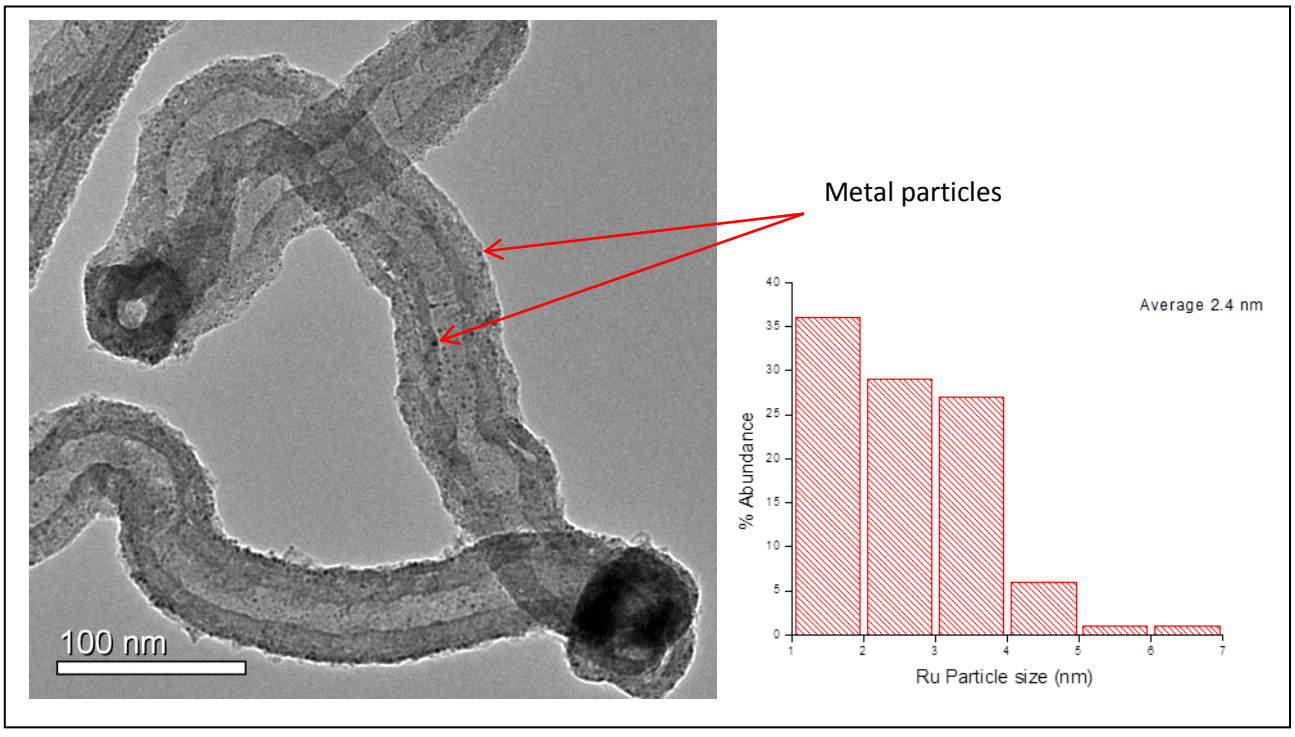


Figure 5.15: TEM image of 10%Ru/CNT-DPM

5.3.5 TGA of synthesised FTS catalysts

TGA was carried out to determine the stability of the catalyst to heat as well as to confirm the Ru loading. The TGA experiments were carried out in air from 35 ˚C to 900 ˚C.

Figure 5.16 shows the TGA profile of 10Ru/CNTR6-IMP before heat treatment. The peak at 402 ˚C was attributed to the decomposition of chlorides from the ruthenium precursor salt. Therefore in later studies the samples were heat treated at 400 ˚C for 3.5 hours to remove the chlorides before the catalyst was used for FTS. The other two peaks (509 ˚C and 554 ˚C) are due to the oxidation of CNTs to form CO_2. Both peaks occur at a lower temperature when compared to those of AGCNT and CNTR6 (section 5.2.3). This was attributed to the catalytic effect of the metal loaded onto the MWCNTs. The TGA profile for the uncalcined 10Ru/CNT-DPM was similar to that of Ru/CNTR6-IMP (Appendix) and therefore heat treatment was carried out under similar conditions before FTS.

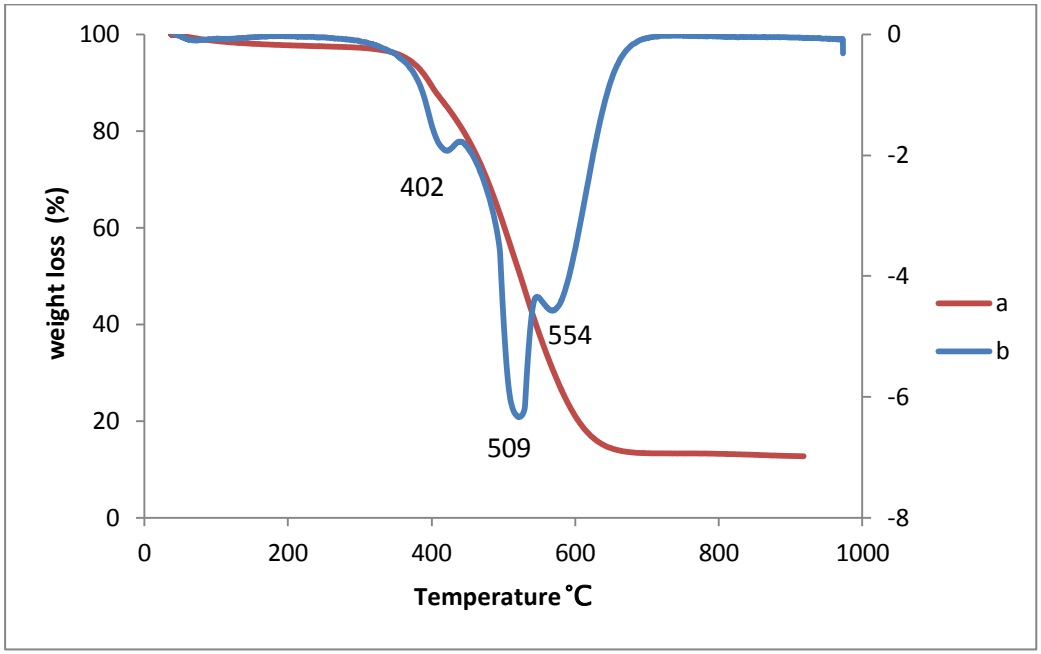


Figure 5.16: TGA plot 10Ru/CNTR6 prepared by impregnation (a) before heat treatment and (b) its derivative curve

The TGA profiles of 10Ru/CNT-DPM and 10Ru/CNT-IMP after heat treatment were similar (Figure 5.17). This meant that the thermal stability of the two catalysts was the same. The profiles also show that similar metal loadings were achieved for both catalysts which made comparison of FTS results obtained from using these catalysts reliable. The residue of 16% was attributed to mainly RuO_2 formation. The Ru loading was found to be 10.5 after also taking into account of 1.5% residue from the Fe-Co catalyst used to make the CNTs.

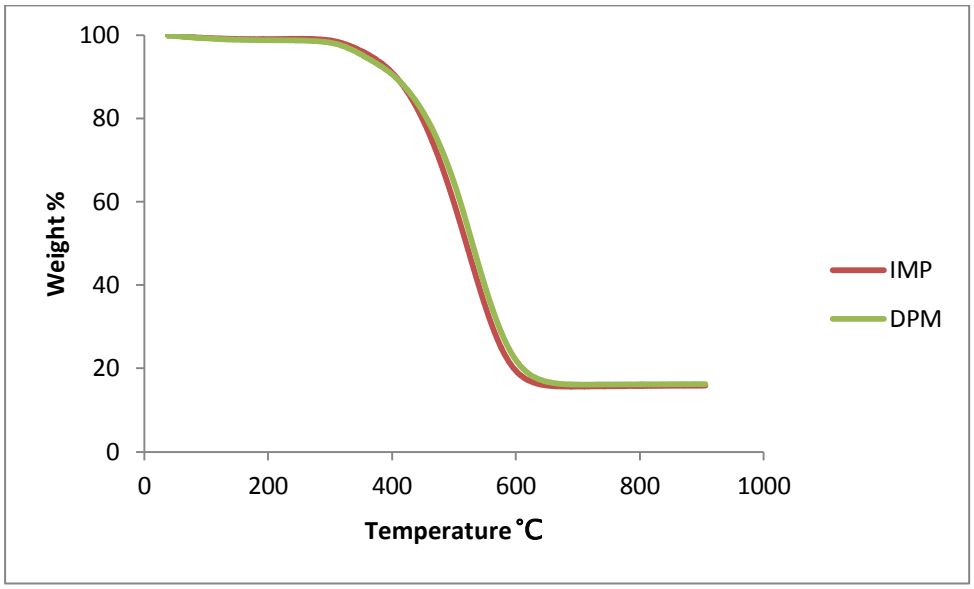


Figure 5.17: TGA plot of 10Ru/CNT-IMP (IMP) and 10Ru/CNT-DPM (DPM) after heat treatment at 400 ˚C under N_2 for 4 hours.

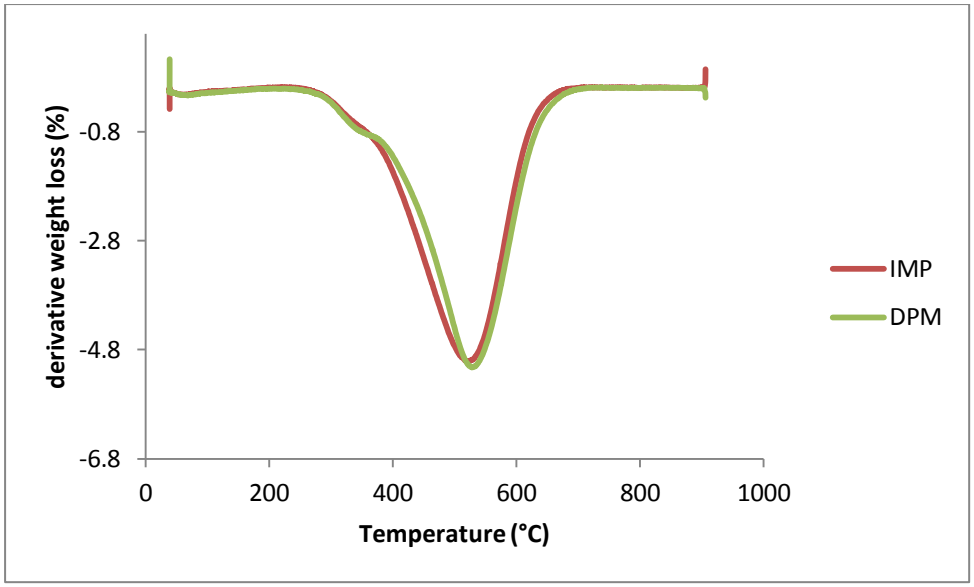


Figure 5.18: Derivative TGA plot of 10Ru/CNT-IMP (IMP) and 10Ru/CNT-DPM (DPM) after heat treatment at 400 ˚C under N_2 for 4 hours.

5.3.6 In situ variable temperature XRD reduction

An in situ VT-PXRD reduction study was carried out on 10Ru/CNTR6-IMP under a 5% H_2/N_2 gas (40 mL/min) mixture. As was shown in section 5.3.1 (Figure 5.11), the heat treated 10Ru/CNTR6-IMP catalyst consists of RuO_2 and metallic Ru (Figure 5.19). From the observed phase transition it can be confirmed that reduction takes place as explained in section 5.3.2.

$Ru^{4+} \rightarrow Ru^{0}$

RuO_2 was completely reduced to metallic Ru at 270 ˚C. This temperature is higher than that determined in the TPR experiment (section 5.3.7). This could be because in the in situ analysis, the H_2 gas passes over the sample whereas in the TPR analysis the H_2 flows through the sample in a U tube reactor. The flow rate and the H_2 content in the reducing gas (5%H_2/Ar (40 mL/min)) used in this in situ XRD analysis was similar to that used in the TPR analysis. The analysis was carried out from 45 ˚C to 850 ˚C and the in situ XRD reduction was carried out from 30 ˚C to 550 ˚C.

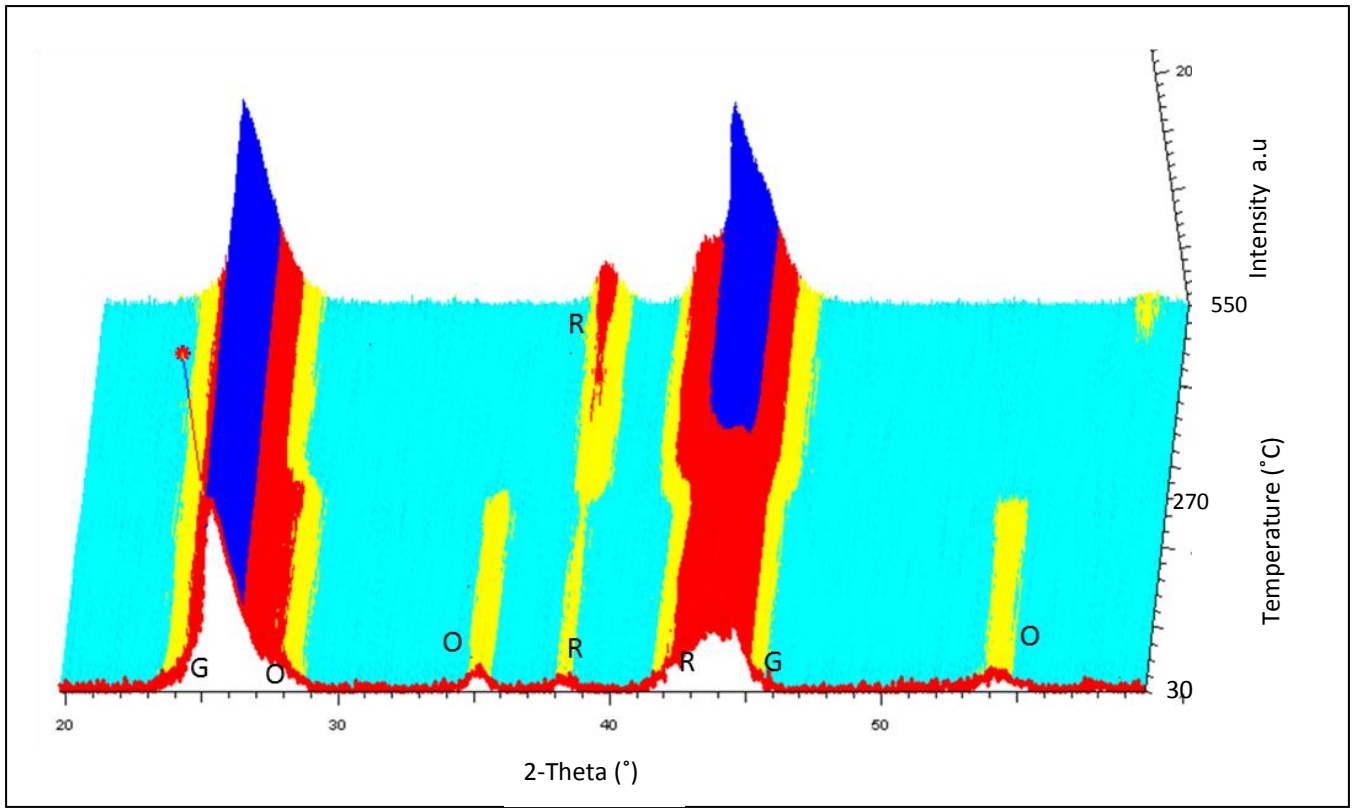


Figure 5.19: VT-PXRD reduction of 10Ru/CNT-IMP; **O**-RuO_2, **R**- Ru metal, **G** – CNTs

The particle size of the Ru was determined using the Scherrer equation (section 2.3.6.) incorporated in the Topas software used for the Rietveld refinement study. The particle size of metallic Ru at 30 ˚C is 4.3 nm while that of RuO_2 at that same temperature is 8.9 nm (Table 5.4). This agrees well with the average TEM value of 8.2 nm. 77% of the metal had already been reduced to metallic Ru (Table 5.6) during heat treatment under an inert (N_2) atmosphere (400 ˚C).

$RuO_{2\,(s)} + C_{(s)} \rightarrow CO_{2\,(g)} + Ru_{(s)}$

The particle size of Ru metal remained almost unchanged during the VT-PXRD reduction indicating that the Ru catalyst was not susceptible to sintering (Figure 5.20). The variation in size is insignificant and within experimental uncertainty.

Table 5.4: VT-PXRD reduction results of 10Ru/CNT-IMP at 30 ˚C and 270 ˚C

Parameter	**30 ˚C**	**270 ˚C**
Rwp	3.73	3.81
x^2	1.23	1.28
CNTR6 %	89.92	87.88
RuO %	2.24 (8.2 nm)	0
Ru %	7.84 (4.3 nm)	11.83 (4.4 nm)

±5%

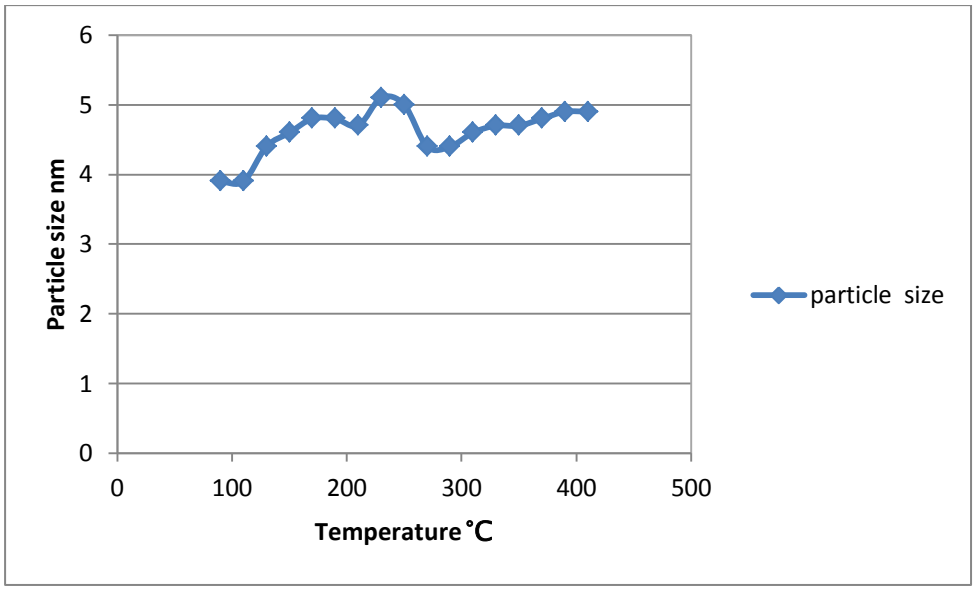


Figure 5.20: Particle size variation of Ru metal during VT-PXRD reduction

5.3.7 Temperature programmed reduction (TPR)

TPR was carried out on both catalysts after heat treatment under N_2 to decompose chlorides. TPR results are shown in Figure 5.21. Both 10Ru/CNT-DPM and 10Ru/CNT-IMP show three reduction peaks. The first two peaks indicate the reduction of ruthenium oxide. RuO_2 is reduced to the metallic state below 200 ˚C in both catalysts. Profiles for both catalysts show two reduction peaks. The first peaks below 100 ˚C were attributed to moisture in the samples. The second peak, which was above 100 ˚C, was attributed to the reduction of RuO_2 to metallic state. However this second peak is much smaller for 10Ru/CNT-DPM than for 10Ru/CNT-IMP. This is because there was less RuO_2 in 10Ru/CNT-

DPM as most of it was reduced during heat treatment under nitrogen as shown by XRD data (section 5.12). Kang et al. (2010) also reported only one reduction peak for ruthenium supported on carbon nanotubes.

The profile of CNTR6 shows a major peak at 665 ˚C. This is the temperature at which gasification of CNTs occurs to form methane (Motchelaho et al., 2011). It can be seen from the reduction profile that hydrogenation of carbon nanotubes to form methane starts at ~300 ˚C. The third peak at 513 ˚C indicates the gasification of CNTs to produce methane. This temperature is lower than that of CNTR6. It is therefore clear that the ruthenium metal on the CNTs catalyses this process. This agrees with TGA results as explained previously (section 5.3.5) where it was shown that the addition of Ru on CNTs makes them less stable in air.

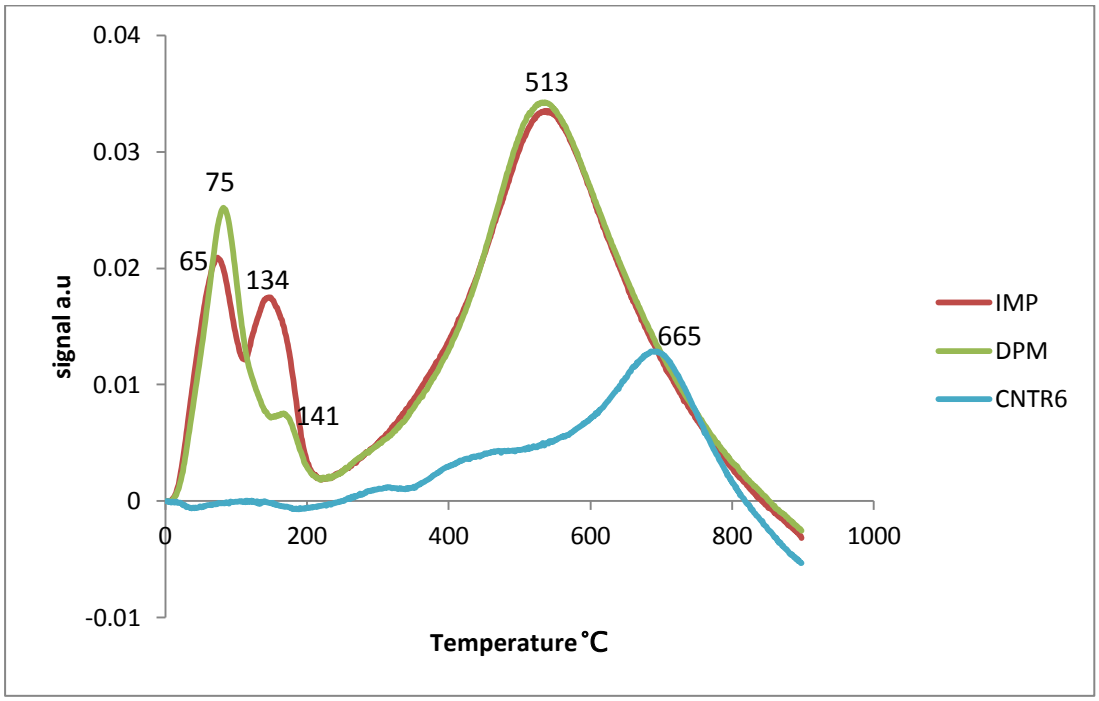


Figure 5.21: TPR profiles of synthesised catalyst and CNTs

5.4 Catalytic performance

In this FTS study, the effect of reaction temperature on the activity and selectivity of the catalyst was investigated. It is well known that a Ru catalyst is active at the lowest of temperatures when supported on common catalyst supports such as alumina and titania (Schulz, 1999). However the effect of operating temperature when ruthenium is supported on MWCNTs has been little studied. The effect of the preparation method on the activity and selectivity of the prepared catalyst has also not previously been investigated. The FTS results were analysed and conversion, activity and olefin: paraffin fraction were determined. In this study an unusually high Ru loading (10%) was used; this was done so as to correlate data with the XRD analysis; this study requires a high Ru loading.

The FTS reaction was carried out at a pressure of 8 bar and a syngas flow rate of 20 mL/min. The H_2: CO ratio was 2:1. Two reaction temperatures (220 °C and 250 °C) were employed for each catalyst (10Ru/CNT-IMP and 10Ru/CNT-DPM). Initially the CO conversion increased to a maximum of 43% average before decreasing with time and reaching a stable state at different CO conversions.

5.4.1 Effect of reaction temperature on FTS

Activity: CO conversion increased when the reaction temperature was increased from 220 °C to 250 °C for both catalysts (Figure 5.22). The initial catalyst activity increased to a maximum of 38 % CO conversion before dropping significantly in the first 24 hours on stream. At 220 °C CO conversion was below 20% for both catalysts (10Ru/CNT-DPM and 10Ru/CNT-IMP) this increased to ca. 30% at 250 °C. At the lower temperature (220 °C) the catalysts were less stable for the 120 hours on stream, deactivating continuously; 10Ru/CNT-DPM being worse than 10Ru/CNT-IMP. This may be due to clogging of active sites due to wax formation (Figure 5.22) (Fujimoto et al., 1985). However at a higher reaction temperature (250 °C) CO conversion for both catalysts stabilised after ca. 24 hours on stream.

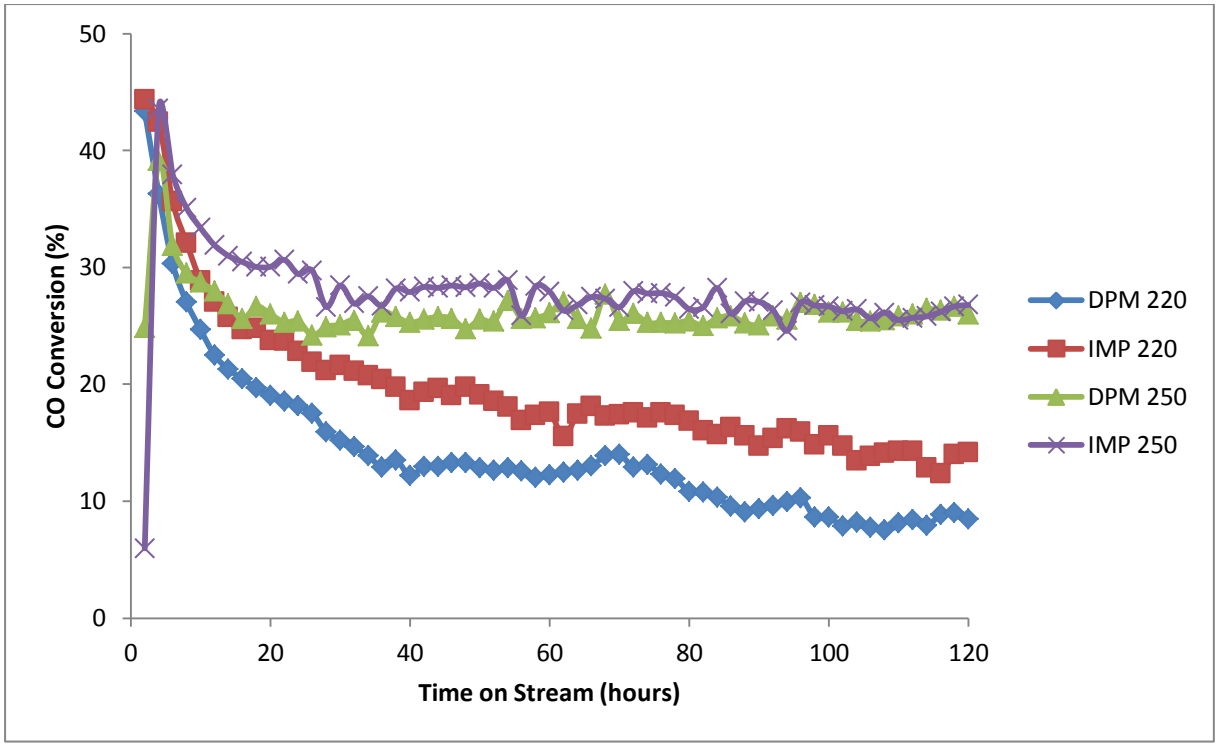


Figure 5.22: CO conversion over a period of 120 hours in FTS

Selectivity: selectivity to methane increased with increased reaction temperature (Table 5.5). Selectivity to methane doubled for both catalysts when the reaction temperature was raised from 220 °C to 250 °C; (10Ru/CNT-DMP, 11.6% to 30.8%; 10Ru/CNT-IMP, 14.2% to 28.1%). Hydrocarbons of higher carbon number were realised when FTS was carried out at 220 °C and less when the FTS temperature was raised to 250 °C. The selectivity to C_5+ for 10Ru/CNT-DMP decreased to 52.2 % from 75.1 % when the reaction was carried out at 250°C and 220°C respectively. A similar trend was observed for 10Ru/CNT-IMP where the selectivity to C_5+ dropped to 51.4% from 70.28%. This is in agreement with what is published in the literature (Schulz, 2009). Tungkamani et al. (2007) observed a similar trend when an investigation was carried out on Ru/MgO-Al_2O_3, Ru/MgO and Ru/Al_2O_3 catalysts. Methane selectivity increased with increasing reaction temperature and more heavier hydrocarbons were realised at lower reaction temperature than at high reaction temperature.

Table 5.5: Activity and selectivity of catalysts during FTS

	220 °C IMP	**220 °C DPM**	**250 °C IMP**	**250 °C DPM**
% CO conversion	19	15	28	26
CO rate * 10^{-6}	0.97	0.65	1.49	1.36
Activity mol/h/g	0.0069	0.0047	0.011	0.0098
α	0.80	0.81	0.78	0.78
Selectivity				
C_1	14.2	11.6	28.1	30.8
C_2-C_4	15.4	13.3	20.4	17.3
C_5-C_{11}	36.98	44.8	31.6	30.8
C_{12}+	33.3	30.3	19.8	21.4
O/O+P ratio (C_2)	0.127	0.204	0.036	0.034

Olefin to paraffin ratio: The olefin ratio was found to be higher when the FTS was carried out a lower temperature (220 °C) when compared to the reaction being carried out at a higher temperature (250 °C) (Table 5.6). This was the trend for C_2 to C_5 except for C_3 where the olefin paraffin ratio was almost similar.

Table 5.6: Olefin to paraffin ratio of the catalyst

O/(O+P) C_n	**220 °C IMP**	**220 °C DPM**	**250 °C IMP**	**250 °C DPM**
C_2	0.13	0.20	0.036	0.034
C_3	0.34	0.32	0.34	0.36
C_4	0.50	0.52	0.19	0.24
C_5	0.44	0.47	0.16	0.19
C_6	-	-	0.032	0.027
C_7	0.09	0.44	-	-

- Not detected

5.4.2 Effect of preparation method on FTS

Activity: 10Ru/CNT-IMP exhibited greater activity than 10Ru/CNT-DMP at 220 °C; however at 250 °C there was no significant difference in their activities (Figure 5.22). The average CO conversion of 10Ru/CNT-IMP at 220 °C was 19.5% whilst that of 10Ru/CNT-DMP was 14.1% at the same temperature. Fujimoto et al. (1985) found that the activity of a highly dispersed Ru/TiO_2 catalyst was lower than that of poorly dispersed Ru/TiO_2 catalysts. The authors also observed a similar trend when Ru/ZrO was used in FTS. This is in agreement with the findings of van Steen. van Steen et al. (2002) also found that a Fe/CNT catalyst prepared by the incipient wetness method was more active in FTS. The catalyst was less dispersed than found for two other catalysts which were prepared by the deposition precipitation method using urea and copper as deposition agents (van Steen et al., 2002). The authors suggested that different phases could be present in the different catalysts due to variances in particle size of the metals on the support.

The 10Ru/CNT-DMP catalyst was more stable when compared to the 10Ru/CNT-IMP catalyst when FTS was carried out at 250 °C. CO conversion stabilised after 20 hours at 250 °C when 10Ru/CNT-DMP was used. However, CO conversion slowly decreased when 10Ru/CNT-IMP was used.

Selectivity: Differences in methane selectivity of the two catalysts were insignificant (Table 5.7). At 220 °C, 10Ru/CNT-IMP showed a higher selectivity to methane than 10Ru/CNT-DMP. A higher selectivity to heavier hydrocarbons was observed for 10Ru/CNT-DMP than 10Ru/CNT-IMP (Table 5.7). This was different from what Kang et al. (2010) observed when they carried out FTS at 260 °C over a Ru/CNT catalyst. Kang et al. found that for Ru/CNT catalysts with mean sizes ranging from 2.3 to 10.2 nm, the particles with a size of 7 nm were optimum, giving the highest selectivity to $C_{10} - C_{20.}$ However Kang et al. (2010) FTS conditions were different from ours (260 °C and 20 bar). In this study the catalyst with mean particle size of 2.4 nm was the one which showed higher selectivity to heavier hydrocarbons than the catalyst which had a mean Ru particle size of 5.4 nm at 220 °C. However when the reaction was carried out at 250 °C there were no significant differences in the selectivity of the two catalysts (table 5.7). This is in agreement with the observations of Carballo et al.

(2011) when they carried out FTS at 250°C and 5.5 bar. Carballo et al. (2011) reported that selectivity in FTS was not greatly influenced by the Ru size for a series of Ru/Al_2O_3 catalysts of Ru particle size in the range 2.9 nm to 23 nm.

Olefin to paraffin ratio: The DPM method gave a higher olefin to paraffin ratio for most hydrocarbon numbers when compared to the IMP catalyst (Table 5.8, Figure 5.23).

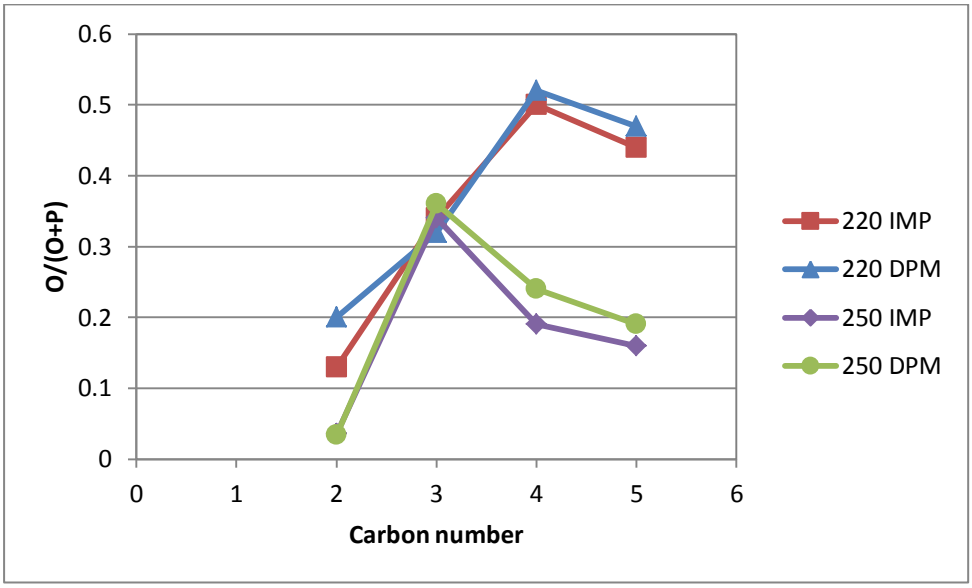


Figure 5.23: Olefin to paraffin ratio

5.4.3 Analysis of spent catalysts

The spent catalysts were analysed by TEM after 120 hours on stream. From the TEM images the catalyst particles had hardly sintered over the period of synthesis (Figure 5.25, Table 5.7). Kang et al. (2010) also made a similar observation for a Ru/CNT catalyst used in FTS after a synthesis period of 10 hours. The observed deactivation when FTS was carried out at 220 ˚C can be attributed to blocking of some of the active sites by wax formation. TGA analysis of the spent 10Ru/CNT-IMP catalysts for reaction temperatures 220 ˚C and 250 ˚C carried out at. The TGA profiles show three mass loss regimes (i) ~270 ˚C (ii) 350 ˚C(iii) at 500 ˚C. The weight loss observed at ~ 500 ˚C was due to the gasification of CNTs as indicated earlier. The two peaks at ~270 ˚C and 350 ˚C can be attributed to evaporation of waxes and

oil trapped within the catalyst. The peak at ~270 ˚C is more pronounced for the spent catalyst for the reaction carried out at 220 ˚C because it contained more waxes than the spent catalyst for FTS reaction temperature at 250 ˚C.

Table 5.7: Ru particle size of spent catalysts

Catalyst	**IMP 220**	**DPM 220**	**IMP 250**	**DPM 250**
Fresh catalyst (nm)	5.3	2.4	5.3	2.4
Spent catalyst (nm)	4.7	3.9	6.0	3.8

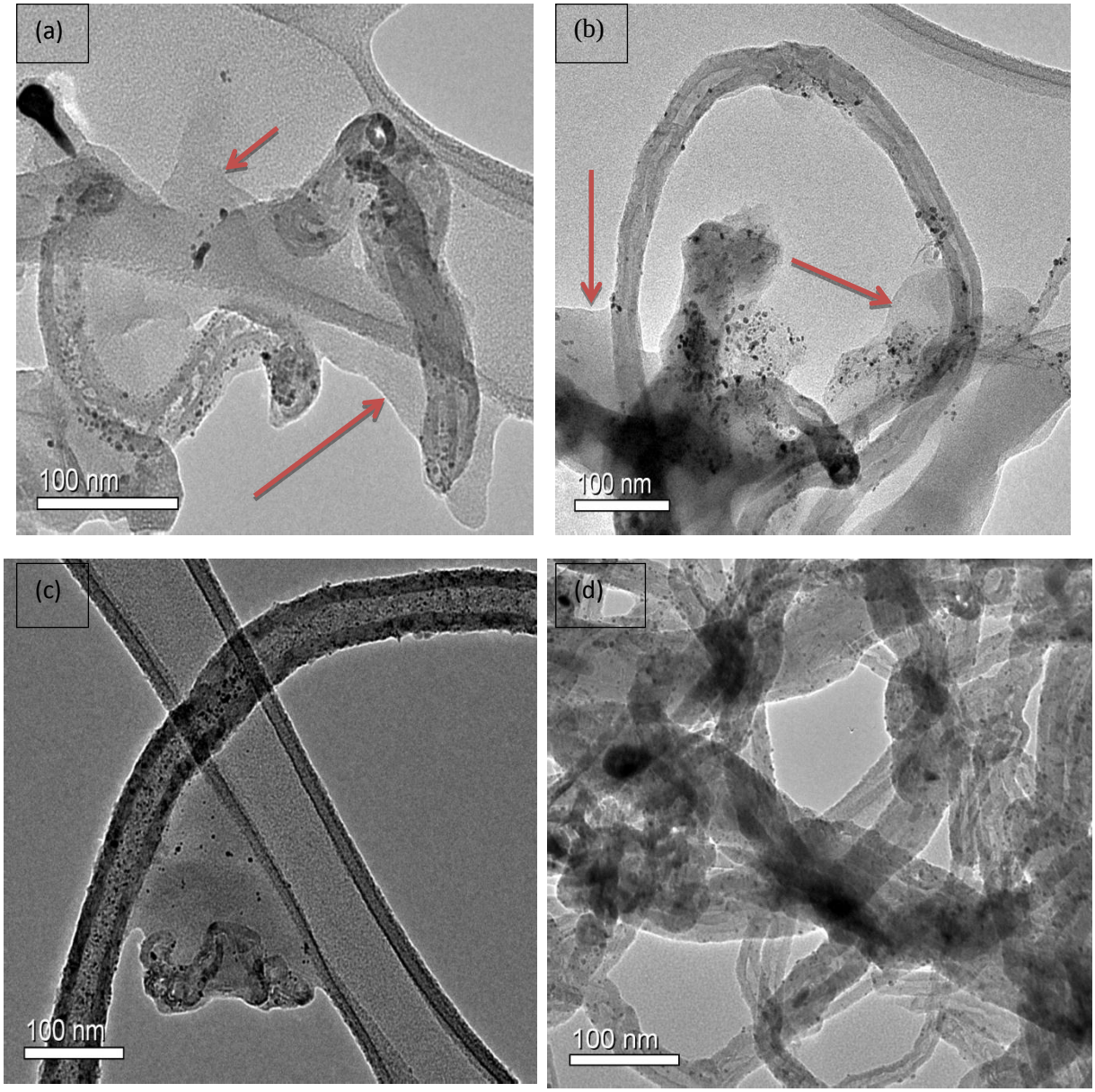


Figure 5.24: Spent catalysts after FTS at 200 ˚C; a- 10Ru/CNTR6-DPM; b- 10Ru/CNTR6-IMP and at 250; c- 10Ru/CNTR6-DPM; d- 10Ru/CNTR6-IMP. The arrows indicate wax present in the analysed samples.

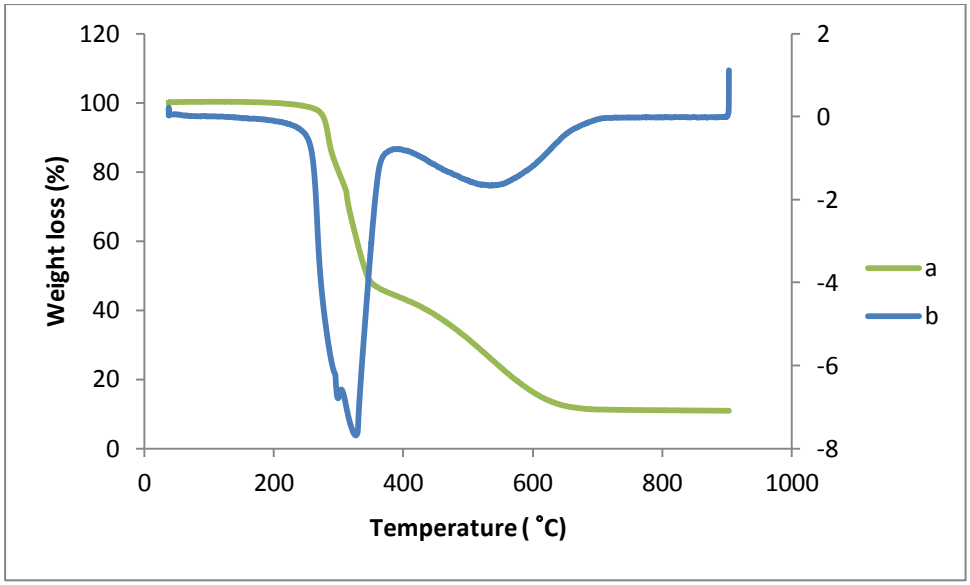


Figure 5.25: TGA profile of (a) spent 10Ru/CNTs-DPM for FTS carried out at 250 ˚C and its derivative (b)

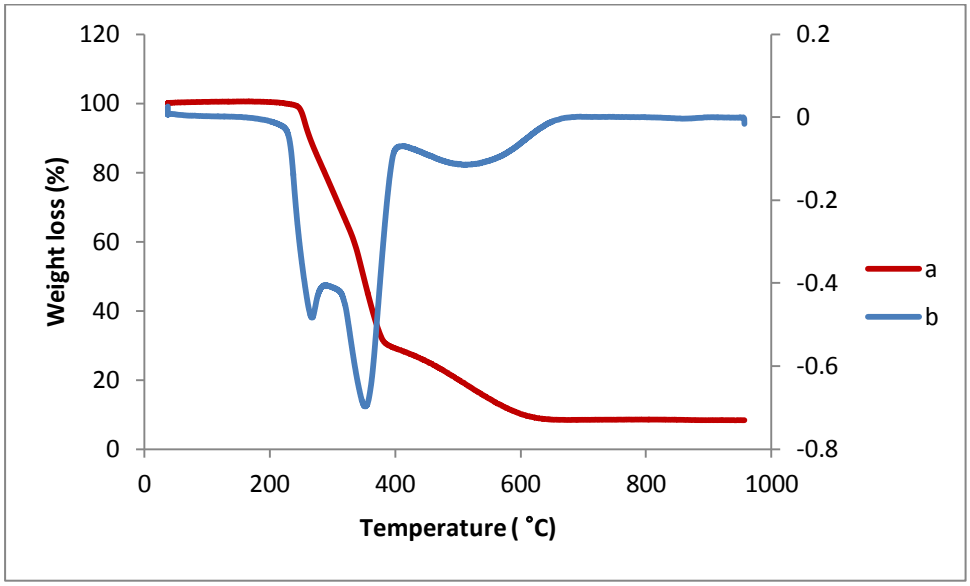


Figure 5.26: TGA profile of (a) spent 10Ru/CNTs-DPM for FTS carried out at 220 ˚C and its derivative (b)

5.5 Conclusion

The temperature, at which FTS was carried out, as expected, had a great influence on the activity and selectivity of the Ru catalysts. Results observed for classical FTS experiments. Thus, selectivity to hydrocarbon with higher carbon numbers was realised at lower temperature and higher selectivity to methane was observed at a higher FTS temperature. A higher fraction of olefin was observed at lower temperature than at higher temperature as expected for all FTS catalysts.

The preparation method did not have great influence on activity and selectivity during FTS though it did have an influence on the particle size and dispersion of the Ru particle.

CHAPTER 6

6 CONCLUSIONS AND RECOMMENDATIONS

6.1 Conclusion

Fe-Co/$CaCO_3$ catalysts were prepared by an incipient wetness impregnation from $Co(NO_3)_2.6H_2O$ and $Fe(NO_3)_3.9H_2O$ precursor salts and analysed mainly by in situ XRD. The major conclusion reached was that the $CaCO_3$ support reacted with the iron and cobalt present in all three catalysts (10% Fe/$CaCO_3$, 10% Co/$CaCO_3$ and 10%Fe-Co/$CaCO_3$) to give a brownmillerite structure with a general formula $Ca_2M_2O_5$ (M= Fe, Co. Fe+Co). When the bimetallic catalyst is reduced an FeCo alloy form which is the active phase in the synthesis of CNTs. It was also concluded that the bimetallic catalyst is easier to reduce than the mono-metallic catalyst which is one of the reasons why it is a better catalyst for CNTs synthesis.

The 10% Fe-Co/$CaCO_3$ catalyst was then used to make multi walled carbon nanotubes (MWCNTs) which were used as a catalyst support for Ru catalysts. A 10% Ru/MWCNT catalyst was synthesised by two methods; (incipient wetness impregnation and deposition precipitation using urea as the deposition agent). These catalysts were characterised by various techniques such as TGA, TPR and TEM. These catalysts were then tested for Fischer Tropsch synthesis.

TEM revealed that the DPM catalyst gave better dispersion with smaller Ru particle sizes. A DPM catalyst was easier to reduce when compared to the IMP catalyst though they were both reduced below 200 ˚C. Ru particles made by IMP were big enough to fill pores of MWCNTs thereby reducing MWCNTs surface area whereas Ru particles did not cause blockage of pores because of their small size. The surface area of the IMP catalyst is 64 m^2/g and that of the DPM catalyst was 92 m^2/g. Ru/ MWCNTs could be totally reduced under an inert atmosphere by the carbon support. Reaction temperature had an influence on the activity and selectivity of the catalysts. Higher reaction temperature results in higher activity. At 250 ˚C the average CO conversion was 30% whereas at 220 ˚C it was 15%. Selectivity to methane increased with increase in reaction temperature. Selectivity to methane was an average 13% at 220 ˚C and this increased to 29 % at 250 ˚C. A higher olefin

fraction was observed at a low reaction temperature. The preparation method had a great influence on the Ru particle size. The average particle size in DPM catalyst was 2.4 nm whilst in the IMP catalyst it was 5.3 nm. However no major influence on activity and selectivity was observed for the two catalysts (Ru/ MWCNT) prepared using the two different methods.

6.2 Recommendations

It is recommended that the actual synthesis of MWCNTs using acetylene be carried out under in situ XRD conditions and the actual active phase be identified and quantified by Rietveld refinement.

For the Ru/MWCNTs further work should be carried out on the effect of particle size. In this work the effect was studied on catalysts with only 2 mean particle sizes. The size range may be extended to get a meaningful trend. Further study on the causes of the deactivation on the Ru catalyst when synthesis is carried out at lower reaction temperature (220 °C) should also be carried out.

REFERENCES

Abbaslou, R.M., Soltan, J., & Dalai, A.K. 2010, "Effects of nanotubes pore size on the catalytic performances of iron catalysts supported on carbon nanotubes for Fischer–Tropsch synthesis" *Applied Catalysis A*, vol. 379, pp. 129-134

Abbaslou, R.M., Tavassoli, A., Soltan, J., & Dalai, A.K. 2009, "Iron catalysts supported on carbon nanotubes for Fischer–Tropsch synthesis: Effect of catalytic site position" *Applied Catalysis A: General,* vol. 367, pp. 47-52

Ajayan, P.M., Ebbesen, T.W., Ichihashi, T., Iijima, S., Tanigaki, K. & Hiura,H. 1993, "Opening carbon nanotubes with oxygen and implications for filling", *Nature,* vol. 362, pp. 522-525.

Ajayan, P.M., "Nanotubes from carbon", 1999, *Chemical Reviews,* vol. 99, pp. 1787-1799

Allcock, H.R. 2008, "Introduction to Materials Chemistry", *John Wiley & Sons*,

Amara, H., Bichara, C., & Ducastelle, F., 2008 "Understanding the Nucleation Mechanisms of Carbon Nanotubes in Catalytic Chemical Vapor Deposition" accessed 9 February 2012 http://arxiv.org/pdf/0712.0748.pdf

Ando, Y., Zhao, X., Sugai, T. & Kumar M. 2004, "Growing carbon nanotubes", *Materials Today,* pp.22–29.

Anton Paar XRK 900 User Manual, Anton Paar GmbH 2005

Atthipalli G., Epur, R., Kumta P.N., Allen B.L. Tang Y., Star A. & Gray J.L., 2011, "The effect of temperature on the growth of carbon nanotubes on copper foil using a nickel thin film as catalyst", *Thin Solid Films,* vol. 519, pp. 5371–5375

Avile´s, F., Cauich-Rodrı´guez, J.V., Moo-Tah, L., May-Pat, A., Vargas-Coronado, R. 2009, "Evaluation of mild acid oxidation treatments for MWCNT functionalization", *Carbon,* vol. 47 pp. 2970–2975

Avouris, P. 2002, "Molecular Electronics with Carbon Nanotubes", *Accounts Of Chemical Research,* vol.35, no. 12, pp. 1026–1034

Bai W., Li D., Wang Y. & Liang J. 2005, "Effects of Temperature and Catalyst Concentration on the Growth of Aligned Carbon Nanotubes", *Tsinghua Science and Technology*, vol. 10 no.6, pp. 729-735

Bahome, M.C., Jewell, L.L., Hildebrandt, D., Glasser, D. & Coville, N.J. 2005, "Fischer–Tropsch synthesis over iron catalysts supported on carbon nanotubes", *Applied Catalysis A: General,* vol. 287, pp. 60–67

Bahome, M.C., Jewell, L.L., Padayachy, K., Hildebrandt, D., Glasser, D., Datye, A.K., D. & Coville, N.J. 2007, "Fe-Ru small particle bimetallic catalysts supported on carbon nanotubes for use in Fischer–Tropsch synthesis", *Applied Catalysis A: General,* vol. 328 pp. 243–251

Bartholomew, C.H. 1991, "L. Guczi (Ed.), New Trends in CO Activation", *Elsevier, Amsterdam,* pp.225

BasicsofXRD.ppt accessed 07/11/12
www.xray.cz/xray/csca/kol2011/kurs/Dalsi.../Basics-of-XRD.ppt

Bayliss., P. 1990, "Revised unit-cell dimensions, space group, and chemical formula of some metallic minerals", *Canadian Mineralogist,* vol. 28, pp. 751-755

Berastegui, P., Eriksson, S.G. & Hull, S. 1999, "A Neutron Diffraction Study of the Temperature Dependence of $Ca_2Fe_2O_5$", *Material Research Bulletin*, vol. 34, no. 2, pp. 303–314

Bernholc, J., Roland, C., & Yakobson, B.I. 1997, "Nanotubes" *Solid State Material Science,* vol.6, pp.706-715

Bodnar Research 2012. Unit cell pictures, Accessed 15/06/2012 http://chemed.chem.purdue.edu/genchem/topicreview/bp/ch13/unitcell.php

Bom, D., Andrews, R., Jacques, D., Anthony, J., Chen, B., Meier, M.S. & Selegue, J.P. 2002 "Thermogravimetric Analysis of the Oxidation of Multiwalled Carbon Nanotubes: Evidence for the Role of Defect Sites in Carbon Nanotube Chemistry", Nano Letters, vol. 2, no. 6, pp. 615-619

Bonard, J.M., Stora, T.S., Salvetat, J.P., Maier, F., Stöckli, T. & Duschl, C. 1997, "Purification and size-selection of carbon nanotubes", Advanced Matter, vol. 9 no.10, pp 827-831

Brunauer, S Emmett P.H & Teller, E 1938 "Adsorption of Gases in Multimolecular Layers", Journal *of American Chemical Society,* vol. 60, pp. 309-319;

Bulavchenko, O.A., Cherepanova, S.V., Malakhov, V.V., Dovlitova, L.S., Ishchenko, A.V. & Ishchenko, S.V.X. 2009, "In situ xrd study of nanocrystalline cobalt oxide reduction", *Kinetics and Catalysis*, Vol. 50, no. 2, pp. 192–198.

Carballo, J.M.G., Yang, J., Holmen, A., García-Rodríguez, S., Rojas, S., Ojeda, M. & Fierro, J.L.G. 2011, "Catalytic effects of ruthenium particle size on the Fischer–Tropsch Synthesis", *Journal of Catalysis,* vol. 284, pp. 102–108

Carlo, A., Pecchia, A., E. Petrolati, E., & Paoloni, C. 2006. "Modelling of carbon nanotube-based device from nanoFETs THz emitters", Nanomodelling II, SPIE vol 6328, pp. 632808–632811.

Cano, L.A., Cagnoli, M.V., Fellenz, N.A., Bengoa, J.F., Gallegos, N.G., Alvarez, A.M., Marchetti, S.G. 2010, "Fischer-Tropsch synthesis. Influence of the crystal size of iron active species on the activity and selectivity", *Applied Catalysis A: General,* vol. 379, pp. 105–110

Cernohorsky, M. 1960, “The ratio method for absulute measurements of lattice parameters with cylindrical cameras” *Acta Crystallographica*, vol. 13, pp. 826-823

Chen, W., Fan, Z., Pan, X., & Bao, X. 2008, “Effect of Confinement in Carbon Nanotubes on the Activity of Fischer-Tropsch Iron Catalyst”, *Journal of American Chemistry Society*, vol 130, pp. 9414–9419

Che, G., Lakshmi, B.B., Martin, C.R. & Fisher, E.R. 1998, “Chemical vapor deposition based synthesis of carbon nanotubes and nanofibers using a template method”, *Chemical Materials,* vol. 10, pp. 260-267

Chen, W., Fan, Z., Pan, X., & Bao, X. 2007, “Tuning of Redox Properties of Iron and Iron Oxides via Encapsulation within Carbon Nanotubes”, *Journal of American Chemistry Society*, vol 129, pp. 7421-7426

Cheng, J., Zhang, X., Luo, Z., Liua, F., Ye, Y., Yin, W., Liu, w & Hanc, Y. 2006, “Carbon nanotube synthesis and parametric study using $CaCO_3$ nano crystals as catalyst support by CVD” *Materials Chemistry and Physics* vol.95 pp. 5–11

Chung. H 1974, “Quantitative Interpretation of X-ray Diffraction Patterns of Mixtures. I. Matrix-Flushing Method for Quantitative Multicomponent Analysis”, *Journal of Applied Crystallography,* vol. 7 pp. 519-525

Claeys, M., & van Steen E. 2002, “On the effect of water during Fischer–Tropsch synthesis with a ruthenium catalyst”, *Catalysis Today,* vol. 71, pp. 419–427

Clearfield, A., Reibenspies, J. & Bhuvanesh N. 2008, “Principles and Application of Powder Diffraction”, *Wiley publications*, chapter 1 pp.

Coelho, A.A. 2007. TOPAS v4.2: General Profile and Structure Analysis Software for Powder Diffraction Data, Bruker AXS, Karlsruhe

Couteau, E., Hernardi, K., Seo, J.W., Thieˆn-Nga, L., Miko, C.S. & Gaal R. 2003, "CVD synthesis of high purity multi-walled carbon nanotubes using $CaCO_3$ catalyst support for large-scale production", *Chemical Physics Letters*, vol.378, pp.9–17.

Cornils, B, Heermann, W.A, Schlogl, R. & Wong C.H. 2000, "Catalysis from A-Z, A concise encyclopedia", *Wiley-VCH,Weinhem*

Coville, N.J., Mhlanga, S.D., Nxumalo, E.N., Shaikjee, A. 2011, "A review of shaped carbon nanomaterials", *South African Journal of Science,* vol. 107, (3/4) pp. 1-15

Dancuart, L.P., & Steynberg, Ap. 2007, "Fischer-Tropsch based GTL Technology: a New Process." pp. 379-399

Das, T.K, Jacobs, G., Patterson, P.M., Conner, W.A., Li, J. & Davis, B.H. 2003, "Fischer–Tropsch synthesis: characterization and catalytic properties of rhenium promoted cobalt alumina catalysts", *Fuel*, vol. 82, pp. 805–815

Deck, C.P, & Vecchio, K. 2005, "Growth mechanism of vapor phase CVD-grown multi-walled carbon nanotubes", *Carbon*, vol. 43, pp. 2608–2617

De La Puente, F.D. & Nierengarten, J.F., 2012 "Fullerenes: Principles and Applications", *Royal society of chemistry publishing*, 2nd Edition, Chapter 15

Delmon, B. & Froment, G.F., 1980, "Catalyst deactivation", *Elsevier,*

Dinnerbier, R.E. & Billinge, S.J.L., 2008, "Powder Diffraction Theory and Practice" *Royal Society of Chemistry Publishing*.

Dry, M.E. 2008 in G. Ertl, H. Knozinger, F. Schuth and J. Weitkamp (Eds.), Handbook of Heterogeneous Catalysis*, Wiley-CVH-Weinheim*, p. 2965.

Ducati, C., Alexandrou, I., Chhowalla, M., Robertson, J., & Amaratunga, G.A.J., 2004. “The role of the catalytic particle in the growth of carbon nanotubes by plasma enhanced chemical vapour deposition, *Journal of Applied Physics,* vol. 95, no. 11, pp. 6387–91.

Duclaux, L. 2002, “Review of the doping of carbon nanotubes (multiwalled and single-walled)”, *Carbon,* vol. 40 pp.1751–1764

Ducreux, O., Rebours, B., Lynch, J., Roy-Auberger, M. & Bazin, D. 2009, “Microstructure of Supported Cobalt Fischer-Tropsch Catalysts”, *Oil & Gas Science and Technology – Review. IFP,* Vol. 64, No. 1 pp. 49-62

Duvenhage, D.J. 1994, “The prepapration, Characterization and Evaluation of Titania Supported Fe:Co Bimetallic Catalysts for the Hydrogenation of CO”, PhD Thesis, University of the Witwatersrand, Johannesburg,

Eilers, J., Posthuma, S.A., & Sie, S.T. 1990, *Catalysis Letters* vol. 7, pp. 253

Emmenegger, C., Bonard, J.M., Mauron, P., Sudan, P., Lepora, A., Grobety, B., Zu¨ttel, A., & Schlapbach, L. 2003, “Synthesis of carbon nanotubes over Fe catalyst on aluminium and suggested growth mechanism”, *Carbon,* vol. 41, pp. 539–547

Enache, D.I., Rebours, B., Roy-Auberger, M. & Revel, R. 2002, “In Situ XRD Study of the Influence of Thermal Treatment on the Characteristics and the Catalytic Properties of Cobalt-Based Fischer–Tropsch Catalysts” *Journal of Catalysis*, vol. 205 pp. 346–353

Endo, M., Hayashi, T. & Kim, Y.A. 2006, “Large-scale production of carbon nanotubes and their applications”, *Pure Apllied Chemistry*, vol.78 no. 9 pp. 1703-1713

Fujimoto, K., Nobusawa, T., Fukushima, T. & Tominaga, H. 1985, “ Activity and selectivity regulation of synthesis gas reaction over supported ruthenium catalysts”, *The Chemical Society of Japan*, vol. 58, pp. 3164-3171

Forbes. R.P. 2011. “The in situ synthesis and thermoresponsive behaviour of selected metal phosphates and metal organic frameworks”, PhD Thesis, University of the witwatersrand

Font Freidea, J.J.H.M., Collinsb, J.P., Naya, B. & Sharp, C. 2007, “A history of the BP Fischer-Tropsch catalyst from laboratory to full scale demonstration in Alaska and beyond”, Fischer-Tropsch Synthesis, Catalysts and Catalysis

Ganguly, R., Siruguri, V., Gopalakrishnan, I.K. & Yakhmi, J.V. 2000, “Stability of the layered Sr3 Ti2 O7 structure in La1.2 (Sr1-x Cax)1.8 Mn2 O7” *Journal of Physics Condensed Matter,* vol.12, pp. 1683-1689

Gaube, J. & Klein, H.F. 2010, “Further support for the two-mechanisms hypothesis of Fischer–Tropsch synthesis”, *Applied Catalysis A: General,* vol. 374, pp. 120–125

Gaube, J. & Klein, H.F. 2008, “The promoter effect of alkali in Fischer-Tropsch iron and cobalt catalysts”, *Applied Catalysis A: General,* vol. 350 pp.126–132

Garcı´a-Garcı´a, F.R., A´ lvarez-Rodrı´guez, J. Rodrı´guez-Ramos,I. & Guerrero-Ruiz, A. 2010, “The use of carbon nanotubes with and without nitrogen doping as support for ruthenium catalysts in the ammonia decomposition reaction”, *Carbon,* vol. 48. p.p. 267 –276

Gibb, T.C. & Matsuo, M. 1990 “A study of the Oxygen-deficient perovskite system $Sr_2Fe_{2-x}Cr_xO_{5+y}$ by Mossbauer spectroscopy”, *Journal of Solid State Chemistry,* vol. 86, pp. 164-174

Gohier, A., Ewels, C.P, Minea, T.M. & Djouadi, M.A. 2008, “Carbon nanotube growth mechanism switches from tip- to base-growth with decreasing catalyst particle size” *Carbon,* vol. 46, pp. 1331 –1338

Govender, N.S., de Croon M.H.J.M. & Schouten, J.C. 2010, "Reactivity of surface carbonaceous intermediates on an iron-based Fischer–Tropsch catalyst" *Applied Catalysis A: General,* vol. 373, pp. 81–89

Guerrero-Ruiz, A., & Rodriguez-Ramos, I. 2005, J.A. Anderson and M.F. Garcia (Eds.), Supported Metals in Catalysis*, Imperial College Press*, London p. 155.

Guo, T., Nikolaev, P., Thess, A., Colbert, D.T. & Smalley, R.E. 1995, "Catalytic growth of single-walled nanotubes by laser vaporization", *Chemical Physics Letters,* vol. 243 pp. 49-54

Guo, T., Nikolaev, P., Rinzler, A.G, TomBnek, D.T., Colbert, D.T., & Smalley, R.E. 1995, "Self-Assembly of Tubular Fullerenes", *Journal of Physical Chemistry,* vol. 99, pp. 10694-10697

Hammond, C. "The Basics of Crystallography and Diffraction", *International Union of Crystallography*, 2nd Edition

Hata, K., Futaba, D.N., Mizuno, K., Namai, T., Yumura, M. & Iijima, S., 2004 "Water-Assisted Highly Efficient Synthesis of Impurity-Free Single-Walled Carbon Nanotubes" *Science,* vol 306, pp. 1362-1364

Hayek, K., Kramer, R & Pafil, Z. 1997, "Metal-support boundary sites in catalysis", *Applied Catalysis A: General*, vol. 162, pp. 1-15

Henrici-Olive, G. & Olive, S. 1976, "The Fischer-Tropsch Synthesis: Molecular Weight Distribution of Primary Products and Reaction Mechanism", *Angewandte Chemie International English Edition in English,* vol. 15, no.3, pp. 136-141

Hernadi, K., Fonseca, A., Piedigrosso, P., Delvaux, M., Nagy, J.B., Bernaerts, D., & Riga, J. 1997, "Carbon nanotubes production over Co/silica catalysts", *Catalysis Letters*, vol. 48, pp. 229-238

Hexana, W.M. & Coville, N.J. 2010, “Indium as a chemical promoter in Fe-based Fischer-Tropsch synthesis”, *Applied Catalysis A: General,* vol. 377, pp. 150–157

HighScore accessed 25/05/2012
http://www.panalytical.com/index.cfm?pid=544

Hill, R.J. & Howard, C.J. 1987, “Quantitative Phase Analysis from Neutron Powder Diffraction Data Using the Rietveld Method” Journal of Applied Crystallography vol. 20 pp. 467-474

Hone, J., Whitney, M. & Zettl, A. 1999," Thermal conductivity of single-walled carbon nanotubes", *Synthetic Metal,* vol. 103, no. 1-3, pp. 2498-2499

Hou, P., Liu, C., Tong, Y., Xu, S., Liu, M. & Cheng H., 2001 “Purification of single-walled carbon nanotubes synthesized by the hydrogen arc-discharge method”, *Journal of Materials Research,* Vol. 16, No. 9, p.p. 2526-2529

Hou, P-X., Liu, C. & Cheng, H-M. 2008, “Purification of carbon nanotubes”, *Carbon,* vol. 46, pp. 2003-2005

Hsieh, C-T., Lin, Y-T., Lin, J-Y. & Wei, J-L. 2009, “Synthesis of carbon nanotubes over Ni- and Co-supported CaCO3 catalysts using catalytic chemical vapor deposition”, *Materials Chemistry and Physics,* vol. 114, pp. 702–708

http://www.owlnet.rice.edu/~rv4/Ajayan/book_springer.pdf accessed 6/11/2012

http://pruffle.mit.edu/atomiccontrol/education/xray/xray_diff.php accessed 23 April 2012

Match!
http://www.crystalimpact.com/ accessed 23 April for Match! software

Huijbregts., W.M.M. & Snel A. 1972, “The protection effectiveness of magnetite layers in relation to boiler corrosion”, *5 th International Congress on Metallic Corrosion Tokio*,

ICDD, The International Center for Diffraction Data, accessed: 21/05/2012, http://www.icdd.com

Iglesia, E., Soled, S.L. & Fiato, R.A. 1992, "Fischer-Tropsch synthesis on cobalt and ruthenium; metal dispersion and support effects on reaction rate and selectivity", *Journal of Catalysis*, vol. 137, pp. 212-224

Iijima, S. 1991, "Helical microtubules of graphitic carbon", *Nature,* vol.354, pp.56-58

Introduction to X-ray Diffraction (XRD) Learning Activity accessed www.asdlib.org/...XRD/LearningActivity_Crystallography.pdf

Jacobs, G., Das, T.K, Zhang, Y., Li, J., Racoillet, G. & Davis, B.H. 2002, "Fischer–Tropsch synthesis: support, loading, and promoter effects on the reducibility of cobalt catalysts" *Applied Catalysis A: General*, vol. 233, pp.263–281

Jacobs, G., Zhang, Y., Das, T.K., Li, J., Patterson, P.M. &. Davis B.H. 2001, "Deactivation of a Ru promoted co/al_2o_3 catalyst for FT Synthesis", *Studies in Surface Science and Catalysis*, vol. 139, pp. 415–422

Jay, A.H. & Andrews, K.W. 1946, "Note on oxide systems pertaining to steel - making furnace slags: FeO-MnO, FeO-MgO, CaO-MnO, MgO-MnO", *Journal of the Iron and Steel Institute London*, vol. 152, pp. 15-18

Robertson. R. 2004, "Realistic applications of CNTs", *Materials today*, http://dx.doi.org/10.1016/S1369-7021(04)00448-1 accessed 09 Feb 2012

Journet, C., Maser, W.K., Bernier, P., Loiseau, A., Lamyde la Chapelle, M., Lefrant, S., Deniard, P., Leek, R. & Fischerk, J.E. 1997, "Large-scale production of single-walled carbon nanotubes by the electric-arc technique", *Nature*, vol. 388 pp.

Kang, J., Zhang, S., Zhang. & Wang, Y., Q., 2009, "Ruthenium nanoparticles supported on carbon nanotubes as efficient catalysts for selective conversion of synthesis gas to diesel Fuel", *Angewandte Chemie International,* vol.48, pp. 2565 –2568

ICSD
Karlsruhe; 2012 ICSD, International Crystal Structure Database accessed 25/05/2012
http://icsd.fiz-karlsruhe.de/

Karlsruhe. 2010, DIFFRAC.EVA: The Next Era in Phase Analysis, Bruker AXS

Kathyayini, H., Nagaraju, N., Fonseca, A. & Nagy, J.B. 2004, "Catalytic activity of Fe, Co and Fe/Co supported on Ca and Mg oxides, hydroxides and carbonates in the synthesis of carbon nanotubes", *Journal of Molecular Catalysis A: Chemical,* vol. 223 pp. 129–136

Keszler, A.M., Nemes, L., Ahmad, S.R. & Fang, A. 2004 "characterisation of carbon nanotube materials by raman spectroscopy and microscopy– a case study of multi walled and single walled samples", *Journal of Optoelectronics and Advanced Materials,* Vol. 6, No. 4, pp. 1269 - 1274

Kikuchi, E., Matsumoto, M., Takahashi, T., Machino, A. & Morita, Y. 1984 "Fischer-Tropsch synthesis over titania-supported ruthenium catalysts", *Applied Catalysis*, vol. 10 pp. 251-260

Kim, B., & Sigmund, W. 2004, "Functionalized Multiwall Carbon Nanotube/Gold Nanoparticle Composites", *Langmuir,* vol. 20 pp. 8239-8242

Kim, P., Shi, L., Majumdar, A., & McEuen, P.L, 2001, "Thermal Transport Measurements of Individual Multiwalled Nanotubes", *Physical Review Letters,* vol 87, no. 21, pp. 215502-215502

Konya, Z., Janos Kiss, J., Oszko, A., Siska, A. & Kiricsi, I. 2001, "XPS characterisation of catalysts during production of multi walled carbon nanotubes", *Physical Chemistry Chemical Physics*, vol.3, pp.155-158

Kumar, M., & Ando, Y. 2010, “Chemical Vapor Deposition of Carbon Nanotubes: A Review on Growth Mechanism and Mass Production”, *Journal of Nano science and Nanotechnology,* vol. 10, pp. 3739–3758

Klug H & Elexandra, L.E. 1974 “X-ray Diffraction Procedures for Polycrystalline and Amorphous Materials”, *John Wiley*

Langford. J.I. & Wilson. A.J.C. 1978, “Seherrer after Sixty Years: A Survey and Some New Results in the Determination of Crystallite Size”, *Journal of Applied Crystallography*, vol. 11, pp. 102-113

Lee, C.J., Park, J., Huh, Y. & Lee, JY. 2001, “Temperature effect on the growth of CNTs using thermal chemical Vapour Deposition”, *Chemical Physics Letters,* vol. 343, pp. 33-38

Lei, W., Zhang, X., Chen, J., Zhao, Z., Cui, Y. & Wang, B. 2011 “Very High Field Emission from a Carbon Nanotube Array With Isolated Sub regions and Balanced Resistances” *, Ieee Transactions On Electron Devices,* vol. 58, no. 10, pp.3616-3621

Li, Y., Zhang, X., Luo, J., Huang, W., Cheng, J., Luo, Z., Li, T., Liu, F., Xu, G., Ke, X., Lin, L. & Geise, H.J. 2004, "Purification of CVD synthesized single-wall carbon nanotubes by different acid oxidation treatments", *Nanotechnology*, vol. 15, no. 11, pp. 1645-1649

Li, J., Jacobs, G., Zhang, Y., Das, T., & Davis, B.H. 2001, “Fischer–Tropsch synthesis: effect of small amounts of boron, ruthenium and rhenium on Co/TiO2 catalysts” *Applied Catalysis A: General,* vol. 223, pp.195–203

Li, X., Yuan, G., Brown, A., Westwood A., Brydson, R., & Rand, B. 2006, “The removal of encapsulated catalyst particles from carbon nanotubes using molten salts”, Carbon vol. 44, pp. 1699-1705

Li X, Cao A, Jung YJ, Vajtai R, & Ajayan PM. 2005, "Bottom-up growth of carbon nanotube multilayers: unprecedented growth", *Nano Letters,* vol. 5 no. 10, pp. 1997–2000

Li, Z., Dervishi, E., Xu, Y., Ma, X., Saini, V., Biris, A.S., Little, R., & Lupu, D. 2008, "Effects of the Fe–Co interaction on the growth of multiwall carbon nanotubes", *The Journal of Chemical Physics,* vol. 129, pp. 074712-074715

Lin, T., Bajpai, V., Ji, T. & Dai, L. 2003, "Chemistry of Carbon Nanotubes", *Australian Journal of Chemistry*, vol. 56, no. 7, pp. 635-651

Lupu, D.M., Biris, A.R., Misan, I., Lupsa, N., Biris, A.S. & Buzatu, & D.A. 2002"Growth of nanoscale carbon structures and their corresponding hydrogen uptake properties", *Particulate Science Technology: An International Journal,* vol. 225 pp.20–34.

Mabena, L.F., Ray, S.S., Mhlanga, S.D. & Coville, N.J. 2011, "Nitrogen-doped carbon nanotubes as a metal catalyst support", *Applied Nanoscience,* vol.1, pp.67–77

Macor® http://www.astromet.com/macor.htm accessed 21/05/2012

Magrez, A., Seo, J.W., Miko, C., Hernadi, K. & Forro, L. 2005, "Growth of Carbon Nanotubes with Alkaline Earth Carbonate as Support", *Journal of Physical Chemistry*, vol. 2005, no. 109, pp. 10087-10091

Magrez, A., Seo, J.W., Kuznetsov, V.L. & Forro, L. 2007, "Evidence of an Equimolar C_2H_2–CO_2 Reaction in the Synthesis of Carbon Nanotubes", *Angewandte Chemie International Edition,* vol. 46 pp. 441–444

Magrez, A., Seo, J.W., Smajda, R., Mionić, M. & Forró, L. 2010, "Catalytic CVD Synthesis of Carbon Nanotubes: Towards High Yield and Low Temperature Growth", *Materials,* vol 3, 4871-4891; doi:10.3390/ma3114871 pp. 4871-4891

McMahon, L.M. Historical Crude Oil Prices (Table), Capital Professional Services, accesed 20/02/2011, <http://inflationdata.com/inflation/inflation_rate/historical_oil_ prices_table.asp>

McCusker, L.B., Von Dreele., R. B., Cox, D. E., Louer. D. & Scardi., P. 1999, "Rietveld refinement guidelines", *Journal of Applied Crystallography,* volume 32, pp. 36-50

McPherson, J., 2010, "An update in heterogeneous catalysis from the Catalysis Society of South Africa", *Platinum Metals Review*, vol. 54, no. 3, pp. 147–15

Merkulov, V.I., Melechko, A.V., Guillorn, M.A., Lowndes, D.H., Simpson, M.L., 2001, "Alignment mechanism of carbon nanofibers produced by plasma-enhanced chemical-vapour deposition", *Applied Physics Letters,* vol. 79 no.18 pp. 2970–2972

Mhlanga, S.D., Mondal, K.C., Carter, R., Witcomb, M.J., & Coville, N.J. 2009, "The effect of synthesis parameters on the catalytic synthesis of multi walled carbon nanotubes using fe-Co/$Caco_3$ catalysts", *South African Journal of Chemistry*, vol. 62, pp. 67–76

Motchelaho, M.A.M., Xiong, H., Moyo, M., Jewell, L.L. & N.J. Coville, 2011, "Effect of acid treatment on the surface of multiwalled carbon nanotubes prepared from Fe-Co supported on $CaCO_3$: Correlation with Fischer-Tropsch catalyst activity", *Journal of Molecular Catalysis A: Chemical,* vol.335 pp.189–198

Motchelaho, M.A.M., 2011. PhD Thesis "Iron and cobalt catalyst supported on carbon nanotubes for use in the Fischer Tropsch synthesis" University of the Witwatersrand.

Moisala, A., Nasibulin, A.G & Kauppinen, E.I. 2003, "The role of metal nanoparticles in the catalytic production of single-walled carbon nanotubes—a review", *Journal of Physics: Condensed Matter,* vol.15 pp. S3011–S3035

Morales, F., Weckhuysen, B.M., 2007, *ChemInform,* vol. 38. pp.1.

Moyo, M., Motchelaho, M.AM., Xiong, H., Jewell, L.L & Coville, N.J. 2012, "Promotion of Co/carbon sphere Fischer–Tropsch catalysts by residual K and Mn from carbon oxidation by $KMnO_4$", *Applied Catalysis A: General* vol.413– 414 pp. 223– 229

Nanotube Picture http://www.personal.reading.ac.uk/~scsharip/tubes.htm accessed 22/05/201

Naseh, M.V., Khodadadi, A.A., Mortazavi, Y., Sahraei, O.A., Pourfayaz, F.& Sedghi, S.M. 2009, "Functionalization of Carbon Nanotubes Using Nitric Acid Oxidation and DBD Plasma", *World Academy of Science, Engineering and Technology,* vol.49 pp.2009

Nessim, G.D. 2010, "Properties, synthesis, and growth mechanisms of carbon nanotubes with special focus on thermal chemical vapor deposition", *Nanoscale,* vol.2, pp. 1306–1323

Nishimura, K., Okazaki, N., Pan L. & Nakayama, Y. 2004 "In situ study of iron catalysts for carbon nanotube growth using x-ray diffraction analysis", *Japanese Journal of Applied Physics,* Vol. 43, No. 4A, pp. L 471–L 474

Okada, Y. & Tokumaru, Y. (1984) "Precise determination of lattice parameter and thermal expansion coefficient of silicon between 300 and 1500 K", *Journal of Applied Physics,* vol. 56, pp. 314-320

Okamoto A. & Shinohara H. 2005, "Control of diameter distribution of single walled carbon nanotubes using the zeolite-CCVD method at atmospheric pressure". *Carbon,* vol.43, pp.431–436.

Oosthuizen, R.S & Nyamori, V.O. 2011, "Carbon nanotubes as supports for Palladium and bimetallicc for Use in hydrogenation reactions", *Platinum Metals Reviews*, vol. 55, no.3 pp. 154–169

Pecharsky, V.K. & Zavalij, P.Y. 2009, "Fundamentals of Powder Diffraction and Structural Characterisation of Materials" *Springer*, Second edition Chapter 8.6 pp. 182-199

Pennington, W.T. 1999, "*DIAMOND* - Visual Crystal Structure Information System" *Journal of Applied Crystallography*", vol. 32, pp. 1028-1029

Perrillat, J-P., Daniel, I., Koga, K.T., Reynard, B., Cardon, H. & Crichton, W.A. 2005, "Kinetics of antigorite dehydration: A real-time X-ray diffraction study", *Earth and Planetary Science Letters* vol. 236 pp. 899– 913

Pigos, E., Penev, E.S., Ribas, M.A., Sharma, R., Yakobson, B.I., & Harutyunyan, A.R, (2011), "Carbon nanotube nucleation driven by catalyst morphology dynamics" *ACS Nano,* vol. 5, no. 12, pp. 10096–10101

Planeix, J.M., Coustel, N.J., Coq, B., Bretons, V., Kumbhar, P.S., Dutartre, R., Geneste, P., Bernier, P., & Ajayan, P.M. 1994, "Application of carbon nanotubes as supports in heterogeneous catalysis", *Journal of American Chemical Society*, vol. 116, pp. 7935-7936

Pour, A.N., Shahri, S.M.K., Bozorgzadeh, H.R., Zamani, Y., Tavasoli, A., Marvast, M.A. 2008, "Effect of Mg, La and Ca promoters on the structure and catalytic behaviour of iron-based catalysts in Fischer–Tropsch synthesis", *Applied Catalysis A: General* vol. 348, pp. 201–208

Ragaini, V., Carli, R., Bianchi C.L., Lorenzetti, D., Predieri, G., & Moggi, P. 1999, "Fischer-Tropsch synthesis on alumina-supported ruthenium catalysts: Influence of morphological factors", *Applied Catalysis A: General,* vol. 139, pp. 31-42

Ramezanipour, F., Greedan, J.E., Grosvenor, A.P., Britten, J., Cranswick, L.M.D., & Garlea, V.O., 2010, "Intralayer Cation Ordering in a Brownmillerite Superstructure: Synthesis, Crystal, and Magnetic Structures of Ca_2FeCoO_5", *Chemistry of Materials,* vol, 22. pp. 6008–6020

Rayner, M.K. 2011, PHD Thesis, "Pretreatment of TiO2-supported Fe, Co and Ru Catalysts: an in situ Powder Diffraction Study", University of the Witwatersrand.

Richter, K & Doppler, P. “An improved X-ray reactor chamber for the simultaneous structural and catalytic characterization of catalysts “, *Solid State Ionics*, vol.101-103, pp.687-695

Rietveld, H.M. 1967, “Line profiles of neutron powder-diffraction peaks for structure refinement”, *Acta Crystallographica*, vol.22 pp.151-152

Rietveld, H.M. 1969, “A Profile Refinement Method for Nuclear and Magnetic Structures”, *Journal of Applied Crystallograph*y, vol.2 pp.65-71

Reuel, R.C. & Bartholomew, C.H. 1985, “Effects of support and dispersion on the CO hydrogenation activity/selectivity properties of cobalt”, *Journal of Catalysis,* vol. 85 pp. 78-88

Rodriguez-Navarro.,C, Ruiz-Agudo., E, Luque, A., Rodriguez-Navarro., A.B & Ortega-Huertas., M. 2009, “Thermal decomposition of calcite: Mechanisms of formation and textural evolution of CaO nanocrystals” *American Mineralogist,* vol. 94, pp. 578–593

Ruoff, R.S., Qian, D. & Liu, W.K. 2003, “Mechanical properties of carbon nanotubes: theoretical predictions and experimental measurements”, *Comptes Rendus Physique,* vol 4, pp. 993–1008

Sarsfield, B.A., Davidovich, M., Desikan, S., Fakes, M., Futernik, S., Hilden, J. L., Tan, J. S. Yin, S., Young, G., Vakkalagadda, B. & Volk, K. 2006, “Powder X-Ray Diffraction Detection Of Crystalline Phases In Amorphous Pharmaceuticals”, *JCPDS-International Centre for Diffraction Data ISSN 1097-0002,* pp. 322-327

Scherrer, P. 1918. Nachr. Ges. Wiss. Gottingen, pp. 98-100.

Schmitt, T.C., Biris, A.S., Miller, D.W., Biris, A.R., Lupu, D., Trigwell, S. & Rahman, Z.U., 2006, “Analysis of effluent gases during the CCVD growth of multi-wall carbon nanotubes from acetylene”, *Carbon,* vol. 44 pp. 2032-2038

Schulz, H. 1999, “Short history and present trends of Fischer–Tropsch synthesis”, *Applied Catalysis A: General,* vol.186, pp. 3–12

See, C.H. & Harris, A.T. 2008, “CaCO3 Supported Co-Fe Catalysts for Carbon Nanotube Synthesis in Fluidized Bed Reactors”, *AIChE Journal,* vol. 54, no. 3 pp. 657-664

Serp, P., Corrias, M., & Kalck, P. 2003, “Carbon nanotubes and nanofibers in catalysis”, *Applied Catalysis A: General,* vol. 253, pp. 337–358

Shaffer, M. S. P., Fan, X. & Windle A. H. 1998, “Dispersion and packing of carbon nanotubes”, *Carbon,* Vol. 36, No. 11, pp. 1603–1612, 1998

Sie, S.T. & Krishna, R. 1999, “Fundamentals and selection of advanced Fischer–Tropsch reactors”, *Applied Catalysis A: General,* vol. 186, pp.55–70

Simonetti, D.A., Jeppe Rass-Hansen, J., Edward L. Kunkes, E.L., Soaresac, R. & Dumesic, J.A., 2007, “Coupling of glycerol processing with Fischer–Tropsch synthesis for production of liquid fuels”, *Green Chem.,* vol. 9, pp. 1073–1083

Software Products, Gatan Inc., http://www.gatan.com/products/software/ accessed 21/05/2012

Song, I.K., Cho, Y.S., Choi, G.S., Park J.B. & Kim, D.J. 2004, “The growth mode change in carbon nanotube synthesis in plasma-enhanced chemical vapor deposition”, *Diamond Related Materials,* vol.13 no. 4-8, pp.1210–1213.

Song, I.K., Yu, W.J., Cho, Y.S., Choi, G.S., & Kim, D. 2004, “The determining factors for the growth mode of carbon nanotubes in the chemical vapour deposition process” *Nanotechnology*, vol. 15 pp. S590–S595

Speakman, S.A “Basics of XRD.ppt”, Accessed 21/05/2012
http://www.xray.cz/xray/csca/kol2011/kurs/Dalsi-cteni/CMSE-MIT/Basics-of-XRD.ppt

Statista
http://www.statista.com/statistics/810/opec-crude-oil-price-development-since-1960/
Accessed 17 September 2012

Steynberg A.P., & Dry, M.E., 2004, "Fischer-Tropsch Technology", *Elsevier, Studies in Surface Science and Catalysis,* v.152,

Styles, M.J., Riley, D.P., Madsen, I.C & Kisi E.H. 2010, "Parametric Rietveld Refinement Applied to In Situ Diffraction Studies" *34th annual condensed matter and materials meeting* http://www.aip.org.au/wagga2010/2010_18.pdf

Su, M., Zheng, B. & Liu, J. 2000, "A scalable CVD method for the synthesis of single-walled carbon nanotubes with high catalyst productivity" *Chemical Physics Letters,* vol. 322, pp. 321–326

Takeda, T., Nagata, M., Kobayashi, H., Kanno, R., Kawamoto, Y., Takano, M., Kamiyama, T., Izumi, F. & Sleight, A.W, 1998 "High-pressure synthesis, crystal structure, and metal-semiconductor transitions in the Tl2 Ru2 0(7-delta) pyrochlore" *Journal of solid state chemistry,* vol.140, pp. 182-193

Tavasoli, A. & Karimi, A. 2005, "Accelerated deactivation and activity recovery studies of ruthenium and rhenium promoted cobalt catalysts in Fischer-Tropsch synthesis", *Iran Journal of chemistry Chemical Engineering,* vol. 24, no. 4,

Tavasoli, A., Trépanier, M., Abbaslou, R.M.M., Dalai, A.K. & Abatzoglou, N., 2009, "Fischer–Tropsch synthesis on mono- and bimetallic Co and Fe catalysts supported on carbon nanotubes" *Fuel Processing Technology* vol. 90 pp. 1486–1494

Terrado, E., Tacchini, I., Benito, A.M., Maser, W.K. & Martinez, M.T. 2009, "Optimizing catalyst nanoparticle distribution to produce densely-packed carbon nanotube growth", *Carbon*, vol. 47 pp. 1989–2001

Terrones, M., Jorio, A., Endo, M., Kim, A., Hayashi, T., Terrones, H., Charlier, J.-C., Dresselhaus G., & Dresselhaus, M.S. 2004. "New direction in nano tube science", *Materials Today*, vol. 7 pp. 30–45

Tetana, Z.N., Mhlanga; S.D., Bepete, G., Krause, R.W.M. & Coville, N.J. 2012, "The synthesis of nitrogen-doped multiwalled carbon nanotubes using an Fe-Co/$CaCO_3$ catalyst", *South African Journal of Chemistry*, vol.65, pp. 39-49

Thess, A., Lee, R., Nikolaev, P., Dai, H., Petit,P., Robert, J., Xu, C., Lee, Y.H., Kim, S.G., Rinzler, A.G., Colbert, D.T., Scuseria, G.E., Tomanek, G., Fischer, J.E. & Smalley R.E. 1996, "Crystalline Ropes of Metallic Carbon Nanotubes", *Science,* vol. 273 no 26, pp. 483-487

Thompson, P., Cox, D.E & Hastings, J.B. 1987, "Rietveld Refinement of Debye-Scherrer Synchrotron X-ray Data from Al_2O_3", *Journal of Applied Crystallography,* vol. 20, pp. 79-83

Trepanier, M., Tavasoli, A., Dalai, A.K, & Abatzoglou, N. 2009 "Fischer–Tropsch synthesis over carbon nanotubes supported cobalt catalysts in a fixed bed reactor: Influence of acid treatment", *Fuel Processing Technology*, vol. 90, pp. 367–374

Trepanier, M., Tavasoli, A., Dalai, A.K, & Abatzoglou, N. 2008 "Co, Ru and K loadings effects on the activity and selectivity of carbon nanotubes supported cobalt catalyst in Fischer–Tropsch synthesis", *Applied Catalysis A: General,* vol. 353, pp. 193–202

Trojanowicz, M. 2006 "Analytical applications of carbon nanotubes: a review", *Trends in Analytical Chemistry*, Vol. 25, No. 5, pp. 480-489

Tungkamani, S Narataruksa., P. Sukkathanyawat, H Kraikul, N Nivitchanyong, S. & Sakakini., B. 2007, "The investigation of Ru based Fischer Tropsch catalyst for the production of synthetic liquid fuels derived from bio-syngas", *Ruthenium based Fischer Tropsch catalyst proceedings of European congress of Chemical Engineering (ECCE-6) Copenhagen, 16-20 September 2007*

Unit Cells pictures accessed 25/05/2012
http://chemed.chem.purdue.edu/genchem/topicreview/bp/ch13/unitcell.php

Van Steen., E. & Frans F. Prinsloo., F.F. 2002, "Comparison of preparation methods for carbon nanotubes supported iron Fischer–Tropsch catalysts", *Catalysis Today,* vol. 71 pp. 327–334

Van Wecham H. M. V. & Sendon, M. M. G., 1994, Studies in Surface Science and Catalysis*, Elsevier, Amsterdam*, Vol. 81, pp. 43

Walters, D.A., Ericson,L.M., Casavant,M.J., Liu,J., Colbert,D.T., Smith,K.A. & Smalley,R.E. 1999, "Elastic strain of freely suspended single-wall carbon nanotube ropes", *Applied Physics Letters,* vol 74, no. 25, pp. 3803-3805

Wyckoff, R. W. G., 1920 "The crystal structures of some carbonates of the calcite group", *American Journal of Science*, vol. 50, pp. 317–360

Will., G. 2006 "Powder diffraction: The rietveld Method and the Two-Stage Method" *Springer,* , Chapter 1 and 2

Xiang R, Luo G, Qian W, Zhang Q, Wang Y. & Wei, F., 2007, "Encapsulation, compensation, and substitution of catalyst particles during continuous growth of carbon nanotubes", *Advanced Materials*, vol. 19, no. 17, pp. 2360–2363

Xiong, H., Motchelaho, M.A.M., Moyo, M., Jewell, L.L. & Coville, NJ. 2010, "Correlating the preparation and performance of cobalt catalysts supported on carbon nanotubes and carbon spheres in the Fischer–Tropsch synthesis", *Journal of Catalysis,* vol 278. pp 26-40.

Xiong, H., Moyo, M., Rayner, M.K., Jewell, L.L., Billing, D.G. & Coville, N.J. 2010, "Autoreduction and catalytic performance of a cobalt fischer–tropsch synthesis catalyst supported on nitrogen-doped carbon spheres", *ChemCatChem*, vol. 2, pp. 514 – 518

Xiong, K., Li, J., Liew, K. & Zhan, X. 2010, “Preparation and characterization of stable Ru nano-particles embedded on the ordered mesoporous carbon material for applications in Fischer–Tropsch synthesis”, *Applied Catalysis A: General*, vol. 389, pp. 173–178

Yamada, T., Namai, T., Hata, K., Futaba, D.N., Mizuno, K., Fan, J., Yudasaka, M., Yumura, M. & Iijima, S. 2006, “Size-selective growth of double-walled carbon nanotube forests from engineered iron catalysts”, *Nature Nanotechnology*, vol.1, pp. 131 - 136

Yasuda, A., Kawase, N., Banhart, F., Mizutani, W., Shimizu, & Tokumoto, H. 2002, “Graphitization Mechanism during the Carbon-Nanotube Formation Based on the In-Situ HRTEM Observation”, *Journal of Physical Chemistry*, vol. 106, pp. 1849-1852

Young, R.A. 1993, “The Reitveld Method” *Oxford Science Publication*, pp. 95-96

Zaman, M., Khodadi, A. & Mortazavi, Y. 2009, “Fischer–Tropsch synthesis over cobalt dispersed on carbon nanotubes-based supports and activated carbon”, *Fuel Processing Technology*, vol. 90, pp. 1214–1219

Zdrojek, M., Gebicki, W., Jastrzebski, C., Melin, T. & Huczko., A 2004, “Studies of multiwall carbon nanotubes using Raman spectroscopy and atomic force microscopy”, *Solide State Phenomena,* vol.99 pp. 265-269

Zhang, Y. & Iijima, S. 1999, “Formation of single-wall carbon nanotubes by laser ablation of fullerenes at low temperature”, *Applied Physics Letters,* vol. 75, no. 20, pp. 3087-3089

Zhao, X., Ohkohchi, M., Wang, M., Iliima, S., Ichihashi, T., & Ando Y. 1997, “Preparation of high - grade carbon nanotubes by hydrogen arc discharge”, *Carbon*, Vol. 35, No. 6, pp. 775-781

Zhu, J., Yudasaka, M. & Iijima, S. 2003, “A catalytic chemical vapor deposition synthesis of double-walled carbon nanotubes over metal catalysts supported on a meso-porous material”, *Chemical Physics Letters,* vol. 380, pp. 496–502

APPENDICES

Appendix A

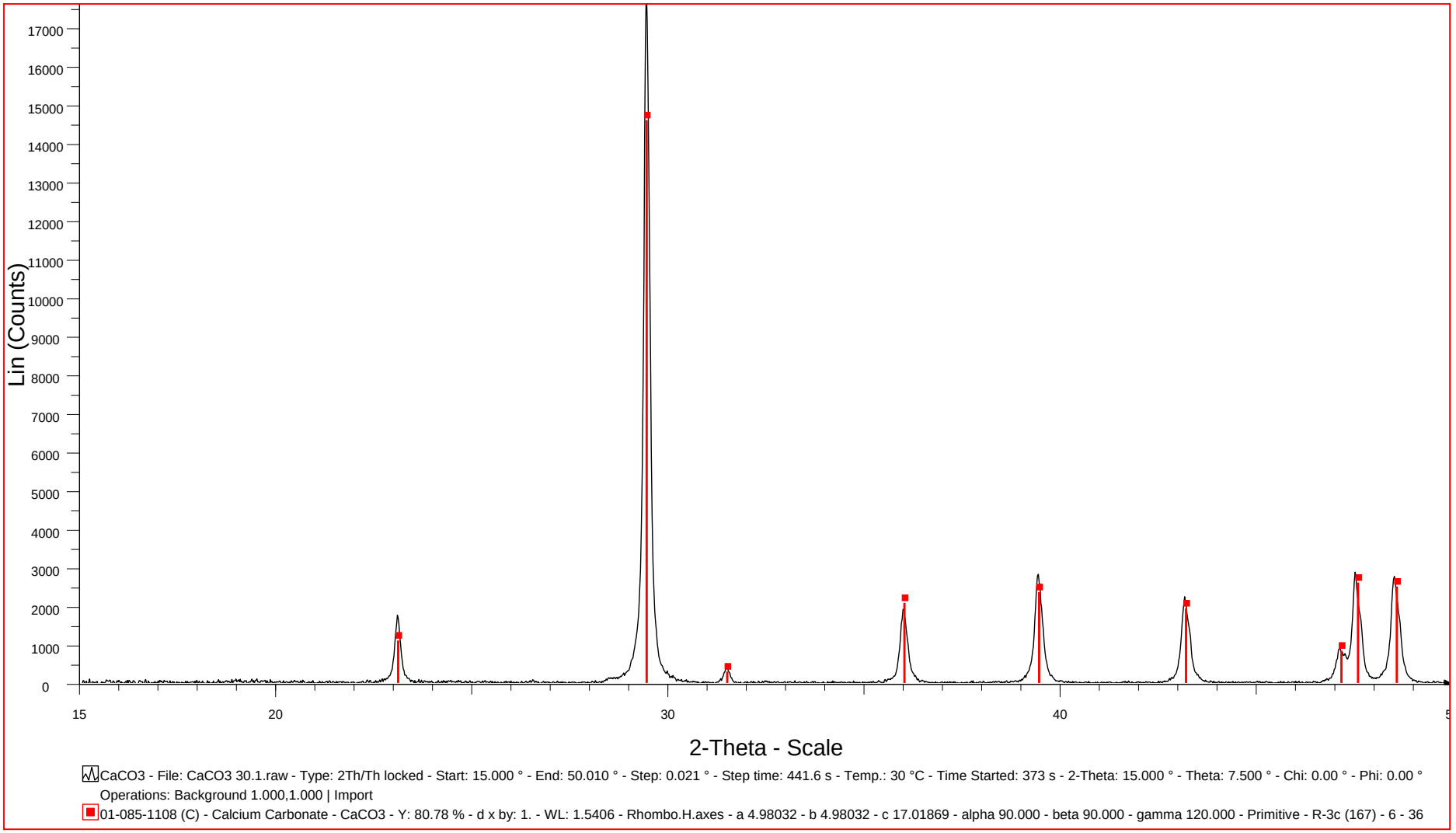


Figure A-1: XRD pattern of $CaCO_3$ at 30 ˚C

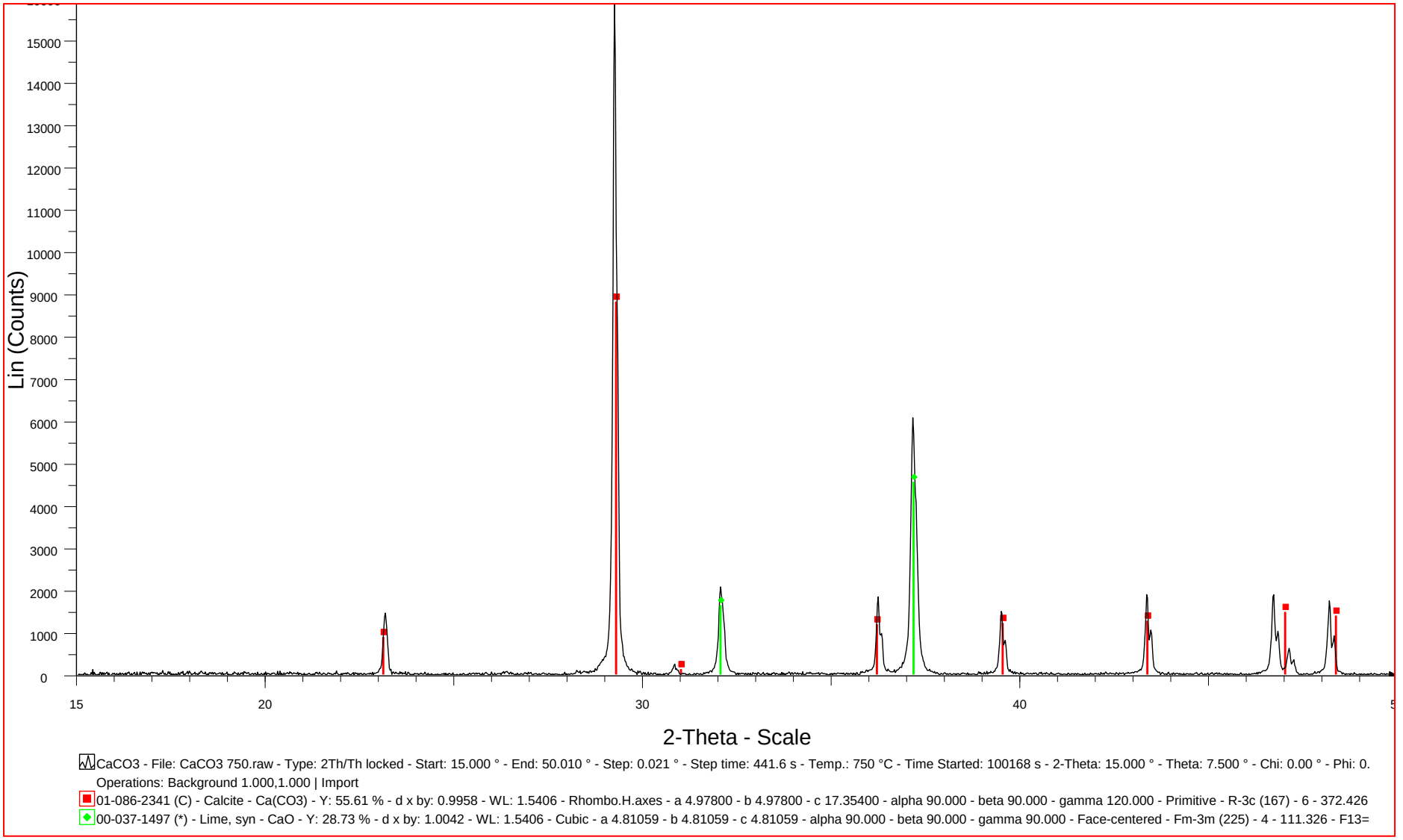


Figure A-2: XRD pattern of CaCO3 at 750 ˚C

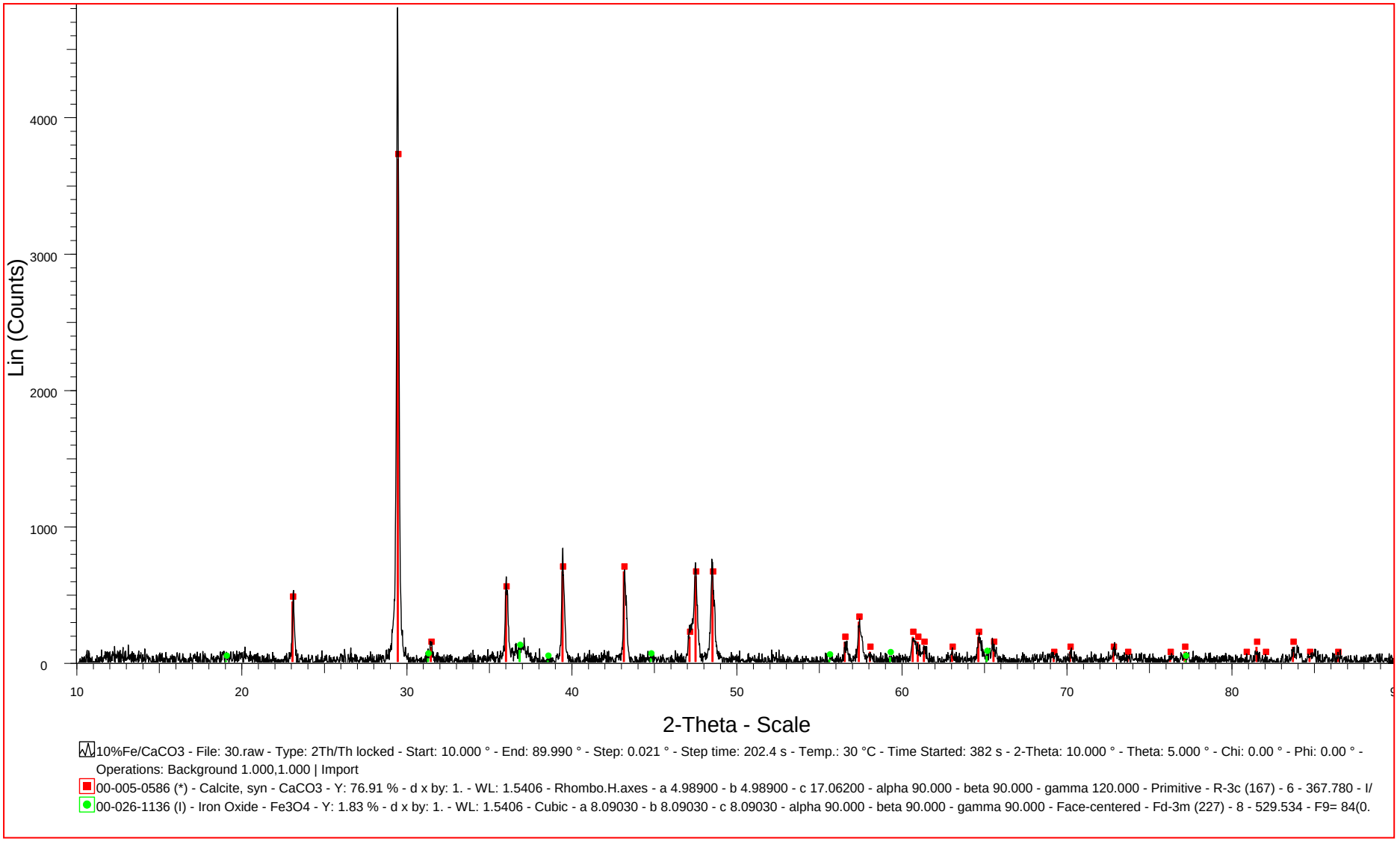


Figure A-3: XRD pattern of 10% Fe/$CaCO_3$ Nitrogen at 30 ˚C

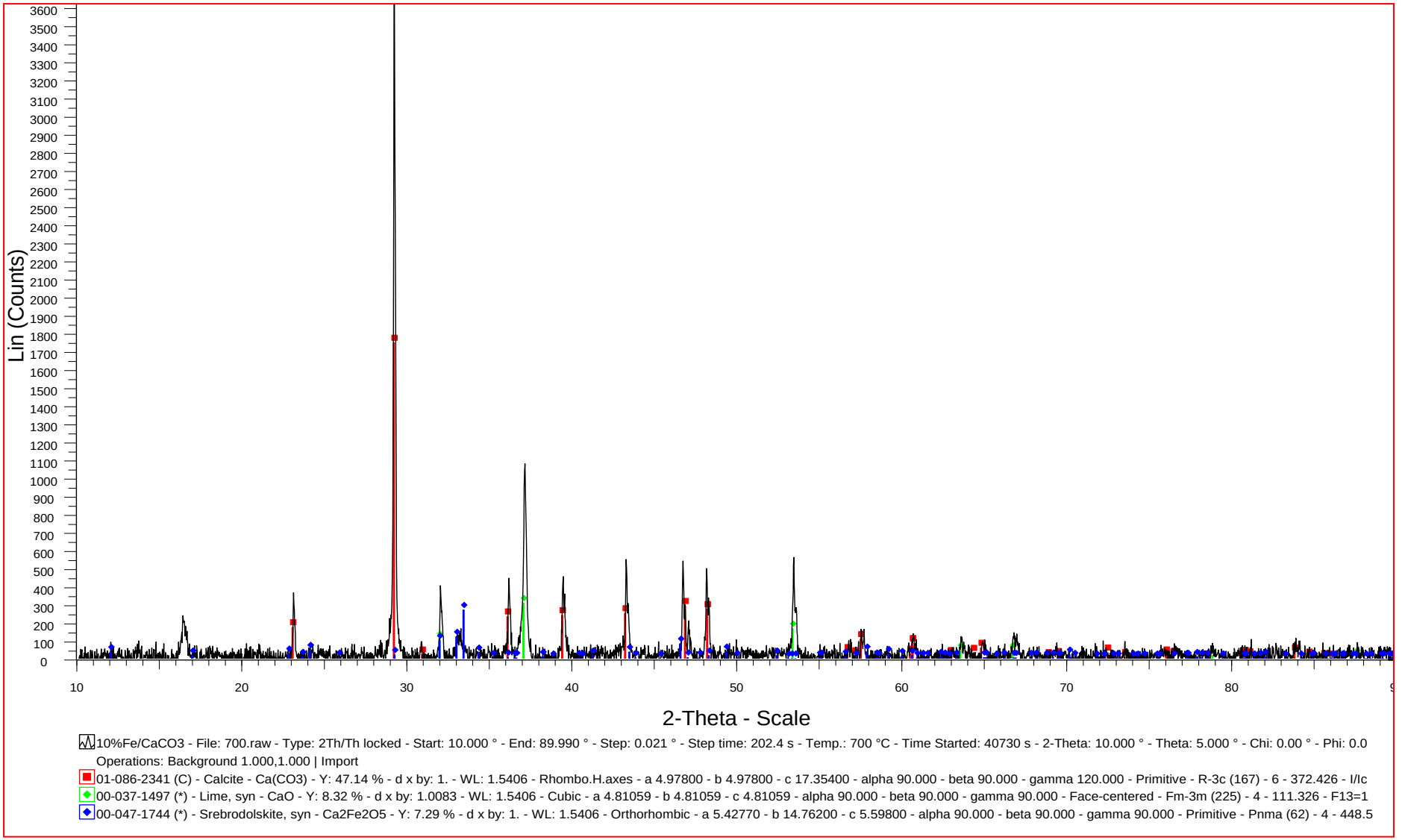


Figure A-4: XRD pattern of 10% Fe/$CaCO_3$ at 700 ˚C

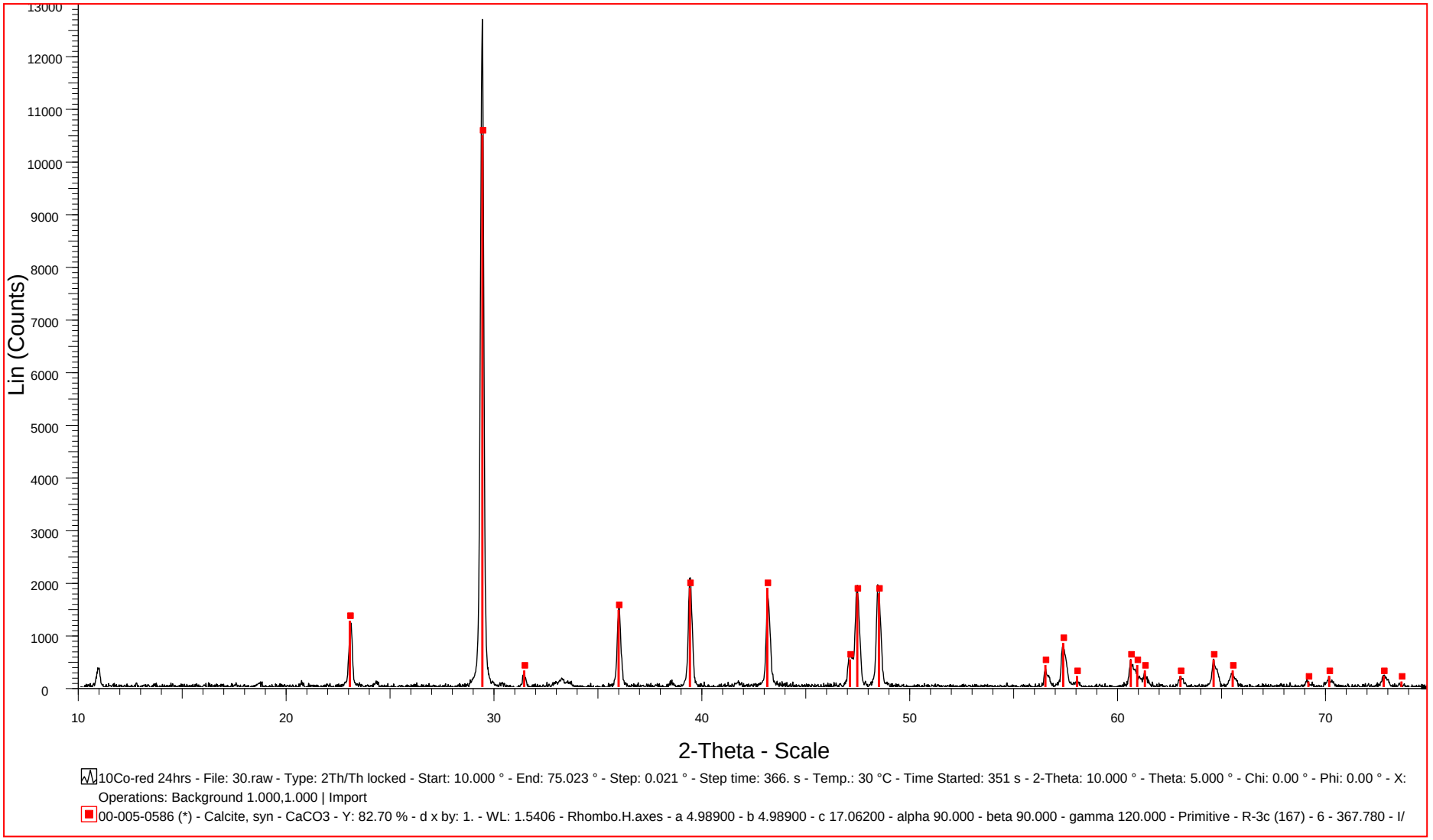


Figure A-5: XRD pattern of 10% Co/$CaCO_3$ at 30 ˚C

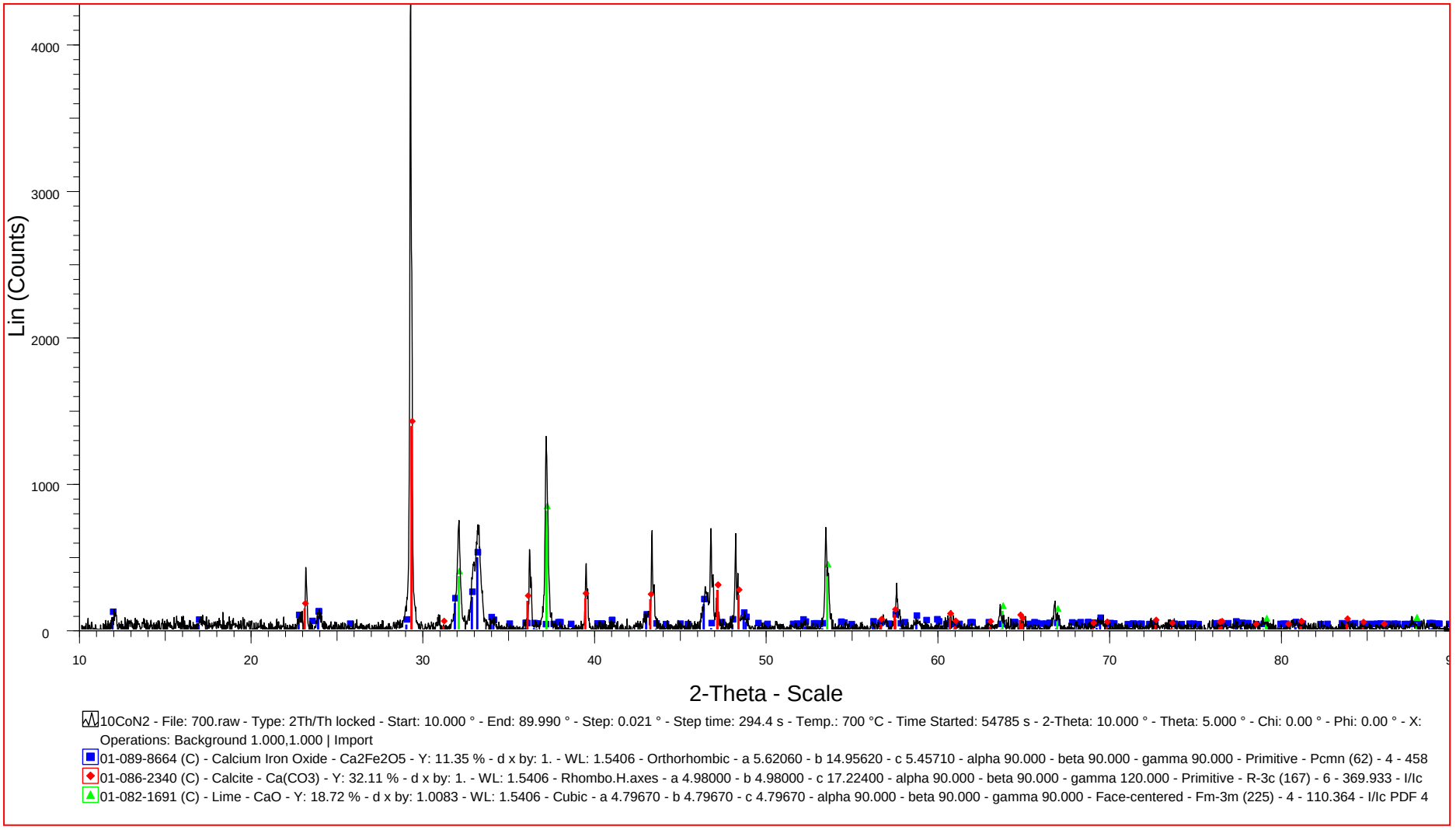


Figure A-6: XRD pattern of 10% Co/$CaCO_3$ at 700 °C

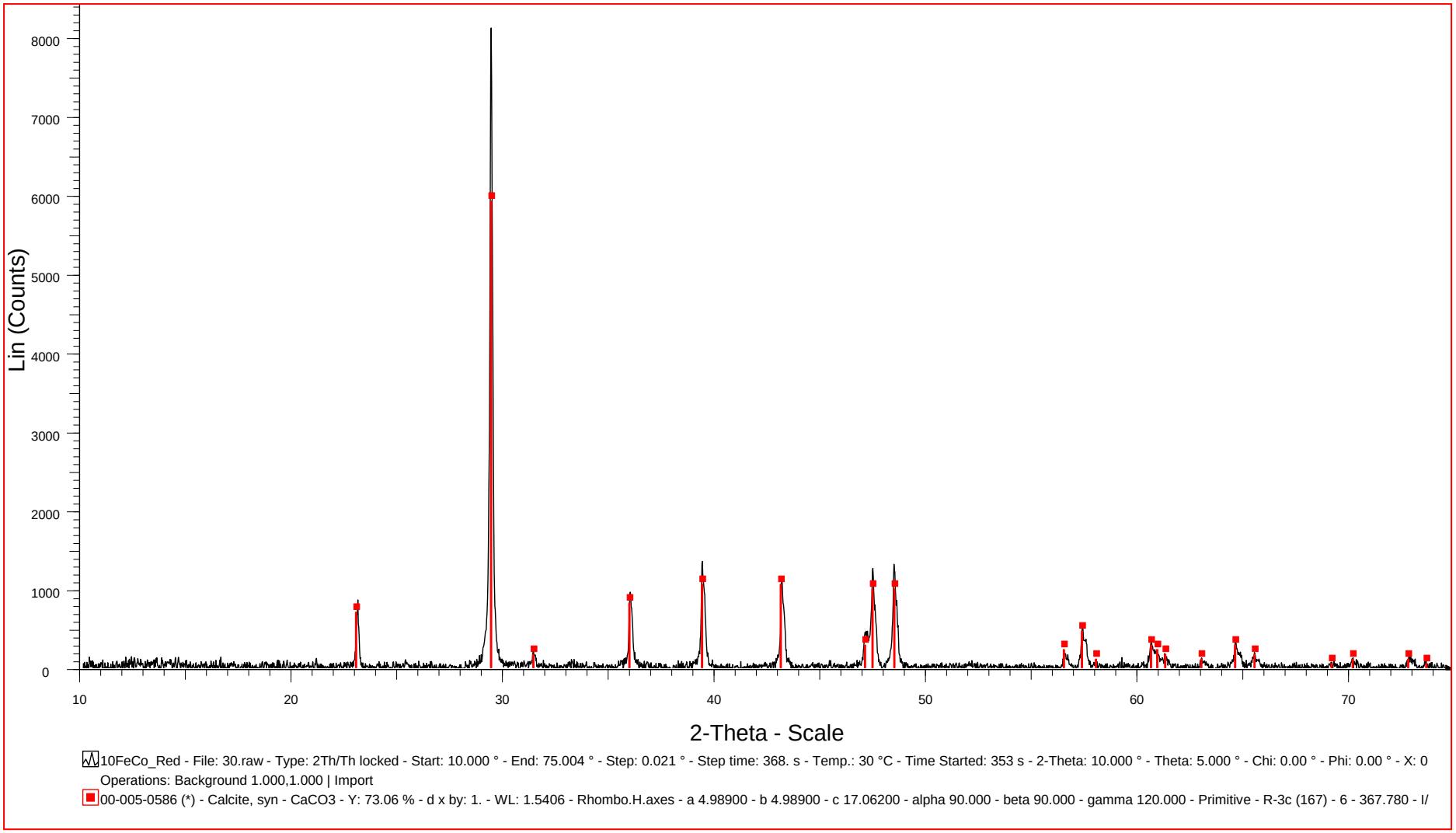


Figure A-7: XRD pattern of 10% Fe-Co/$CaCO_3$ at 30 ˚C

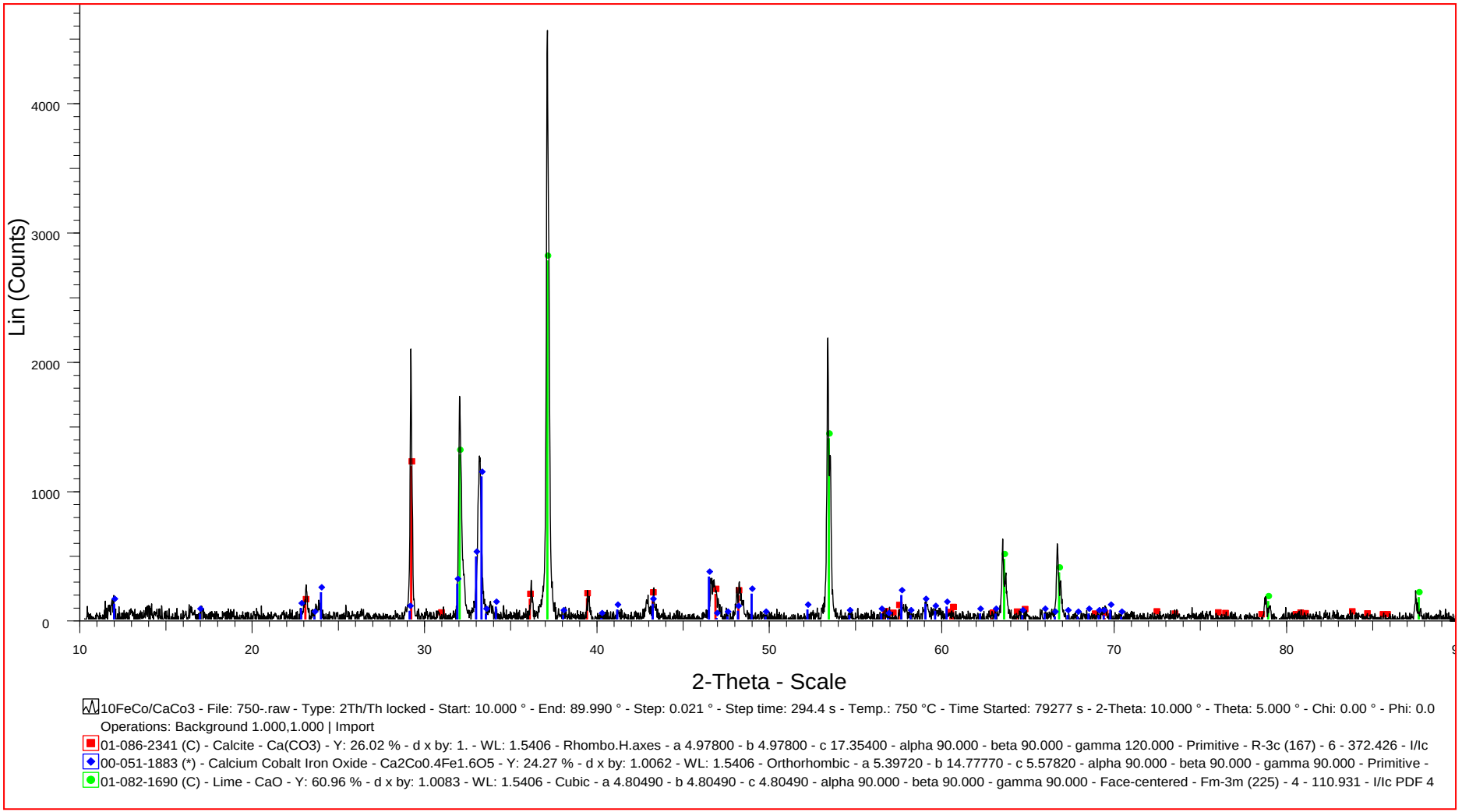


Figure A-8: XRD pattern of 10% Fe-Co/$CaCO_3$ at 750 ˚C

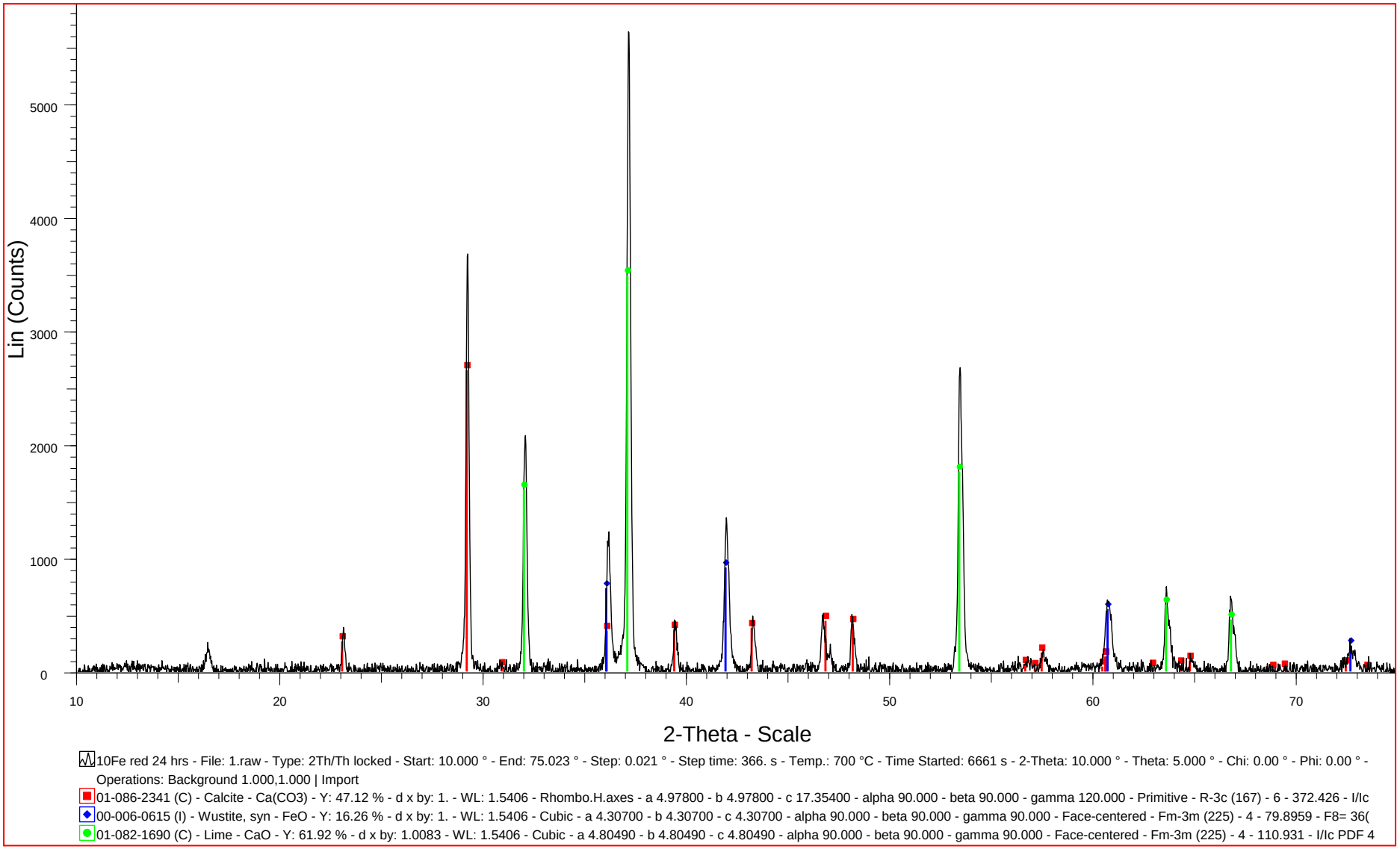


Figure A-9: In Situ reduction of 10% Fe/$CaCO_3$ XRD pattern after 1 hour

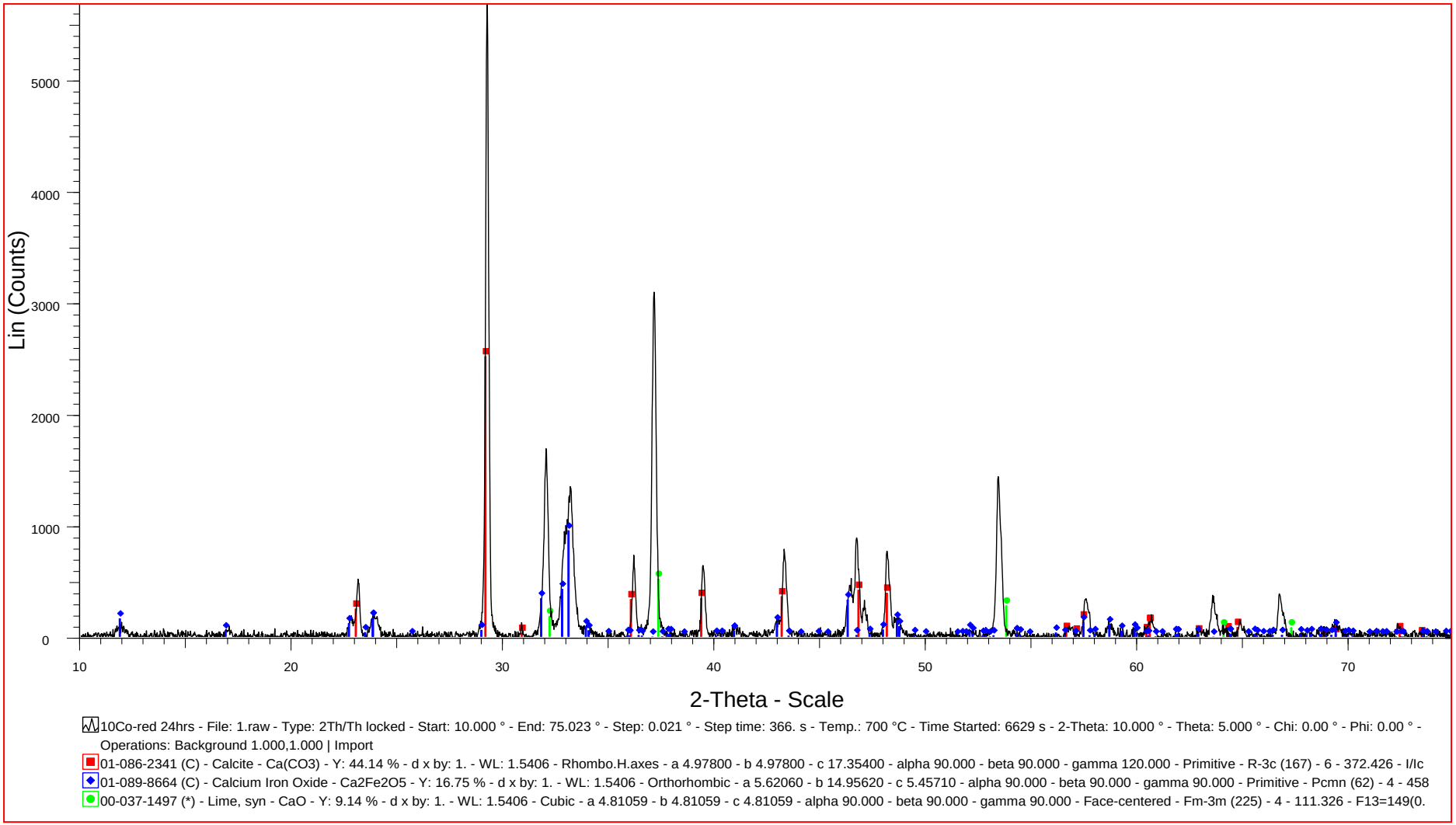


Figure A-10: In Situ reduction of 10% Co/$CaCO_3$ XRD pattern after 1 hour

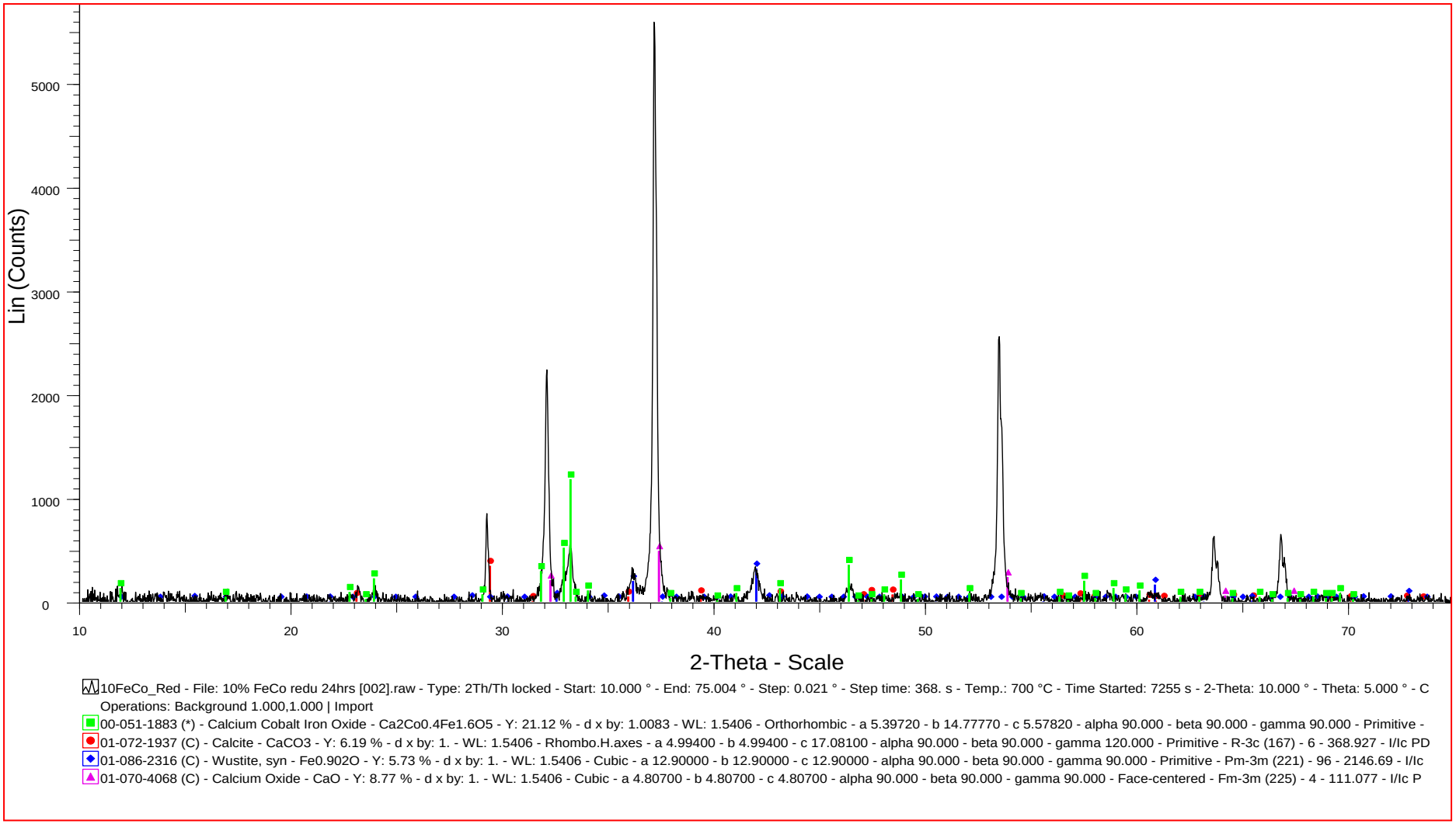


Figure A-11: In Situ reduction of 10% Fe-Co/$CaCO_3$; XRD pattern after 1 hour

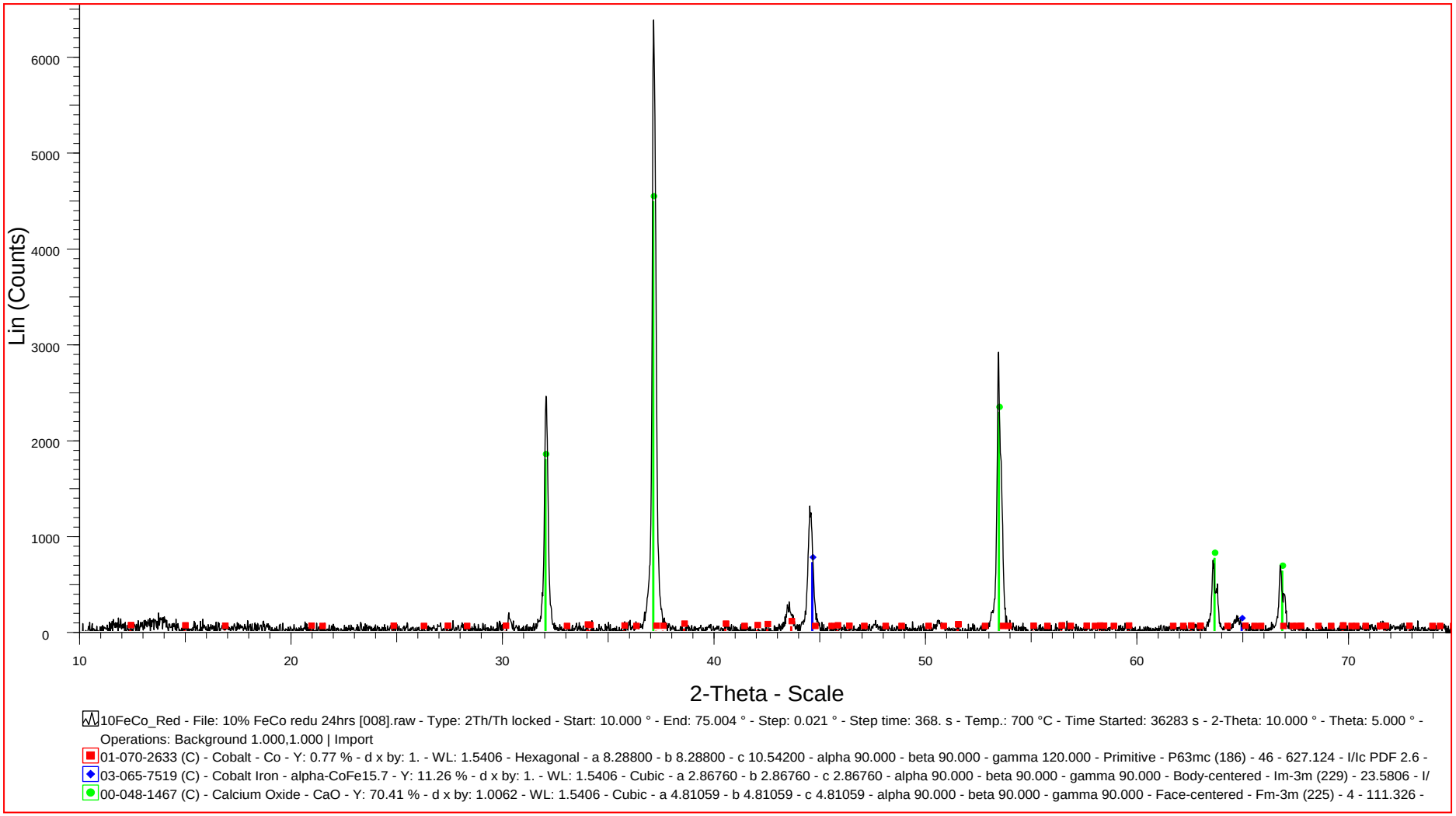


Figure A-12: 10% Fe-Co/$CaCO_3$ after 3 hours

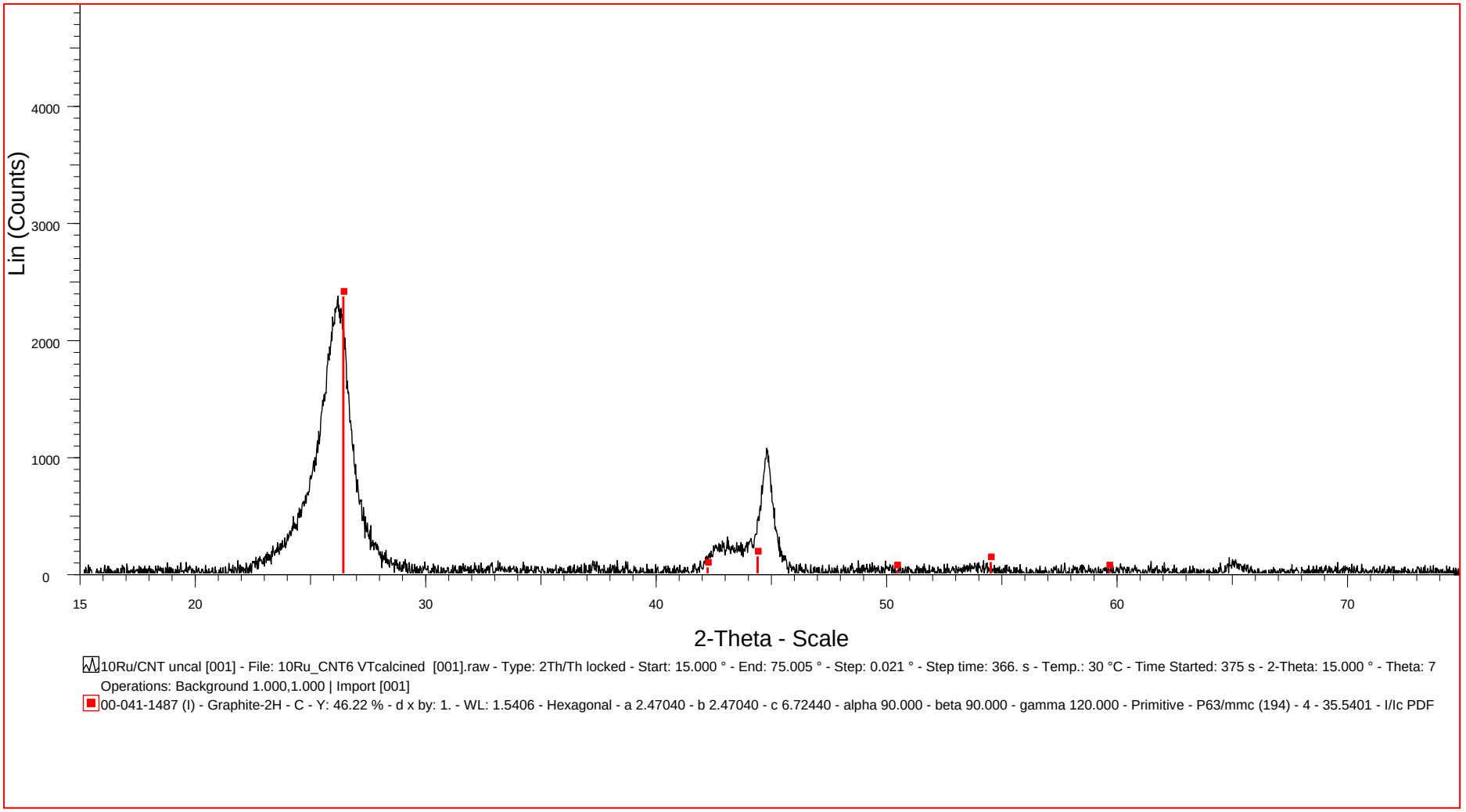


Figure A-13: 10Ru/CNT-IMP in situ calcination XRD pattern taken at 30 °C

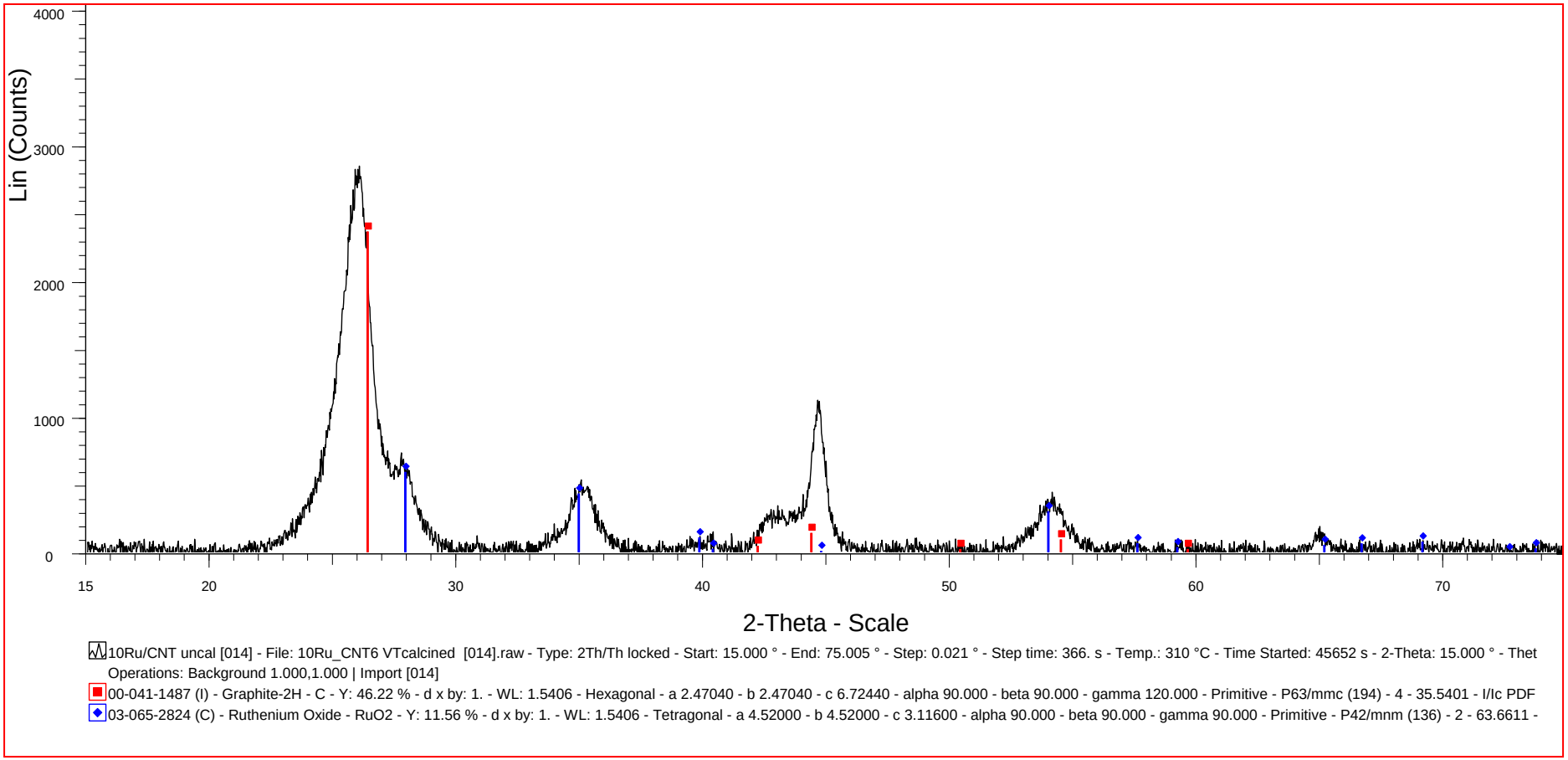


Figure A-14: 10Ru/CNT-IMP in situ calcination XRD pattern taken at 310 °C

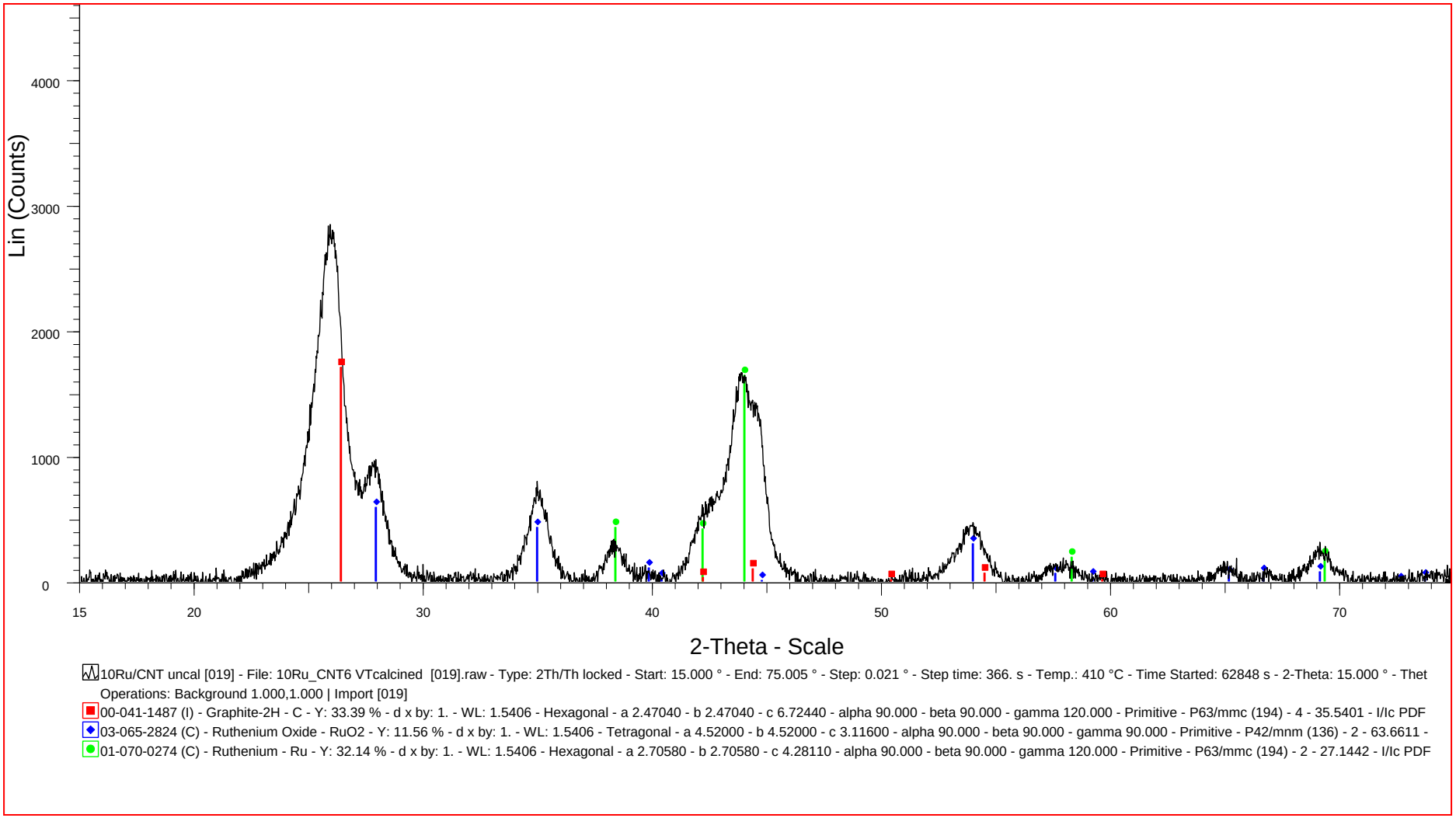


Figure A-15: 10Ru/CNT-IMP in situ calcination XRD pattern taken at 410 °C

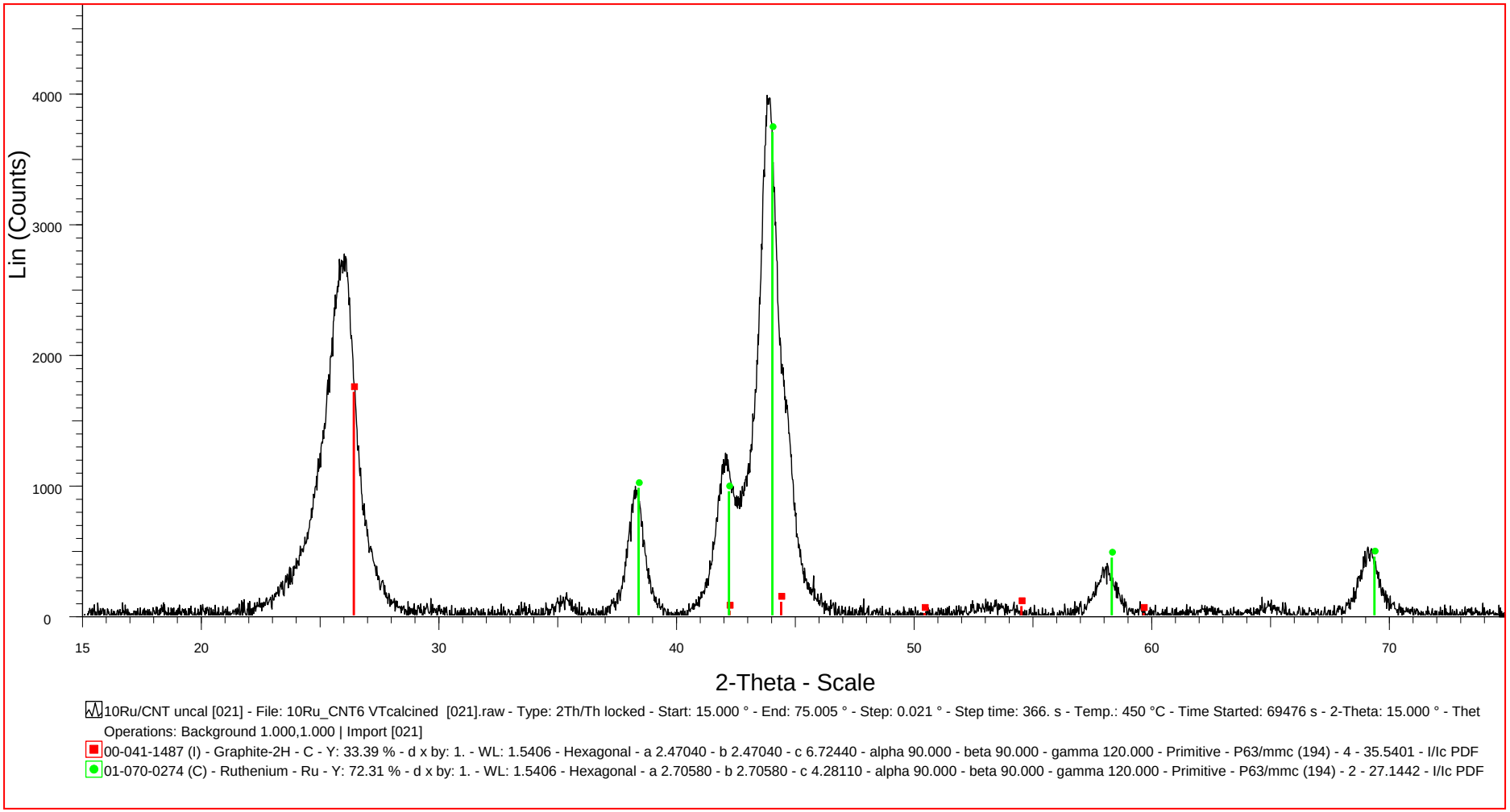


Figure A-16: 10Ru/CNT-IMP in situ calcination XRD pattern taken at 450 °C

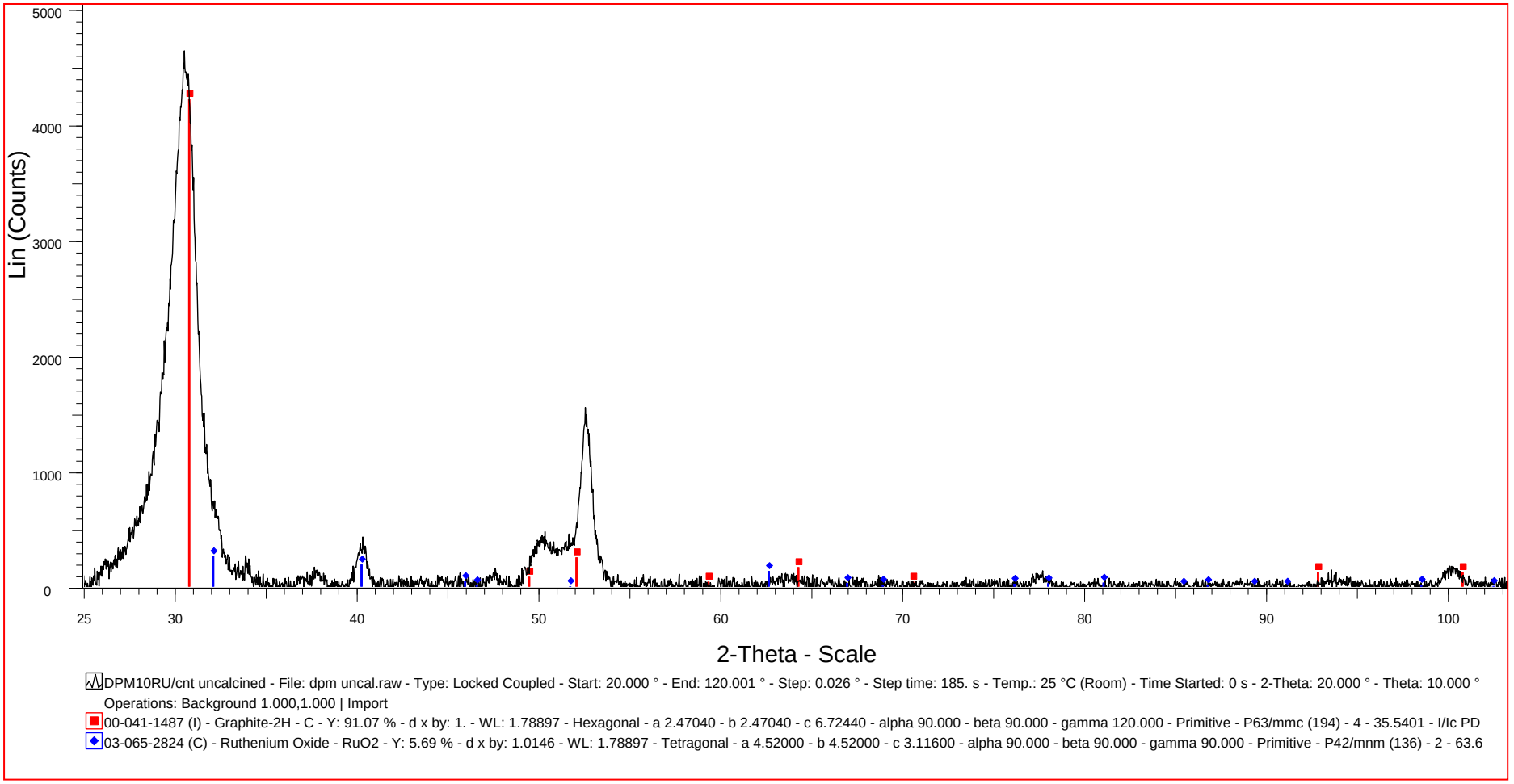


Figure A-17: 10Ru/CNT-DPM before heat treatment under nitrogen

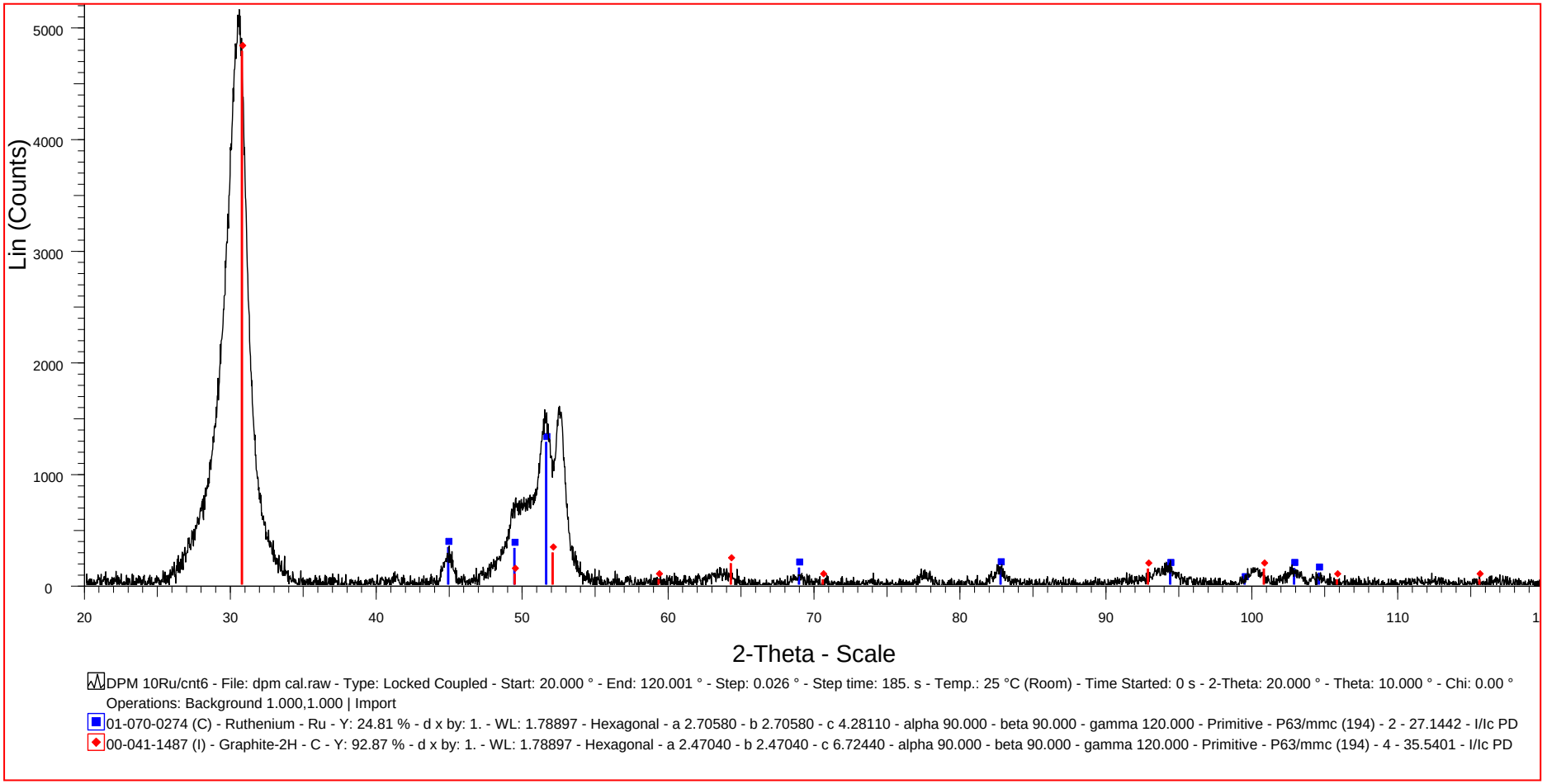


Figure A-18: 10Ru/CNT-DPM after heat treatment under N_2

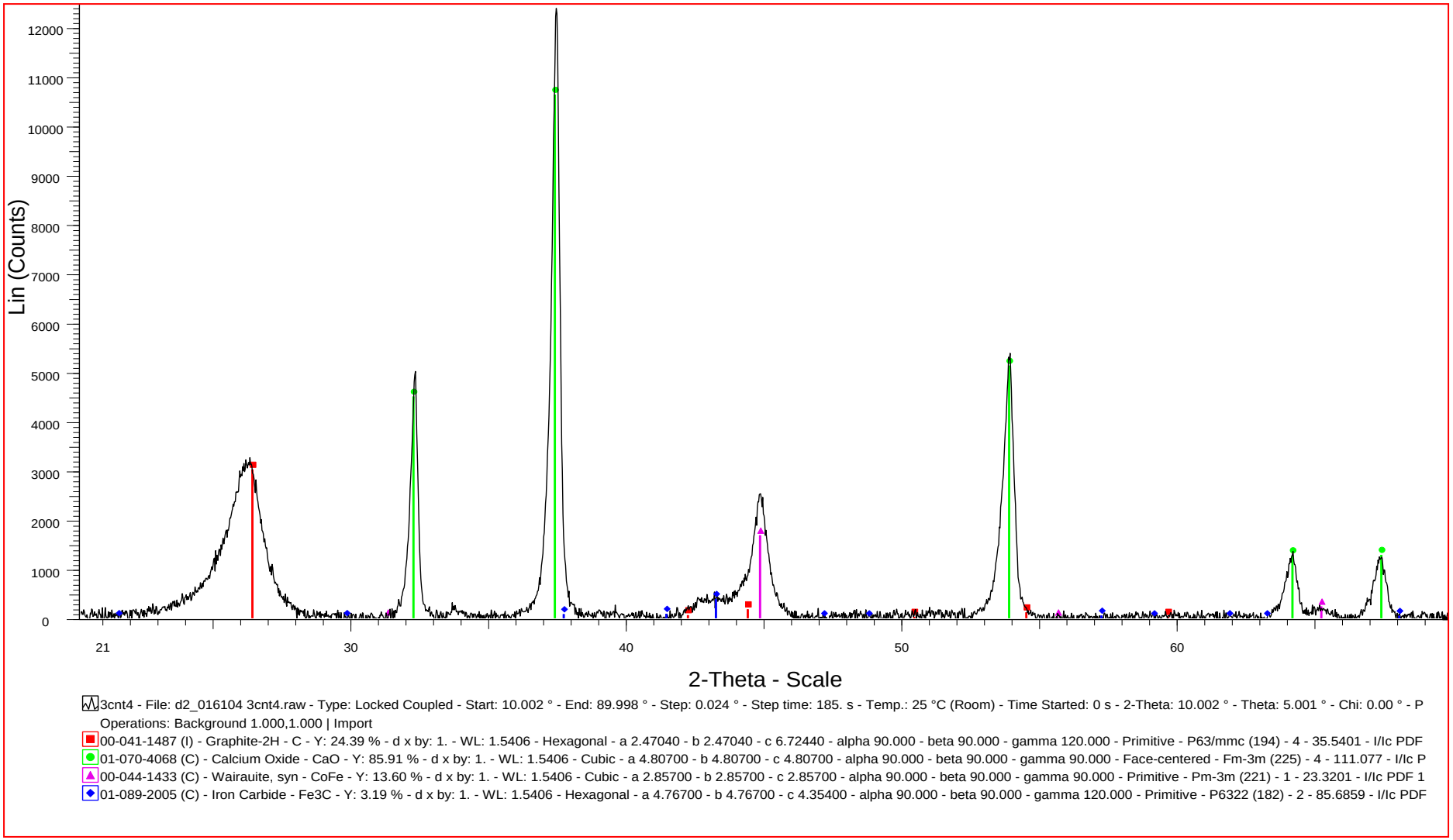


Figure A-19: XRD pattern of As grown CNTs

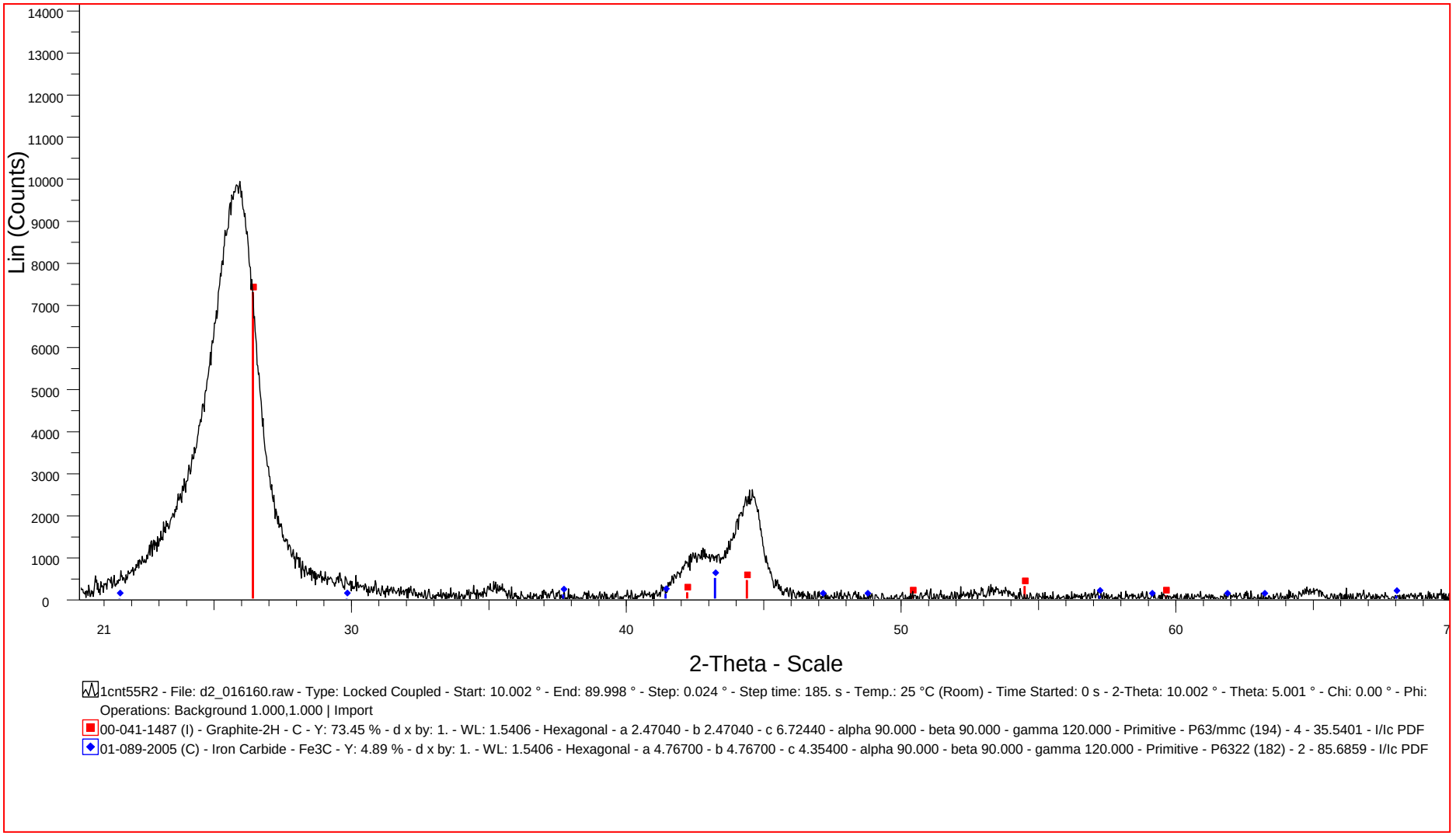


Figure A-20: XRD pattern of CNTS –(CNTR6)

Appendix B

Table B-1: Files on the disc that accompany this dissertation

Experiment	**Folder Name**
Heat treatment under N_2	$CaCO_3$ 10Fe_ $CaCO_3$-N_2 10Co_ $CaCO_3$-N_2 10FeCo_ $CaCO_3$-N_2 350-850 10Ru_CNTs-N_2
In situ reduction	10Fe_ $CaCO_3$-reduction 10Co_ $CaCO_3$-reduction 10FeCo_ $CaCO_3$-reduction 10Ru_CNTs-reduction